EXPERIMENTAL AND THEORETICAL ANALYSIS OF ISOTHERMAL AUSTENITE DECOMPOSITION IN ULTRA-LOW AND LOW CARBON STEELS

SUBMITTED BY
FARHAN IMTIAZ

SUPERVISED BY
Univ.Prof. Dipl.-Ing. Dr.techn. ERNST KOZESCHNIK

(INSTITUTE OF MATERIALS SCIENCE AND TECHNOLOGY)

VIENNA, NOVEMBER 2010

DISSERTATION SUBMITTED FOR THE DEGREE OF
"DOKTOR DER TECHNISCHEN WISSENSHAFTEN"
AT THE FACULTY OF
MECHANICAL AND INDUSTRIAL ENGINEERING
VIENNA UNIVERSITY OF TECHNOLOGY (TUWIEN)
VIENNA, AUSTRIA

TECHNISCHE UNIVERSITÄT WIEN
Vienna University of Technology

Dedicated
to
My Teachers, Beloved parents, Family members
and
People of Pakistan
(Suffering from most devastating flood of the country's history)

ACKNOWLEDGEMENTS

First of all I will like to acknowledge the financial support provided by Higher Education Commission (HEC), Government of Pakistan during my PhD studies. Indeed I express my heartiest gratitude to my supervisor, Univ.Prof. Dipl.-Ing. Dr.techn. Ernst Kozeschnik. I took lot of inspiration and guidance from his critical, encouraging and knowledgeable reviews which made it possible to convert my thoughts into thesis. I am also thankful for his financial support provided for participation in High-Speed Quenching Dilatometer 805A (by BÄHR Thermoanalyse) training course, MatCalc training course, Thermec Conference 2009 and PTM-2010 Conference.

I am grateful to Dipl.-Ing.Dr.rer.nat. Piotr Warczok for the assistance he provided to understand the MatCalc software package along with Prof. Ernst Kozeschnik.

I am indebted to Heidemarie Knoblich and Natalia Paulenko for preparation of my samples for metallography and digital grain analysis with state of the art Tegra doser-5, Tegra force-5 and Tegra Pol-31 grinding and polishing machines. I am equally obliged to Christian Zaruba for his kind help for installation of DICTRA, Exceed software packages on Linux and solution of computer problems and software installations.

It is my pleasure to recognize the help of Dagmar Fischer, Silvia Windisch and Tanja Grünwald for various administrative matters of the institute.

At the end how I can forget to acknowledge my wife (Nudrat Naeem) and daughters (Abeera Farhan and Naveera Farhan) for their support and patience. Finally I will say special thanks to my father (Dr. Muhammad Imtiaz Hanif) and mother (Farzana Imtiaz) for their kind prayers and encouragement.

ABSTRACT

The aim of the present work is to investigate the mechanism of the austenite to ferrite transformation in ultra-low to low carbon steels. In this regard industrial quality steels were machined into standard hollow and solid cylindrical samples and thermally treated in a high-speed quenching dilatometer. The austenitization temperature for hollow samples was 950°C, whereas it was 950 and 1100°C for solid samples. The target isothermal transformation (IT) temperatures are chosen between 890 and 660°C. Samples were soaked at 950°C for 300s and at 1100°C for 600s. After soaking specimens were quenched to their respective target IT temperatures. For solid samples cooling rate of 40K/s was used while for hollow samples objective was to obtain maximum possible cooling rates. In the present study cooling rates up to 3400K/s were successfully obtained with hollow samples.

At relatively higher target temperatures, the austenite to ferrite transformation started after reaching the IT temperatures. In case of comparatively lower target IT temperatures austenite decomposition has started before reaching the IT temperatures. Hollow samples of ultra-low carbon steel and all samples of low carbon steel with maximum alloying content are not sensing this discrimination between lower and higher IT temperatures regimes. All target IT temperatures of hollow samples of ultra-low carbon steel were showing the onset of the austenite to ferrite transformation before reaching the target IT temperature while all samples of low carbon steel with maximum alloying elements have shown austenite decomposition after reaching the target IT temperatures.

Dilatation data of all samples of ultra-low to low carbon steel were used to sketch the experimental isothermal time temperature transformation (I-TTT) diagrams. MatCalc and DICTRA simulations were carried out to construct the theoretical isothermal time temperature precipitation (I-TTP) diagrams for comparison purpose and to understand the mechanism responsible for decomposition of austenite and growth of ferrite. The intension in this regard was to see the influence of nucleation kinetics as MatCalc considers it and DICRA will not. From the comparison of experimentally measured I-TTT and theoretically calculated I-TTP diagrams it seems evident that present experiments are showing strong dependency on the nucleation kinetics.

From the mechanism point of view, hollow samples of ultra-low carbon steel were showing interface-controlled and, eventually, two-stage transformation kinetics. Solid samples of this alloy were showing diffusion-controlled, interface-controlled and two-stage transformation kinetics. The hollow and solid samples of low carbon steel austenitized at 950°C with lower and intermediate alloying contents were showing diffusion-controlled, two-stage and massive transformation mechanisms whereas solid samples which are austenitized at 1100°C were not showing any complete interface-controlled massive transformation mechanism. In comparison low carbon alloy with maximum alloying element content were showing only diffusion-controlled transformation kinetics irrespective of the cooling rate or type of sample.

TABLE OF CONTENTS

CHAPTER 1: INTRODUCTION

Decomposition of austenite has attracted the interest of researcher for many decades. This is mainly due to the variety of different austenite decomposition products. During decomposition, the crystal structure of austenite changes from face-centered cubic (fcc) to body-centered cubic (bcc). There are two competing mechanisms by which this change in crystal structure can take place (with respect to the chemical compositions of the sample used) i.e. displacive or reconstructive. Massalski has considered interface controlled massive transformation as regular class of solid-state reactions (figure 1.1). In contrast Christian and Bhadeshia have characterized it also as reconstructive transformation mechanism (see e.g., References ([1]-[6])).

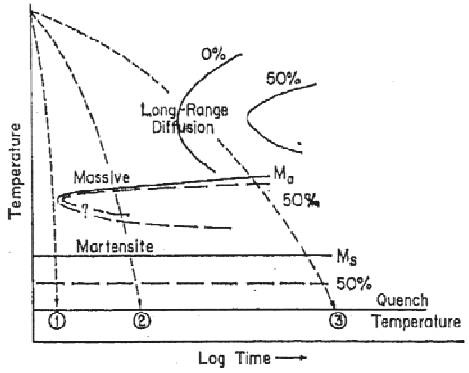

Figure 1.1: A schematic time - temperature - transformation diagram (TTT), showing the possible conditions for the occurrence of a massive transformation. Unlike in the case requiring long-range diffusion, the curve representing the 50% transformation line in the massive transformation is drawn close to the 0% line in order to indicate the rapidity of the transformation process [5].

Austenite to martensite transformation is displacive in nature. Martensite has a body-centered tetragonal structure where tetragonality increases with carbon content. Martensite formation in plain carbon steel is connected with a minimum quenching rate, which reaches very high values with decreasing carbon content. In the case of ultra-low carbon steel having less than 0.005%C, the minimum cooling rate capable of producing a martensitic structure exceeds 35000K/s. Cooling rates of approximately 10,000K/s are required for martensitic or displacive reactions in carbon contents from 0.004 to 0.013 wt%. With 0.1%C martensite is observed following quenching rates of less than 5000K/s (see e.g., References ([5],[6])). Since these high rates are not achieved in the present experimental setup and at the same time target IT temperatures are chosen in such a way that they are not suitable for austenite to martensitic transformations. Austenite is assumed to be transformed into ferrite only, with either short range (interface controlled) or long range (diffusion controlled) transfer of atoms.
Although the austenite to ferrite transformation is the most studied phase transformation there is still considerable lack of understanding as far as the exact mechanisms of nucleation and growth of ferrite grains and interface movement and the detailed role of segregation is concerned. Bibby and Parr [7] has showed that the austenite to ferrite transformation start temperature for almost pure carbon steel decreases with increasing cooling rates (upto 5000K/s) and then becomes constant for a series of cooling rates from 5000 to approximately 30000K/s. Militzer [8] from their experiments on ultra-low carbon steel have described that increasing the cooling rate decreases the transformation temperatures and refines the ferrite grain size. For an initial grain size of approximately 40μm, the transformation start temperature decreases from 895 to 860°C, with the increase in cooling rate from 1 to 195K/s.

Kozeschnik and Gamsjäger [1] in contrast have shown that up to 160K/s the onset of the austenite to ferrite transformation was 897°C. This transformation temperature is almost 37°C higher than the results of [8].
Kozeschnik and Gamsjäger [1] have also observed a two-stage transformation behavior in 0.007 wt%C steel in both, two phase γ and α regions as well as the single phase α region. They find that this observation can be attributed to the transition from a thermally activated interface controlled reaction to a slower diffusion controlled reaction. They also observed that the transformation commonly started already during fast quenching and before reaching the final isothermal annealing temperature. Liu et al. ([9], [10]) have studied a 0.01 at%C steel alloy isochronally and a 0.04 at%C steel alloy isothermally. In the isochronal study [9], they also observed the two-stage transformation mechanism. They concluded that the transformation starts with diffusion controlled reaction and then shifted to an interface controlled mechanism.
In the isothermal study [10] they also observed the similar two-stage transformation mechanism as described by Kozeschnik and Gamsjäger [1]. They also concluded that the nature of mechanism during isochronal annealing and during isothermal annealing is essentially different with respect to the mechanisms involved.
We have seen above that some discrepancy exists between the results of various researchers. Understanding of the decomposition kinetics of austenite is of immediate relevance for metals processing industry, because phase transformations are the basis of microstructure-forming processes in many alloys.
Recently a trend has also developed which involves reducing the carbon concentration of steel down to the ppm level to improve the ductility and weldability and to lower the ductile-brittle transition temperature. Since the austenite to ferrite transformation is the last process that determines the microstructure of hot-rolled steel, fundamental knowledge is required to comprehensively control this transformation such that final products of desired microstructure can be made (e.g., references ([9], [10])).
It seems necessary to investigate the mechanism of the austenite to ferrite transformation for scientific understanding and industrial practice. In this regard in the present study ultra-low carbon steel is investigated along with low carbon steels in terms of their isothermal transformation behavior. The specimens of these steels are austenitized and quenched such that transformation occurs either in the two-phase austenite plus ferrite region, or in extrapolated ferrite one-phase region, under suppression of pearlite formation. The experimental investigations are complemented by computer simulations for the austenite to ferrite phase transformation using the software packages MatCalc ([11], [12]) and DICTRA [13]. This study is aimed at performing a systematic investigation of the austenite to ferrite transformation.
The present chapter has shortly addressed the discrepancies among the results of various researchers and also summarized our approach to solve the problem in short. Chapter 2 describes the motivation and objective of the thesis more elaborately. In Chapter 3, state of the art is described in detail. Chapter 4 describes experimental set up for our project and Chapter 5 is describing the procedural details of the MatCalc and DICTRA simulations along with theoretical dilatation profiles. In Chapter 6, experimental and simulated results are compared for understanding of the mechanism involved in controlling the kinetics of the austenite to ferrite transformation. Conclusions of the present study are briefed in Chapter 7. References, additional details and list of equipments and software packages used are identified in the Chapter 8 and appendix respectively.

CHAPTER 2: MOTIVATION AND OBJECTIVE

Kozeschnik and Gamsjäger [1] have studied the decomposition of austenite in Fe-C model alloy. Their results have shown the presence of a two-stage austenite to ferrite transformation mechanism in ultra-low carbon steel having 0.007%C. In their study the austenite to ferrite transformation has initiated at very low driving force and hence showing very low undercooling. The transformation perhaps starts almost immediately after entering the austenite and ferrite two-phase region. This is in contrast to previous experience, which tells that considerable undercooling is necessary to start the transformation under these conditions. In their study, they have shown that previous analyses have not taken into account that segregation to prior austenite grain boundaries tremendously influences the ferrite grain nucleation. The differences in nucleation behavior are attributed to some segregation present in the previous studies in contrast to almost no segregation in the samples they have used for their experiments.

The results of the study [1] have initiated interest to study this important phenomenon in systematic manner and more detail due to the importance of the phenomenon for scientific understanding. This is the basic motivation behind the present study.

In the present study, variations in alloys are made in such a way that they contain almost solute free to solute segregated boundaries. Variation in cooling rates is given to see the effect of nucleation. Austenitization temperature was changed to see how the austenite grain size effects the phase transformation. Under such conditions understanding the mechanism controlling the kinetics is the prime objective of the present research.

CHAPTER 3: STATE OF THE ART

3.1 Morphological variants of austenite decomposition products in steel

There are essentially four morphological variants of austenite decomposition products namely ferrite, pearlite, bainite and martensite. Figure 3.1 is showing the sketch of these products.

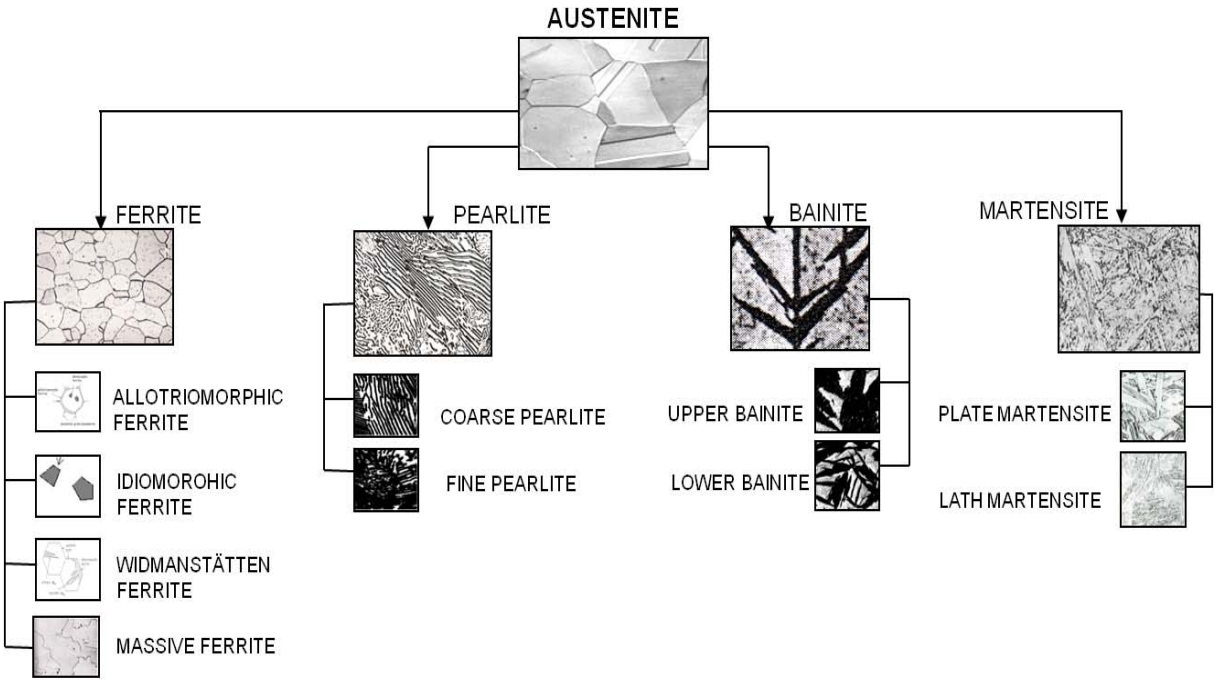

Figure 3.1: Morphological variants of austenite decomposition products in steel.

From the mechanism point of view ferrite has been classified into four forms: allotriomorphic ferrite, idiomorphic ferrite, widmanstätten ferrite and massive ferrite ([2], [3], [14]). Ferrite is also present in pearlite and bainite in different shapes. Martensite has the body central tetragonal structure and the tetragonality increases with carbon content [6]. For low to ultra-low carbon steels tetragonality decreases and with decreasing carbon content martensite takes the shape of normal ferrite.

3.2 Definitions of austenite decomposition products in steel

3.2.1 Allotriomorphic ferrite

The term 'allotrimorphic' is from Greek which means that phase is crystalline in internal structure but not in outward form i.e. the shape of that ferrite does not reflect its crystalline symmetry. The reason for the above behavior is that the allotriomorphic ferrite nucleates at prior austenite grain boundaries and tends to grow along the grain boundary ([3], [15], [16]). Their growth rate along the boundary is faster than the growth rate in a normal direction. Figure 3.2a illustrates the growth along the boundary and figure 3.2b illustrates the growth in a normal direction. The schematic figure 3.3 and figure 3.4 show that allotriomorphic ferrite grows along the grain boundary i.e. nothing indicates that it has a bcc structure or crystalline facets.

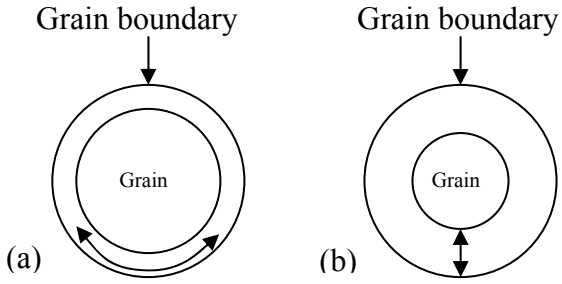

Figure 3.2: (a) Growth along the grain boundary, (b) growth in a normal direction to the boundary.

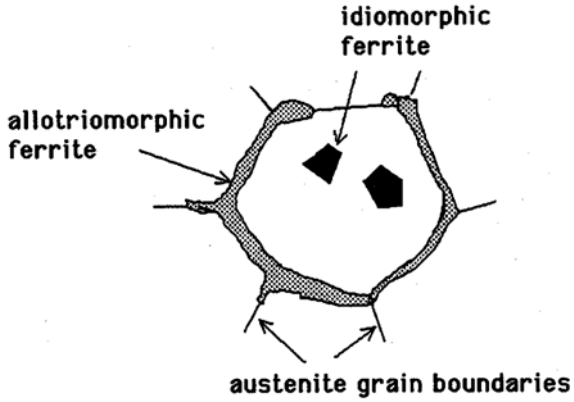

Figure 3.3: Schematic diagram of allotriomorphic and idiomorphic ferrite ([15], [16]).

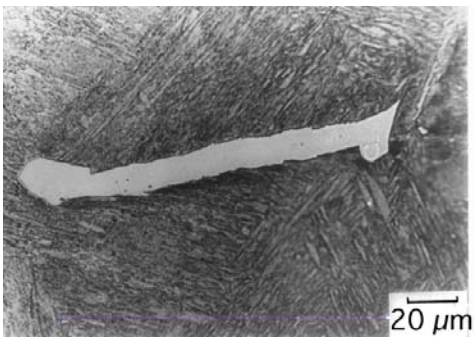

Figure 3.4: Microstructure of allotriomorphic ferrite growing along the prior austenite grain boundary ([3], [15], [16]).

3.2.2 Idiomorphic ferrite

By contrast if ferrite is nucleated inside the grain perhaps on a nonmetallic inclusion present in the steel, we call it idiomorphic ferrite. It has some aspect of the crystallography of ferrite because it exhibits crystallographic facets as can be seen in figure 3.5. The grain tends to be more equiaxed i.e. roughly the same dimension in all directions. Some times in steel, nonmetallic inclusions (controlled additions) are deliberately added to stimulate the formation of ferrite grain inside the austenite grain (i.e. parent austenite grain). Idiomorphic is again from the Greek meaning that its shape has some relationship to the crystalline symmetry because of crystallographic faceting ([3], [15], [16], [17]). Figure 3.5 shows the metallograph of an idiomorphic ferrite.

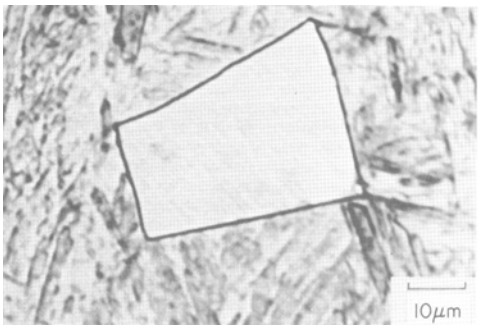

Figure 3.5: Microstructure of idiomorphic ferrite ([15], [16]).

3.2.3 Widmanstätten ferrite

Under the optical microscope Widmanstätten ferrite appears in the shape of a thin wedge, whereas this wedge is classified as between plate or lath [3]. If Widmanstätten ferrite nucleates directly from the austenite boundary then it is called primary Widmanstätten ferrite. On the other hand if Widmanstätten ferrite nucleates from allotrimorphic ferrite then it is called secondary Widmansttäten ferrite (figure 3.6) [17].

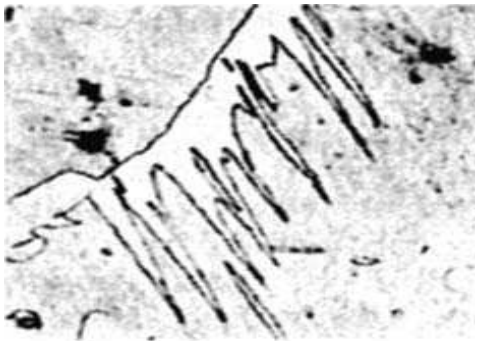

Figure 3.6: Wedge shaped Widmanstätten ferrite plate obtained as a result of isothermally holding the 0.34 wt%C at 725°C for 15 minutes ([15], [16], [17]).

3.2.4 Massive ferrite

Massive ferrite has the distinction that it inherits the composition of parent austenite. Massive ferrite growth is principally possible below T_0. Massive growth does not involve long range diffusion. Massive ferrite grains nucleate at austenite grain boundaries and grow rapidly into the surrounding γ. The growing ferrite can cross the parent austenite boundaries and the grain size of product phase can be greater than the product phase. The transformation proceeds until all the austenite is consumed [3]. The complete consumption of austenite means that as a result of transformation we will get a single phase having large grains. These grains may have equiaxed morphology due to impingement or having an irregular appearance because of rapid growth. In general we can say that massive ferrite may consist of random equiaxed grains but the grain boundaries may be more jagged and their shape related to growth conditions. According to Bhadeshia, massive ferrite cannot strictly be classified as separate morphology and transformation begins with the growth of idiomorphs or allotriomorphs. In contrast Massalski is considering the massive transformation as separate possible reaction competing the martensite ([3], [5], [6]). Figure 3.7 is showing the microstructure of massive ferrite.

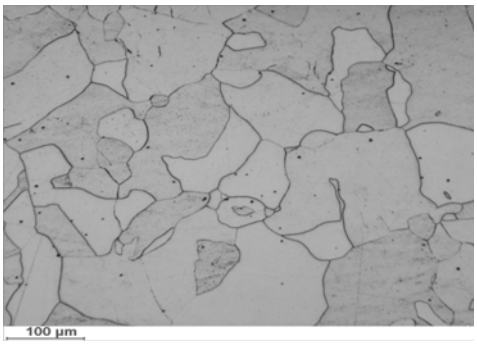

Figure 3.7: Microstructure of massive ferrite obtained as a result of rapid quenching of 0.007%C ultra-low carbon steel [1].

3.2.5 Pearlite

There are three horizontal lines in the Fe-C equilibrium diagram representing three reactions. Pearlite is the product of that reaction which is obtained at the lowest temperature. Figure 3.8 represent the schematic of that reaction in which a solid phase called austenite is transformed into two solid phases i.e. ferrite and cementite on cooling.

$$\text{Austenite } \_\gamma\ (0.8\%C) \underset{\text{Heating}}{\overset{\text{Cooling}}{\rightleftharpoons}} \text{Ferrite}\_\alpha\ (0.025\%C) + \text{Cementite}\_Fe_3C\ (6.7\%C)$$

Pearlite is a fine eutectoid, lamellar mixture of ferrite and cementite. Its structure is similar to the finger prints. The thickness ratio of the ferrite and cementite layers in pearlite is approximately 8 to 1 ([18], [19]). Figure 3.9 is showing the photomicrograph of coarse and fine pearlite.

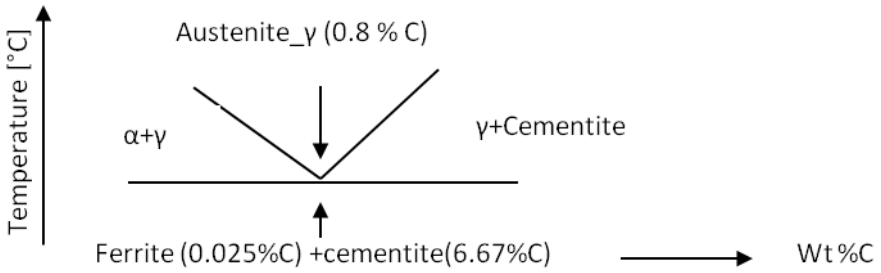

Figure 3.8: Schematic representation of eutectoid reaction in the Fe-C equilibrium diagram resulting pearlite which is a finger print mixture of ferrite and cementite phases.

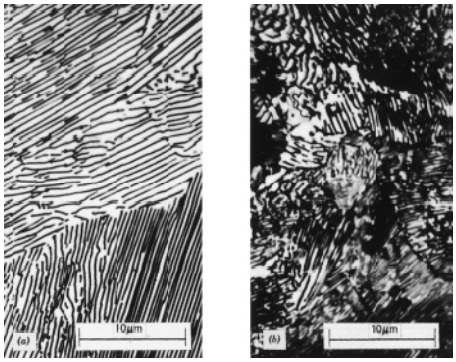

Figure 3.9: Photomicrograph of (a) coarse pearlite and (b) fine pearlite [19].

3.2.5.1 Coarse pearlite

Coarse pearlite is obtained at relatively higher temperature. Coarse and fine pearlite morphologies are differentiated on the basis of interlamellar spacing. The minimum interlamellar spacing S_{min} is inversely proportional to undercooling below the eutectoid temperature [6].

$$S_{min} \propto (\Delta T)^{-1} \qquad \text{(eq. 3.1)}$$

The velocity of pearlite colonies is constant and given by the following equation [6]

$$v = kD_C^{\gamma}(\Delta T)^2 \qquad \text{(eq. 3.2)}$$

Where k is the thermodynamic term, which is roughly constant. D_C^{γ} is the diffusivity of carbon in austenite i.e. the γ phase. Just below Ae_1 carbon can diffuse a greater distance relative to higher undercoolings from Ae_1 and this is the reason that interlamellar spacing close to eutectoid temperature is higher. Observed interlamellar spacing may vary from approximately 1µm at high temperature to 0.1µm at lower temperature.

3.2.5.2 Fine pearlite

In contrast to coarse pearlite, fine pearlite is obtained at a higher undercooling from eutectoid temperature. At low temperature carbon diffusion rate decreases and so the interlamellar spacing. Here it must be noted that less time is required for transformation of the austenite to ferrite in case of fine pearlite. This is because at higher undercooling a higher driving force is available to drive the reaction. This fact is shown in the figure 3.10.

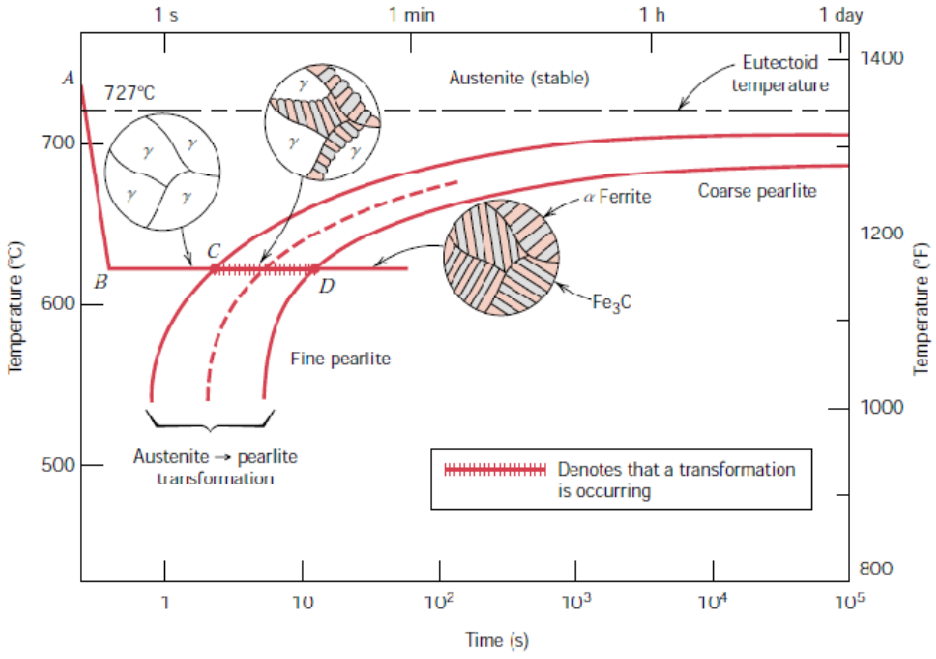

Figure 3.10: Isothermal transformation diagram of eutectoid steel containing 0.8%C, showing that higher time is required to obtain the coarse pearlite from austenite than fine pearlite [19].

As mentioned above that the interlamellar spacing could reach to 0.1µm, which means that it will be difficult to resolve the individual features of fine pearlite and etching will reveal all the interfaces and the observed microstructure will appear dark.

3.2.6 Bainite

In 1934 this morphological variant was given a name bainite in the honor of E.C. Bain who has presented the first ever photomicrograph of bainite, taken at a magnification of X1000. Davenport and Bain discovered this microstructure calling it initially 'acicular, dark etching aggregate' and afterwards bainite as they were confusing it with 'martensite troostite' [20]. Bainite is a non lamellar aggregate of ferrite and cementite. Its microstructure is quite distinct from pearlite. It is obtained when austenite is supercooled to large supersaturations below the nose of the pearlite transformation curve. Bainite has its own characteristic C curve overlapping with the pearlite curve. Figure 3.11 is presenting the schematic of above said C curve. The high range and low range variants of bainite are called upper bainite or feathery bainite and lower bainite or acicular bainite ([6], [20]).
Figure 3.12 is representing the difference between different morphological variants in eutectoid steel [20].

3.2.6.1 Upper bainite

Upper bainite forms at relatively higher temperature. In figure 3.13a we can see that upper bainite consists of very fine platelets of ferrite separated by regions of cementite. The ferrite plate is about 10μm in length and 0.2μm in thickness [21].

3.2.6.2 Lower bainite

This morphological variant of bainite forms at relatively lower temperature and is also called acicular or fine bainite. Lower bainite by contrast also has cementite precipitation inside the plate of ferrite (figure 3.13b). At the same time the amount of cementite present between the ferrite plates is also smaller if we compare it with upper bainite [21].
Notice the scale used in figure 3.13. It is below the resolution of optical microscope. In optical microscope the wavelength of light used is 500 to 600nm i.e. 0.5 to 0.6μm. It is difficult to resolve individual plates with optical microscope. For resolving the individual details of plate transmission electron microscope (TEM) is used. Under the optical microscope the plates in figure 3.13 are observed as interfaces in the regions of bainite. When these regions are etched i.e. attacked with the etchant they will be observed as dark regions and TEM will be used for the details of individual plates [21].

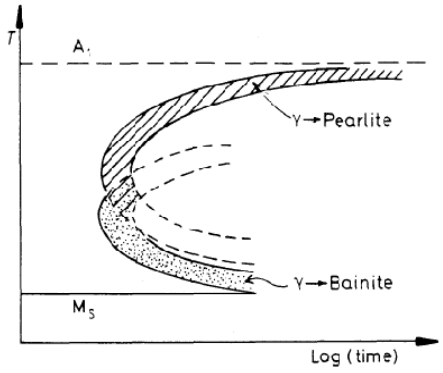

Figure 3.11: Schematic of the TTT diagram representing the transformation curves of pearlite and bainite [6].

3.2.7 Martensite

Martensite is the term used in physical metallurgy to describe the common diffusionless nature of phase transformations. It is the transformations in which the individual atomic movement from start to completion of the reaction is less than one inter atomic spacing. It was

given the name 'martensite' by Floris Osmond in 1895 in honor of German metallurgist Adolf Martens [22]. In steels it is obtained by rapid quenching. The quenching rates should be such that suppress the diffusion controlled transformation product e.g. ferrite, pearlite and even bainite (in which the nucleation requires that the carbon should deplete).

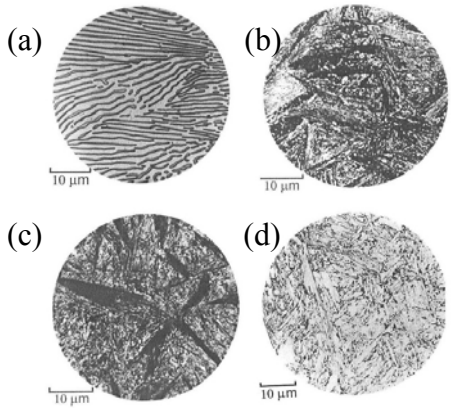

Figure 3.12: Microstructure in a eutectoid steel: (a) Pearlite formed at 720°C; (b) bainite obtained by isothermal transformation at 290°C; (c) bainite obtained by isothermal transformation at 180°C: (d) martensite [20].

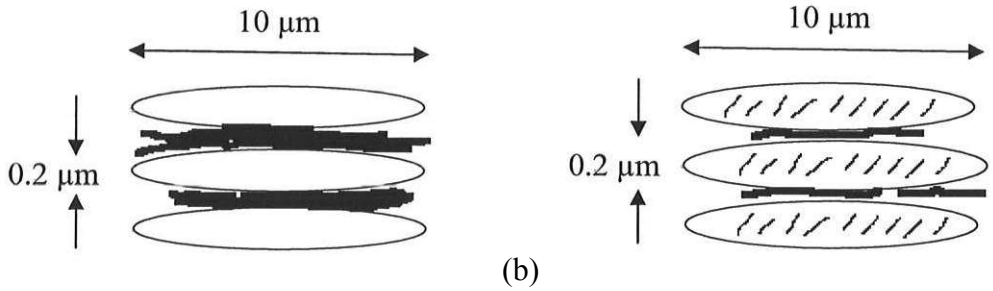

Figure 3.13: Morphological variants of bainite: (a) upper bainite (also called feathery bainite) and (b) lower bainite (also called as acicular bainite) [21].

At high cooling rates there is no chance of diffusion and the growth rate in martensitic transformations (also called displacive or athermal or military transformations) is so high that nucleation becomes the controlling step. As the nature of transformation is athermal so it does not follow Avrami transformation kinetics (i.e. the kinetic equations used for isothermal transformations) ([6], [22]).
Koistenen and Marburger equation is generally used to describe the kinetics of the martensitic transformations [17] and is given as follows

$$1 - V_{\alpha'} = \exp[\beta(M_s - T)] \qquad \text{(eq. 3.3)}$$

Where $V_{\alpha'}$ = Fraction of martensite formed, β = -0.011, M_s= martensite start temperature
T= temperature below M_s.
It can be seen that the volume fraction of martensite is simply related to undercooling below the martensite start temperature. Time does not come in this equation. Physical reason for this is that there is distribution of nuclei in the austenite as they get activated less and less important nuclei becomes activated as they are undercooled below the martensitic start temperature. When we run out of that certain potency of nuclei the transformation stops.

After then further undercooling is required to stimulate the less important nuclei ([15], [16], [17]). This phenomenon is schematically presented in the figure 3.14.

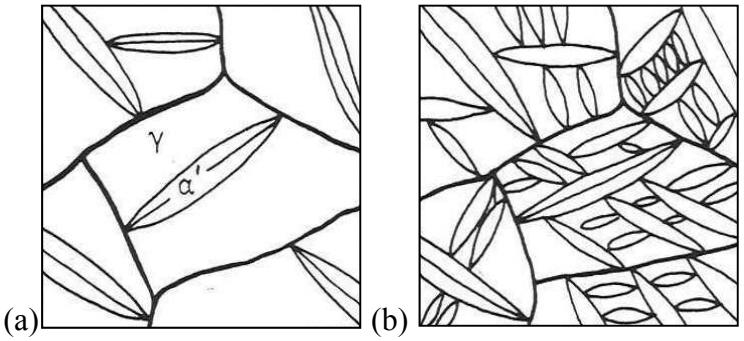

Figure 3.14: Growth of martensite at (a) low undercooling and (b) higher undercooling below M_s. Fraction transformed depends only on the number of nucleation sites triggered, with less potent sites contributing at higher undercoolings ([6], [17]).

Usually, the formation of a single plate of martensite takes 10^{-5} to 10^{-7}s (i.e. 10µs to 100ns) to reach its full size. This speed is comparable to the speed of sound [6] (which is ~5960 m/s in steel [23]).
As can be seen in the figure 3.14 that martensite (α') has a lens like structure and the diameter of the lens is appproaching the diameter of the grain. The density of plates is depending on the undercooling and not on the grain size. It means that the martensite obtained at higher undercooling (figure 3.14b) will be finer and the steel will be stronger than the morphology obtained at low undercooling below M_s (figure 3.14a). From the crystallographic point of view martensite has the body central tetragonal structure (BCT) and the tetragonality increases with carbon content. Martensite transformation produces a change of crystal structure without a change in composition. There are essentially two morphological variants of martensite namely lath martensite and plate martensite .

3.2.7.1 Lath martensite

Laths are composed of bundles of flat, narrow plates that grow side by side as shown in the figure 3.15 [22]. This morphological variant is generally not very hard as it appears in low carbon steel. The hardness of martensite increases with the carbon content so does the morphology [22]. With increase in carbon content the tetragonality increases which distorts the normal bcc ferrite lattice. In the case of ultra-low carbon steel, cooling rates of approximately 10,000K/s are required for martensitic or displacive reactions in carbon contents from 0.004 to 0.013 wt%C [5].

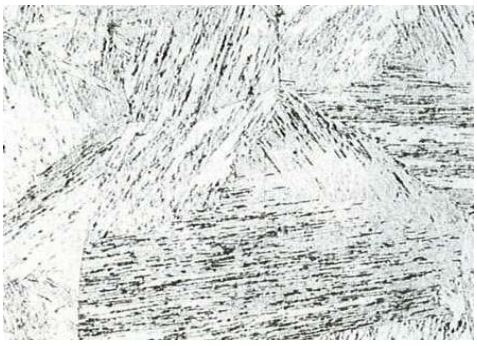

Figure 3.15: Lath martensite in low carbon steel [22].

3.2.7.2 Plate martensite

This morphological variant of martensite is showing flat, narrow plates growing individually instead of bundles as shown in the figure 3.16. This type of microstructure is presenting much more hardness due to higher carbon content.

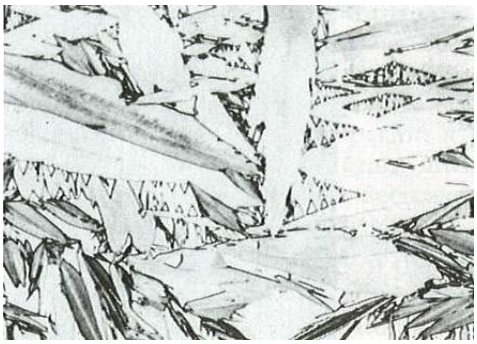

Figure 3.16: Plate martensite in high carbon steel [22].

3.3 Austenite decomposition mechanism

During austenite decomposition atoms are rearranged from the parent austenite which has an fcc crystal structure to the bcc / bct crystal structure. This rearrangement is obtained either by reconstructive (civilian) transformation mechanism or by a displacive (military) transformation mechanism and virtually all solid-state phase transformations can be described in the context of these two mechanisms [25]. Figure 3.17 presents the classification of different austenite decomposition products in terms of the mechanism which is believed to be followed for these transformation products.

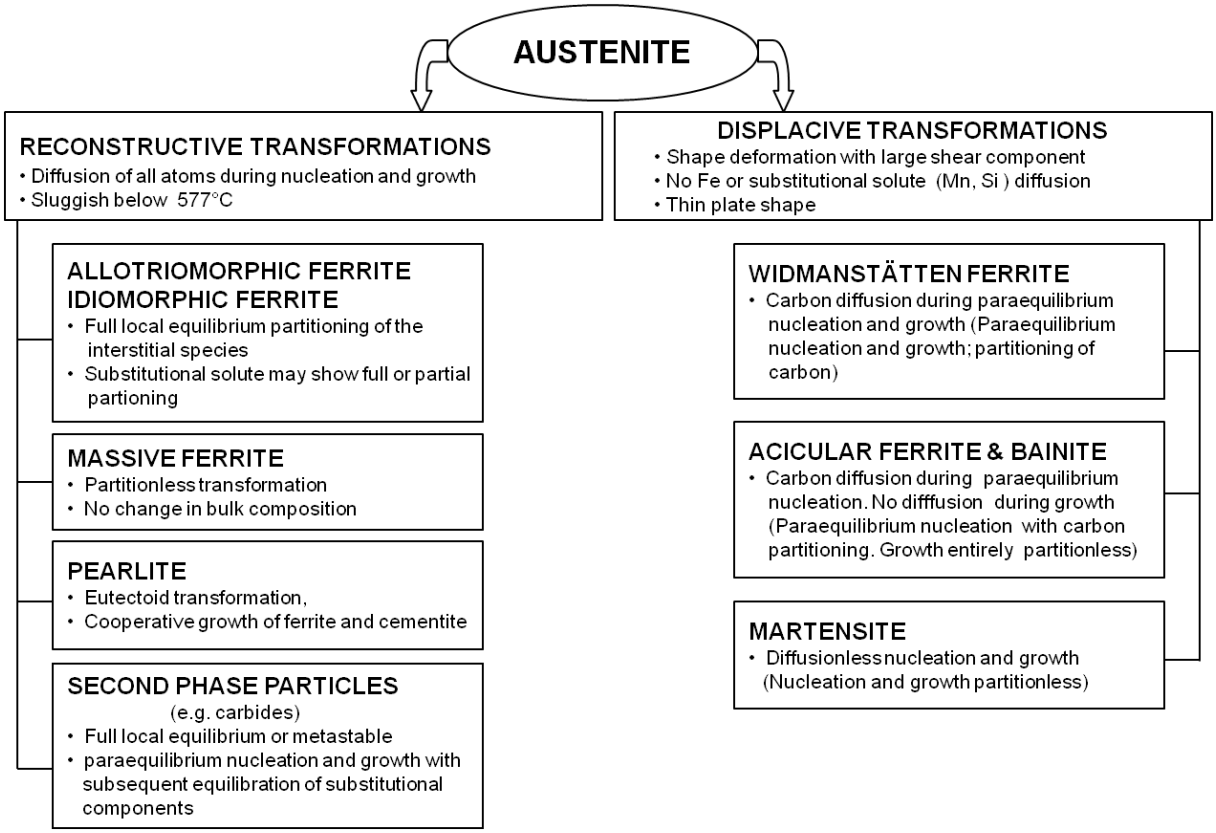

Figure 3.17: Summary of the characteristics of phase transformation in steels following the classification scheme of Bhadeshia ([2], [20]).

3.4 Mechanism of austenite decomposition to ferrite

There is some interest over the recent years amongst the researchers ([1], [8], [9], [10]) to investigate the mechanism of the austenite to ferrite transformation in ultra low to low carbon steels. Millitzer [8] stated that in ultra-low carbon steel the growth rate is controlled by the mobility of the austenite to ferrite interface. The ferrite obtained as a result of the interface controlled transformation mechanism is defined as massive ferrite. In case of commercial low carbon high strength low alloy (HSLA) steels ferrite growth was controlled by carbon diffusion in austenite and by Mn and Nb solute drag like effects. Kozeschnik and Gamsjäger [1] have observed a two-stage transformation behavior in 0.007 wt%C steel. They find that this can be attributed to the transition from a thermally activated interface controlled reaction to a slower diffusion controlled reaction. They also observed that the transformation has commonly started already during fast quenching and before reaching the final isothermal annealing temperature. Liu et al. ([9], [10]) have studied a 0.01 at%C steel alloy isochronally and a 0.04 at%C steel alloy isothermally. In the isochronal study, they also observed the two-stage transformation mechanism. They concluded that the transformation starts as a diffusion controlled reaction and then shifts to an interface controlled mechanism. In the isothermal study they also observed the similar two-stage transformation mechanism as described by Kozeschnik and Gamsjäger [1]. They also conclude that the nature of mechanism during isochronal annealing and during isothermal annealing is essentially different with respect to the mechanisms involved.
Now in the following section basic theory behind the diffusional and massive transformation will be described from the work of Van der Ven and Delaey [14], Coates [26], Bhadeshia ([17], [21]), Kozeschnik [2] and Massalski [5].

3.4.1 Mechanism in a binary Fe-C system

Van der ven and Delaey [14] have written a review paper on transformations in Fe-C and Fe-C-Mn alloys. Some of the details regarding the transformation mechanism in a binary Fe-C alloy will now be depicted.
He considered a binary Fe-C steel that has been cooled from a temperature T_1 where γ is stable to temperature T_2 in the two phase field where both α and γ are in equilibrium with each other. If by cooling the steel from T_1 to T_2 the partial transformation of γ to α can be suppressed, then the molar Gibbs free energy of metastable γ phase will lie on point A of figure 3.18.

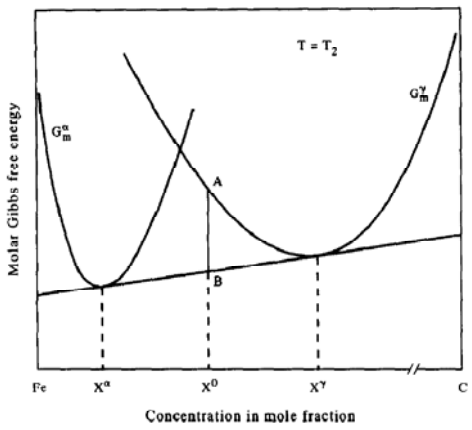

Figure 3.18: Molar Gibbs free energy diagram at a temperature T_2. The distance A-B is equal to the total free energy of transformation for an alloy with a bulk composition X^0 [14].

If steel is subsequently held at T_2 a certain fraction of the metastable γ will transform to α. Given sufficient time, the steel will lie on point B of figure 3.18. In equilibrium the steel will thus consist of two phases α and γ determined by the lever rule. The total molar Gibbs free energy dissipated during transformation is given by the distance between A and B of figure 3.18 [14].

In the initial stages of the transformation, the concentration within the bulk of the γ phase is still equal to the average concentration of the alloy X^0. The chemical potential of the Fe and C atoms in the bulk of the γ phase are then equal to the intersection of the tangent to A with the Gibbs free energy axis at $X = 0$ and $X = 1$, as illustrated in figure 3.19. In general, the molar Gibbs energy of the precipitate and matrix will not remain constant during the transformation. This is especially true for molar Gibbs energy of the precipitate in the initial stages of the growth. At the beginning of the transformation, the spherical precipitates are small and hence there will be a non-negligible increase of the pressure within α as a result of capillarity. For spherical precipitates with isotropic interface tension, the increased pressure P due to the curvature of the interface can be written as [14]

$$P = \frac{2\sigma}{r} \qquad \text{(eq. 3.4)}$$

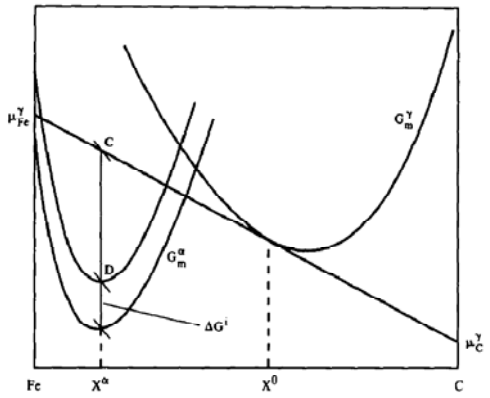

Figure 3.19: Molar Gibbs free energy diagram illustrating the effect of capillarity on the growing precipitate phase α. The distance C-D is equal to the molar free energy disspated by the incremental growth of α precipitate when the bulk concentration of the matrix is X^0 [14].

Where σ is the interface tension and r is the radius of the spherical precipitate. The increase of molar Gibbs free energy due to the effect of surface tension can be written in the form $\Delta G^i = PV_m$, where V_m is the molar volume of the precipitate for the concentration at which the precipitate forms. This term can be added to the molar Gibbs free energy of α phase as illustrated in the figure 3.19 (It is assumed according to Hillert (see for example [14]) that the capillarity effect changes the pressure only in the precipitate). As the precipitate grows in size, the capillarity effect will diminish in relative importance and the Gibbs free energy of the precipitate will approach the G^{α}_{m} curve corresponding to the bulk α phase. The molar free energy dissipated by the incremental growth of α precipitate is given by the distance C-D in figure 3.19.

The distance C-D can be divided in a portion corresponding to the molar free energy dissipated by diffusion ΔG^d and a portion corresponding to the molar free energy dissipated by interface migration ΔG^m (figure 3.20). ΔG^d is the free energy dissipated by one mole of Fe and C with an overall concentration X^{α} when this collection of atoms is transported from the bulk of the matrix to the γ-α interface by diffusion. ΔG^m is the Gibbs free energy dissipated by one mole of Fe and C atoms with an overall concentration X^{α} when this collection of

atoms changes its chemical state at the interface as a result of the transformation reaction γ→α. The line through point E and tangent G_m^α as illustrated in figure 3.20 determines the concentration in the γ phase at the γ-α interface. This interface concentration will be called as $X^{\gamma-\alpha}$ (see figure 3.20).

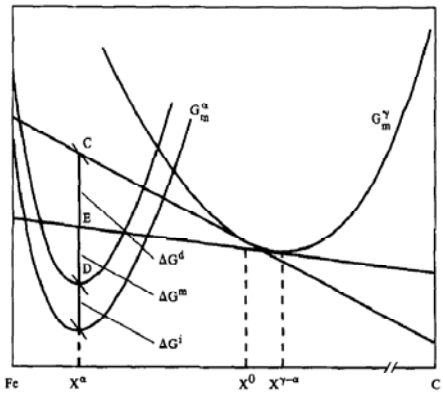

Figure 3.20: Molar Gibbs free energy diagram. The distance C-E corresponds to the free energy dissipated by volume diffusion and the distance E-D corresponds to the free energy dissipated by interface migration [14].

When the free energy of transformation is dissipated solely by the diffusion of different components to and from the precipitate interface, then ΔG^m of figure 3.21 will be negligible and point E will lie on the capillarity adjusted G_m^α curve. The concentration in the γ phase at the interface is then determined by the common tangent to G_m^α and G_m^γ where we assume that G_m^α has been adjusted for capillarity effects. The concentrations at the interface separating α and γ are such that the chemical potentials of each component are constant across the interface. Under this assumption, the growth rate of the precipitate is **diffusion controlled**. We shall call this situation growth with local equilibrium (LE) (figure 3.21). When, on the other hand, the free energy of transformation is dissipated by interface migration only, the concentration in the matrix phase at the interface will be the same as in the bulk of the matrix phase. The transformation is then said to be **interface controlled**. Whether or not a transformation is interface controlled or diffusion controlled depends on the relative size of the expressions for the dissipation of free energy by interface migration and by diffusion.
For many diffusional phase transformations at relatively high temperatures, the assumption that the Gibbs free energy dissipated by interface migration is negligible is a realistic approximation. The long range volume diffusion of the different elements from the bulk of the γ phase to the precipitate involves many atom jumps. The motion of an interface on the other hand, requires essentially only a very limited number of atom jumps for each atom involved. Furthermore, the activation energy for the transfer across an incoherent interface (which is a more or less disordered region) is likely to be less than that for diffusion in a crystal structure.

3.4.2 Mechanism in a ternary Fe-C-X system

When dealing with ternary systems, surfaces are involved instead of planes. On putting a tangent plane in contact with those surfaces, equilibrium can be defined by all three species having the same chemical potential in both phases (i.e. γ and α). In figure 3.22 intercepts are written as $\mu_{Fe}^\alpha = \mu_{Fe}^\gamma$ on iron (Fe) axis, $\mu_C^\alpha = \mu_C^\gamma$. on carbon (C) axis and $\mu_{X=Mn}^\alpha = \mu_{X=Mn}^\gamma$. on manganese ($X = Mn$) axis. So the general condition of equilibrium is no matter how many components you have in the system is $\mu_i^\alpha = \mu_i^\gamma$. In case of more than two phases $\mu_i^\alpha = \mu_i^\gamma = \mu_i^\beta$ and this is the definition of equilibrium that the free energy of species is uniform wherever we look.

When these points are plotted on the phase diagram, tie-lines can be easily obtained. In case of ternary systems additional degree of freedom is involved. By rocking the tangent plane on the free energy surfaces of the ferrite and austenite (rocking is such that tangent plane did not lose its contact with these surfaces), a whole set of tie-lines can be produced (figure 3.23). From the set of tie-lines selection of appropriate tie-line, which will define the concentration of interface from the phase diagram (i.e. thermodynamic information) is again an issue.

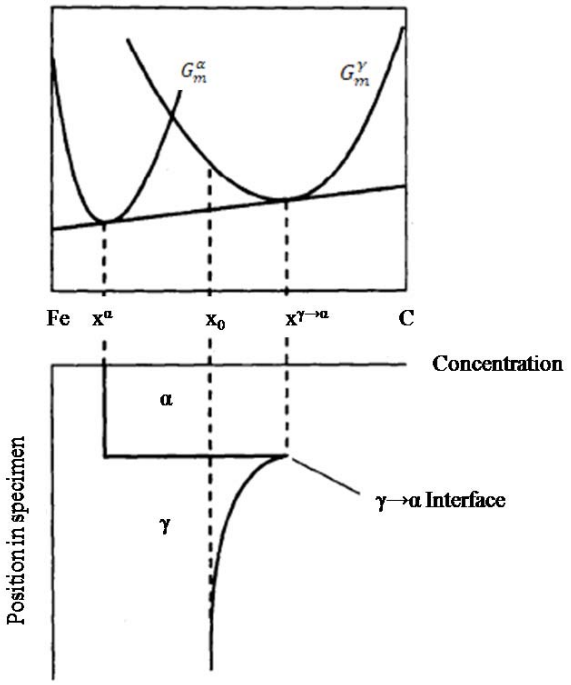

Figure 3.21: Illustration of the local equilibrium approximation. The common tangent to the Gibbs free energy curves of the precipitate and the matrix phases determine the interface concentrations [14].

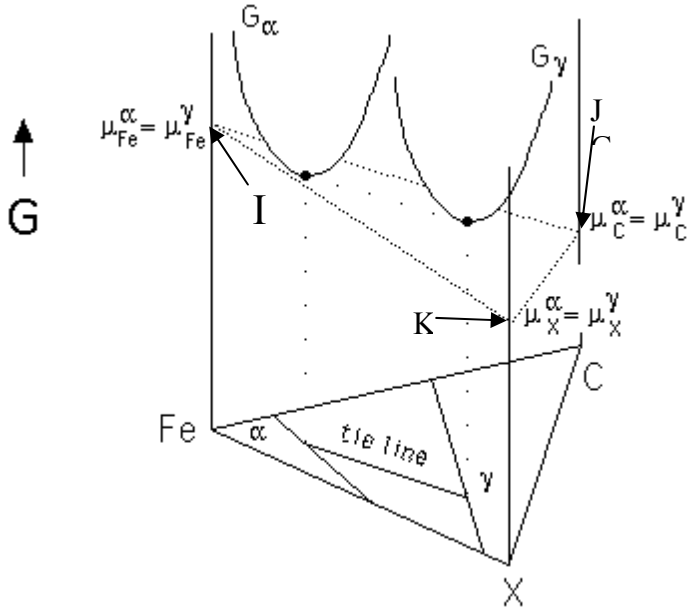

Figure 3.22: Free Energy surface for Fe-C-X system where X is Mn [21].

Consider figure 3.23, which is actually the flat portion of the figure 3.22 (can be identified as its base for understanding).This is actually the constant temperature (isothermal) portion of the ternary phase diagram. It has the ferrite, austenite and the alpha plus gamma phase fields containing the tie-lines obtained from rocking the tangent plane on the surfaces of alpha and gamma by maintaining the contact with these free energy surfaces. Now maintaining the condition [17] that the rate at which solute is partitioning is equal to diffusion flux from the interface can be written as

$$(C^{\gamma\alpha} - C^{\alpha\gamma})\frac{dz}{dt} = -D\frac{dc}{dz} \cong -D\frac{(\bar{C} - C^{\gamma\alpha})}{\Delta z} \qquad \text{(eq. 3.5)}$$

As the interface moves, the rate at which the solute is partitioned is equal to the rate at which the solute is carried away from the interface (diffusion flux is down the gradient). In order to maintain these concentration gradients i.e. between $C^{\gamma\alpha}$ and $C^{\alpha\gamma}$ the rate solute partitioned must be equal to the rate at which theses are carried away from the interface (in other words the diffusion rate is also the reflection of the rate of solute partitioning).
For two diffusing species two equations are required to show the rate partitioning and rate diffusion activities. These equations [21] are given below

$$J_1 = -D_{11}\nabla C_1 - D_{12}\nabla C_2 \qquad \text{(eq. 3.6)}$$
$$J_2 = -D_{22}\nabla C_2 - D_{21}\nabla C_1 \qquad \text{(eq. 3.7)}$$

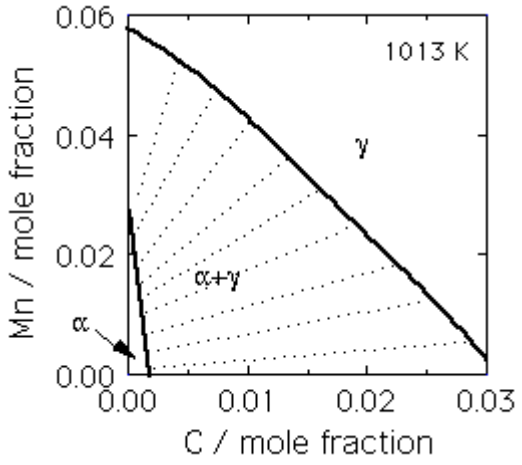

Figure 3.23: Isothermal section showing C, Mn and tie-lines [21].

In terms of carbon and manganese, we can write these equations as [21]

$$J_1 = \left(C_C^{\gamma\alpha} - C_C^{\alpha\gamma}\right)v = \left(C_C^{\gamma\alpha} - C_C^{\alpha\gamma}\right)\frac{dz}{dt} = -D_C\nabla C_C - D_{C,Mn}\nabla C_{Mn} \qquad \text{(eq. 3.8)}$$
$$J_2 = \left(C_{Mn}^{\gamma\alpha} - C_{Mn}^{\alpha\gamma}\right)v = \left(C_{Mn}^{\gamma\alpha} - C_{Mn}^{\alpha\gamma}\right)\frac{dz}{dt} = -D_{Mn}\nabla C_{Mn} - D_{Mn,C}\nabla C_C \qquad \text{(eq. 3.9)}$$

The above equations are interpreted as the diffusion flux of specie 1 (J_1) e.g. carbon will not only depends upon the gradient of its own concentration (i.e ∇C_C) but also on the gradient of the concentration of second specie i.e. manganese (∇C_{Mn}). Similarly the diffusion flux of specie 2 (J_2) will depend not only its own concentration gradient but also on the concentration gradient of the specie 1 i.e. carbon.

It is also important to remember the nature of the solute i.e. carbon is interstitial solute and manganese is the substitutional solute. The interstitial solute is diffusing faster than the substitutional solute. At a temperature around 600°C, interstitial solute e.g. carbon can diffuse 8 order of magnitude faster than substitutional solute e.g. manganese ($D_c \approx 10^8 D_{Mn}$).
For simplification, neglect the interaction term ([14], [21]) (i.e. the second product in the above equations which in first case is the effect of gradient of Mn on C, and in second case is the effect of C on Mn) because they can be very small.

$$J_1 = \left(C_C^{\gamma\alpha} - C_C^{\alpha\gamma}\right)v = \left(C_C^{\gamma\alpha} - C_C^{\alpha\gamma}\right)\frac{dz}{dt} = -D_C \nabla C_C \qquad \text{(eq. 3.10)}$$

$$J_2 = \left(C_{Mn}^{\gamma\alpha} - C_{Mn}^{\alpha\gamma}\right)v = \left(C_{Mn}^{\gamma\alpha} - C_{Mn}^{\alpha\gamma}\right)\frac{dz}{dt} = -D_{Mn} \nabla C_{Mn} \qquad \text{(eq. 3.11)}$$

We have a pair of equations here, which we have to solve simultaneously given that the diffusion coefficient of carbon is eight orders of magnitude larger than of manganese. Consider the following figure 3.24. Point A gives the concentration of carbon in ferrite which is in equilibrium with austenite (i.e. $C^{\alpha\gamma}$) on the carbon axis side, and shows concentration of Mn in ferrite which is in equilibrium with austenite (i.e. $Mn^{\alpha\gamma}$) on the Mn axes. Similarly point B gives the concentration of carbon in austenite which is in equilibrium with ferrite (i.e. $C^{\gamma\alpha}$) on the carbon axis side, and shows concentration of Mn in austenite which is in equilibrium with ferrite (i.e. $Mn^{\alpha\gamma}$) on the Mn axes side. Point P shows the average concentration of alloy corresponding to their axes.
Now what we have to do is to pick a tie-line which reduces the gradient of carbon to compensate for its large diffusion coefficient. Imagine that if an alloy has composition Z (figure 3.25). We want to see which tie-line determines the diffusion controlled growth.
If a vertical line is drawn through point Z then the carbon concentration in austenite is given by point A and it is same as the average composition of the alloy i.e. $\bar{C} = C^{\gamma\alpha}$. So the diffusion profile will become flat (in figure 3.25 it is shown flat [21] for convenience but actually it is showing negligible gradient ([26], [27]) i.e. driving force for fast diffuser [26] being reduced essentially to zero).

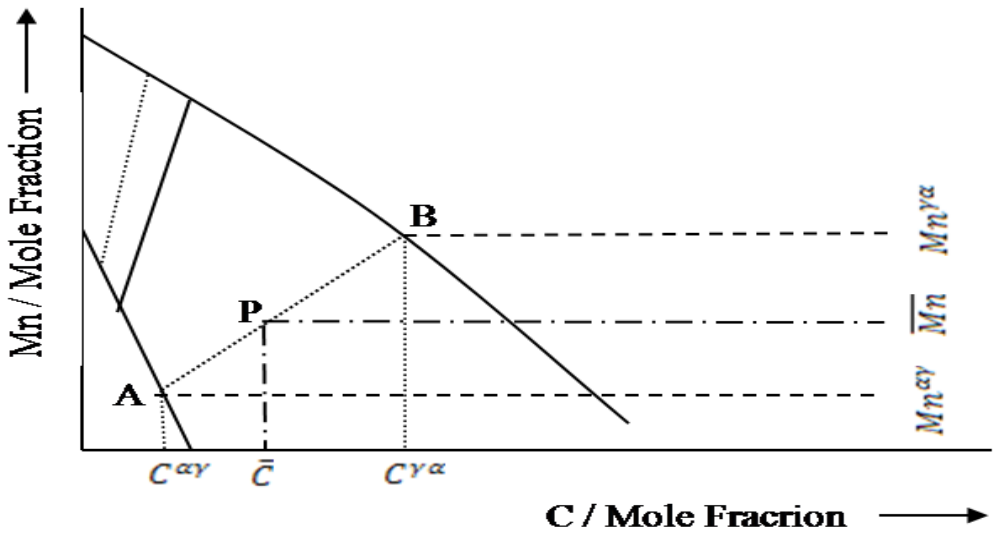

Figure 3.24: Representation of carbon and manganese concentration on the isothermal plot.

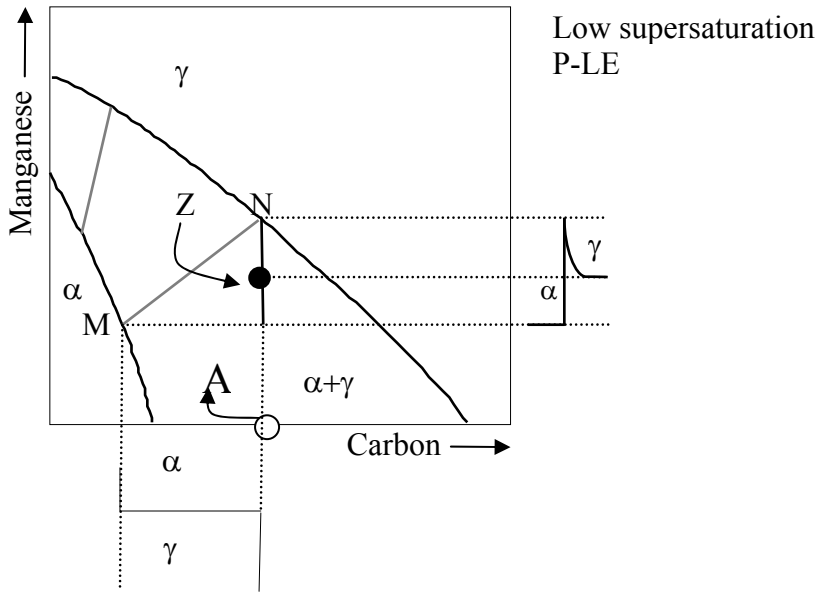

Figure 3.25: Tie-line for low saturation partitioning local equilibrium (P-LE) mode mechanism ([14], [17], [21], [26], [27]).

So if a vertical line is drawn through Z and pick 'MN' as tie-line as shown in the figure 3.25, then what happened is that the gradient of carbon flattened and therefore the large diffusion coefficient of fast diffuser (i.e. C) is compensated by forcing a small gradient. In this way Mn can keep pace with the C. In the above figure 3.25, it can also be seen that the concentration profile of Mn shows long range diffusion of Mn. There is lot of partitioning of Mn that is why it is called P-LE i.e. **partitioning local equilibrium** mode. It occurs at a low supersaturation. In this case, the alloy is supercooled only a little bit outside of the austenite phase field.
Now instead of making the gradient of carbon flat, Mn gradient can also be increased. This will be the case which will allow little partitioning of Mn constituent. Now consider the alloy having a composition as shown by point Y in figure 3.26. Draw a horizontal line through the point Y. This situation will create the condition where Mn concentration of ferrite will be the same as the average Mn concentration. In this way JK represents the tie-line. Now the gradient of Mn becomes extremely steep. It compensates for the slow diffusion of Mn. This is the condition which will allow long range diffusion of C and almost zero partitioning of Mn.
In other word the reconstructive drag which was present in partitioning local equilibrium mode (P-LE) exerted by substitutional constituent (i.e. Mn in the present case) will not be present in the present case. So this is known as NP-LE i.e. **negligible partitioning local equilibrium** mode. It occurs at high supersaturations.
Now consider figure 3.27 ([17], [21], [26]). It has a series of tie-lines obtained through thermodynamics getting equal potentials. By drawing the right hand triangle on each of these tie-lines, joining the vertices of these triangles will create the PQ line. The PQ curve divides the α+γ phase field into P-LE and NP-LE regions. Horizontal and vertical lines of the triangles are defining the two modes. So, a system naturally chooses a manner to satisfy the two equations simultaneously maintaining the mass balance. In the above case instead of finding the tie-line corresponding to given bulk composition a bulk composition was sought which gives the same tie-line.
In the above cases diffusion controlled growth was studied with a system having two solutes. In the similar way extension of diffusion controlled growth for more than two solutes is also possible. In such cases more than two equations will be there and their simultaneous solution will describe the diffusion or partitioning of these solutes.

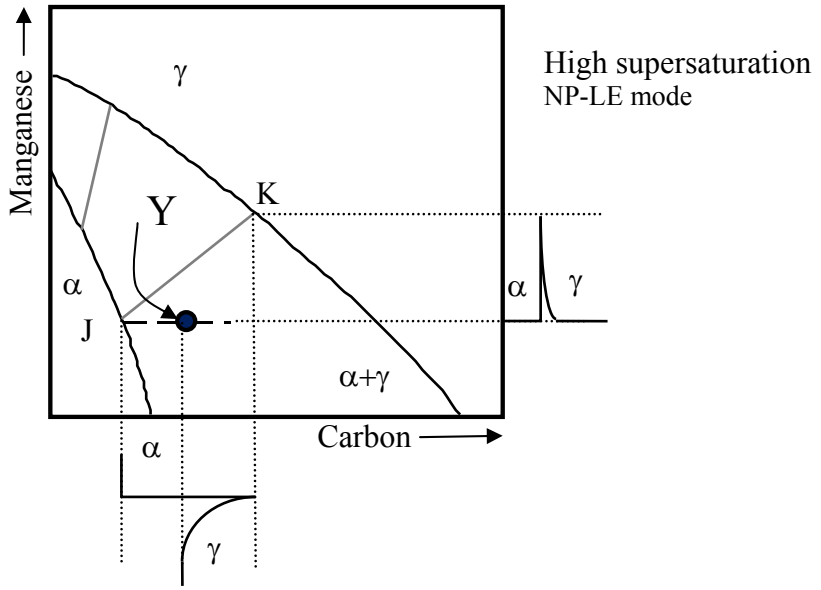

Figure 3.26: Tie-line for high supersaturation negligible partitioning local equilibrium (NP-LE) mode mechanism ([14], [17], [21], [26], [27]).

So far we have discussed diffusion controlled growth with equilibrium being maintained at the interface. In other words the interface compositions are connected by a tie-line of the phase diagram. Now as the transformation temperature drops, the diffusion of Mn becomes increasingly slow, and what we get is the breakdown of equilibrium. Consider the concentration profile of Mn in figure 3.26. It is very steep; eventually the diffusion distance becomes less than interatomic spacing. This means that Mn simply stops diffusing. But carbon can continue partitioning between the two phases. In such cases terminology is shifted from equilibrium to **partial equilibrium (paraequilibrium)** and the phase diagrams in such conditions are called paraequilibrium phase diagram like as shown in the figure 3.28. That means a phase diagram in which Mn does not diffuse but carbon does partition between austenite and ferrite. Now again question arises that whether horizontal line will be used or vertical. It will be horizontal as we are in the NP-LE region and Mn concentration in the ferrite and austenite is identical. Strictly speaking it is the ratio of the Mn to Fe atoms which remains constant.

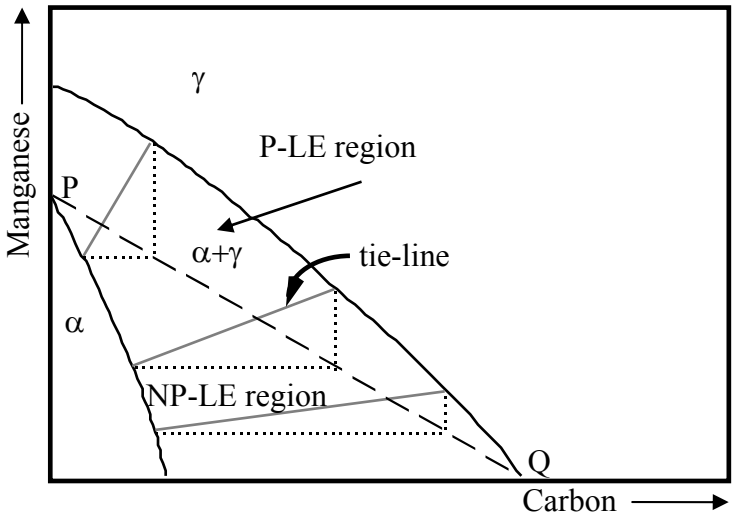

Figure 3.27: Division of α+γ phase field into P-LE and NP-LE regions ([17], [21], [26]).

It is no longer an equilibrium diagram. It is a constrained equilibrium, in which carbon is allowed to reach homogenous chemical potential to the constraint that the substitutional solute does not partition. So this is almost like a binary system i.e. all the equations of a binary are used to calculate the growth rate. This is because only carbon is diffusing.

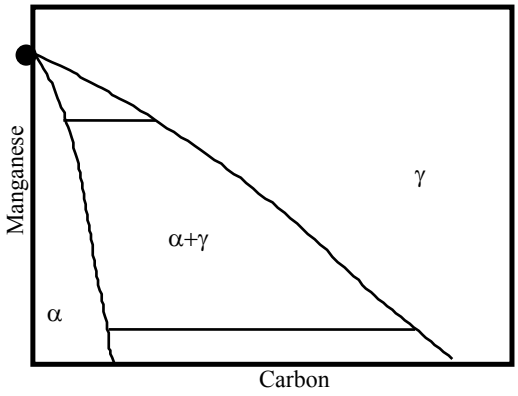

Figure 3.28: Paraequilibrium phase diagram [21].

Now notice that there is one other difference here, if we compare it with the equilibrium phase diagram. The large gap between the ends of the α and α+γ phase fields and the α+γ and γ phase fields on the Mn axes vanish to a point in figure 3.28. At the point this gap vanishes (represented by black dot in figure 3.28), we have no C and the Fe and Mn behave like a pure substance i.e. ferrite goes to austenite at a particular concentration for a particular temperature. If in an equilibrium diagram, a paraequilibrium phase diagram is shown, it will look like the one shown in figure 3.29.

There is another interesting point that ortho (equilibrium) and paraequilibrium phase diagram are meeting at points L and P in figure 3.29. It means that if there is no Mn then there is no difference between a binary and ternary, points L and P show zero Mn on the horizontal carbon axes (i.e. at zero Mn concentration). So both para and equilibrium meet at points L and P. So both ortho and paraequilibrium phase diagram meet when the Mn becomes zero as shown in the figure 3.29.

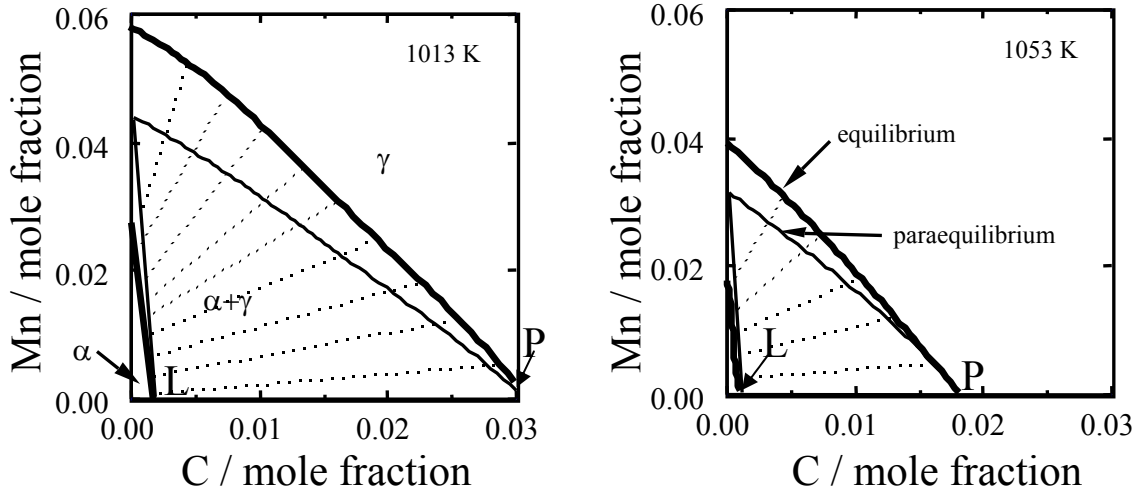

Figure 3.29: Paraequilibrium diagram shown in an equilibrium diagram ([17], [21]).

Here we have dealt with the special case of constrained equilibrium, where Mn does not partition. Effectively it becomes a binary system. Vast majority of steel, because we are interested in fine grain structure, are transformed for this purpose at a low temperature. The paraequilibrium phase diagram will be applied instead of equilibrium phase diagrams. From

the above discussion it is also required to specify the critical conditions under which the α-γ interface (i) abandons the paraequilibrium state and (ii) adopts the local equilibrium state (i.e. specifications of the transition range between growth mechanisms via the two states). An obvious approach is to estimate the ‘‘spike’’ thickness of X (i.e. Mn in above case) and compare it with what are assumed to be physically reasonable values for growth via the two modes. If the bulk composition lies in the P-LE region of the equilibrium phase diagram, the precipitate growth rate is determined by diffusion of X (which partitions between α and γ, figure 3.25). Because X partitions, mass conservation requires that the effective width of the distribution of X in γ quickly becomes orders of magnitude greater than the atomic dimensions. Thus, on the basis of this kinetic approach, the paraequilibrium mode is of effectively no significance if the bulk composition lies in the P-LE region. If the bulk composition lies in the NP-LE region of the equilibrium phase diagram, the corresponding ‘‘spike’’ thickness, Δs, is given by [14]

$$\Delta s \sim \frac{2D_{22}}{v} \qquad \text{(eq. 3.12)}$$

Or sometimes written as [2]

$$\mathrm{d} \sim \frac{D}{v} \qquad \text{(eq. 3.13)}$$

If Δs is calculated to be less than the thickness of the α-γ interface, it will be assumed that the spike is nonexistent and that paraequilibrium exist at the interface. On the other hand if Δs is more than ~5 times greater than the α-γ interface thickness, it will be assumed that the corresponding ‘‘spike’’ is physically realizable and the NP-LE exists at the interface. Although these criteria are ad hoc, they must suffice until more fundamental criteria are established [26].

3.4.3 Comparison of LOE and LPE growth kinetics

Kozeschnik [2] has analyzed how the choice of equilibrium model affects the transformation kinetics in interstitial / substitutional alloys. He considered local orthoequilibrium (LOE) and paraequilibrium (LPE) models.
He considered a ternary alloy Fe-3wt%Mn-0.05wt%C and the austenite / ferrite transformation at 650°C in an austenite half cell with 50μm size. He first applied the paraequilibrium / orthoequilibrium concept and estimated the solute spike for each diffusing element based on the equation 3.13. He adopted the following limits
Paraequilibrium: d_spike < 5Å
Orthoequilibrium: d_spike > 15Å
Figure 3.30 presents the results of the simulations and compares the very different growth kinetics of the reaction as well as the transformation path. The left diagram shows the position of the transformation front as evaluated with the paraequilibrium / orthoequilibrium model. As the width of the spike is below atomic dimensions, the reaction initiated without partitioning of manganese (Mn) i.e. under paraequilibrium control with only carbon long range diffusion. As the transformation reached paraequilibrium conditions, the velocity of the interface decreases rapidly (due to soft-impingement) and diffusion of Mn becomes operating. However, as the ferrite fraction under full equilibrium conditions is less than under paraequilibrium, the interface moves in the backward direction again. Due to slow Mn diffusion in austenite, the interface position first moves over the position given by full thermodynamic equilibrium

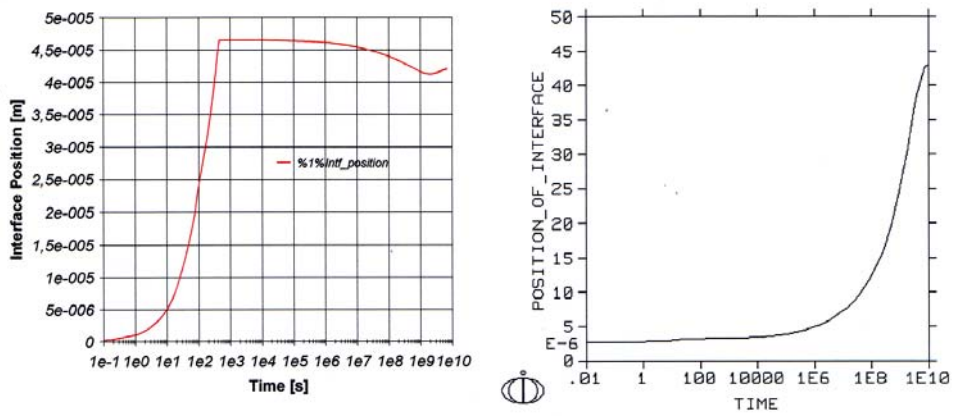

Figure 3.30: Position of austenite / ferrite interface as a function of time: orthoequilibrium / paraequilibrium concept (left, MatCalc) and orthoequilibrium (right, DICTRA) [2].

and reaches the final position only after 10^{10} seconds (approximately 317 years).
In the comparison of results with the predictions bases on the NPLE / OLE concept, it is clearly seen that the reaction is severely retarded by Mn diffusion within the interface. The reaction is not really started even after 10^6 seconds (approximately 12 days).
Figure 3.31 presents the calculated elemental profiles at different stages of the austenite / ferrite reaction as evaluated with the LPE / OLE concept.

3.4.4 Massive ferrite

Massalski [5] and Bhadeshia [3] have reviewed the massive ferrite morphology. Some of the salient features of their work will be summarized as under.
In 1930 Phillips established that a rapid quenching could produce a non-martensitic composition invariant solid state reaction in the Cu-Zn system [5]. The term 'massive structure' was first used by Greninger in 1939 to describe the patchy (massive) appearance of the microstructure of fcc α-phase grains obtained by quenching to solvent-rich, high temperature bcc β phase in the system Cu-Al [5]. Since then advancement have shown that massive transformations are exhibiting following characteristic features [5]

(i) Change in phase transformation occurs by diffusion which involves a rapid non-cooperative transfer of atoms.
(ii) Parent and product have the same chemical composition.
(iii) During transformation only volume change is involved. In this regard transformation to the product phase is completed very rapidly.
(iv) It is a reversible process.
(v) Massive transformation exhibits nucleation and growth which is thermally activated.
(vi) High heating and cooling rates are involved in the massive transformations i.e. they must be sufficient enough to suppress the equilibrium phase separation which involves long range diffusion where change in chemical composition is the thermodynamic requirement. At the same time cooling rates should not be as high to allow martensitic transformations.

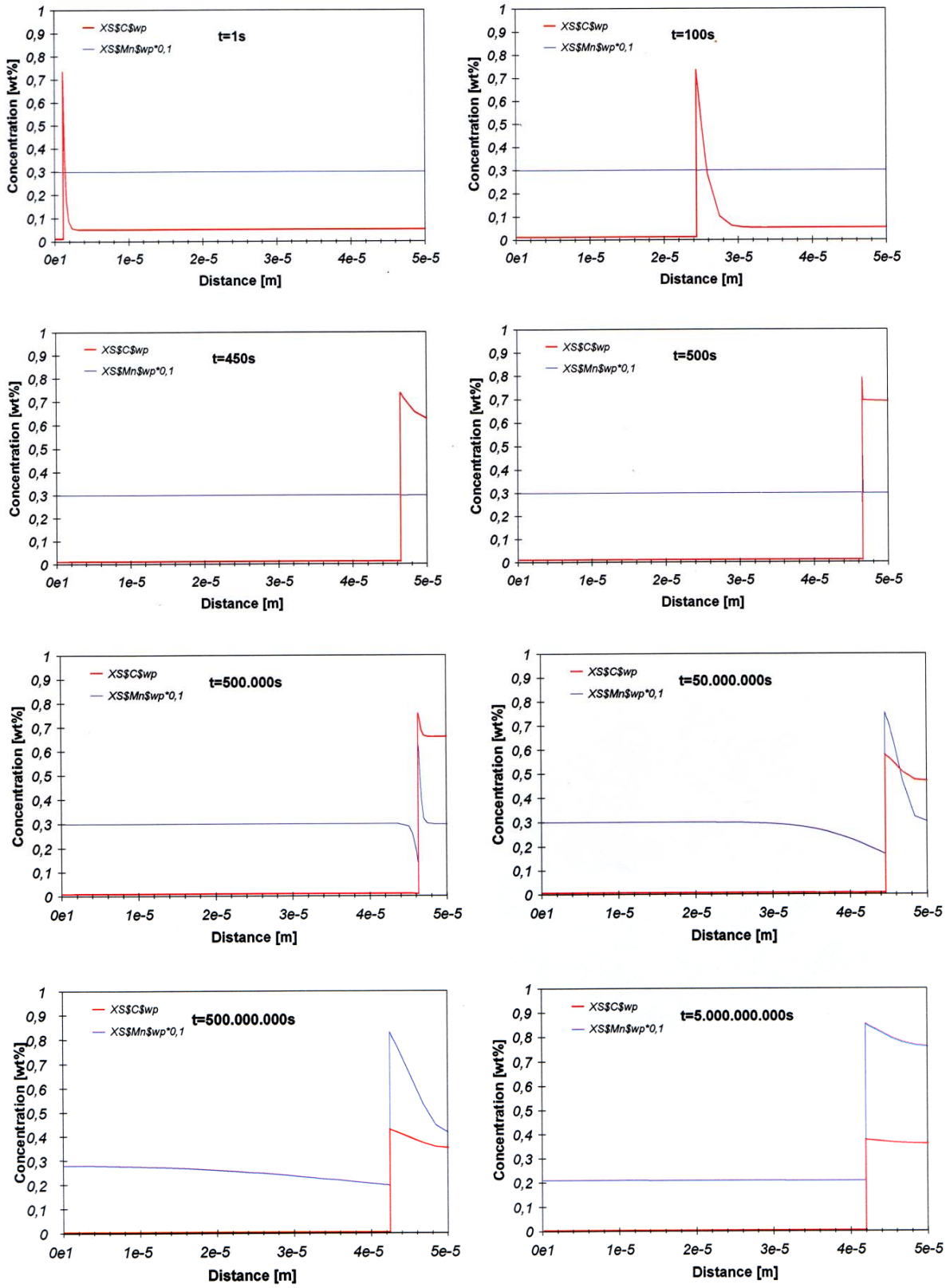

Figure 3.31: Calculated C and Mn profiles at various points of the austenite decomposition reaction [2].

Difference between martensitic and massive transformations

Both martenite and massive phases do not involve partitioning, parent and product phases have the same chemical composition and at the same time both phases are obtained at high cooling rates [5]. In this regards it seems necessary to see the characteristic differences which make them distinguished from each other.

(i) Shape change is a basic feature of martensitic transformations which causes rumpling of free surfaces. In contrast massive transformations do not involve shape changes during transformation.
(ii) Martensitic transformations require higher cooling rates in comparison to massive transformations.
(iii) Martensitic transformations are highly displacive in nature. The transformation occurs through cooperative movement of atoms. In massive transformations displacement of atoms is not cooperative.
(iv) The morphology of martensite is either lath-type (block-like, patchy appearance), characterized by a substructure of dislocation tangles, or acicular (needle-like appearance on a polished face), exhibiting internal twining within the martensite plate. In comparison, in a massive transformation the resultant microstructure contains random equiaxed grains.
(v) Both martensitic and massive transformation occurs below the T_0 temperature. The interface responsible for growth during massive transformation is believed to be incoherent while for martensite this is highly coherent.
(vi) Martensitic transformations are characterized by high dislocation densities in comparison to massive transformations.
(vii) The onset of massive transformation occurs at higher temperature in comparison to martensitic transformations as far as transformations in steels are concerned. In Fe-C and Fe-Ni alloys, for a range of cooling rates the transformation start temperature becomes independent of cooling rates. This gives a step or plateau in the transformation start temperature versus cooling rate plot (figure 3.32). For a massive transformation this step is observed at low cooling rates and higher transformation start temperature. In comparison in martensitic transformations this step occurs at higher cooling rates and lower transformation start temperature.

'Two plateau' behavior is limited as a criterion for distinguishing between massive and martensitic transformations, but may be useful when the competing product phases are difficult to distinguish metallographically. Some investigations have used the presence and absence of surface rumpling of a prepolished sample as a criterion for a martensitic transformation, but this is clearly inadequate in cases when martensites are of the fine lath type, or when the massive reaction produces plastic flow (and, therefore, some free surface disturbance) due to volume changes. Unfortunately, in some alloys such as Fe-Mn, only one plateau temperature is observed, over a wide range of quenching rates, and additional observations have been inconclusive in determining whether the reaction is massive or martensitic. Hence, instead of two plateau behavior, three structures can be differentiated in terms of the internal structure using transmission electron microscopy.

The data of Swanson and Parr ([5], [42]) shown in figure 3.33 indicate that the 'two plateau' behavior, in which the first plateau represents a massive transformation, is not observed beyond the Fe-7 at%Ni alloy, there being only one temperature plateau in the Fe-10 at%Ni alloy. The transformation in the region beyond the 7 at%Ni may thus be regarded as martensitic, or at least bainitic, in agreement with the observed cell or lath-like substructures, and high dislocation densities characteristics of martensite in carbon steels.

There is however, a small disagreement between the data of Speich and Swann and Swanson and Parr (see for instance [5]). Speich and Swann regard alloys in the range of 6 at%Ni to be martensitic on the basis of electron microscope work, where as Swanson and Parr report a massive transformation plateau temperature for the 7 at%Ni alloy (see for example [5]).

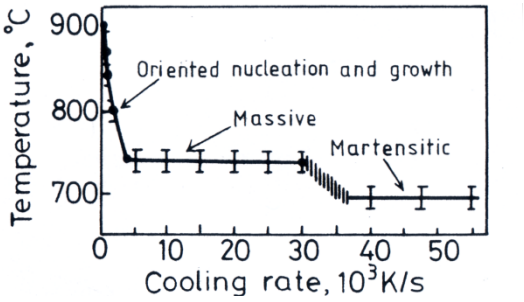

Figure 3.32: Effect of cooling rate on the austenite decomposition start temperature plotted for pure iron [7].

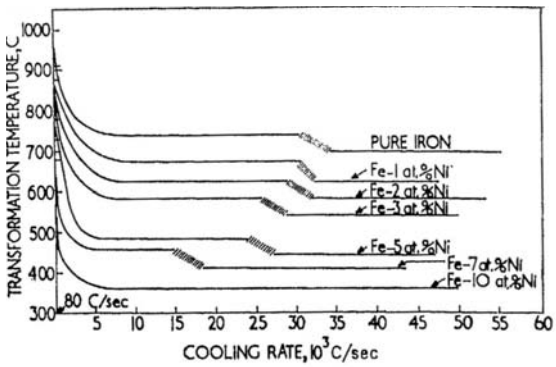

Figure 3.33: Austenite decomposition start temperatures plotted as a function of cooling rates for iron and Fe-Ni alloys [5].

Composition invariance during austenite to massive ferrite transformation

In binary alloys, precipitate growth without a composition change can occur below the T_0 temperature (at T_0, parent and product phases have the same free energy) [3]. The curve representing T_0 as a function of solute concentration lies within the two-phase field where the parent and product phases co-exist in equilibrium. Massive transformation sometimes seems to occur only when the parent phase is transformed at a temperature within the single-phase field. This may be because at low undercoolings below T_0, the massive transformation initiates at nuclei whose composition differs from that of the matrix. As a result, nuclei become surrounded by a solute enriched or depleted zone; for the nucleus to develop into massive phase, it has to be able to consume the excess solute and accelerate to the steady-state massive growth rate.

Hillert has proposed a novel explanation of many of the characteristics of massive reactions in ferrous alloys based solely on growth consideration [3]. His approach relies on the fact that all reported experiment has been conducted on alloys containing traces of interstitials as impurities. It is proposed that even in dilute binary Fe-C alloys, it is possible to obtain ferrite of the same composition as the parent austenite, while maintaining 'local equilibrium' at the interface. Since $x_1^{\gamma\alpha} >> \bar{x}_1$ (figure 3.34), there exist a narrow carbon concentration spike ahead of the interface. The height of the spike is not equal to $x_1^{\gamma\alpha}$. With constraint that $x_1^{\gamma} = x_1^{\gamma\alpha}$, it is only possible to get composition invariant growth when the alloy is transformed within the α phase field when $f = 1$ (since $x_1^{\alpha\gamma}$ is otherwise less than $\bar{x}_1$), so that the model explains why massive transformations may not occur in the two-phase α+γ field even though the T_0 Curve lies in this field.

Under these circumstances, the growth of massive ferrite can be expected to occur under mixed diffusion and interface-control, some of the free energy of transformation being dissipated in driving the diffusion of C in the austenite ahead of the interface. This loss of free energy can be subtracted from the total driving force and the rate of interface motion obtained by substituting the residue into an equation for interface-controlled growth. The calculated interface velocity was found to initially increase sharply with decreasing temperatures, the plot of temperature vs. decreasing growth rate have to form a 'C' curve. If growth is considered to be the limiting factor in overall transformation kinetics, then this C curve is considered to be replicated in the TTT diagram of the alloy. The model therefore predicts the existence of a plateau (at the temperature corresponding to $x_1^{\alpha\gamma} = \bar{x}_1$) in the relevant 'C' curve of the TTT diagram and hence explains the first plateau in continuous cooling experiments.

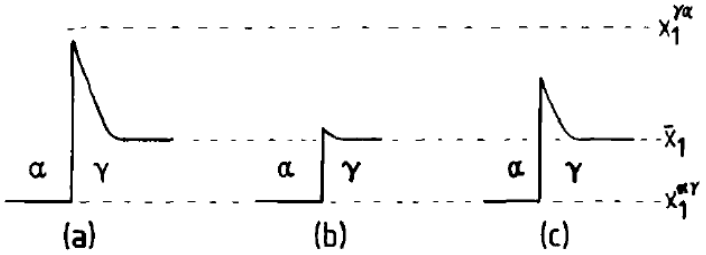

Figure 3.34: Carbon concentration profile at a α / γ interface moving under: (a) diffusion-control, (b) interface-control; and (c) mixed interface and diffusion-control [3].

3.5 Solid state nucleation

The physical mechanism involved in the nucleation of ferrite from austenite depends on the temperature at which the transformation starts, which is determined by the cooling rate. There is antinomy among the scientist in terms of how cooling rate affects the transformation start temperature in ultra low carbon steel. Back in 1964, Bibby and Parr (figure 3.32) [7] showed that for a range of cooling rates, the transformation start temperature decreases with increasing cooling rate. After this another range of cooling rate exists for which transformation start temperature becomes independent of cooling rates. Militzer (figure 3.35a) [8] and Liu et al. (figure 3.35b) [9] in their experimentations for ultra-low carbon steels showed that transformation start temperature decreases with increasing cooling rate.

In reconstructive nucleation an embryo with the composition and crystal structure of the new phase is first of all considered to form at local chemical heterogeneity in the matrix. This can occur, for example, due to statistical fluctuations in compositions, possibly amplified by thermodynamic segregation of solutes to lattice defects. Solute partitioning at the interface between the matrix and the embryo is assumed to be close to that at thermodynamic equilibrium. For transformation to occur the embryo must reach a critical size and the new phase must then be able to grow by some mechanism, such as atomic transport by diffusion. Examples of this type of nucleation include the austenite to ferrite transformation on cooling through the A_3 temperature, solidification, the continuous precipitation of carbides and nitrides in austenite to ferrite, and the transformation of ferrite to austenite on heating.[29]

During nucleation an interface is created which separates the target phase from the parent phase. At the interface, the solute contents in the ferrite embryo and in the austenite correspond to the local equilibrium values. Composition gradients are therefore formed in the two phases as illustrated in figure 3.36. For the embryo to grow, the corresponding solute fluxes must be ensured by diffusion. In the case of binary Fe-C alloys, it is carbon diffusion in the austenite which determines the rate of displacement of the interface. However, in commercial steels, the diffusion of substitutional solutes retards both formation and growth of

embryos. Moreover, their interaction with the interface can create a solute drag effect similar to that which impedes grain growth. The growth kinetics therefore depends on the rate of this solute exchange, involving diffusion over large distance in both austenite and ferrite. In the solid state, heat diffuses much faster than matter, so that the kinetics of interface displacement is governed by solute diffusion. Figure 3.37 schematically illustrates the effect of temperature on the growth rate. The driving force for growth is small at high temperatures, but increases as the temperature falls. In contrast, diffusion rates become greater as the temperature rises. Like the nucleation rate, the growth rate therefore goes through a maximum as the temperature falls.[29]

In early 1900s, scientists have tried to understand and quantify the initial stages of the formation of new phases [30]. Traditional theory of reconstructive nucleation assumes that it is possible to describe the appearance of the first crystal of the new phase using the macroscopic concepts of classical thermodynamics [29]. In the coming sections, the solid state nucleation of new phase will be described.

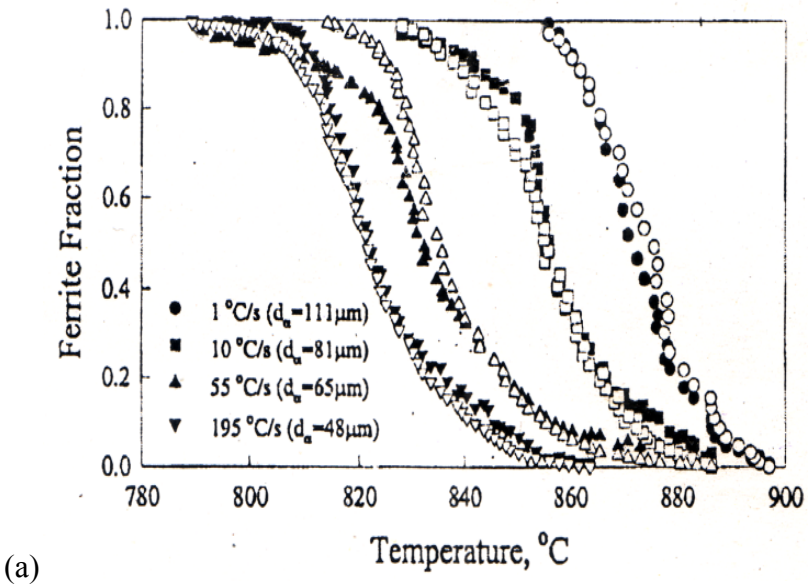

(a)

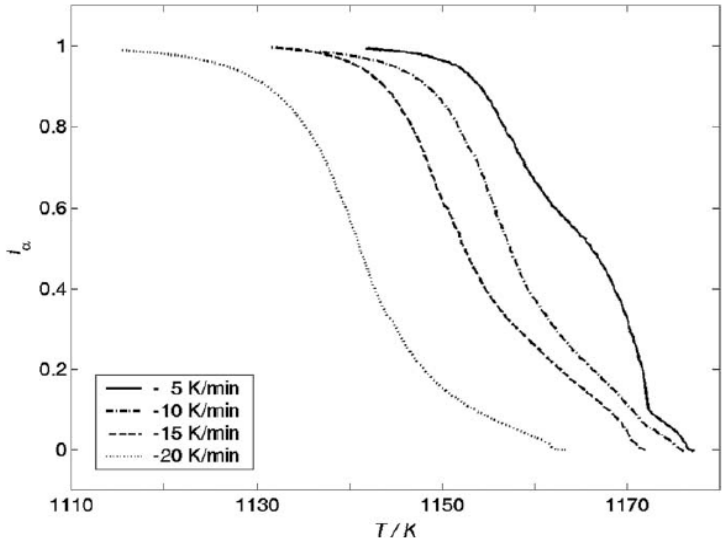

(b)

Figure 3.35: Effect of cooling rate on the transformation temperature of (a) Ultra-low carbon steel having 0.002 wt%C [8], (b) Ultra-low carbon steel having 0.01 at%C [9].

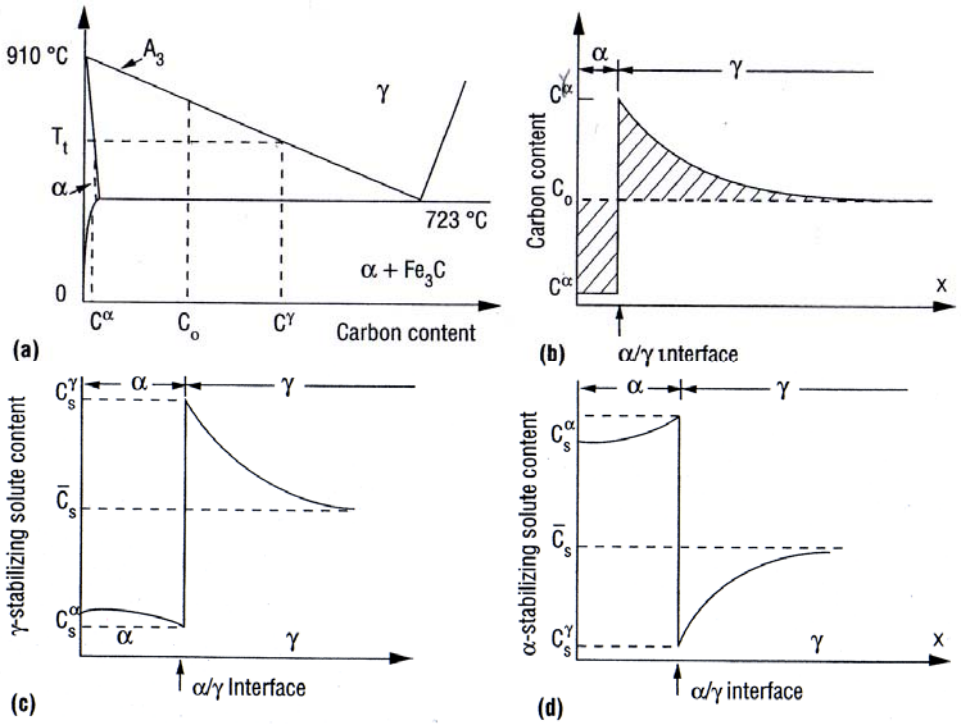

Figure 3.36: Schematic diagrams showing concentration gradients at the ferrite-austenite interface. (a) equilibrium diagram; (b) carbon concentration gradients at the transformation temperature; (c) concentration gradients for austenite stabilizing solutes; (d) concentration gradients for ferrite stabilizing solutes [29].

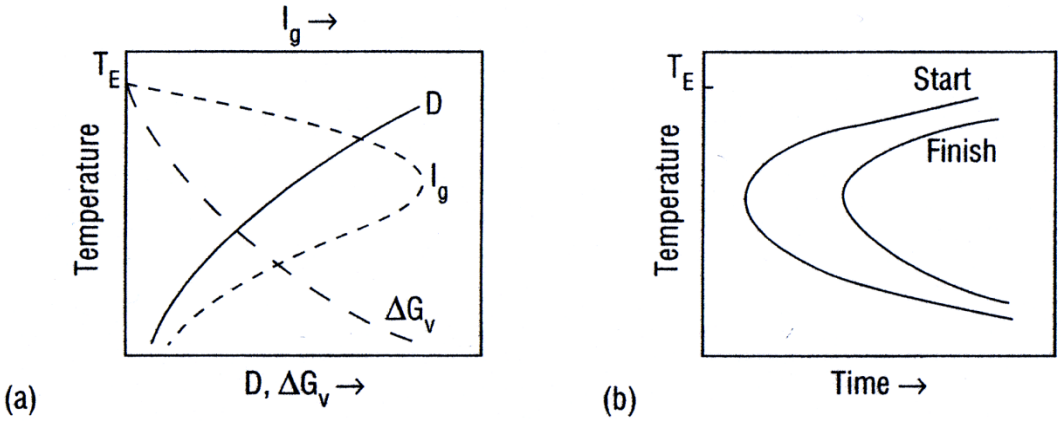

Figure 3.37: (a) Schematic variation of growth rate with temperature. D is the diffusion coefficient, ΔG_v is the free energy for transformation, and I_g is the embryo growth rate. (b) Schematic overall kinetics of the nucleation and growth processes [29].

3.5.1 Quantification of homogeneous nucleation

Porter and Easterling [6] and Kozeschnik [30], for instance, have described the models for quantification of nucleation processes. Following section will briefly describe these models.
The free energy change associated with the nucleation process will have three contributions [6].

1. At temperature where the new phase is stable, the creation of a volume *V* of new phase will cause volume free energy reduction of $V\Delta G_v$.

2. The new phase creates an interface between parent and product phase. This interface has some area A and interfacial energy γ. The area of interface will give rise to a free energy increase of $A\gamma$.
3. The new phase having volume V will not fit perfectly into the space originally occupied by the parent phase or matrix phase and it will give rise to misfit strain energy ΔG_s per unit volume of the new phase.

Addition of above contributions [6] will give the variation in free energy change as follows

$$\Delta G = -\frac{4}{3}\pi r^3(\Delta G_v - \Delta G_s) + 4\pi r^2\gamma \qquad \text{(eq. 3.14)}$$

Where
ΔG = free energy change associated with nucleation process, r = radius of the new phase, ΔG_v = free energy change per unit volume of the new phase, ΔG_s = misfit strain energy per unit volume of the new phase, $4/3\pi r^3$ = volume of the new phase (assuming that the new phase is spherical), $4\pi r^2$ = surface are of the new phase (assuming that the new phase is spherical).

The variation of free energy change as a function of radius is shown in figure 3.38. In solid state nucleation, the misfit strain energy reduces the effective driving force for transformation to (ΔG_v-ΔG_s).

In order to find critical radius (r^*) and value of free energy at critical radius i.e. G^*, differentiation of the above expression is required

$$\left|\frac{d(\Delta G)}{dr}\right|_{r=r^*} = \left|\frac{d(-\frac{4}{3}\pi r^3(\Delta G_v-\Delta G_s)+4\pi r^2\gamma)}{dr}\right|_{r=r^*} = 0 \qquad \text{(eq. 3.15)}$$

The above differentiation yields

$$r^* = \frac{2\gamma}{(\Delta G_v-\Delta G_s)} \qquad \text{(eq. 3.16)}$$

At r^*, $\Delta G=\Delta G^*$ [6]

$$\Delta G^* = -\frac{4}{3}\pi\left(\frac{2\gamma}{(\Delta G_v-\Delta G_s)}\right)^3(\Delta G_v - \Delta G_s) + 4\pi\left(\frac{2\gamma}{(\Delta G_v-\Delta G_s)}\right)^2\gamma \qquad \text{(eq. 3.17)}$$

Simplification of above expression gives

$$\Delta G^* = \frac{16\pi\gamma^3}{3(\Delta G_v-\Delta G_s)^2} \qquad \text{(eq. 3.18)}$$

For initiation of a single nucleation event, the critical nucleation energy G^* must be overcome and the probability P_{nucl} that this process occurs can be expressed as [30]

$$P_{nucl} \sim exp\left(-\frac{G^*}{kT}\right) \qquad \text{(eq. 3.19)}$$

Where k is the Boltzmann constant and T is the absolute temperature. From the probability of an individual nucleation event, the frequency of nucleation events in unit volume and unit time can be deduced. The respective quantity J is denoted as the nucleation rate and it quantifies the number of nuclei that are created in unit volume per unit time. The units of J are [events/(m^3s)]. Under steady state conditions, the nucleation rate J_{ss} is proportional to the probability P_{nucl} of a single nucleation event multiplied by the total number of possible nucleation sites N_0.

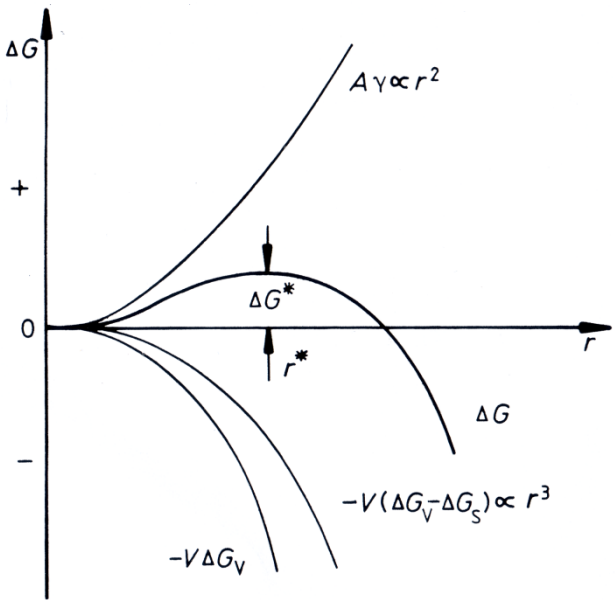

Figure 3.38: Variation of free energy change as a function of radius [6].

The rigorous treatment of nucleation in the framework of classical nucleation theory (CNT) delivers that the steady state nucleation rate can be interpreted as the flux of clusters in cluster size space, which grows to from critical to overcritical size and, in condensed systems, J_{ss} can be written as [30]

$$J_{ss} = N_0 Z \beta^* exp\left(-\frac{G^*}{kT}\right) \qquad \text{(eq. 3.20)}$$

In equation 3.20, the additional quantities Z and β^* have been introduced. The Zeldovich factor Z is related to the fact that the critical size of a nucleus is not exactly given by the maximum of the cluster formation energy. An additional energy contribution from thermal activation kT has to be taken into account because the thermal vibration destabilizes the nucleus as compared to the inactivated state. Z is often of the order of 1/40 to 1/100 and thus decreases the effective nucleation rate.
The atomic attachment rate β^* takes into account the long-range diffusive transport of atoms, which is necessary for nucleus formation if the chemical composition of matrix and precipitate differs.
When taking the incubation time τ for nucleation into account in the expression for the nucleation rate, most pragmatic approach is to multiply the steady state nucleation rate J_{ss} by a smooth function, which is zero at time t = 0, and which approaches unity at times $t > \tau$. In CNT, the traditional expression is [30]

$$J = J_{ss} \ . \ exp\left(-\frac{\tau}{t}\right) \qquad \text{(eq. 3.21)}$$

And we finally obtain [30]

$$J = N_0 Z \beta^* exp\left(-\frac{G^*}{kT}\right) exp\left(-\frac{\tau}{t}\right) \quad \text{(eq. 3.22)}$$

The transient nucleation rate *J* describes the rate at which nuclei are created per unit volume and unit time taking into account the incubation time τ.
The transient nucleation rate given in equation 3.22 can be rigorously derived for binary alloys. However, already in ternary systems, the applied methodology becomes involved and treatment of higher-order systems are more or less lacking. In a first approximation, equation 3.22 can nevertheless be applied to multicomponent systems, provided that extended expressions for some of the quantities that appear in this relation are used [30].
In equation 3.22, it is found that some of the quantities are already applicable to the multicomponent systems "as they are". For instance, the number of potential nucleation sites N_0 is independent of the number of components and the Zeldovich factor *Z* as well as the critical nucleation energy G^* already contain full multicomponent thermodynamic information. The critical quantity, which contains kinetic quantities describing multicomponent diffusive fluxes, is the atomic attachment rate β^*. An approximate multicomponent expression has been derived in ref. [11] in the modeling of multicomponent multiphase precipitation kinetics based on the thermodynamic extremal principle. The corresponding expression is presented in table 3.1 together with expressions for the other necessary quantities for evolution of multicomponent nucleation rates [30].

Table 3.1: Expression for evolution of multicomponent nucleation kinetics based on equation 3.22 [30]

Quantity		*Value*	*Comment*
Z (dim. less)	Zeldovich factor	$\left[\frac{-1}{2\pi kT}\frac{\partial^2 \Delta G}{\partial n^2}\right]^{\frac{1}{2}}$	n . . . number of atoms in the nucleus
β^* s^{-1}	Atomic attachment rate	$\frac{4\pi\rho^{*2}}{a^4\Omega}\left[\sum_{i=1}^{n}\frac{(c_{ki}-c_{0i})^2}{c_{0i}D_{0i}}\right]^{-1}$	ρ^* . . . crit. nucl. radius a . . . atomic distance Ω . . . molar volume c_i . . . concentrations D_{0i} . . . diffusion coeff.
ΔG^* (J)	Critical nucleation energy	$\frac{16\pi}{3}\frac{\gamma_k^3}{F^2}$	F . . . effective driving force γ . . . interfacial energy
ρ^* (m)	Critical nucleation radius	$\frac{2\gamma_k}{F}$	
τ (s)	Incubation time	$\frac{1}{2\beta^* Z^2}$	

3.5.2 Quantification of heterogeneous nucleation

According to Porter and Easterling [6] nucleation in solids, as in liquids is almost always heterogeneous. Suitable nucleation sites are defects such as dislocations, grain boundaries, stacking faults, inclusions, and free surfaces, all of which increase the free energy of the material. If the creation of the nucleus results in the destruction of the defect, some free energy (ΔG_d) will be released thereby reducing (or even removing) the activation energy barrier. The equivalent to equation 3.14 for heterogeneous nucleation is [6]

$$\Delta G = -V(\Delta G_v - \Delta G_s) + A\gamma - \Delta G_d \quad \text{(eq. 3.23)}$$

The most probable nucleation sites for the present work involve grain boundaries, which include grain corners or grain edges, so the focus will be on the grain boundaries as nucleation sites.

Nucleation on Grain Boundaries

Ignoring any misfit strain energy, an optimum embryo shape should be one which minimizes the total energy. The optimum shape for an incoherent grain-boundary nucleus will consequently be two abutted spherical caps as shown in figure 3.39, with θ given by [6]

$$cos\theta = \gamma_{\alpha\alpha}/2\gamma_{\alpha\beta} \quad \text{(eq. 3.24)}$$

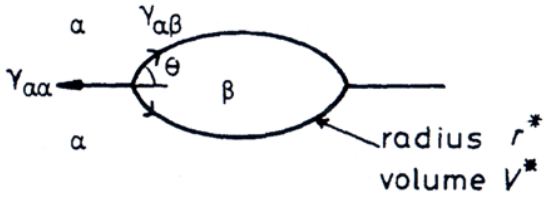

Figure 3.39: The critical nucleus size (V^*) for grain boundary nucleation [6].

(Assuming $\gamma_{\alpha\beta}$ is isotropic and equal for both grains). The excess free energy associated with the embryo will be given by [6]

$$\Delta G = -V\Delta G_v + A_{\alpha\beta}\gamma_{\alpha\beta} - A_{\alpha\alpha}\gamma_{\alpha\alpha} \quad \text{(eq. 3.25)}$$

Where V is the volume of the embryo, $A_{\alpha\beta}$ is the area of α/β interface of energy $\gamma_{\alpha\beta}$ created, and $A_{\alpha\alpha}$ the area of the α/α grain boundary of energy $\gamma_{\alpha\alpha}$ destroyed during the process. The last term of the above equation is simply ΔG_d in equation 3.23 (i.e. $\Delta G_d = A_{\alpha\alpha}\gamma_{\alpha\alpha}$).
The critical radius of the spherical cap will be independent of the grain boundary and given by [6]

$$r^* = 2\gamma_{\alpha\beta}/\Delta G_v \quad \text{(eq. 3.26)}$$

and the activation energy barrier for heterogeneous nucleation will be given by [6]

$$\frac{\Delta G^*_{het}}{\Delta G^*_{hom}} = \frac{V^*_{het}}{V^*_{hom}} = s(\theta) \quad \text{(eq. 3.27)}$$

where $S(\theta)$ is the shape factor given by [6]

$$S(\theta) = \frac{1}{2}(2 + cos\theta)(1 - cos\theta)^2 \quad \text{(eq. 3.28)}$$

The ability of a grain boundary to reduce ΔG^*_{het}, i.e. its potency as a nucleation site, depends on $cos\theta$, i.e. on the ratio $\gamma_{\alpha\alpha} / 2\gamma_{\alpha\beta}$.
V^* and ΔG^* can be reduced even further by nucleation on grain edges or grain corners, figure 3.40 and figure 3.41. Figure 3.42 shows how $\Delta G^*_{het} / \Delta G^*_{hom}$ depends on $cos\theta$ for the various grain boundary nucleation sites.

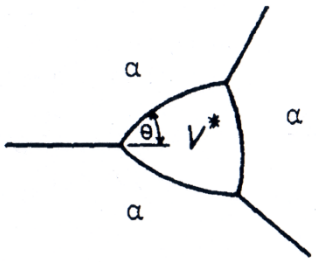

Figure 3.40: Critical nucleus shape for nucleation on a grain edge [6].

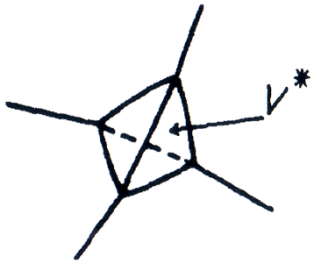

Figure 3.41: Critical nucleus shape for nucleation on a grain corner [6].

High-angle grain boundaries are particularly effective nucleation sites for incoherent precipitates with high $\gamma_{\alpha\beta}$. If the matrix and precipitate are sufficiently compatible to allow the formation of lower energy facets then V^* and ΔG^*_{het} can be further reduced as shown in figure 3.43. The nucleus will then have an orientation relationship with one of the grains. Such nuclei are to be expected whenever possible, since the most successful nuclei, i.e. those which form most rapidly, will have the smallest nucleation barrier.
Other planar defects such as inclusion / matrix interfaces, stacking faults and free surfaces can behave in a similar way to grain boundaries in reducing ΔG^*. Note, however, that stacking faults are much less potent sites due to their lower energy in comparison to high-angle boundaries.

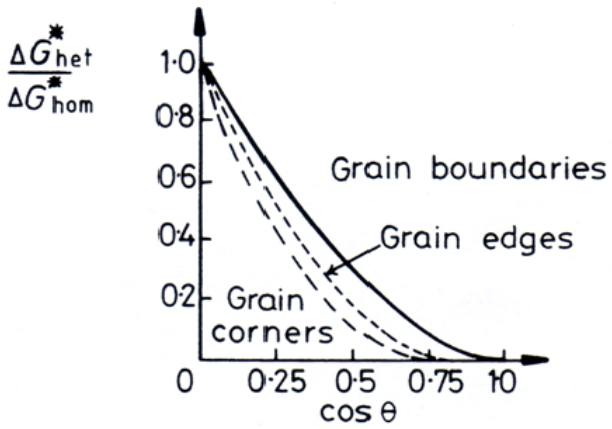

Figure 3.42: The effect of θ on the activation energy for grain boundary nucleation relative to homogeneous nucleation [6].

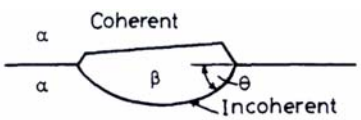

Figure 3.43: The critical nucleus size can be reduced even further by forming a low energy coherent interface with one grain [6].

3.5.3 Rate of heterogeneous nucleation

Porter and Easterling [6] have given the expressions for the assessment of heterogeneous nucleation rates. According to them if the various nucleation sites are arranged in order of increasing ΔG_d, i.e. decreasing ΔG^*, the sequence would be roughly homogeneous sites, dislocations, stacking faults, grain boundaries (and interface boundaries) and free surfaces. Nucleation should always occur most rapidly on sites near the end of the mentioned list. However the relative importance of these sites in determining the overall rate at which the alloy will transform also depends on the relative concentration of the sites. For homogeneous nucleation every atom is a potential nucleation site, whereas only those atoms on grain boundaries, for example, can take part in boundary-assisted nucleation.
If the concentration of heterogeneous nucleation sites is C_1 per unit volume, the heterogeneous nucleation rate will be given by an equation of the form [6]

$$N_{het} = \omega C_1 exp\left(-\frac{\Delta G_m}{kT}\right) exp\left(-\frac{\Delta G^*}{kT}\right) \text{ nuclei m}^{-3} \text{ sec}^{-1} \qquad \text{(eq. 3.29)}$$

Where ΔG_m = activation energy for the atomic migration per atom, ΔG^* = critical nucleation energy or activation energy barrier and in the above expression ω is a factor that includes the vibration frequency of the atoms and the area of the critical nucleus.
This is plotted as a function of temperature in figure 3.44. Note that, as with heterogeneous nucleation in liquids, measurably high nucleation rates can be obtained at very small driving forces. The relative magnitudes of the heterogeneous and homogeneous volume nucleation can be given by [6]

$$\frac{N_{het}}{N_{hom}} = \frac{C_1}{C_0} exp\left(\frac{\Delta G^*_{hom} - \Delta G^*_{het}}{kT}\right) \qquad \text{(eq. 3.30)}$$

(Differences in ω and ΔG_m are not so important and have been ignored) Since ΔG^* is always smallest for heterogeneous nucleation the exponential factor in the above equation is always a large quantity which favors a high heterogeneous nucleation rate. However, the factor (C_1/C_o) must also be taken into account, i.e. the number of atoms on heterogeneous nucleation sites relative to the number within the matrix, for grain boundary nucleation [6]

$$\frac{C_1}{C_0} = \frac{\delta}{D} \qquad \text{(eq. 3.31)}$$

Where δ the boundary thickness and D is is the grain size. For nucleation on grain edges and corners (C_1/C_o) becomes reduced even further to $(\delta/D)^2$ and $(\delta/D)^3$. Therefore a 50μm grain size taking δ as 0.5mm gives $\delta/D = 10^{-5}$. Consequently grain boundary nucleation will dominate over heterogeneous nucleation if the boundary is sufficiently potent to make the exponential term in equation 3.30 greater than 10^5. Values for C_1/C_o for other sites are listed in table 3.2.

Table 3.2: C_1/C_0 for various heterogeneous nucleation sites [6]

Grain boundary	Grain edge	Grain corner	Dislocations	
$D = 50$ μm	$D = 50$ μm	$D = 50$ μm	10^5 mm^{-2}	10^8 mm^{-2}
10^{-5}	10^{-10}	10^{-15}	10^{-8}	10^{-5}

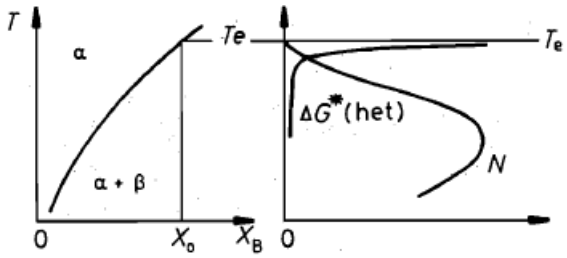

Figure 3.44: Rate of heterogeneous nucleation during precipitation of new phase (β) in alloy X_0 as a function of undercooling [6].

3.6 Precipitate growth

According to Porter and Easterling [6] growth of precipitate behind a planar incoherent interface is given by

$$v = \frac{D(C_0 - C_e)^2}{2x(C_\beta - C_e)(C_\beta - C_0)} \quad \text{(eq. 3.32)}$$

Where v is the velocity or growth rate of the interface, x is the thickness of the growing phase, D is the interdiffusion coefficient, C_β is the concentration of solute in the growing precipitate, C_0 is the concentration of solute in the bulk and C_e is the equilibrium concentration. C_β, C_0, and C_e are the thermodynamic quantities obtained from the phase diagrams.
The model presented in equation 3.32 is based on the assumptions that (i) the interfacial compositions are determined by local thermodynamic equilibrium, (ii) planar symmetry is used, and (iii) the concentration profile in the surrounding matrix can be approximated by a linear profile [30].
If it is assumed that the molar volume (V_m) is constant, the concentration in equation 3.33 is replaced with mole fraction ($X = C\ V_m$). Furthermore, for the sake of simplicity it can often be assumed that $(C_\beta - C_0) \approx (C_\beta - C_e)$.
Integration of equation 3.32 then gives

$$x = \frac{\Delta X_0}{(X_\beta - X_e)}\sqrt{Dt} \quad \text{(eq. 3.33)}$$

$$v = \frac{\Delta X_0}{2(X_\beta - X_e)}\sqrt{\frac{D}{t}} \quad \text{(eq. 3.34)}$$

Where ΔX_0 is the supersaturation prior to precipitation.
The following points are important to note regarding these equations
1. $x \propto \sqrt{Dt}$, i.e. precipitate thickening obeys a parabolic law.
2. $v \propto \Delta X_0$, i.e. for a given time the growth rate is proportional to the supersaturation
3. $v \propto \sqrt{\frac{D}{t}}$

Similarly Porter and Easterling [6] have given the growth rate of a plate like precipitate as

$$v = \frac{D\Delta X_0}{k(X_\beta - X_r)} \cdot \frac{1}{r}\left(1 - \frac{r^*}{r}\right) \quad \text{(eq. 3.35)}$$

Where k is the numerical constant (~1), r is the critical nucleus radius and C_r is the increase in equilibrium concentration (C_e) due to the Gibbs-Thomson effect.

For spherical precipitate, growth rate can be described by following equation [30]

$$\frac{d\rho}{dt} = \frac{D}{\rho}\frac{(C_0 - C_e)}{(C_\beta - C_0)} \quad \text{(eq. 3.36)}$$

If S supposed to be dimensionless supersaturation then

$$\frac{d\rho}{dt} = D\frac{S}{\rho} \quad \text{(eq. 3.37)}$$

In the above expression ρ is the position of the interface, i.e., the radius of the precipitate and $\dot{\rho} = \frac{d\rho}{dt}$ is the interface velocity, namely the growth rate of the precipitate.

3.7 Modelling of phase transformations

In 2004, J. Svoboda, F.D. Fischer, P. Fratzl and E. Kozeschnik presented a model which is called SFFK model. This model was implemented in MatCalc along with Kampmann and Wagner model. Kampmann and Wagner numerically integrated the rate equations for the change of particle radius and number density so their model was called numerical Kampmann-Wagner i.e. NKW Model [31].
In the present section the details of the NKW, SFFK model and comparison of SFFK model with other models will be described in the subsections 3.7.1, 3.7.2 and 3.7.3 respectively. At the end some details of the DICTRA and the related model used for the austenite to ferrite transformation will also be described as in the present perspective both MatCalc and DICTRA were used for the simulation of TTP diagrams to generate information about the operative transformation mechanism.

3.7.1 Numerical Kampmann-Wagner model

Both CNT and the growth laws (as described earlier) for the evolution of the precipitate radius represent ordinary differential equations. On integration of these equations in time, the evolution of all precipitates in the system is obtained. The following methodology has been suggested by Kampmann and Wagner ([30], [32]) and implemented by Kozeschnik et al. [12] in the MatCalc software package to solve the problem:

- Consider a system with unit volume. Divide time into discrete intervals Δt.
- Evaluate the nucleation rate for this time period. If $J > 0$
  - Create $N_{m+1} = J(t)\Delta t$ ((number of nuclei/volume.time)*time) precipitates. Collect all new N_{m+1} precipitates in a precipitate class with identical radius ρ_{m+1} and identical chemical composition. Let m be the number of existing precipitate classes in the class array.
  - Assign a radius ρ_{m+1} to the precipitate class, which is slightly larger than the critical nucleation radius ρ^* (r^* is used in some text).
- Evolve the radius ρ_k of all existing precipitate classes according to $\Delta\rho_k = (\rho_k/t)\Delta t$ with $k = 1, \ldots\ldots, m$.
- If the radius ρ_k of a precipitate class drops below a certain limit, remove the precipitate class from the array and decrease m by 1.
- If a new class of precipitates has been nucleated, increase m by 1.
- Repeat the steps until the finish time is reached.

This algorithm is commonly known as the numerical Kampmann-Wagner (NKW) model. With this methodology, in every time interval, a new precipitate class is created (provided that CNT yields a positive nonzero nucleation rate) and the growth kinetics of the existing precipitate classes is evaluated. A flow chart of this process is shown in figure 3.45 ([30], [12]).

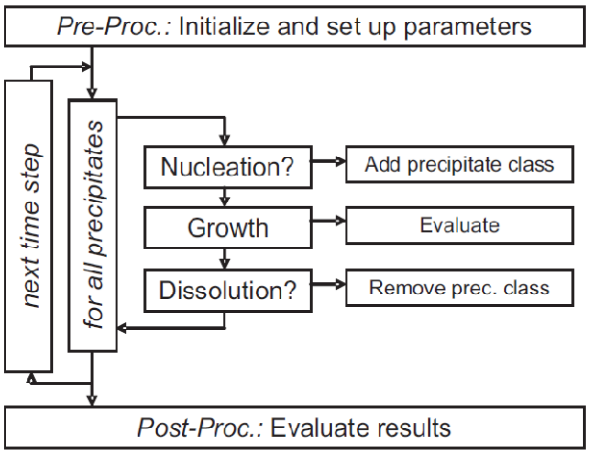

Figure 3.45: Typical scheme for numerical integration of the evolution equations for precipitate nucleation and growth ([12], [30]).

3.7.2 SFFK model

The SFFK model is based on the Onsager extremal thermodynamic principle, which states that a thermodynamic system evolves with a constraint maximum Gibbs free energy dissipation. It is also important to recognize that the representation of the total free energy of the system according to the SFFK model involves only mean quantities for the composition of the matrix as well as the precipitates. There are no concentration profiles involved in the formulation, which makes the SFFK model a classical mean-field approach [30].
Before discussing the free energy dissipation it is important to note the various contributions of free energy. These contributions are schematically presented in the figure 3.46 and ensemble in the equation 3.38 (see for example [11], [12], [30], [33]).

$$G = \sum_{i=1}^{n} N_{0i}\mu_{0i} + \sum_{k=1}^{m} \frac{4\pi\rho_k^3}{3}\left(\lambda_k + \sum_{i=1}^{n} c_{ki}\mu_{ki}\right) + \sum_{k=1}^{m} 4\pi\rho_k^2\gamma_k \qquad \text{(eq. 3.38)}$$

From figure 3.46 and equation 3.38 it can be seen that there are two major contributions i.e. matrix and precipitate contributions. The precipitate contribution is essentially composed of mechanical, chemical and interfacial contributions. Now a brief description of the various contributions of free energy are described as below
The matrix contribution is obtained by summation of the products of all moles of component N_{0i} with the corresponding chemical potentials μ_{0i}. The subscript ‘‘0’’ is related to the quantities of the matrix, whereas the subscript k denotes quantities of the precipitate with the index k.
λ_k is the mechanical free energy per unit volume and its multiplication with the volume of the spherical particle in contact with the matrix i.e. $\frac{4\pi\rho_k^3}{3}$ gives the mechanical energy contribution for Gibbs free energy from the precipitate / s. c_{ki} is the mean chemical composition and μ_{ki} is the chemical potential of component i. The product of mean chemical composition and the chemical potential gives the chemical energy per unit volume and when

this product is multiplied with the volume of that precipitate then it will give the chemical contribution to the Gibbs free energy from the precipitate. For the collective contribution, chemical and mechanical are added. The summation over k in the second term is performed over all m precipitates.

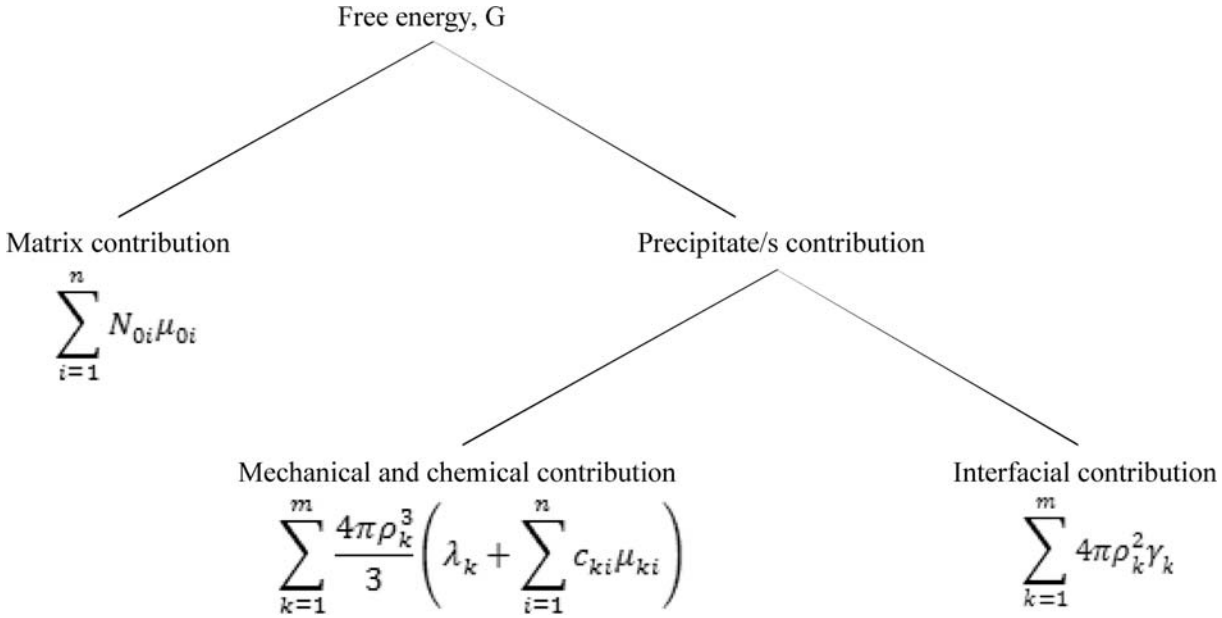

Figure 3.46: Schematic representation of various contributions to the free energy.

The third term takes into account the energy contribution of the precipitate-matrix interfaces. The specific interfacial energy γ_k is multiplied by the precipitate surface area $4\pi\rho_k^2$ and summation is performed over all precipitates k.
The subscript ''k'' used in the precipitate terms denotes quantities of the precipitate with the index k.
When precipitation occurs, this free energy is dissipated to take the system toward a more stable thermodynamic state. The classical dissipation products in phase transformation reactions are transformation heat (which is transported away) or entropy. In the SFFK model, three dissipation mechanisms are assumed to be operative ([11], [12], [30], [33]). These are

1. Dissipation by interface movement (~ friction): In order to move the interface, some driving pressure is required. The interface resists this pressure with a force. This force is comparable in its character to a friction force. This resistance against the driving pressure dissipates energy and the total rate of dissipation due to interface migration can be written as

$$Q_1 = \sum_{k=1}^{m} \frac{4\pi\rho_k^2}{M_k}\dot{\rho}_k^2 \qquad \text{(eq. 3.39)}$$

where M_k is the interface mobility.
2. Dissipation by diffusion inside the precipitate: The rate of Gibbs free energy dissipation due to diffusion inside the precipitate is given by

$$Q_2 = \sum_{k=1}^{m}\sum_{i=1}^{n} \frac{4\pi RT\rho_k^5}{45c_{ki}D_{ki}}\dot{c}_{ki}^2 \qquad \text{(eq. 3.40)}$$

3. Dissipation by diffusion inside the matrix:. The third contribution to the dissipation is more difficult to obtain and can only be evaluated in an approximate manner. It is assumed that the distance between the individual precipitates is sufficiently large such that the diffusion profiles of the individual precipitates do not overlap, the diffusive flux outside the precipitate can be expressed as

$$Q_3 \approx \sum_{k=1}^{m}\sum_{i=1}^{n}\frac{4\pi RT\rho_k^3}{c_{0i}D_{0i}}\left(\dot{\rho_k}(c_{0i}-c_{ki})+\frac{\rho_k\dot{c_{ki}}}{3}\right)^3 \quad \text{(eq. 3.41)}$$

The total rate of dissipation is given as

$$Q = Q_1 + Q_2 + Q_3 \quad \text{(eq. 3.42)}$$

The maximization of the Gibbs free energy dissipation rate $\dot{G}$ predicted by the Onsager thermodynamic extremal principle is given by [31]

$$\dot{G}+Q_1 + Q_2 + Q_3 = 0 \quad \text{(eq. 3.43)}$$

$$\frac{dG}{d\rho_k} = -\frac{1}{2}\frac{dQ}{d\dot{\rho}_k} \ (k = 1,\dots,m) \quad \text{(eq. 3.44)}$$

$$\frac{dG}{dc_{ki}} = -\frac{1}{2}\frac{dQ}{d\dot{c}_{ki}} \ (k = 1,\dots,m; i = 1,\dots,n) \quad \text{(eq. 3.45)}$$

A linear system of equations for each precipitate is obtained, which describes the change of radius and its composition according to [31]

$$\sum_{j=1}^{n+1} A_{ij}Y_j = B_i \quad \text{(eq. 3.46)}$$

The variables Y_j denote the rates $Y_j \equiv \dot{c}_{ki}$ $(i = 1,\dots,n)$, $Y_{n+1} \equiv \dot{\rho}_k$ and the Lagrange multipliers $Y_{n+1+j} \equiv \nu_{kj}$ $(j = 1,\dots,p_k)$. The latter are related to stoichiometric constraints of the precipitates [31].
The thermodynamic extremal principles leads to a linear set of evolution equations for each individual precipitate, which provides the growth rate $\dot{\rho}_k$ and the rate of change of chemical composition $\dot{c}_{ki}$ on the basis of the independent state variables of the precipitation system. For a single sublattice, the coefficients A_{ij} in equation are given with [30]

$$A_{n+1n+1} = \frac{1}{M_k} + RT\rho_k\sum_{i=1}^{n}\frac{(c_{ki}-c_{0i})^2}{c_{0i}D_{0i}} \quad \text{(eq. 3.47)}$$

$$A_{1i} = A_{i1} = \frac{RT\rho_k^2}{3}\frac{(c_{ki}-c_{0i})^2}{c_{0i}D_{0i}} \ (i = 1,\dots,n) \quad \text{(eq. 3.48)}$$

$$A_{ij} = \frac{RT\rho_k^3}{45}\frac{(c_{ki}-c_{0i})}{c_{0i}D_{0i}}\delta_{ij} \ (i = 1,\dots,n, j = 1,\dots n) \quad \text{(eq. 3.49)}$$

The symbol δ_{ij} is the Kronecker delta, which is zero if $i \neq j$ and one if $i = j$. The right-hand side of equation 3.46 reads

$$B_i = -\frac{\rho_k}{3}(\mu_{ki}-\mu_{0i}) \ (i = 1,\dots,n) \quad \text{(eq. 3.50)}$$

$$B_{n+1} = -\frac{2\gamma}{\rho_k} - \lambda_k - \sum_{i=1}^{n} c_{ki}\,(\mu_{ki}-\mu_{0i}) \quad \text{(eq. 3.51)}$$

Further details regarding this model can be found in the papers of Svoboda et al. [11] and Kozeschnik et al. ([12], [33]).

3.7.3 Comparison of growth kinetics of different models

Figure 3.47 presents the comparison of growth kinetics of different models as a function of supersaturation [30]. The Zener solution is for planar interfaces, while the other three solutions are for spherical symmetry. In this regard, the Zener model is only presented for the comparison purpose. Among the other three solutions, at low supersaturation all the three spherical solutions have exact agreement whereas substantial differences only occur if S becomes larger. In view of the fact that the SFFK model is a mean-field model with considerable degree of abstraction, that is, without detailed concentration profiles, the agreement is reasonable [30].

3.7.4 DICTRA

DICTRA is basically an abbreviation of diffusion (DI) controlled (C) transformation (TRA). According to Andersson et al. [13] this software was developed for the simulation of the rate of transformation in processes which involve long-range diffusion and moving phase boundaries. Due to the complexity in the treatment of multicomponent diffusion and moving boundaries the geometries are limited to one dimensional (planar, cylindrical and spherical) cases. These geometries can still successfully be used to model many processes of practical and scientific interest. The general structure of this software is shown in figure 3.48 [13].
From figure 3.48 it can be seen that for simulation purposes multicomponent thermodynamics and diffusion data is obtained from the thermodynamic database (TDB) and diffusion database (DTB) respectively. Diffusion coefficients are calculated from the mobilities in the databases for diffusion and thermodynamic factors from the thermodynamic databases. The different models in DICTRA are then based on solution of the multicomponent diffusion equations. All models except the one-phase model also use phase equilibria calculated in Thermo-Calc [13].
Once the system takes all the information from the databases i.e. concentration from the phase diagrams and information regarding diffusion coefficient from diffusion database, it requires some model to calculate the growth rate or velocity with which the transformation proceeds. This involves solution of multicomponent diffusion equations. The models employed in the software are shown in table 3.3 along with their application. Austenite to ferrite transformation is studied with the help of the moving boundary model so this model will be briefly described in the next sections. For further details readers are referred to the work of Andersson et al. [13] and Borgenstam et al. [34].

3.7.4.1 Moving boundary model

During austenite to ferrite phase transformation an interface (AB in figure 3.49) is created which separates the parent austenite and the product ferrite into two regions. The growth rate of this interface is determined by the rate of diffusion to and from the interface.
The above scenario is pictured in figure 3.49 where ferrite is growing into austenite in a binary system under isothermal conditions. The concentrations are obtained from the phase diagram shown on the right hand side and the corresponding concentration profiles are shown on the left hand side of the figure 3.49. The formulation of flux balance equation in order to conserve the number of moles of a component k is described as [13]

$$v^{\alpha} C_k^{\alpha} - v^{\gamma} C_k^{\gamma} = J_k^{\alpha} - J_k^{\gamma} \quad k = 1,2 \ldots n \qquad \text{(eq. 3.52)}$$

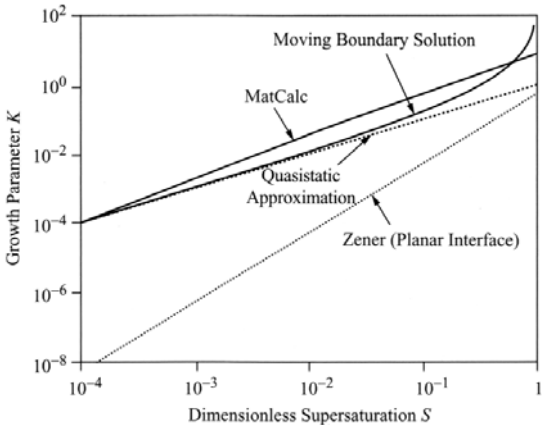

Figure 3.47: Comparison of the growth equations for the growth of precipitates [30].

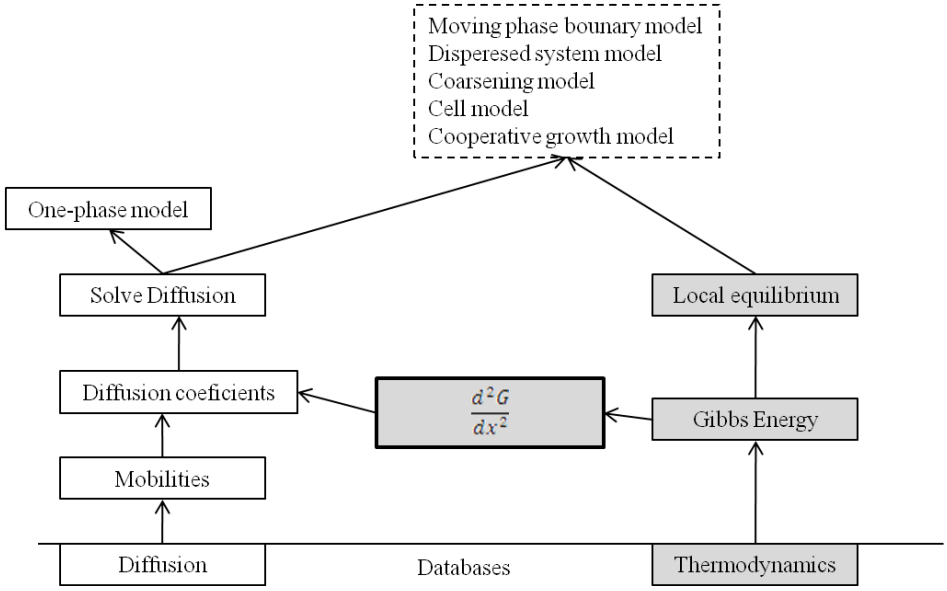

Figure 3.48: General structure of the DICTRA software. The grey boxes show functions supplied by ThermoCalc, which is used as a subroutine by DICTRA [13].

Figure 3.49 Growth of ferrite into austenite in a binary system under isothermal conditions. The corresponding concentration profile is shown in lower left part of the figure and the phase diagram in the lower right part of the figure [13].

Where v^{α} and v^{γ} are the interface migration rates in the α and γ phases respectively. C_k^{α} and C_k^{γ} are the concentrations of component k in α and γ phases respectively close to the phase interface and J_k^{α} and J_k^{γ} are the associated diffusional fluxes.
The integration in time is carried out by initially calculating the boundary conditions at the phase interface. Thermodynamic equilibrium is assumed to hold locally at the interface. This assumption, usually referred to as the local equilibrium hypothesis, is commonly applied and allows the boundary conditions to be determined. After this the diffusion problem in each one-phase region can be solved. The migration rate is obtained by solving the flux-balance equation 3.52. In case of multicomponent systems, this will generate a system of non-linear equations, which has to be solved by an iterative procedure.

Table 3.3: Models in DICTRA and their applications [13]

Sr. No.	Model name	Application of model
1	One-phase model	Homogenization of one-phase alloy Carburizing and decarburizing of steels
2	Moving boundary model	Austenite to ferrite transformation Carbide dissolution during austenitizing of steel Certain aspects of solidification
3	Model for diffusion in dispersed system	Carburization of high-temperature alloys Interdiffusion in composite materials Gradient sintering of cemented carbide work-tool pieces
4	‘‘Cell’’ model	Dissolution of particle distribution Simultaneous dissolution of particles of several different phases
5	Coarsening model	Coarsening of γ' particles Coarsening of carbides in austenite Coarsening of carbo-nitrides in ferrite
6	Cooperative growth model	Growth of pearlite in binary and multicomponent systems

CHAPTER 4: EXPERIMENTAL

4.1 Dimensions of the standard samples

Industrially produced quality steel alloys were used for the present experimental investigation. The as-received alloys were machined into hollow and solid cylindrical samples having standard dimensions as shown in the figure 4.1. As these samples have low concentration of carbon, their hardness is relatively low. Due to softness of the sample some tolerance must be given in order to facilitate the machining process. This tolerance is roughly 1 to 5 percent for length, 2 to 7 percent for diameter and 10 to 50 percent in wall thickness.

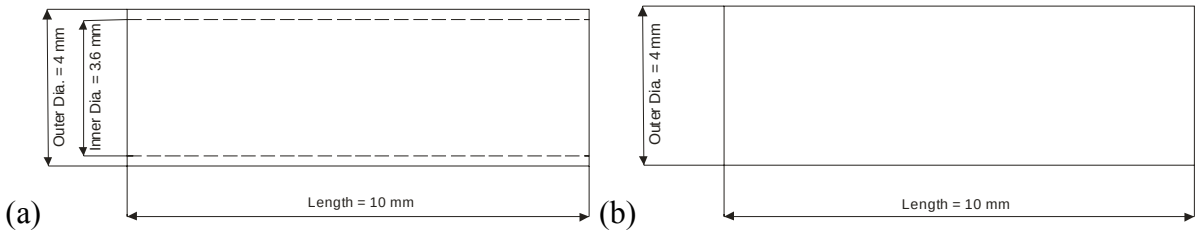

Figure 4.1: Dimensions of the standard hollow (a) and solid (b) cylindrical samples used in the present experimental investigation [35].

4.2 Chemical composition of ultra-low to low carbon steels

In the present experimental investigation four steel alloys were used. The chemical composition of these alloys is given in table 4.1 with respect to the relevant alloying elements. The complete chemical composition of these alloys is given in appendix-1. According to the carbon content these alloys can be divided into two categories i.e. ultra-low and low carbon steels. In the ultra-low carbon steel, the carbon content is 0.004 wt%C whereas in the low carbon steels, C is varied from 0.029 to 0.111 wt%.

Table 4.1: Chemical composition of alloys A, B, C and D

Type of Steel	Alloy	C (wt%)	Mn (wt%)	Si (wt%)
Ultra-Low Carbon	A	0.004	0.06	0.006
Low Carbon	B	0.029	0.326	0.009
	C	0.047	0.374	0.055
	D	0.111	0.932	0.167

4.3 Metallographic investigation of as-received samples

4.3.1 Mounting of the as-received specimens

The machined samples of the ultra-low to low carbon steels were mounted in a mixture of Araldite AY 103-1 (Europe) and Ren HY 956 (by Huntsman A.M (Europe)). The above mixture can be mixed in the following given compositions depending upon the quantity required for mounting one to several samples (e.g. 6).

1. 20 g Harz AY 103 + 3.4 g Härter Ren HY 956
2. 60 g Harz AY 103 + 10.2 g Härter Ren HY 956
3. 100 g Harz AY 103 + 17 g Härter Ren HY 956

4.3.2 Grinding and polishing of the as-received samples

State of the art equipment from Struers (TegraPol-31, TegraForce-5 and TegraDoser-5) was used for the grinding and polishing purpose. The grinding and polishing papers, suspensions, lubricants, forces and process parameters are given in table 4.2 for solid samples. It should be noted here that minor adjustment in the described parameters in the table 4.2 are always employed and it depends on the present condition of the specimen under microscope at that time.

Table 4.2: Program used for grinding and polishing of cylindrical solid samples of ultra-low to low carbon steel

Steps	Grinding / Polishing Cloth	Lubricant	Flow rate	Suspension	Flow rate	Force [N N]	Speed [RPM]	Direction	Process Time [min]
1	MD-Piano 220	Water	AN	-	-	20/130	300	>>	1
2	MD-Largo	DP-Blue	5/10	DP-P 9µm	5/10	20/180	150	>>	5
3	MD-DUR	DP-Blue	5/11	DP-P 3µm	9/11	30/180	150	>>	5
4	MD-Mol	DP-Red	5/10	DP-P 1µm	7/10	10/30	150	>>	5
5	MD-Chem	-	-	OP-S	5/8	10/30	150	>>	2

Definitions of the terminologies used in the table 4.2 are given in appendix-2.

4.3.3 Etching of the as-received samples

2%Nital (e.g. 2ml of Nitric Acid + 98ml Ethanol) was used for the etching purposes. The etching time was varying between ~ 3 to 10s).

4.3.4 Microstructure of the as-received samples

Microstructures of the as-received samples were obtained in both longitudinal (along the length) and transverse (along the diameter) cross-sections. Figure 4.2 represents the transverse cross-section of ultra-low to low carbon steel used for this investigation, whereas figure 4.3 is showing the longitudinal cross-section of the above mentioned steel. The grain analysis was carried out with Axio Vision (Release 4.7) [36]. Results of this grain analysis are displayed in table 4.3.

The diameters and the microstructures of the transverse and longitudinal cross-sections of the ultra-low to low carbon steels do not show any big differences except for the microstructure of steel D (figure 4.3d), which is showing alignment of carbon in the rolling / machining direction.

The microstructure of the ultra-low carbon steel consists of mainly the ferritic (bright) structure, whereas the microstructure of low carbon steel consist of ferrite (bright) and eutectoid mixture of ferrite and cementite which gives a dark appearance because their resolution is beyond the resolution limit of the optical microscopy.

Table 4.3: Measured grain diameter in the as received samples of alloys A, B, C and D

Alloy	GRAIN DIAMETER	
	TRANSVERSE Cross-section (µm)	LONGITUDINAL Cross-section (µm)
A	110	106
B	21	28
C	21	26
D	16	13

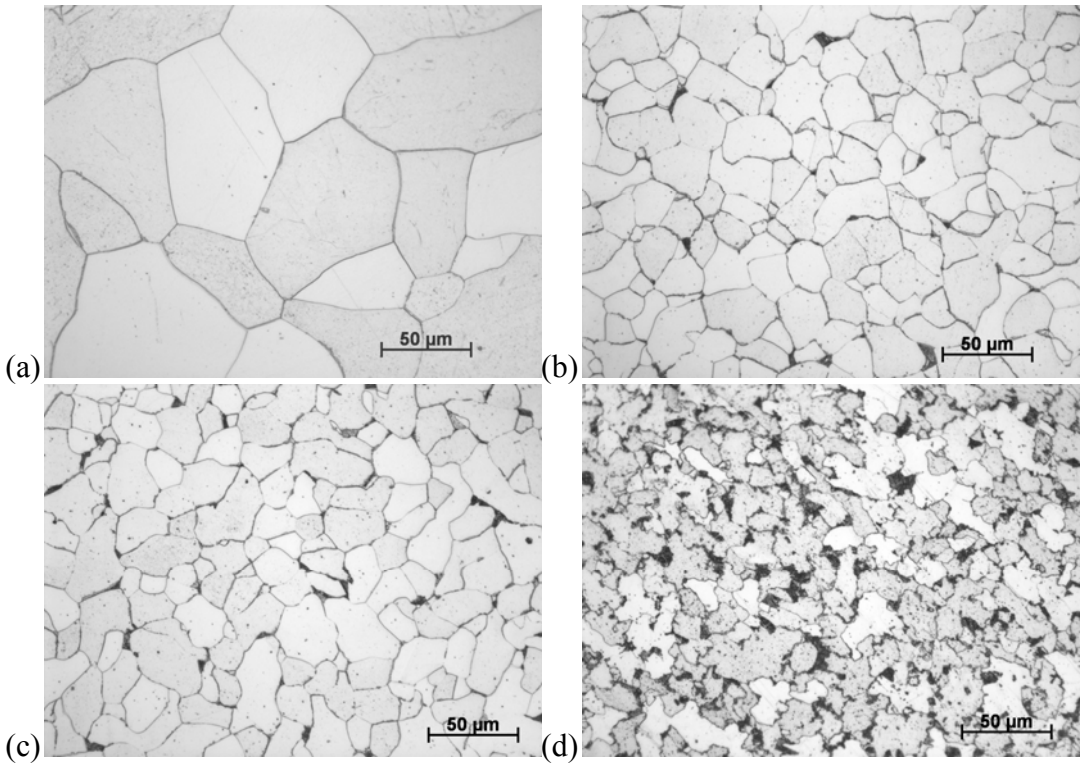

Figure 4.2: Transverse cross-section of (a) alloy A, (b) alloy B, (c) alloy C and (d) alloy D.

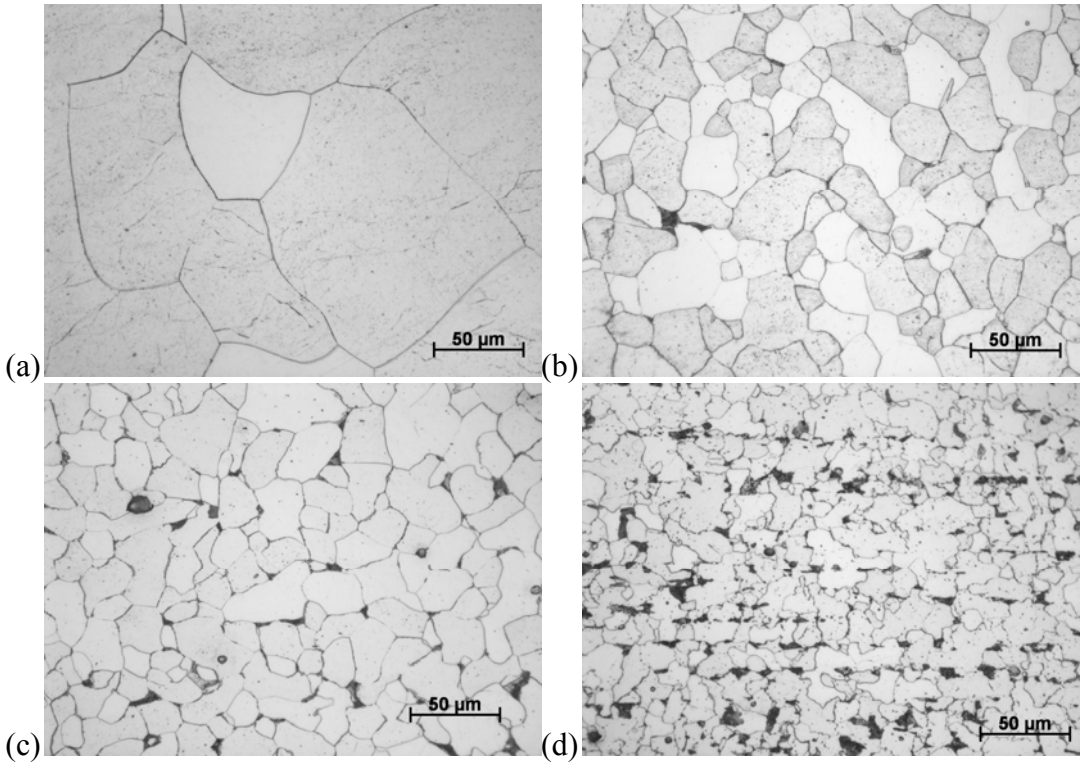

Figure 4.3: Longitudinal cross-section of (a) alloy A, (b) alloy B, (c) alloy C and (d) alloy D.

4.4 Experimental setup to measure thermal and dilatation profiles

State of the art high-speed quenching dilatometer 805A (by BÄHR Thermoanalyse) was used for the experimental investigation of the austenite to ferrite transformation in ultra-low to low carbon steel. Here, only those components will be described which are critical for the present experimental work. Table 4.4 summarizes the general features of this equipment.

Table 4.4: General features of the high-speed quenching dilatometer by BÄHR [35]

Features	High-Speed Quenching Dilatometer (805 A)
Temperature Range, depending on sample material	20°C-1500°C -15°C-1100°C
Heating Principle	Inductive
Atmosphere	Inert gas, vacuum, air
Resolution, Δl/°C	0.05µm/0.05°C
Solid geometry	Solid samples / hollow samples
Heating Rate	max. 4000K/s
Cooling rate	max. 2500K/s

In order to study phase transformations, appropriate heat treatment programs are designed in the dilatometer and executed. The software associated with the dilatometer replicate this program into thermal profiles during running of the experiment. This heat treatment causes various volumetric changes in the sample. These volume changes are recorded and the output is displayed in form of dilatation profiles. In this regard thermal and their corresponding dilatation profiles for alloy A (for example) are shown in figure 4.4 for the hollow sample. In case of solid samples of alloy A, these profiles are shown in figure 4.5 with austenitization temperature (T_{aus}) of 950°C and in figure 4.6 with austenitization temperature of 1100°C.

4.4.1 Description of replicated thermal profiles

The thermal profile can be divided into five segments.

(i) Heating segment (AB in figure 4.4a, figure 4.5a and figure 4.6a)

(ii) Austenitization segment (BC in figure 4.4a, figure 4.5a and figure 4.6a)
Quenching / cooling segment (CD in figure 4.4a, figure 4.5a and figure 4.6a). In this segment especially for lower temperatures heat of transformation is released which disturbs the thermal profile and its corresponding dilatation profiles.

(iii) Isothermal annealing segment (DE in figure 4.4a, figure 4.5a and figure 4.6a)

(iv) Quenching segment (EF in figure 4.4a). Fifth segment i.e. EF is not shown in figure 4.5a and figure 4.6a because the exact time for completion of phase transformation is not known. In this regard the segment DE is overestimated during programming and the segment EF is introduced eventually as the completion of γ→α transformation reaction is observed i.e. data recording is manually switched off. As the data recording is manually switched off so the segment EF is generally not recorded in such cases.

4.4.2 Description of recorded dilatation profiles

When the designed thermal cycle is executed in the dilatometer it causes various volumetric changes. These volumetric changes are recorded in the dilatometer and displayed in the form of dilatation profiles. From the dilatation profiles various characteristic features of phase transformations occurring in the samples can be identified. During heating and cooling phase

changes are observed and these changes are located by observing the slopes of the dilatation profiles. When there is a change in crystal structure, the slope is also changed. Actually this is the basic reason why a dilatometer can be used for studying phase transformations. The shown dilatation profiles of alloy A for hollow (figure 4.4b, c & d) and solid samples (with T_{aus} of 950°C (figure 4.5b & c) and T_{aus} of 1100°C (figure 4.6b & c)) can also be divided into various segments according to the observed changes. The expected cause of these observed changes will now be described briefly.

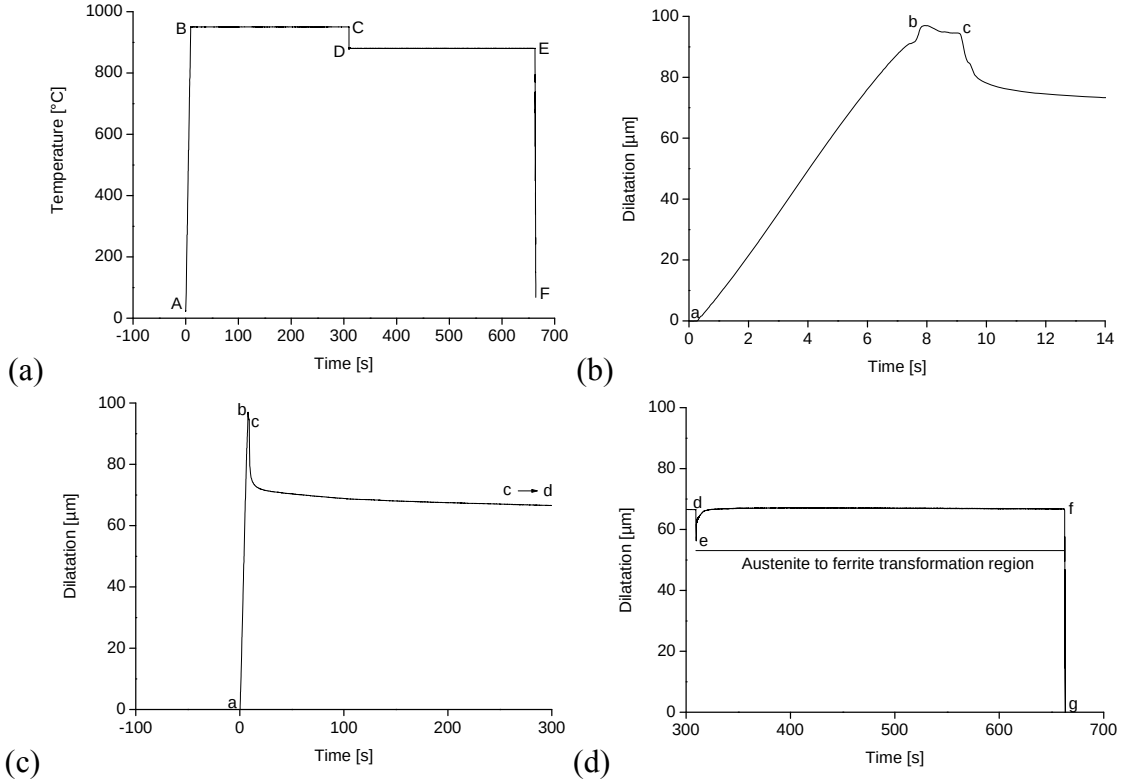

Figure 4.4: Complete thermal (a) and their corresponding dilatation profile (b, c and d) of hollow sample of alloy A showing the region in which the austenite to ferrite transformation occurs (segment ef) as a result of austenite decomposition (segment de).

4.4.2.1 Observed volume changes during heat treatment

The observed volume changes during heat treatment of hollow and solid samples (of alloy A as an example) are shown in figure 4.4 (b, c and d), figure 4.5 (b and c (with austenitiztion temperature of 950°C)) and figure 4.6 (b and c (with austenitiztion temperature of 1100°C)) respectively. For description purpose the dilatation profile has been divided into ab, bc, cd, de, ef anf fg segments.

ab segment: In this segment, the sample naturally expands as a result of heating to austenitization temperatures. During heating, small fluctuation (change in slope) before the $\alpha \rightarrow \gamma$ transformation are observed. These fluctuations are due to the ferromagnetic to paramagnetic transition of ferrite.

bc segment: In this segment, the $\alpha \rightarrow \gamma$ transformation occurred.

cd segment: In this segment, for hollow samples, contraction of austenite was observed during soaking of the sample at austenitization temperature. Here it should be mentioned that normally the slope is changed thrice. Once due to change in crystal structure, secondly after the change in crystal structure the sample again follows the heating program up to the austenitization temperature and thirdly due to soaking at austenitization temperature. In the hollow sample the second step was missing. Instead a contraction was observed. It is assumed

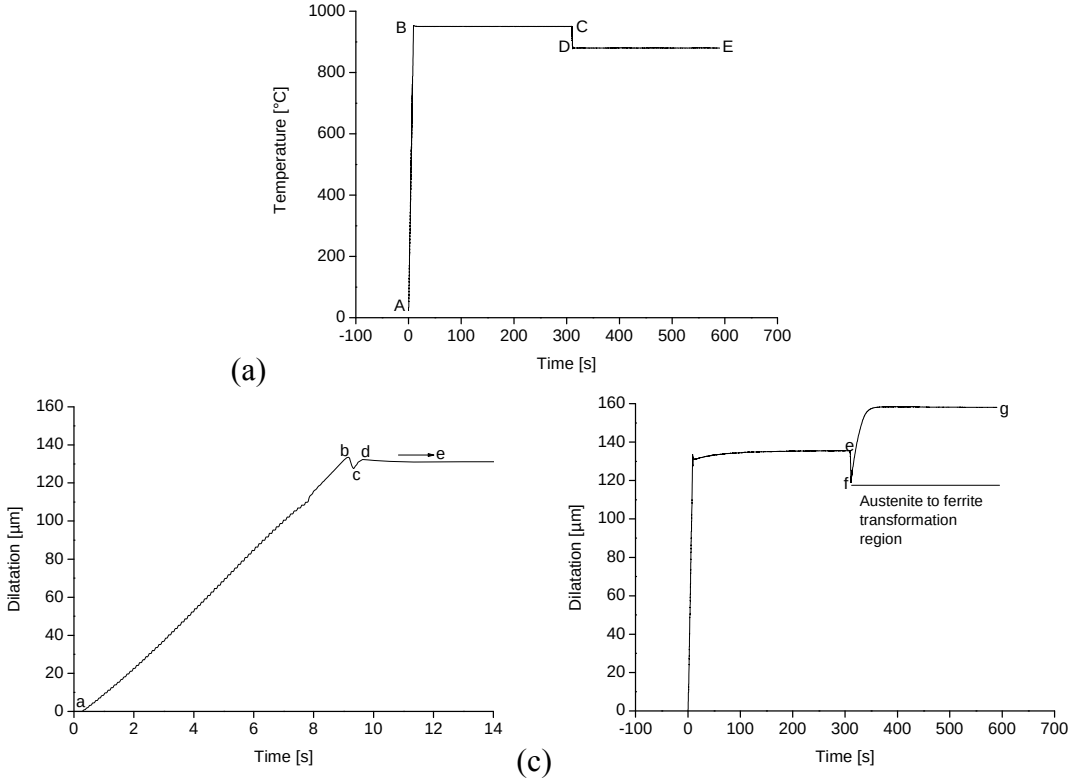

Figure 4.5: Complete thermal (a) and their corresponding dilatation profile (b and c) of alloy A for solid sample with T_{aus} = 950°C showing the region in which the austenite to ferrite transformation occurs (segment fg) as a result of austenite decomposition (segment ef).

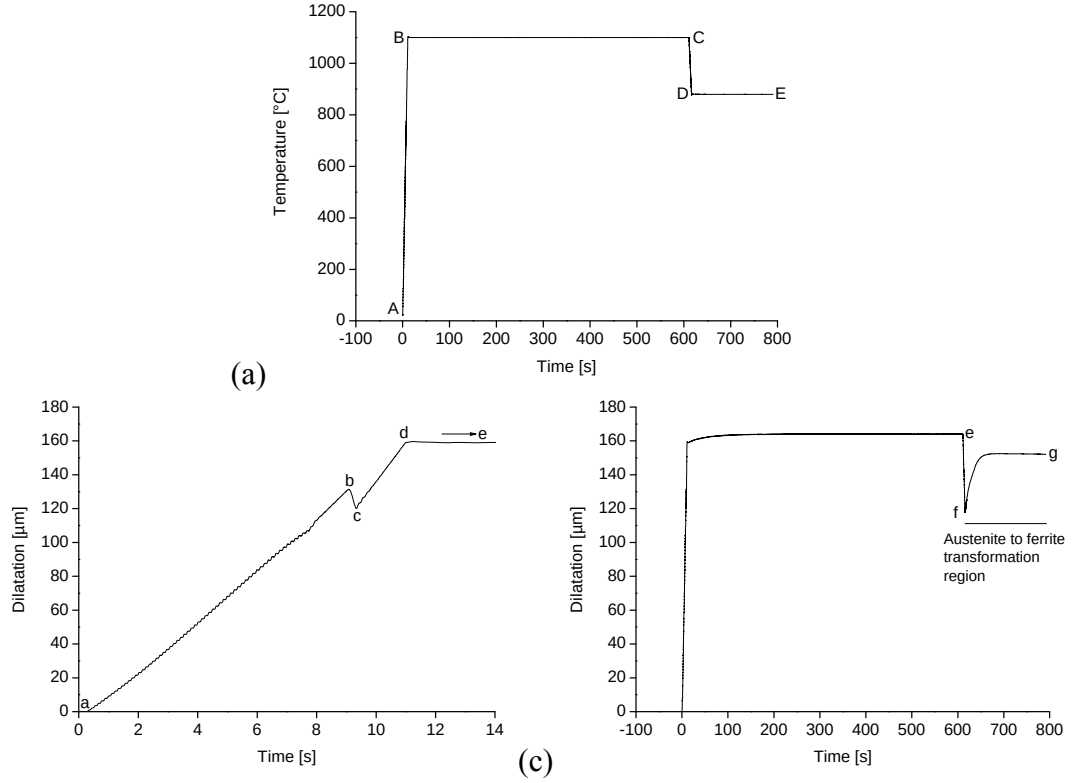

Figure 4.6: Complete thermal (a) and their corresponding dilatation profile (b and c) of alloy A for solid sample with T_{aus} = 1100°C showing the region in which the austenite to ferrite transformation occurs (segment fg) as a result of austenite decomposition (segment ef).

that this effect is due to the softening of the sample. The hollow sample due to low carbon content was mechanically weak and softens at a high temperature (> 900°C). In consequence the resulting dilatation is not enough to pull apart the push rods and transfer the signal to LVDT. Instead the force exerted by the push rods to hold the sample in between the push rod causes slight deformation and, thus, contraction of the sample. In solid samples, the cd segment (figure 4.5b and figure 4.6b) is showing the second change in slope where sample naturally expands as a result of heating to the austenitization temperatures.

de segment: This segment for hollow samples is showing the contraction of austenite as a result of its quenching down to the isothermal annealing temperature. In case of solid samples this segment is showing soaking at austenitization temperature.

ef segment: This segment for hollow samples is showing the $\gamma \rightarrow \alpha$ transformation whereas for solid samples it is showing contraction of austenite before the onset of $\gamma \rightarrow \alpha$ transformation.

fg segment: This is the last segment in hollow samples. In this segment, the sample is quenched and afterwards data recording is completed. For solid samples this is the segment where $\gamma \rightarrow \alpha$ transformation takes place.

gh segment: In solid samples the last segment is the gh segment. In figure 4.5 and figure 4.6 this segment is not shown because the data recording is terminated after observing that the phase transformation is completed. We can observe this segment in the appendix-3, where thermal and corresponding dilatation profiles for alloys B, C and D are shown.

For hollow samples de and ef and for solid samples ef and fg segments are the main focus of the present study because decomposition of austenite and evolution of ferrite takes place in these segments.

4.4.3 High-speed quenching dilatometer

Heat treatment of the samples was carried out in the chamber of the high-speed quenching dilatometer 805A (by BÄHR Thermoanalyse) as shown in figure 4.7. Heating of the samples was carried out in the coil as shown in figure 4.8. Three silica rods (glass type) can also be seen which are present there to assist the measuring of dilatation and thermal profiles. In figure 4.8, a gap in the push rod can be seen. The sample to be tested is placed in that gap and then this sample is pushed forward in between the coil before running the test. Variation in the temperature is measured by using S-type thermocouples (Platinum (Pt)/Rhodium (Rh) 10% - Platinum (Pt)). The thermocouple is attached with the one of three connecting positions available in the chamber for quantitative measurement of heating and cooling processes. These connectors are shown in figure 4.9. From three available positions, the top one (marked by 1) is reserved for the control thermocouple whereas the rest of the positions are for normal temperature measurement thermocouples. The control thermocouple on one end is attached with the sample while the other end is connected with the dilatometer for feeding the temperature inputs. This assembly is shown in figure 4.10. The thermocouple is attached to the sample by using a spot welding machine (see figure 4.11).

As mentioned in figure 4.4a, there are five segments in the thermal cycle. Out of these, two segments are associated with cooling / quenching of the samples. Two types of quenching / cooling are used in the present study. One is employed for the solid samples where cooling only from the outer surface of the sample was possible. For cooling purpose quenching gas is injected from the holes (figure 4.12) present in the interior of the coil used for induction heating. In this way this coil has dual functions i.e. it is used for both heating and cooling purposes.

For high speed quenching where hollow samples are used, two types of cooling are required i.e. from the outer surface and through the inner walls so as to ensure higher cooling / quenching rates. For this purpose an additional rubber pipe is attached which supplies the quenching gas through the hole present in the push rods to the inner walls of the hollow sample.

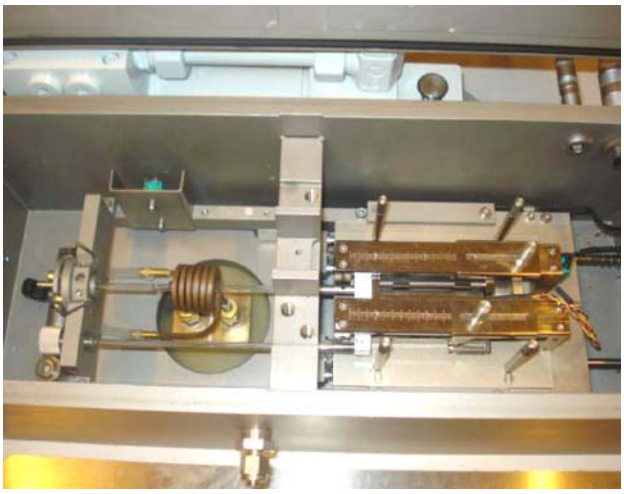

Figure 4.7: Chamber containing heating, cooling and dilatation measurement system.

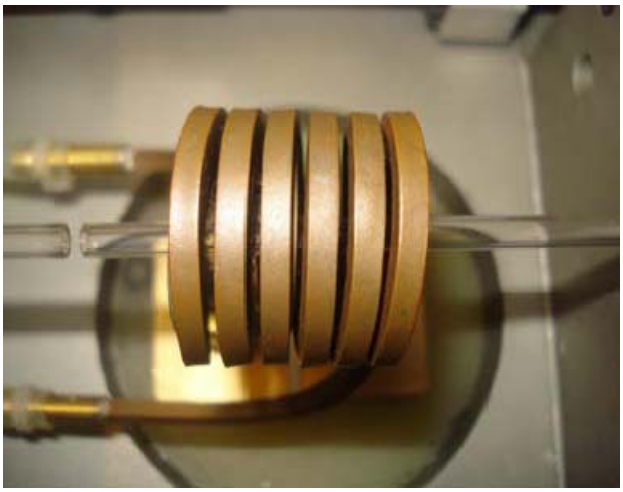

Figure 4.8: Coil used for heating and cooling of the samples to be tested.

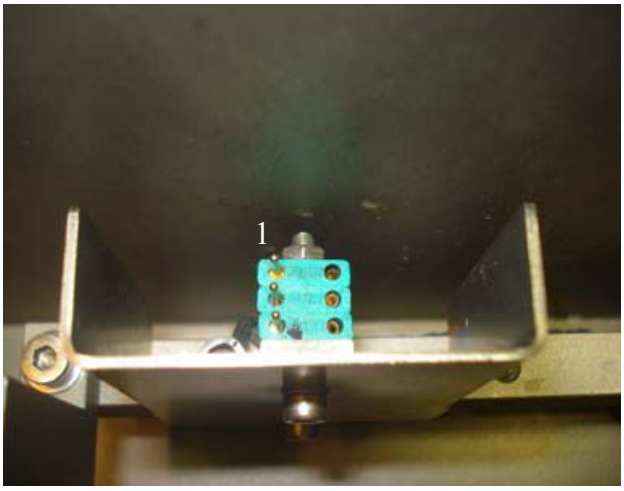

Figure 4.9: Three connecting positions for thermocouples. The top position is for control thermocouple and rest of the two positions are for normal temperature measurements.

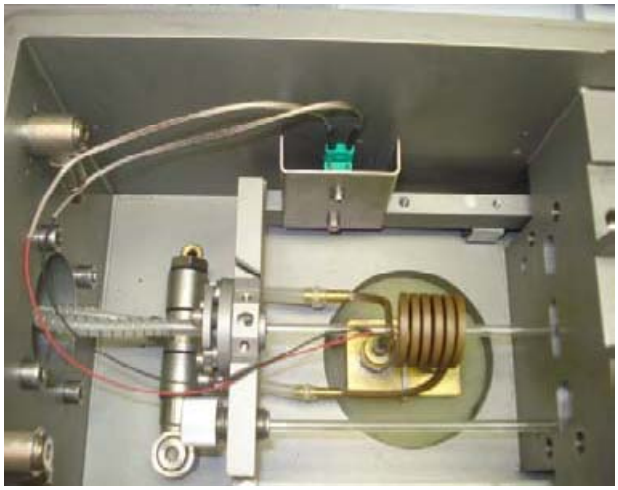

Figure 4.10: S-type (Pt/Rh 10%-Pt) thermocouple attachment with the dilatometer and sample.

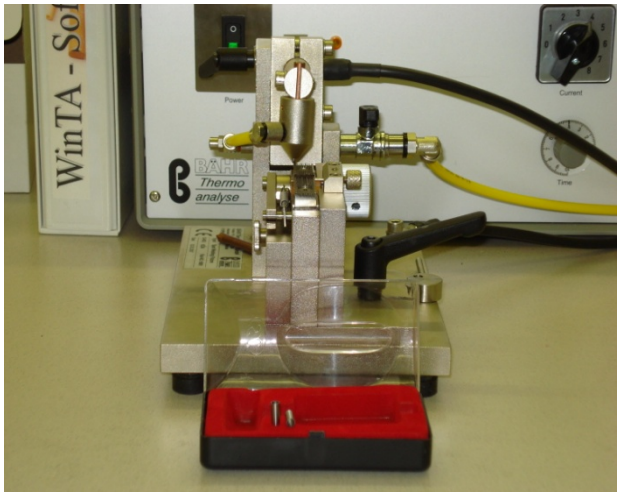

Figure 4.11: Spot welding machine used for attachment of the sample with the thermocouple.

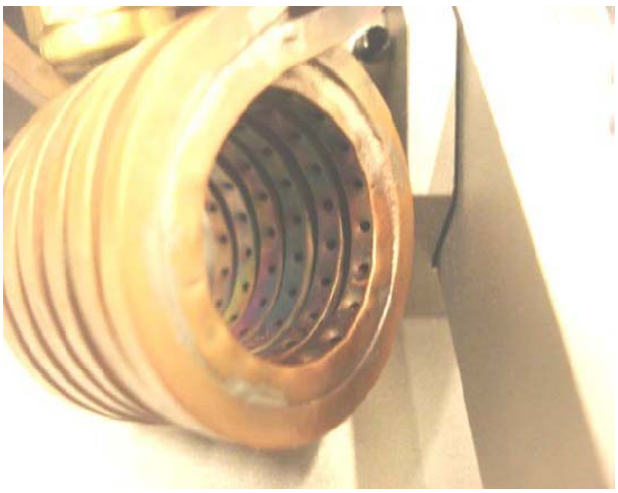

Figure 4.12: Holes in the coil for spraying the quenching gas on the top of the sample for cooling purpose.

Figure 4.13 is showing the two types of assemblies. Figure 4.13a is showing the normal assembly inside the chamber used with solid samples whereas figure 4.13b is showing the assembly specially employed for high speed quenching.
Three types of inert gases are commonly employed for quenching purposed. Table 4.5 is showing their heat absorbing capacity in terms of the specific heat capacity [37].

(a) 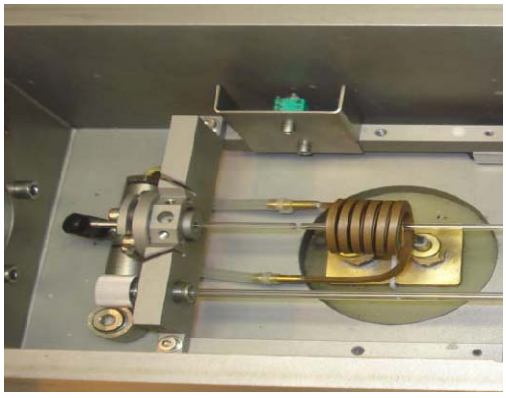 (b) 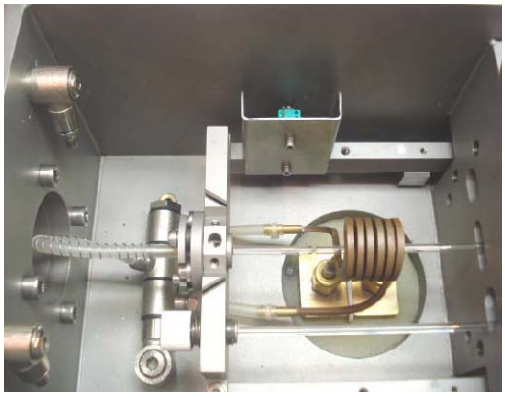

Figure 4.13: Assembly in the chamber (a) normally used for heat treatment of solid samples (b) specially used for hollow samples with additional rubber pipe on the left to ensure cooling through inner walls and to obtain high cooling rates.

Table 4.5: Specific heat capacity of helium, nitrogen and argon gases

No.	Quenching Gas	Specific heat capacity [J/kg.K]
1	Helium (He)	5190
2	Nitrogen (N)	1040
3	Argon (Ar)	520

Referring to table 4.5, helium is selected as a quenching gas to ensure maximum quenching rates for this study. When fast cooling / heating rates are used, the transition from one segment to other (e.g. from heating rate defining segment AB to the austenitization segment BC in the figure 4.4a) is not instantaneous. Obviously oscillations in the thermal profiles are observed in terms of undershoots and overshoots. In order to reduce the amplitude and earlier damping of these oscillations in the thermal profile, fine tuning of parameters is employed with a PID controller. In this controller the precision is obtained by adjustment of control parameters Xp, Tn and Tv. These parameters can be adjusted for each temperature segment but the usual recommendation is to use same Xp, Tn and Tv parameter for the whole heat treatment segment to avoid larger fluctuations in HF power profile.
For the present study the values of the control parameters Xp, Tn and Tv used in the heat treatment of alloys A, B, C and D are shown in table 4.6. For gas flow control parameters Xp, Tn and Tv are also used but these are not very critical. For majority of the segments values of control parameters Xp, Tn and Tv was 10, 50 and 0.5 respectively. In some segments 5, 200 and 5 was also used.
Dilatation profiles are obtained by measuring the change in lengths of the specimens. In case of expansion or contraction, glass rods transfer this signal to the LVDT (linear volumetric differential transducer) as shown in the figure 4.14.
As already mentioned, there are three glass rods (figure 4.13) used for dilatation measurements. Between the two glass rods there is a gap for holding the sample to be tested. To hold the sample firmly a spring is used. This spring is shown in figure 4.14. Any stretch of the spring increases the force on the sample through LVDT part of the glass rod because only that part is mobile and the other glass rod is fixed. The third glass rod is some sort of

reference rod and it also fixes the assembly while measuring. Its fixture is controlled with a back spring as shown in figure 4.15 (not in view in figure 4.14).

Table 4.6: Values of the control parameters Xp, Tn and Tv used in various segments of the thermal profiles during heat treatment of alloys A, B, C and D for all IT temperatures

No.	Alloy	Type of sample	Austenitization Temperature [°C]	Xp	Tn	Tv
1	A	Hollow	950	28	150	0.2
2	B	Hollow	950	28	150	0.2
3	C	Hollow	950	28	150	0.2
4	D	Hollow	950	28	150	0.2
5	A	Solid	950	100	200	0.2
6	B	Solid	950	100	200	0.2
7	C	Solid	950	100	200	0.2
8	D	Solid	950	100	200	0.2
9	A	Solid	1100	100	200	0.2
10	B	Solid	1100	100	200	0.2
11	C	Solid	1100	100	200	0.2
12	D	Solid	1100	100	200	0.2

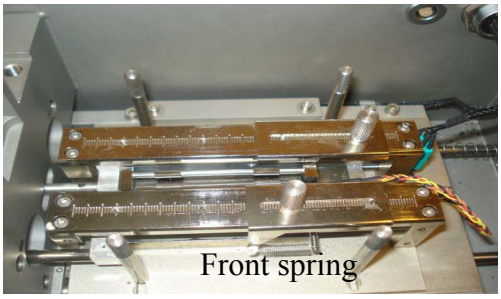

Figure 4.14: LVDT used for recording dilatation profiles.

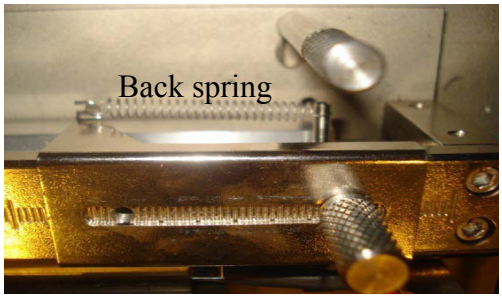

Figure 4.15: Back spring of LVDT.

4.5 Programmed thermal treatment

4.5.1 Programmed thermal treatment used for hollow samples

Hollow cylindrical samples of the alloys A, B, C and D were thermally treated according to the thermal program as shown in figure 4.16. These samples were heated at a rate of 100K/s to the austenitization temperature (T_{aus}) of 950°C. After soaking for 300s (i.e. 5 minutes) at this temperature, these samples were quenched to their respective target isothermal transformation (IT) temperatures. The details of these IT-temperatures for the hollow samples of alloys A, B, C and D are shown in figure 4.16.

At IT-temperature, the austenite (γ) to ferrite (α) transformation is allowed to complete. After completion of the transformation the sample is quenched. This quenching portion is either the part of the programmed thermal cycle or can be employed manually by interrupting the annealing process. Normally the heating segment (ab) and the soaking at austenitization temperature (segment bc) is carried out in vacuum. In the experimentation with hollow samples, very high cooling rates are involved. These cooling rates are causing jumping of the samples during the quenching (cd) segment. So instead of vacuum another method is employed with the recommendation of the BÄHR Company. The detail of this method is given in appendix-4. Here the essence of this method will be described.

This method involves manual production of the desired environment before data recording. The chamber is evacuated by maintaining 5 X 10^{-4} mbar pressure in the chamber. The purpose of this step is to make the environment cleaner and flushing of the oxygen present in the chamber. Then the protective gas such as helium is flushed to such an extent that it maintains an under pressure ranging from 0.10 to 0.20 bar which is necessary to close the lid of the chamber and avoid exposure of the chamber to the outer environment.

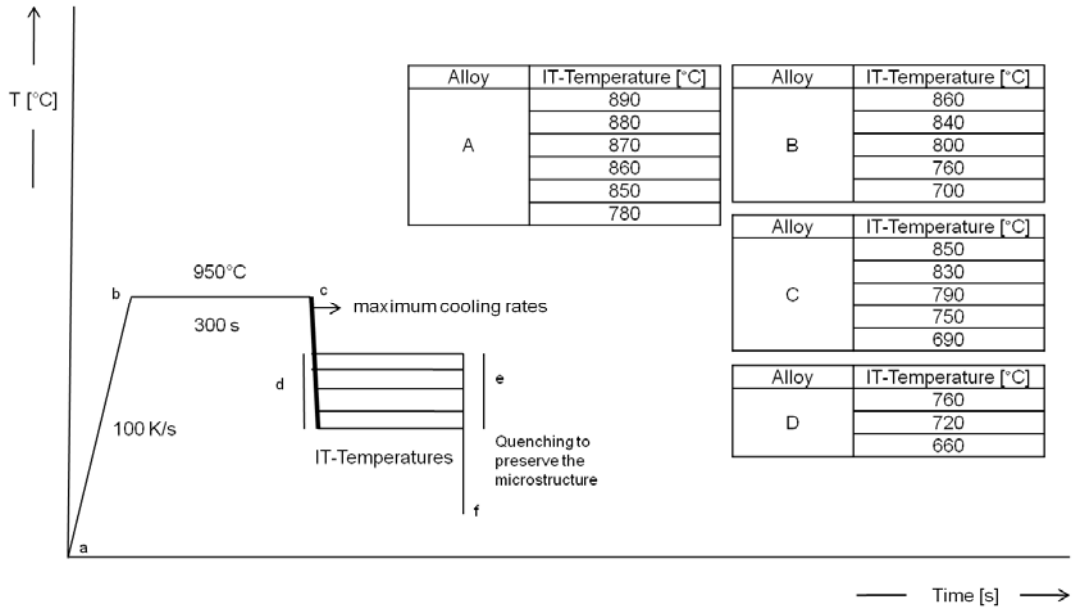

Alloy	IT-Temperature [°C]
A	890
	880
	870
	860
	850
	780

Alloy	IT-Temperature [°C]
B	860
	840
	800
	760
	700

Alloy	IT-Temperature [°C]
C	850
	830
	790
	750
	690

Alloy	IT-Temperature [°C]
D	760
	720
	660

Figure 4.16: Schematic of the thermal program applied for heat treatment of hollow samples of alloys A, B, C & D.

After soaking the samples are quenched (segment cd) to IT-annealing temperatures. The quenching is obtained by using the helium quenchant. Two options are available in high-speed quenching dilatometer by BÄHR. One is the controlled one, in which only the cooling rate is defined during programming the segment. This type of option is used for normal heat treatments, while for very high quenching rate control of the bigger valve for helium jet is used. In this type of quenching, helium valve opening is optimized to reach the IT-annealing temperature. This type of cooling is called uncontrolled cooling. The specialty of this cooling method is that when it is applied to the hollow samples it cools the sample not only from the outer surface but also from the inner walls of the sample. In this way very high quenching rates can be obtained. These quenching rates can be measured by taking the slope of the thermal profiles (i.e. segment cd (ref. figure 4.16)). Optimized valve opening times to reach the IT-annealing temperatures and their corresponding measured cooling rates for the hollow samples of the alloys A, B, C and D (for the segment cd i.e. quenching segment from the austenitization temperature to the IT-temperature) are given in table 4.7.
The samples were held at IT-temperatures (segment de (ref. figure 4.16)) for the time necessary for the completion of the austenite (γ) to ferrite (α) transformation.

4.5.2 Programmed thermal treatment used for solid samples

Two different austenitization temperatures (T_{aus}) were used for the experimentation involving solid cylindrical samples. One series of experiments is completed with T_{aus} = 950°C while the other with T_{aus} = 1100°C. The soaking time for 950°C was 300 s (i.e. 5 minutes) whereas this was 600 s (i.e. 10 minutes) in case of 1100°C.

The schematic of the thermal treatment applied to the solid samples is shown in figure 4.17. The samples were heated at a rate of 100K/s to reach the austenitization temperature (segment ab (ref. figure 4.17)). After soaking (segment bc (ref. figure 4.17)), these samples were cooled at a rate of 40K/s to reach the target IT-temperatures (segment cd (ref. figure 4.17)). Here controlled cooling was employed for the heat treatments. In the experiments with the solid samples only that valve opening time is registered which is necessary to maintain the programmed cooling rate of 40K/s. Here high jet of helium is not required because it can disturb the thermal as well as their corresponding dilatation profiles, so the small valve was allowed to function on its turn during programming the heat treatment segment in the dilatometer. The valve openings and their corresponding measured cooling rates are presented in table 4.8. For the rest of the thermal cycle i.e. for segment de and ef, the procedure is similar to the treatment given to hollow samples (section 4.5.1).

Table 4.7: Optimized valve opening times to reach the IT-temperatures and their corresponding measured cooling rates for the hollow samples of alloys A, B, C and D

Alloy	IT-Temperature [°C] Segment de (ref. figure 4.16)	Optimized valve opening time to reach IT-Temperature [ms] Segment cd (ref. figure 4.16)	Corresponding measured cooling rates [K/s]
A	890	18	900
	880	20	700
	870	26	1850
	860	25	1500
	850	31	2700
	780	50	3400
B	860	26	1300
	840	34	2100
	800	57	2150
	760	72	2200
	700	110	2900
C	850	28	850
	830	25	2400
	790	35	2650
	750	36	2800
	690	44	3300
D	760	56	2500
	720	71	2600
	660	83	3000

4.6 Experimentally measured thermal and dilatation profiles

Experimentally measured thermal and their corresponding dilatation profiles of alloys A, B, C and D are shown in figure 4.18 for hollow samples, figure 4.19 for solid samples with T_{aus} of 950°C and figure 4.20 for solid samples with T_{aus} of 1100°C. Here only the part of dilatation is shown which is in the scope of this work i.e. the austenite to ferrite transformation. For this purpose, these figures are started from the point where soaking time at the austenitization temperature is finished. For convenience all figures are transformed to zero time for thermal profiles, and zero time and zero dilatation for their corresponding dilatation profiles. Here only 2s data is shown for hollow samples and 20s data for solid samples. Complete data for thermal and dilatation profiles during the austenite to ferrite transformation is shown in appendix-5.

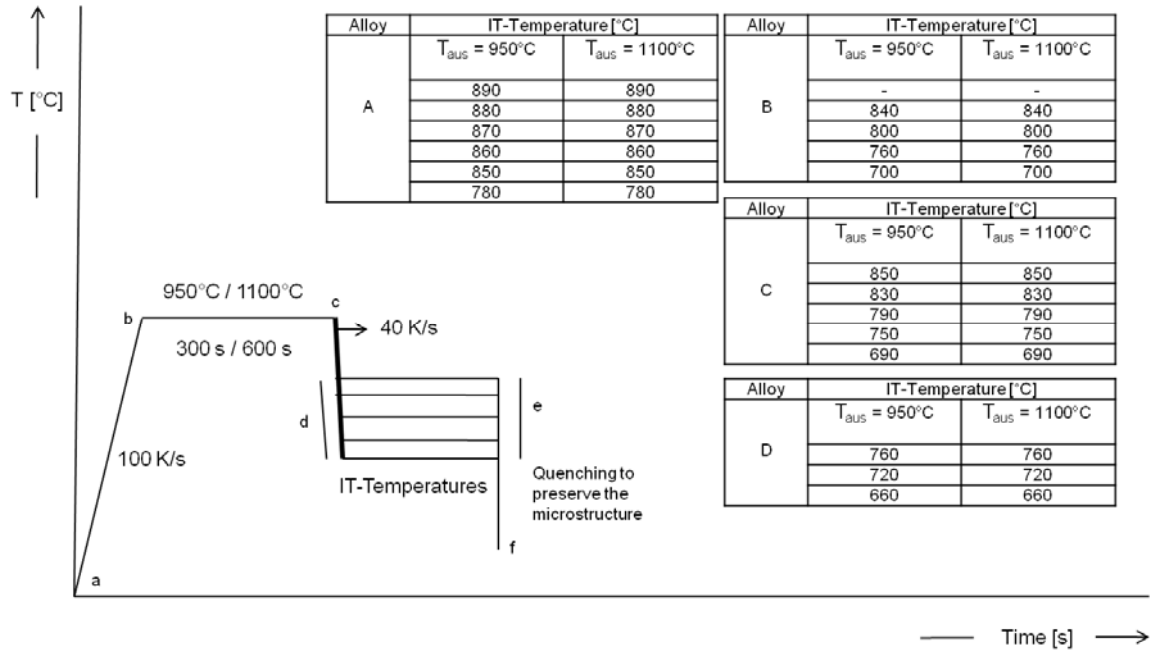

Alloy	IT-Temperature [°C]	
	T_{aus} = 950°C	T_{aus} = 1100°C
A	890	890
	880	880
	870	870
	860	860
	850	850
	780	780

Alloy	IT-Temperature [°C]	
	T_{aus} = 950°C	T_{aus} = 1100°C
B	-	-
	840	840
	800	800
	760	760
	700	700

Alloy	IT-Temperature [°C]	
	T_{aus} = 950°C	T_{aus} = 1100°C
C	850	850
	830	830
	790	790
	750	750
	690	690

Alloy	IT-Temperature [°C]	
	T_{aus} = 950°C	T_{aus} = 1100°C
D	760	760
	720	720
	660	660

Figure 4.17: Schematic of the thermal program applied for heat treatment of solid samples of alloys A, B, C & D.

Table 4.8: Programmed valve opening times to reach the IT-temperatures with 40K/s and their corresponding measured cooling rates for the solid samples of alloys A, B, C and D

Alloy	IT-Temperature [°C] Segment de (ref. figure 4.16)		Optimized valve opening time to reach IT-Temperature [s] Segment cd (ref. figure 4.16)		Corresponding measured cooling rates [K/s]	
	T_{aus} = 950°C	T_{aus} = 1100°C	T_{aus} = 950°C	T_{aus} = 1100°C	T_{aus} = 950°C	T_{aus} = 1100°C
A	890	890	1.5	5.25	40	40
	880	880	1.75	5.5	40	40
	870	870	2	5.75	40	40
	860	860	2.25	6	40	40
	850	850	2.5	6.25	40	40
	780	780	4.25	8	40	40
B	840	840	2.75	6.5	40	40
	800	800	3.75	7.5	40	40
	760	760	4.75	8.5	40	40
	700	700	6.25	10	40	40
C	850	850	2.5	6.25	40	40
	830	830	3	6.75	40	40
	790	790	4	7.75	40	40
	750	750	5	8.75	40	40
	690	690	6.5	10.25	40	40
D	760	760	4.75	8.5	40	40
	720	720	5.75	9.5	40	40
	660	660	7.25	11	40	40

4.6.1 Measured thermal and dilatation profiles of hollow samples

Thermal profiles of the hollow samples of alloy A are shown in figure 4.18a. Here it should be necessary to mention that the objective of these experiments is to obtain very high cooling rates. These cooling rates are not obtained with solid samples where normal dilatation procedures are applied. According to ASTM standard A 1033-04 [38], undershoot of 20°C are

allowed and the thermal profile should be stable within 2 seconds. Secondly normal heat treatment is also not possible to obtain such high cooling rates, so valve opening was optimized (these values are shown in table 4.7) to reach the IT-temperatures with maximum possible cooling rates.
Thirdly to avoid the plasticity effects it was necessary to use only the fresh samples with minimum application of holding force necessary to hold them firmly between the push rod. Under such circumstances the thermal profile of alloy A and in one thermal profile at 700°C (figure 4.18c) for alloy B are showing some undershoots and overshoots.
Although these thermal profiles are nicely fulfilling the criterion of undershoot and stability within two seconds but these undershoot and overshoots are particularly critical for assessment of nucleation behavior in ultra-low carbon steels (alloy A). For the hollow samples of low carbon steel (alloys B, C and D) the IT annealing temperatures were obtained with reasonable accuracy. The only exception was the IT annealing temperature of 700°C where an overshoot of approximately 30°C was observed. The values of undershoots and overshoots found in the experiments of hollow samples of alloy A are shown in table 4.9.

Table 4.9: Values of undershoots and overshoots observed in the thermal profile of alloy A

Alloy	Isothermal Annealing Temperature [°C]	Undershoot [°C]	Overshoot [°C]
A	890	3	2
	880	3	1.2
	870	2.9	2.9
	860	2.3	6.4
	850	5.1	11
	780	0	25

Apparently it seems necessary to find a procedure to eliminate the effects of undershoots and overshoots on the dilatation profiles and also to find the transformation start temperature to assess the nucleation characteristics. In this regard a pragmatic approach was adopted to correct the disturbed dilatation profiles due to undershoots and over shoots. For finding the transformation start temperature, the procedure described by Kozeschnik and Gamsjäger [1] was principally used. In this regard experimentally measured dilatation was compared with theoretically calculated temperature versus change in length profiles (These profiles are simulated for alloys A, B, C and D using the software MatCalc and are shown in chapter 5 (section 5.3)).

4.6.1.1 Procedure for correction of dilatation profiles

Step 1: The appropriate first step was to plot the experimentally measured dilatation profile. Figure 4.21a is showing the figure where the dilatation obtained is plotted as a function of time for the hollow sample of material A which was quenched from 950°C to the IT annealing temperature of 850°C.
Step 2: In the second step, the following analysis was made

i. For convenience this plot was transformed in order to start the dilatation as well as time from zero.
ii. The point of deviation from the linear portion of dilatation profile was measured by drawing a line. This line was tangent to that part of the dilatation profile where austenite is showing contraction in response to quenching. In figure 4.21b this point appears to be -12.6µm. This point was used to compare with theoretically calculated temperature versus dilatation profile simulated for alloy A (please see chapter 5 (figure 5.20a) for this graph). This comparison suggests that the austenite

to ferrite transformation was started at 896°C. It is evident that the transformation has started before reaching the target IT annealing temperature. Here undershoots can be easily corrected by shifting the lowest contraction point / s. The lowest contraction point was measured to be -16.6µm.

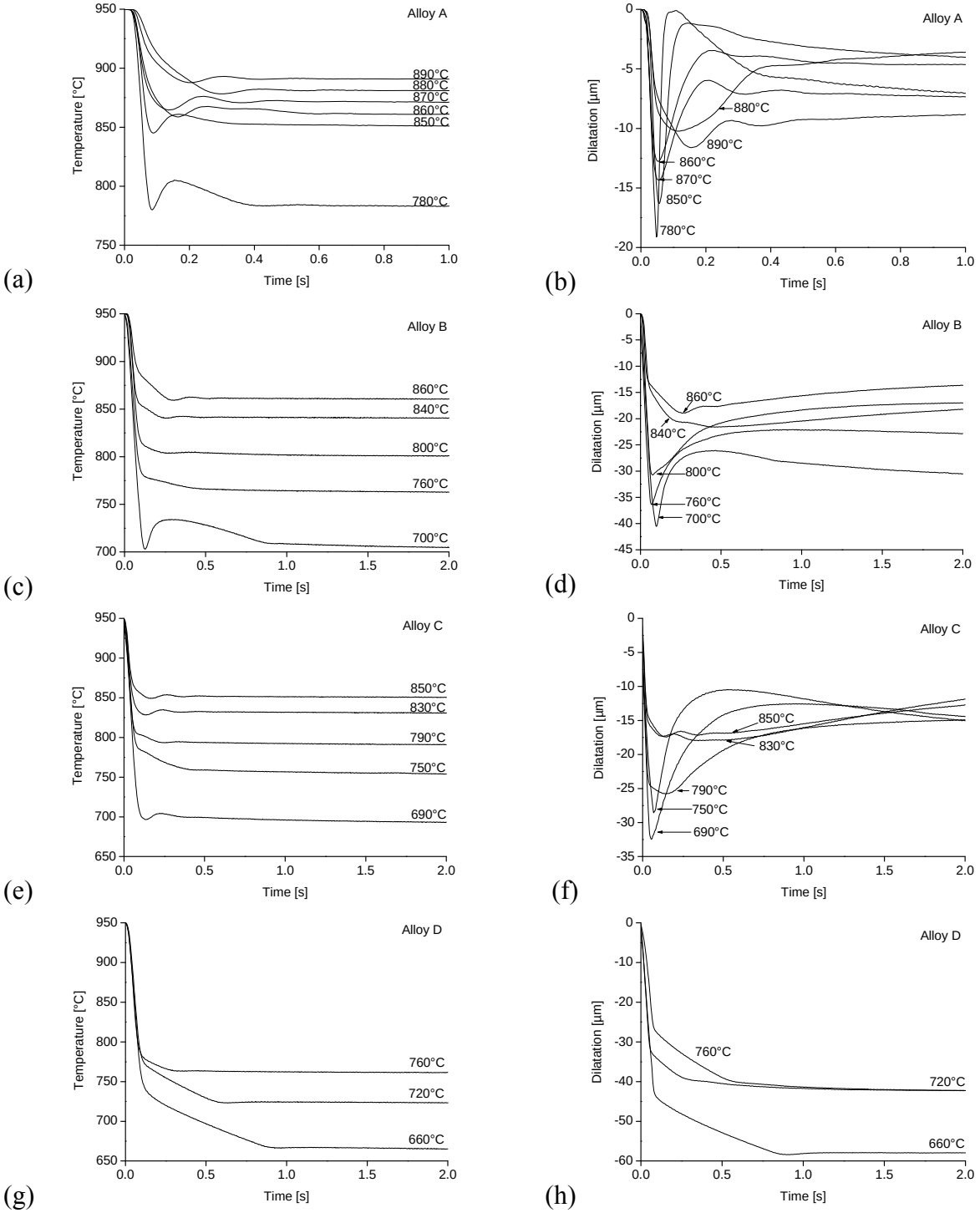

Figure 4.18: Experimentally measured thermal and dilatation profiles of alloys A, B, C and D obtained as a result of thermal treatment (figure 4.16) of the hollow samples.

iii. Sometimes the contraction portion of the austenite is showing more than one slope. In such circumstances hit and trial method has to be used in order to find the

appropriate value which gives a suitable value of measured austenite-ferrite boundary. The suitability of that value is decided on the basis of, for example, the equilibrium start temperature or the T_0 temperature. This particular case is applied for the dilatation profile of 880°C.

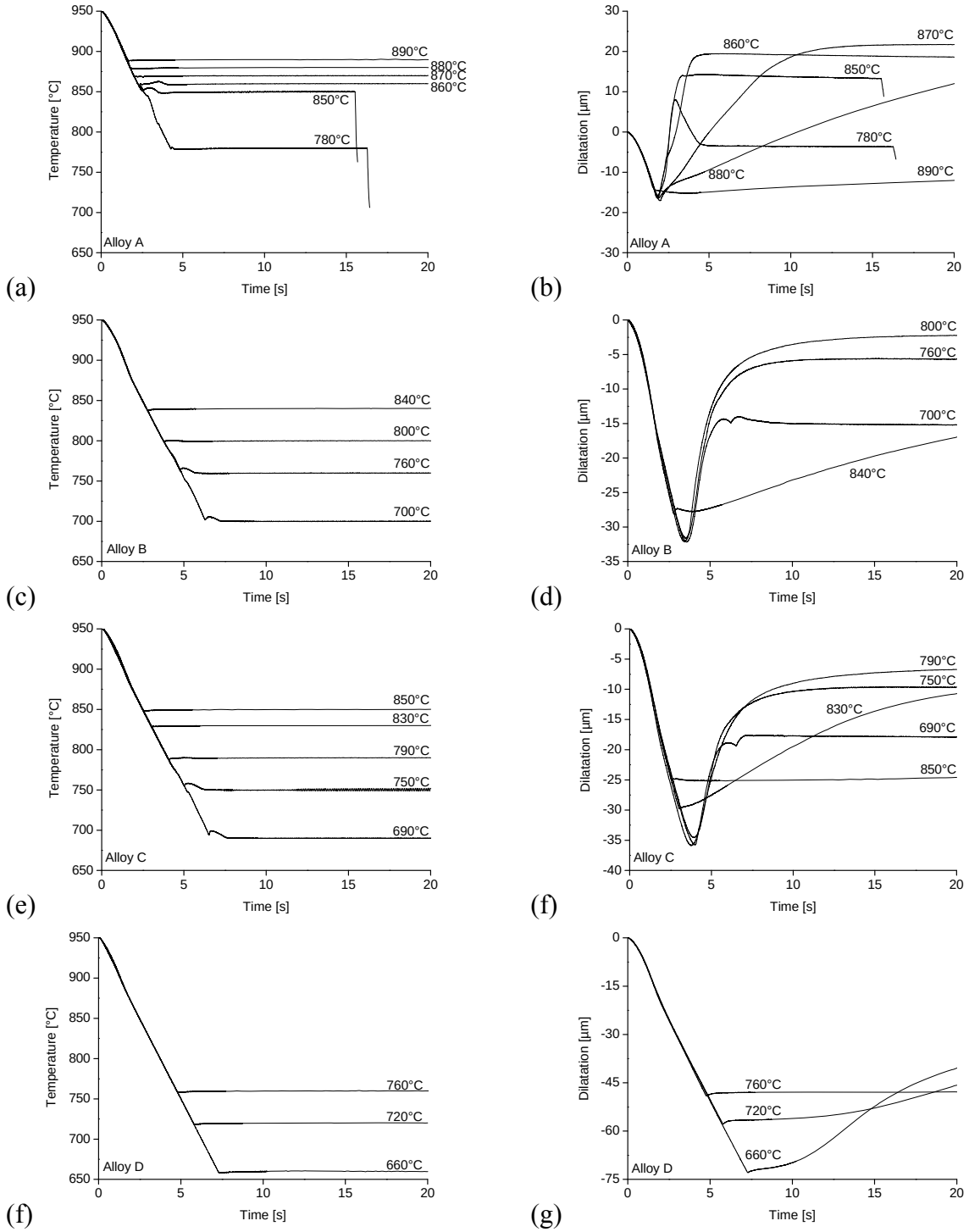

Figure 4.19: Experimentally measured thermal and dilatation profiles of alloys A, B, C and D obtained as a result of thermal treatment (figure 4.17) of the solid samples with T_{aus} of 950°C.

Step 3: Now the data points around the lowest contraction point (-16.6µm in case of IT annealing temperature of 850°C for hollow sample of material A) are removed. Figure 4.21c

is showing how these data points are removed for the case of 850°C for hollow samples of alloy A.

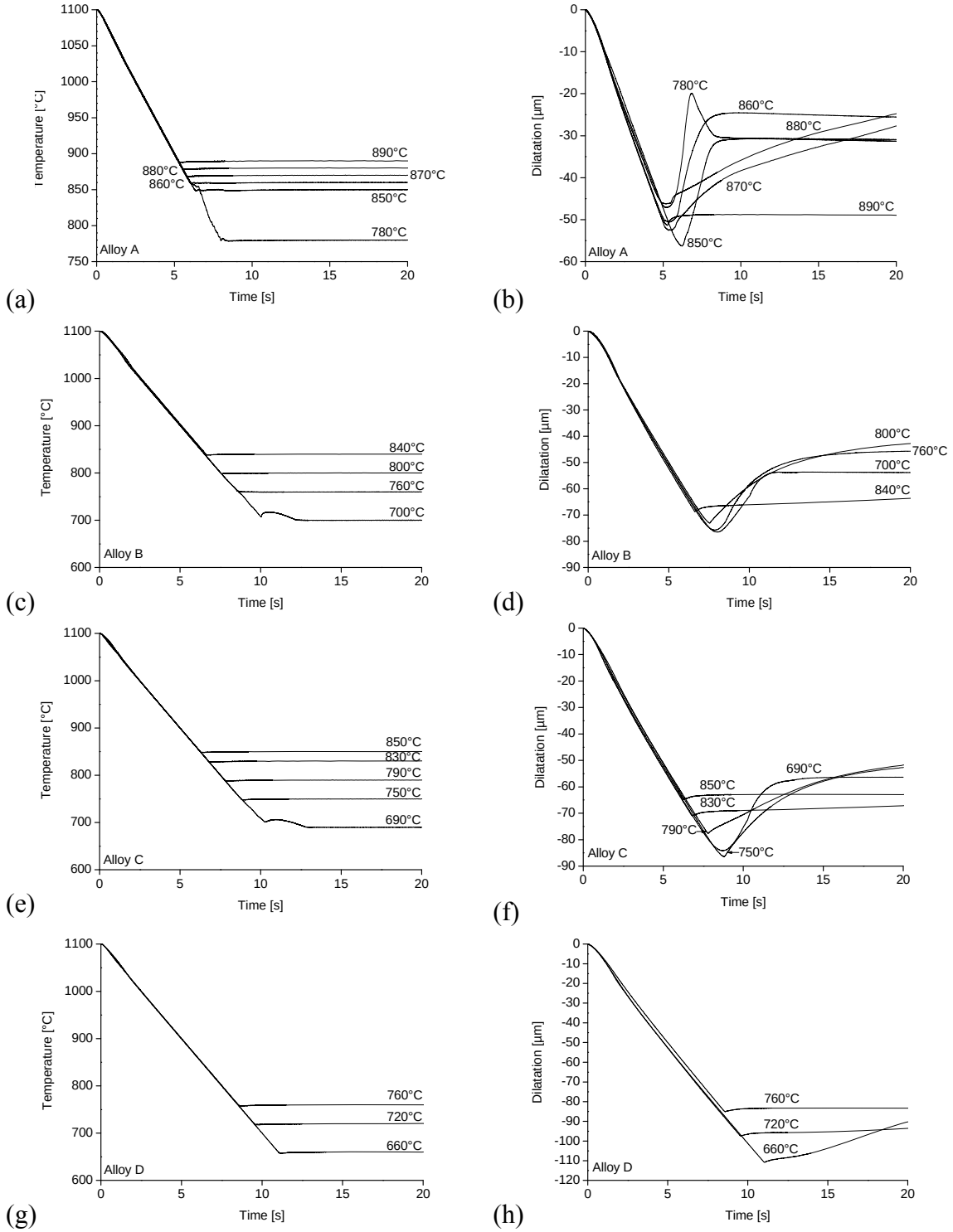

Figure 4.20: Experimentally measured thermal and dilatation profiles of alloys A, B, C and D obtained as a result of thermal treatment (figure 4.17) of the solid samples with T_{aus} of 1100°C.

Step 4: The lowest point of contraction in the dilatation profile is adjusted by comparing the value of undershoot with the theoretical calculated plot of temperature versus change in length. In case of hollow samples of alloy A, for IT annealing temperature of 850°C, the

undershoot value was measured to be 5.1 which corresponds to the dilatation values of 1.2µm. -16.6µm is adjusted by adding 1.2µm into this value. Similar treatment is also applied to the locus of points adjacent to this point to smoothen the overall curve. This adjustment is shown in figure 4.21d.

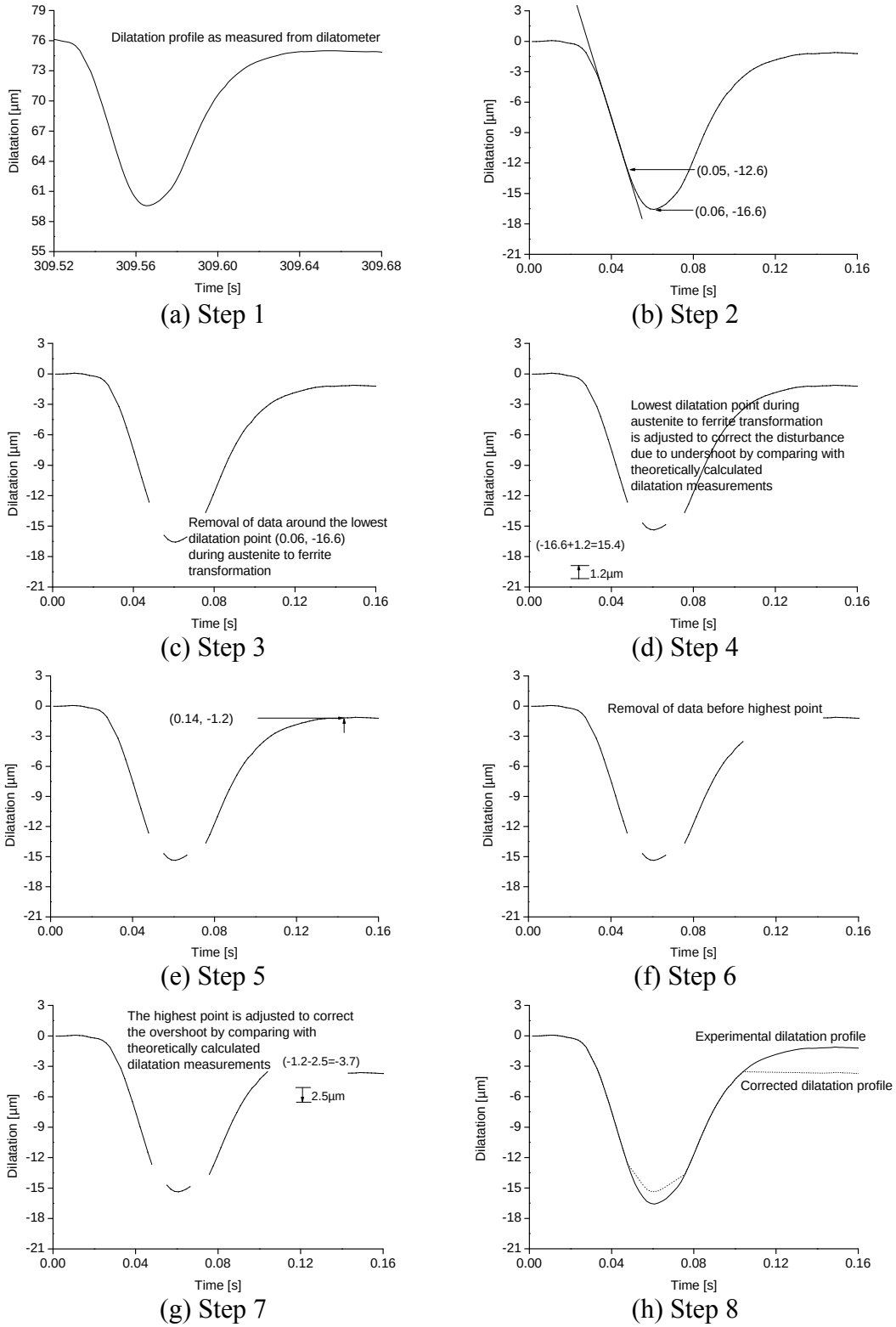

Figure 4.21: Different steps required for correction of experimentally measured dilatation profiles of the hollow samples of alloys A, B, C and D.

Step 5: Similarly the highest point during the austenite to ferrite transformation part was located. This value for hollow sample of material A was found to be -1.2µm (figure 4.21e).
Step 6: Remove the data points before above measured point in step 5 (figure 4.21f).
Step 7: All the data after the point -1.2µm were shifted by the same method which was applied in step 4 to adjust undershoot. The overshoot in case of an IT annealing temperature of 850°C for hollow sample of material A was measured to be approximately 11°C which corresponds to a dilatation value of 2.5µm. From the dilatation versus temperature plot 20°C corresponds to 4.6µm and in this regard 11°C corresponds to 2.5µm. This value is subtracted from the value of -1.2. The same procedure is applied for all the data points after -1.2. This gives the curve a downward shift (figure 4.21 g) to adjust the overshoot observed in experimentally measured dilatation profile.
Step 8: The gaps due to removal of data points are adjusted by crafting the data from the as measured dilatation profile (figure 4.21a). The corrected and experimental profiles are compared in Figure 4.21h for a hollow sample of alloy A, which was annealed at an IT temperature of 850°C.
The above mentioned steps were also applied for all IT annealing temperatures ranging from 890 to 780°C. Comparison of experimentally measured and corrected dilatation profiles for these temperatures are shown in figure 4.22. Similar procedure was also adopted to adjust the disturbance in the dilatation profile of the hollow sample of alloy B which was quenched from 950°C to the IT annealing temperature of 700°C. Figure 4.23 is showing the comparison of experimentally measured and corrected dilatation profiles.

4.6.2 Measured thermal and dilatation profiles of solid samples

In figure 4.19, thermal and their corresponding dilatation profiles of solid samples of alloys A, B, C and D with T_{aus} of 950°C are shown. In this regard the following observations are significant

(i) Some disturbance was observed in the thermal profiles of solid samples of alloy A for IT annealing temperatures of 860°C and below, while 870°C and all above IT annealing temperatures are not showing any disturbance. With the addition of alloying elements i.e. solid samples with T_{aus} of 950°C of alloys B and C this disturbance shifts to lower temperatures. In contrast to solid samples of alloys A, B and C, the thermal profiles of alloy D do not show any disturbance due to heat of transformation.

(ii) The dilatation profile of solid samples with T_{aus} of 950° of alloy A is showing that transformation of the austenite to ferrite started almost from the same point. These samples are not showing any degree of undercooling with decreasing IT annealing temperatures from 890 to 780°C. For alloy B, the increase in contraction was obtained only once i.e. from 840 to 800°C and the magnitude of contraction for 800 to 700°C do not change with change in IT annealing temperatures.
With addition of alloying elements i.e. solid samples of alloy C are showing increase in contraction twice. The first increase is obtained when the IT annealing temperature was changed from 850 to 830°C and the second increase was obtained by further lowering the IT annealing temperature to 790°C. The IT annealing temperatures of 750 and 690°C do not contribute further change in length during contraction. The change in length with decreasing IT annealing temperature is particularly pronounced for alloy D where the magnitude of contractions shows increase with decreasing the IT annealing temperature from 760 to 660°C.

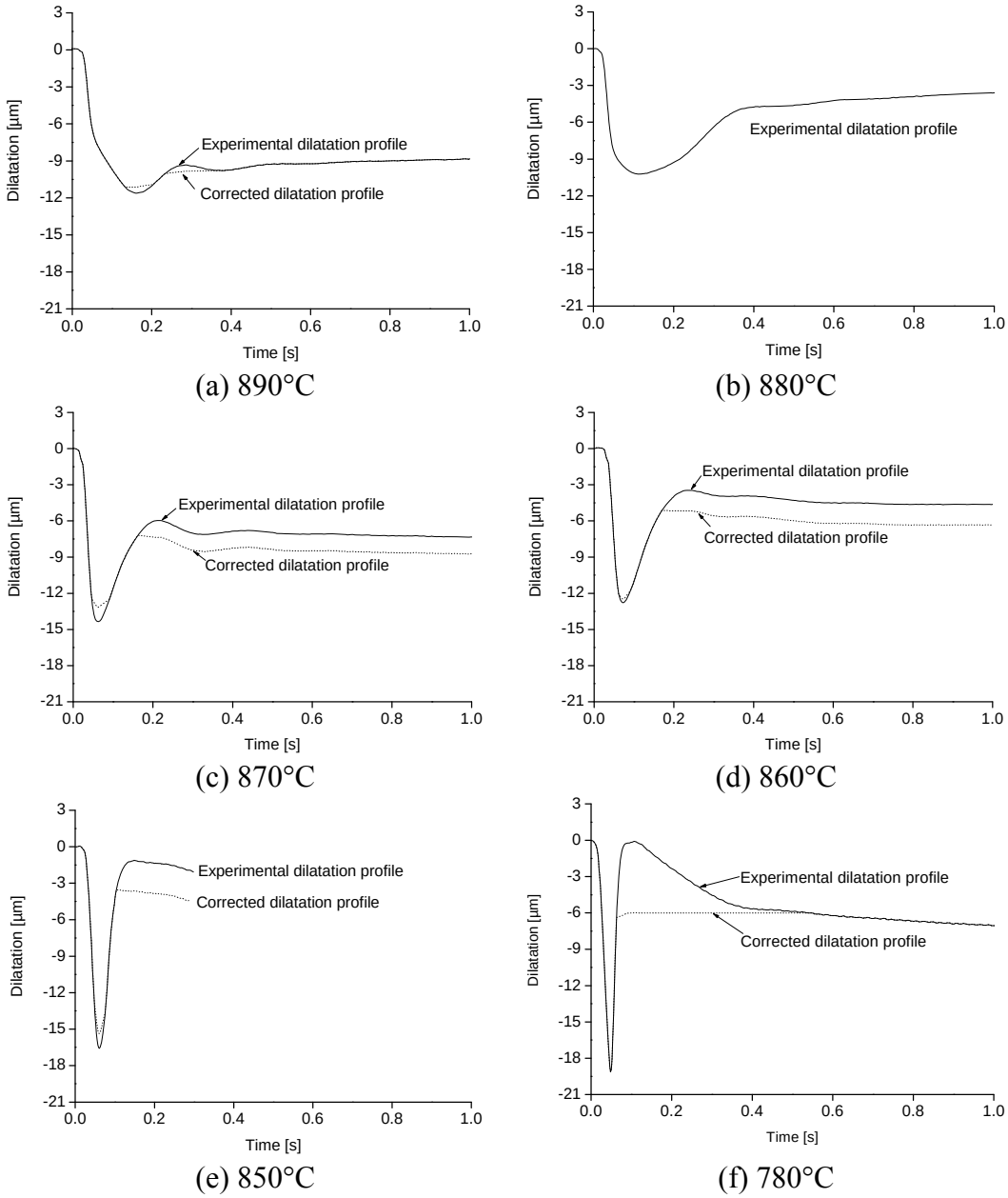

Figure 4.22: Comparison of experimentally measured and corrected dilatation profiles for the hollow sample of the alloy A.

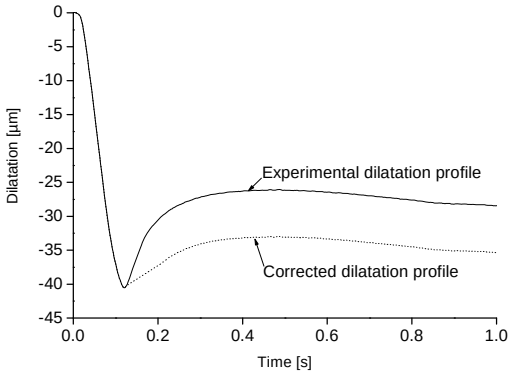

Figure 4.23: Comparison of experimentally measured and corrected dilatation profile for the hollow sample of the alloy B obtained at an IT of 700°C.

(iii) The comparison of the heat treatment of hollow and solid samples of alloy B for an IT annealing temperature of 860°C showed an interesting observation. The hollow sample has showed onset of the austenite to ferrite transformation after immediately reaching the IT temperature whereas the solid sample has not showed any signs of transformation even after approximately one hour.

The thermal and their corresponding dilatation profiles for the solid samples of alloys A, B, C and D with T_{aus} of 1100°C are shown in figure 4.20. The following observations are worth noting if we compare these profiles with profiles of solid samples with T_{aus} of 950°C.

(i) For alloy A, the release of the heat of transformation was delayed when the sample was cooled to a target IT temperature of 780°C. With T_{aus} of 950°C this heat was released at 860°C. When austenitization temperature was 950°C all the samples were showing almost the same amount of contraction whereas in case of 1100°C this was variable in magnitude for different target IT temperatures.

(ii) For alloys B and C, the release of heat of transformation was also delayed as a result of higher austenitization. In case of austenitization at 950°C this release was observed for alloy B and C at 760 and 750°C respectively. With higher austenitization this release is shifted to lower temperatures i.e. 700°C for alloy B and 690°C for alloy C.

(iii) As far as contraction of austenite is concerned in the dilatation profiles, the last three target IT temperatures for alloy B (i.e. 800, 760 and 700°C) and alloy C (790, 750 and 690°C) were showing the same amount of contraction. Now as a result of austenitization at higher temperature (i.e. 1100°C) apparently same amount of contraction is restricted to the last two IT temperatures for both alloys B and C.

(iv) For alloy D neither the release of heat of transformation nor the same amount of contraction was observed with variation of target temperatures and austenitization temperatures for solid samples.

4.7 Microstructure and grain analysis of the heat treated samples

The procedure used to obtain the microstructure of the heat treated samples of alloys A, B, C and D was similar to that described in the section 4.3 for as received samples of alloys A, B, C and D . The only difference was the procedural setup used to obtain the microstructures of the hollow samples. The details of this program are displayed in table 4.10. Similarly Axio Vision (Release 4.7) [36] and ImageJ [39] were used for digital grain analysis.

Table 4.10: Details of the Program used for grinding and polishing of hollow cylindrical samples of alloys A, B, C and D

Steps	Grinding / Polishing Cloth	Lubricant	Flow rate	Suspension	Flow rate	Force [N/N]	Speed [RPM]	Direction	Process Time [min]
1	MD-Piano 220	Water	AN	-	-	20/120	300	>>	1
2	MD-Largo	DP-Blue	5/10	DP-P 9µm	5/10	20/120	150	>>	4
3	MD-DUR	DP-Blue	5/10	DP-P 6µm	5/10	20/120	150	>>	4
4	DP-Mol	DP-Red	5/10	DP-P 3µm	5/10	20/120	150	>>	4
5	OP-Chem	-	-	OP-S	5/8	10/30	150	>>	3

CHAPTER 5: SIMULATIONS

This chapter will describe the procedural steps involved in the calculations for construction of phase diagrams, isothermal time temperature precipitation (I-TTP) diagrams and theoretical dilatation profiles as a function of time. Phase diagrams of alloys A, B, C and D are simulated in both orthoequilibrium (OE) and paraequilibrium (PE) conditions with the MatCalc software package ([11], [12]). I-TTP diagrams of alloys A, B, C and D are simulated with both MatCalc and DICTRA [13] software packages. In order to quantitatively assess the temperature at which the nucleation of ferrite started, it is necessary to compare the measured and calculated dilatation profiles. In the previous chapter we have seen how experimental dilatation profiles of Fe-C-Mn-Si model alloy were obtained with the help of a dilatometer and in this chapter procedural steps will be described to simulate the theoretical dilatation profiles with the help of the MatCalc software package.

5.1 Calculation of phase diagrams of alloys A, B, C and D

Ortho and paraequilibrium phase diagrams were calculated first with the MatCalc software package to assess the nucleation conditions of ferrite in austenite. In this regard, steps involved in the calculations of the phase diagrams for alloys A, B, C and D are described below with:

Step 1: Setting up the system
Step 2: Equilibrium calculation
Step 3: Calculation of solubility temperature (Tsol) of target phases
Step 4: Tracing of phase boundary

5.1.1 Setting up the system

Create a new work space file. In order to define the thermodynamic conditions select elements and the phases from the “mc_sample_fe.tdb” (version = 1.14) thermodynamic database.
In the context of the interesting regions, the phases involved are austenite (FCC_A1), ferrite (BCC_A1) and cementite (CEMENTITE). The elements involved are Fe, C, Mn and Si. The screen shots of the selection of alloying elements and phases are shown in figure 5.1.
The chemical composition is selected as per table 4.1. The screen shot of chemical composition used for the calculations of phase diagram of alloy B for example is shown in figure 5.2.
The constraint tab from the MatCalc phase status dialog, in the global menu bar, is used to select the ortho and paraequilibrium conditions. Figure 5.3 is showing this selection in case of sketching the phase diagram in orthoequilibrium condition for the ferrite phase. The screen shot with austenite and cementite selection from phase details will show the same element status. In the similar way figure 5.4 is showing this selection for paraequilibrium conditions.

5.1.2 Equilibrium calculation

The phase diagram is made up of a number of phase boundaries. The equilibrium calculation is the first step for tracing boundaries of a particular phase. Following steps will be involved in performing this calculation for alloy B for example.

Step 1: From the calculation menu bar use the equilibrium option.

Step 2: When the equilibrium option is selected, a box will appear. For tracing of the ferrite (BCC_A2) boundary, calculate equilibrium at 900°C. The last two lines of the output window will indicate

T: 900 C (1173.16 K), GibbsEnergy: -54887.134 J
- OK -

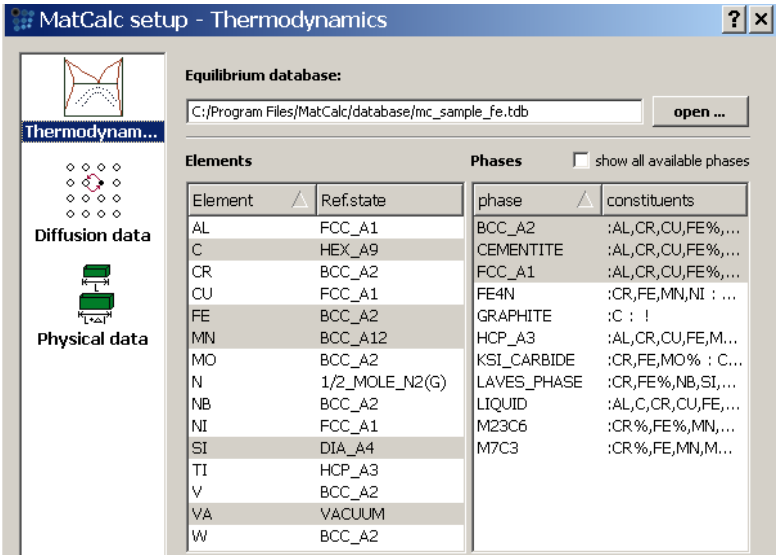

Figure 5.1: Screen shot of MatCalc showing the selections of elements from thermodynamic database mc_sample_fe.tdb.

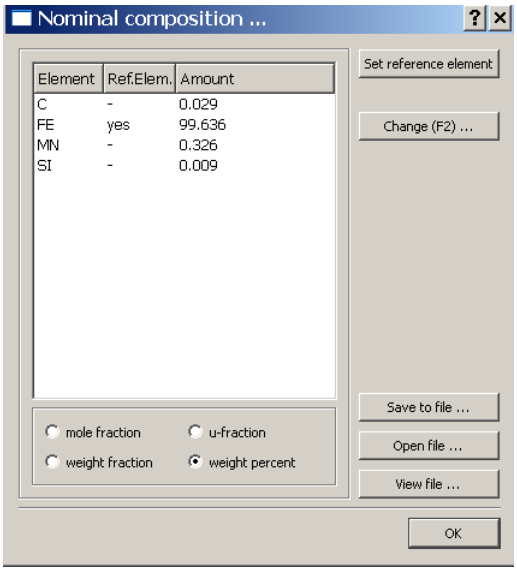

Figure 5.2: Screen shot of the selection of chemical composition for alloy B.

5.1.3 Calculation of the solubility temperature (Tsol) of target phases

The second step, for finding a point on the phase boundary (and overall third step), is to search the BCC_A2 boundary for example. The steps involved in this regard are
Step 1: From the calculation menu bar use the search phase boundary option.
Step 2: When the search phase boundary option is selected a box will appear. In this box from the type option select temperature, from the target option select BCC_A2 and parent phase FCC_A1 will automatically be selected. With these selections, when the "go" button is pressed, the following message indicates

Tsol 'BCC_A2': 884.04 C (1157.20 K) iter: 2, time used: 0.08 s

Now the system has found the point on the boundary and appearance of T_{sol} in the last line of the output window has also confirmed this finding.

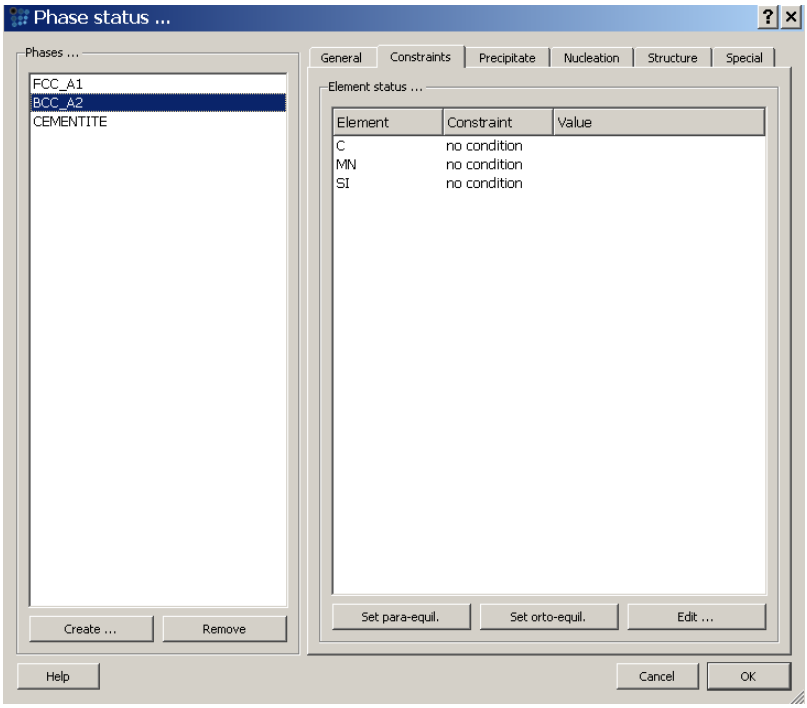

Figure 5.3: Condition used from constraint tab in the phase status of global menu bar to draw the phase diagram of Fe-C-Mn-Si alloy under orthoequilibrium conditions.

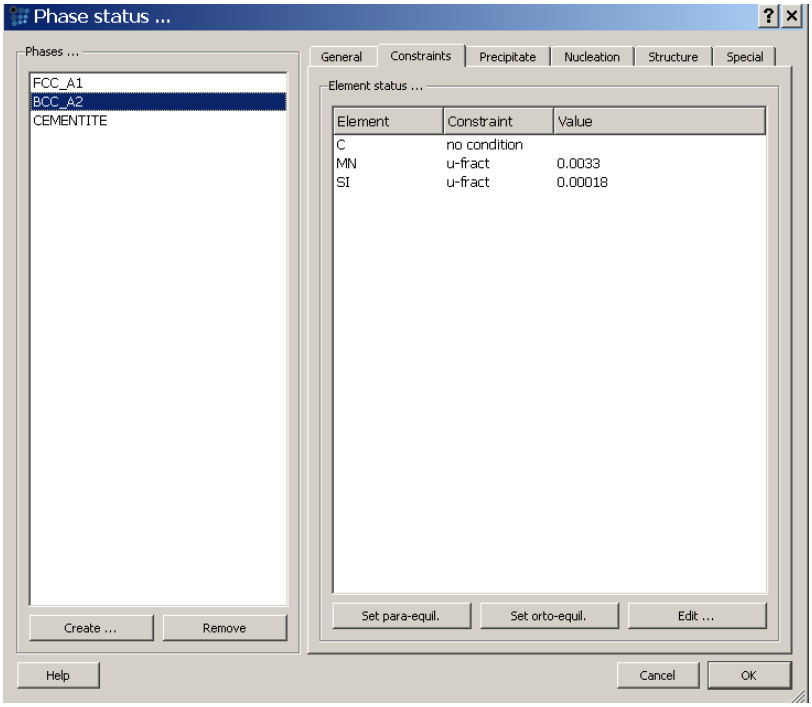

Figure 5.4: Condition used from constraint tab in the phase status of global menu bar to draw the phase diagram of Fe-C-Mn-Si alloy under paraequilibrium conditions.

5.1.4 Tracing the phase boundary with the help of stepped calculations

The major step is now tracing the boundary with the help of a stepped calculation. The following steps are involved in this calculation

Step 1: From the calculation menu bar use the stepped calculation option.
Step 2: When the stepped calculation option is selected a box will appear. From this box select the following options for performing the stepped calculation for tracing the BCC_A2 boundary
Type option: Phase boundary, Range options: Start option = $5e^{-4}$, Stop option = 1, Step interval = $1e^{-3}$, Boundary Condition options: Element = C, Target phase = BCC_A2, Max T_step (i.e. maximum temperature step) = 20.
With temperature in Celsius and composition in wt% options, press the "go" button to perform the calculations. The last four lines in the output window will appear as below (this message can be changed with different versions of MatCalc in terms of time so OK message is the most relevant message)

1002, 0.01 s, 0.000500, T=896.42 C (1169.58 K), its 4, FCC_A1 - OK -
Steps: 1003, CalcTime: 8.48 s
AktStepVal: 0.000500
- OK –

If we will follow the similar steps for tracing the boundaries of other phases then complete phase diagram can be generated. Figure 5.5 is showing calculated phase diagram for alloys A, B, C and D. In these phase diagrams, additionally, the T_0-line was also drawn for the particular alloy system.

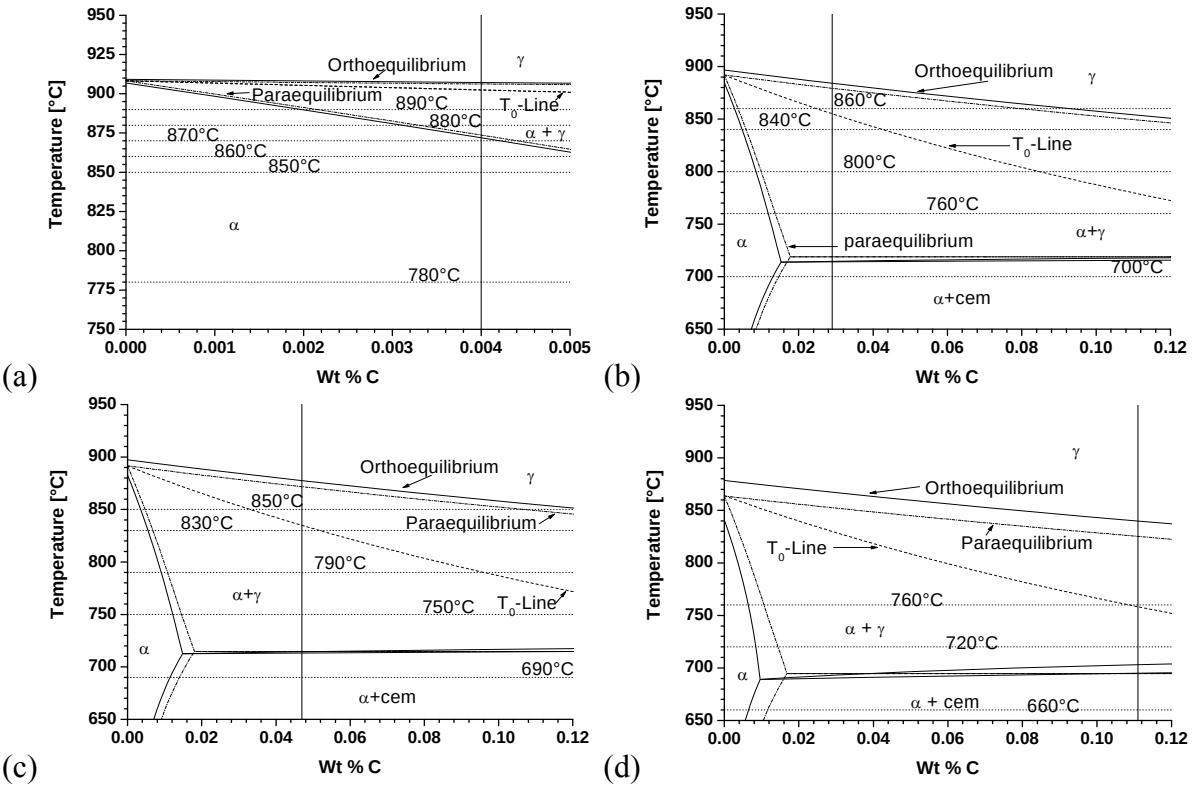

Figure 5.5: Calculated equilibrium phase diagrams in ortho and paraequilibrium conditions of (a) alloy A, (b) alloy B, (c) alloy C and (d) alloy D.

5.2 Calculations for construction of I-TTP diagrams

In order to construct the theoretical isothermal time temperature precipitation (I-TTP) diagrams of the Fe-C-Mn-Si model alloys, calculations are performed with DICTRA and MatCalc software packages. Following sections will describe how these simulations are performed with these software packages.

5.2.1 Calculation of I-TTP diagrams with DICTRA

In DICTRA, for calculations of I-TTP diagram, first, the position of the interface as a function of time is obtained at a particular IT temperature. From this profile, times for 10, 50 and 90% completion of the austenite to ferrite transformation are calculated. In the similar way these times are obtained for other target IT temperatures. When all of these times against their particular target IT temperature are arranged and joined in a temperature versus time plot, the I-TTP plot is obtained. This plot consists of three curves representing 10, 50 and 90% transformation of the new phase at the particular target IT temperature.
In order to get the position of interface versus time plot, the following inputs are generally required for performing calculations with the DICTRA

(i) Thermodynamic database
(ii) Mobilitiy database
(iii) Austenitization temperature
(iv) Cooling rates
(v) Isothermal temperatures
(vi) Grain size
(vii) Precipitate geometry
(viii) Driving force
(ix) Chemical composition

(i) Thermodynamic database: In the present study for calculation of the position of the interface at a particular IT temperature, thermodynamic information is obtained from the TDB-TCFE6 (TCS steel / Fe-Alloys Database V6) thermodynamic database. This database is available with the DICTRA software package.
(ii) Mobility database: DICTRA requires some diffusion database for kinetic assessments. In the present study, the mob2 (TCD Alloys Mobility Database V2) mobility database is used for kinetic calculations. This database is also available with the DICTRA software package.
(iii) Austenitization temperatures: The first step in order to define the thermal cycle is the selection of the austenitization temperature. In the present study, 950 and 1100°C were used as austenitization temperatures.
(iv) Cooling rates: In DICTRA, the onset of austenite decomposition will start as the cooling curve hits the equilibrium austenite-ferrite boundary of the particular alloy system. In the present study cooling rates were adjusted according to the experimental thermal cycles. The details of these cooling rates for alloys A, B, C and D can be found in figure 4.16 and figure 4.17 for hollow and solid samples respectively.
(v) Isothermal temperatures: The isothermal temperatures were selected according to thermal cycles planned for experimental program of the heat treatment of alloys A, B, C and D (figure 4.16 and figure 4.17).
(vi) Grain size: Although we are calling it theoretical diagrams, still the grain size inputs were mainly taken from the measured grain sizes of the heat treated samples of alloys A, B, C and D (table 6.1, table 6.5, table 6.9 and table 6.13 respectively). Due to difficulty of austenite grain size measurement at austenitization temperatures (T_{aus}) (i.e. 950°C / 1100°C), an

assumption was made in which the austenite grain size was considered equal to the ferrite grain size obtained after transformation at a particular target IT temperature.

(vii) Precipitate geometry: Kozeschnik and Gamsjäger [1] have shown that spherical geometry has described the details of diffusion control transformation behavior very well for ultra-low and low carbon steel. In his regard we also took the spherical geometry for our study.

(viii) Driving forces: After crossing the equilibrium austenite-ferrite boundary for a particular alloy system the driving force becomes positive and the onset of the austenite to ferrite begins to start. Normally a default value of $1e^{-5}$ is given which represents a small degree of driving force in terms of undercooling. In the present work most of the times the value of $1e^{-4}$ was used. Slight alterations were given in this parameter where the DICTRA calculations crashed at this value. In such cases $1e^{-4}$ is replaced with $1e^{-3}$. It is also necessary to mention that for most of the cases the calculations crashed at $1e^{-2}$. From calculations it was found that these alterations do not have much influence on the 10 to 90% of transformation times for the present study.

(ix). Chemical composition: The chemical compositions were taken according to table 4.1 for alloys A, B, C and D

Once these input parameters are defined, simulations are required to start with making some adjustments in simulation conditions. These adjustments are shown in appendix-6. After the completion of successful simulation it is required to obtain output in the graphical or tabular format.

As stated above, to draw the I-TTP diagram for particular alloy systems more than one simulation are required. Table 5.1 is showing details in terms of the number of simulations performed to generate the I-TTP plots for alloys A, B, C and D in the present study. It is also necessary to mention that in the single ferrite phase region DICTRA does not give results for the cooling rates used for the present study because of the limitations of the local equilibrium model.

Table 5.1: Number of simulations performed to construct the I-TTP diagrams for alloys A, B, C and D

Alloy	Number of simulations		
	Hollow samples	Solid samples	
	T_{aus}	T_{aus}	
	950°C	950°C	1100°C
A	2	2	2
B	5	4	4
C	5	5	5
D	3	3	3

Now, the procedure will be briefly described for the assessment of the onset of austenite decomposition and how 10, 50 and 90% of transformation times from the position of interface versus time plot are calculated in case of alloy D for example.

Step1: After austenitization at 950°C, the sample is cooled to isothermal annealing temperature (which is 760°C in case of figure 5.6). DICTRA is not considering the nucleation kinetics and instead it is assumed that the moment when the cooling curve hits the A_3 line, onset of austenite decomposition will start.

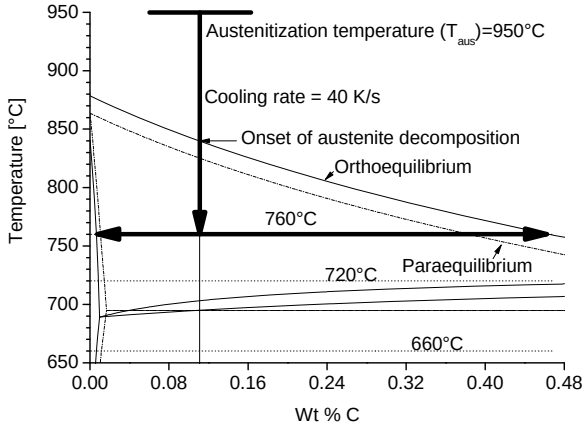

Figure 5.6: Schematic of the target IT temperature in phase diagram of alloy D.

Step 2: At time t = 0, we have only austenite. According to our assumption, the grain size of austenite is equal to the grain size of ferrite. In austenite, ferrite has to nucleate and grow. The grain size of alloy D, which was annealed at an isothermal temperature of 760°C, was found to be 25µm. In order to take into account the grain impingement half grain size 12.5µm is taken for simulation. As we are feeding grain size in meters so we will write $12.5e^{-6}$ for austenite grain size in DICTRA. This situation is shown schematically in figure 5.7.

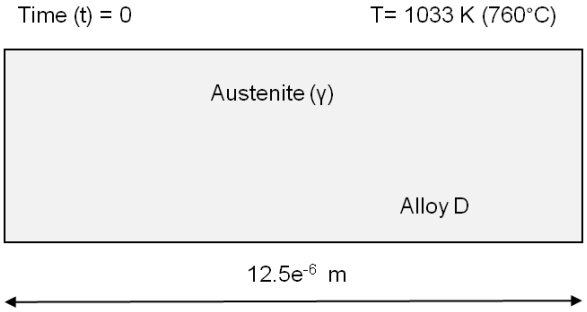

Figure 5.7: Schematic representation of the austenitic grain at time t = 0.

Step 3: At time t > 0, ferrite will begin to grow in a cell of size of $12.5e^{-6}$. This is schematically shown in figure 5.8.

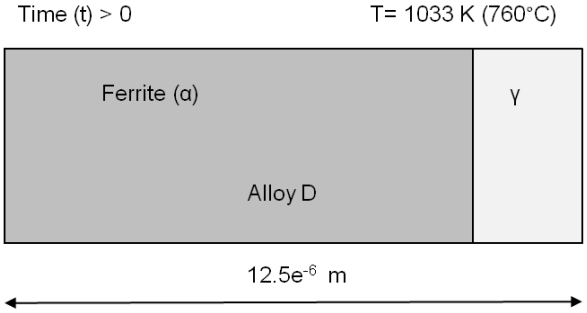

Figure 5.8: Schematic representation of the austenitic to ferrite transformation at time t > 0.

Step 4: After completion of transformation for the given simulation time (i.e. 1000 s), position of interface profile is obtained as a function of time. The schematic of this graph is shown in figure 5.9. In this regard, first of all the initial and final points representing the 0% to 100% transformation is determined. Then, time against 10, 50 and 90% transformation can

be found. The procedure is described below in numeric form for the schematic diagram shown in figure 5.9.

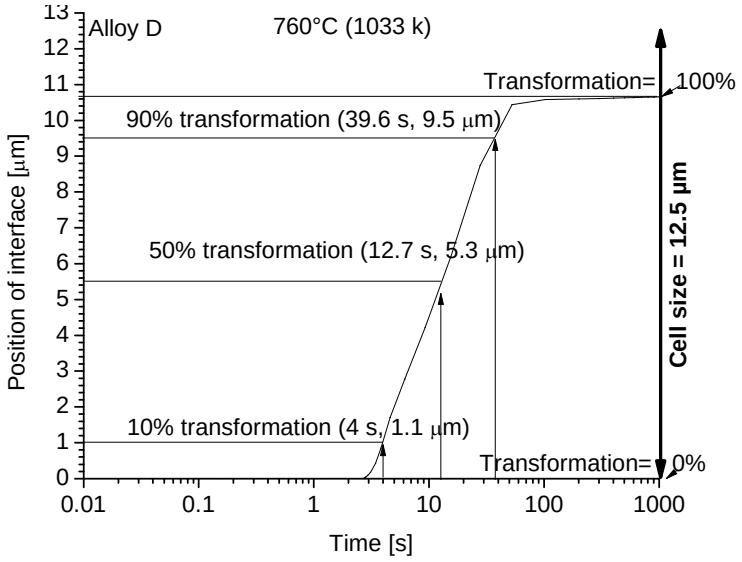

Figure 5.9: Schematic of the position of interface profile as a function of time for the determination of 10, 50, 90% completion of transformation for theoretical determination of I-TTP diagram.

Initial point (0% transformation) = 0 μm, Final point (100% transformation) = 10.6 μm
Difference = 10.6- 0 = 10.6 μm, 10% of difference = 0.1 * 10.6= 1.06 μm,
50% of difference = 0.5 * 10.6= 5.3 μm, 90 % of difference = 0.90 * 10.6= 9.5 μm

Position of interface after 10% transformation = 0+1.06 = 1.06 μm
Position of interface after 50% transformation = 0+5.3 = 5.3 μm
Position of interface after 90% transformation = 0+9.5 = 9.5 μm

Time for 10% transformation (against 1.06 μm) = 4 s
Time for 50% transformation (against 5.3 μm) = 12.7 s
Time for 90% transformation (against 9.5 μm) = 39.6 s

If similar calculations are also performed for target IT temperatures of 720 and 660°C then we will also get three points at each of these temperatures respectively. If these three points for every target IT temperature are joined then we will get the I-TTP plot of alloy D. This diagram is shown in figure 5.10. In a similar way, we can also calculate the I-TTP diagram for alloys A, B and C as well.
Generally a macro file is made and all the alternations like cooling rate, target IT temperature, grain size, alloy composition and driving forces are made in this file and simulations are run to get the position of interface profile as a function of time. The macro file used for the DICTRA simulations for the calculations of positions of interface profiles as function of time for ultra-low to low carbon steel is shown in the appendix-6.
The above said macro file was generated by using DICTRA service version 24(pl4) on Linux, Copyright (1993, 1995) Foundation for Computational Thermodynamics, Stockholm, Sweden. For the output, position of interface profile as a function of time was obtained by using Exceed software package version: 11.0.0.0 (Copyright © 1991-2005 Hummingbird Ltd.).

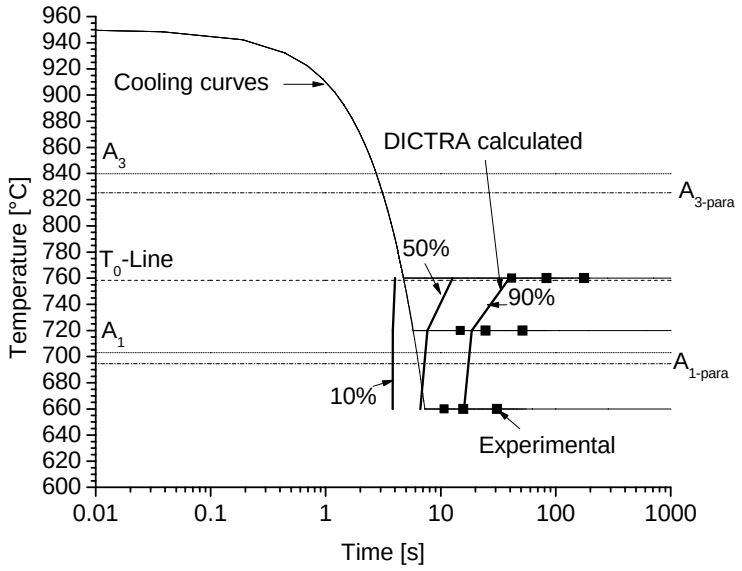

Figure 5.10: DICTRA calculated I-TTP diagram for alloy D.

5.2.2 Calculation of I-TTP diagrams with MatCalc

In MatCalc software, I-TTP plots can be directly obtained from the calculations. The input parameters (obtained from the experimental set up and measurements) for MatCalc calculations are listed as under

(i) Heat treatment input
(ii) Grain size
(iii) Chemical composition

Heat treatment cycles as shown in figure 4.16 and figure 4.17 are also used for the present simulations as well. The details of the grain size obtained after heat treatment are shown in table 6.1, table 6.5, table 6.9 and table 6.13 for alloys A, B, C and D respectively. These grain sizes act as indirect adjustment values that are used as target quantities in correction of the calculated interfacial energy (CIE) of the ferrite phase (i.e. BCC_A2). For example, if it is assumed that the ferrite grain diameter obtained after the heat treatment is 40µm, then that value of the correction factor for the interfacial energy will be taken such as to give a final ferrite grain radius of 20µm.
The chemical composition is used according to table 4.1 for alloys A, B, C and D.
In lines of above described points, the major steps involved in the calculation of I-TTP plots for alloys A, B, C and D with the software MatCalc are summarized as

Step 1: Setting up the system
Step 2: Establishment of precipitation domain
Step 3: Selection of options for defining the phase status
Step 4: Calculation of TTP diagram

5.2.2.1 Setting up the system

In this step, elements and phases are selected from the "mc_sample_fe.tdb" (version = 1.14) thermodynamic database. From elements, select Fe, C, Mn, Si and VA for calculating the I-TTP diagram of Fe-C-Mn-Si model alloy. If paraequilibrium nucleus composition is selected

from the nucleation tab submenus in the phase status selection from the global menu bar, then this will also give the simulations in constraint Fe-C quasi-binary alloy conditions.
As the present study is dealing with the austenite to ferrite transformation, austenite and ferrite are the proper selection from the phase selection options in the thermodynamic database.
For the selection of chemical composition in the composition option from the global menu bar table 4.1 is referred. In case of calculation of the paraequilibrium I-TTP diagram of alloy D for example the sequence of elements and their corresponding chemical composition are

C = 0.111 wt%, Fe = 98.79 wt%, Mn = 0.932 wt%, Si = 0.167 wt% (figure 5.2)

For simulation of I-TTP diagrams, the kinetic information is obtained from the diffusion database "mc_sample_fe.ddb" (version 1.02).

5.2.2.2 Establishment of precipitation domain

At the end of austenitization and before quenching, austenite is present in the sample with a certain grain size. As thermally activated processes are dealt within the present study, the new phase has to emerge after nucleation. To define austenite as matrix phase in the precipitation domain and for the definition of its grain size following steps are performed.

Step 1: From the global submenu click the precipitation domain or simply press Ctrl+F8.
Step 2: When Ctrl+F8 is pressed a box (figure 5.11) appears. From this box austenite is selected as matrix phase in two steps.
In first step, from the precipitation domain field press new tab button. When this tab is pressed, a new box appears. Write austenite in this box and then move to the phase tab. In the phase tab, from the matrix phase option select FCC_A1 (i.e. austenite) as the matrix phase.
In the second step move to the structure phase tab and in the structure phase field insert the desired grain size. 25 μm can be selected just for example. This will establish austenite as matrix phase (having 25 μm) in the precipitation domain.
In the present study, the grain size as obtained from heat treatment at a particular target temperature was used. In order to take into account the grain sizes obtained against their particular IT temperature a new function (e.g. grain(T$C)) was defined. In order to define this function it is necessary that a table with the same name (e.g. grain) should be present in table submenu from the global main menu. Figure 5.12a is showing this table for example where column 1 is showing the target IT temperatures and column 2 is showing the experimental grain sizes at these IT temperatures.
When ferrite is defined as precipitate in the phase status then this precipitate will automatically be attached to the above defined matrix phase.

5.2.2.3 Selection of options for defining the phase status

This is a very important step in sketching of I-TTP diagrams. In this step, ferrite is defined as a new precipitate phase. Nucleus composition and nucleation sites are selected and values are given to precipitate classes and interfacial energy.

Definition of ferrite as precipitate

In order to define ferrite as the precipitate phase, open the phase status submenu from the global menu bar or press F8 key (section 5.1.1 (figure 5.3)). Now press the precipitate tab and from the phases field on the left, first select BCC_A2 (ferrite) and then press the create tab. When this tab is pressed a drop box will appear asking for the options of phase type. From the list of phase types select "precipitate". This procedure will create the precipitate of ferrite phase which will appear as BCC_A2_P0 in the phase field below FCC_A1 and BCC_A2.

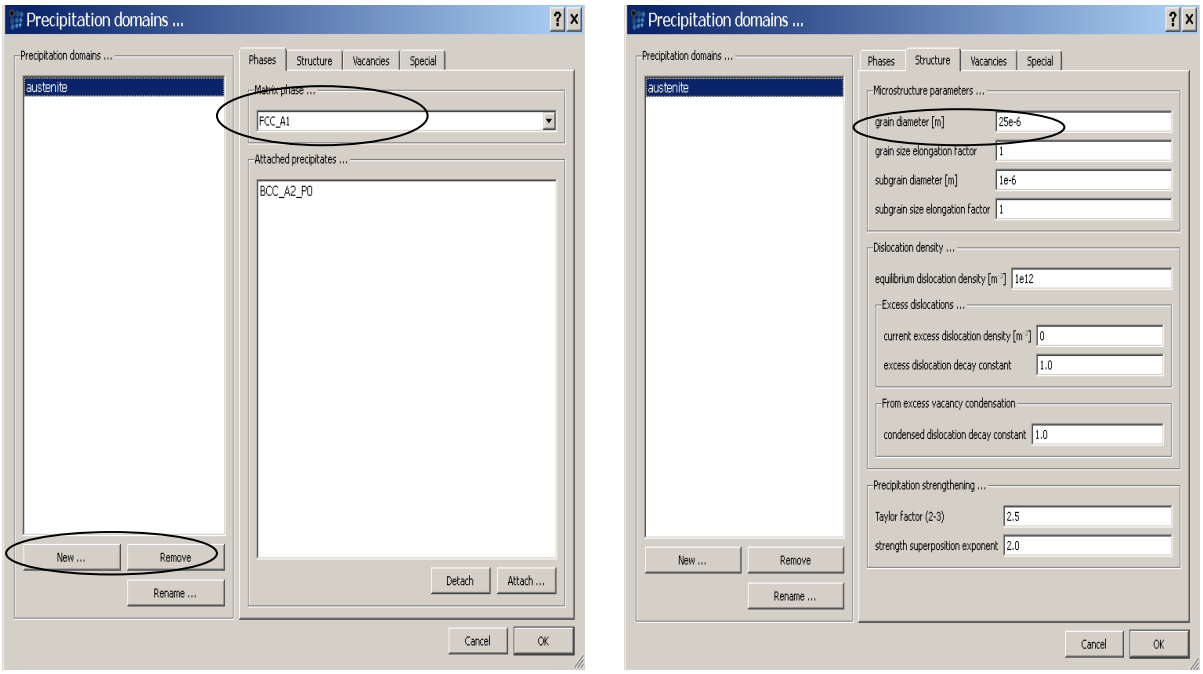

(a) (b)

Figure 5.11: (a) Establishing austenite as matrix phase in the precipitation domain (when ferrite will be defined as precipitate phase then the ferrite precipitate (BCC_A2_P0) will be attached with the matrix austenite. (b) Setting of austenite grain size.

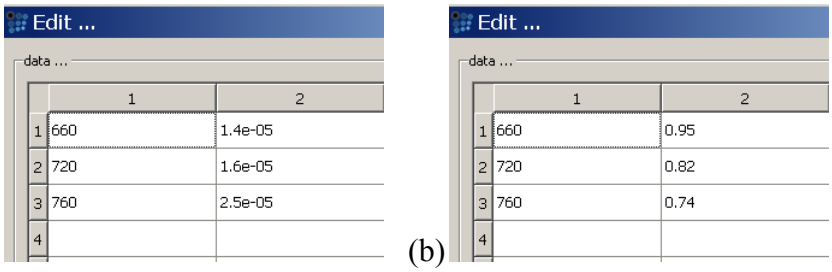

(a) (b)

Figure 5.12: Defining tables for values of grain sizes (a) and correction factors at their corresponding target IT temperatures for calculating I-TTP diagram of alloy D.

Now first select the newly created precipitate and then select precipitate option from the phase status submenu. Insert 25 in the '# size classes:' option and initialize the process and accept the warning message. The precipitates are considered as belonging to a number of classes of particles with the same radius and composition. Classes are created, rearranged and deleted during the calculation, allowing simulation of the precipitate size distribution. Then attach the precipitate with matrix austenite / precipitation domain from the "attached to pd" option in the precipitate set up field in the precipitate sub menu.

Insertion of interfacial energy of ferrite

Now move to precipitate properties field in the precipitate sub menu. In this field we have to insert the correction factor for the calculated interfacial energy (CIE) of the ferrite (BCC_A2) phase. First of all uncheck the auto option and by doing so following message appears in the option of interfacial energy

0.99*CIE$BCC_A2

This line means 99% (i.e. 0.99) of the calculated interfacial energy (CIE) of the ferrite phase is used for calculations. This is a very important input parameter. For the simulation of I-TTP diagram of alloy D in paraequilibrium conditions at an isothermal temperature of 760°C with obtained grain size of 25µm, the value of interfacial energy calculated was 0.74*CIE$BCC_A2. 0.74 is the correction factor in this expression that is adjusted to give the experimental ferrite grain size. Its calculation is depending on the thermal cycle (having austenitization temperature, cooling rate and target IT temperature information), grain size, nucleus composition and nucleation site information. The whole I-TTP diagram can be simulated from the set of these values calculated at their particular target IT temperatures. In the present study values of correction factors are defined in the form of tables (figure 5.12b).
Now move towards selection of options for the nucleation condition of the precipitate of ferrite.

Selection of nucleus composition and nucleation site

In the nucleus tab sub menu, from the nucleus composition option in the general field, select para-equilibrium. The choice of nucleus condition can be selected on the basis of experimental results. For the nucleation site field options again experimental results will be consulted. Previous study [1] have used grain corner as the nucleation sites. In the present study it is also found that the new phase will nucleate on grain boundary and the grain corners are the most probable nucleation sites. In this regard from the nucleation site option select grain corner only. The final selection of all the fields of the nucleation tab is shown in figure 5.14.

5.2.2.4 Calculation of the I-TTP diagram

Once the system has read the thermodynamic database, diffusion database and at the same time selection of chemical composition, precipitation domain, precipitate phase, number of classes, attachment of precipitate with matrix, interfacial energy, nucleus composition and nucleation site have been completed then calculation of I-TTP can be started. For taking the output in graphical form either use create new window from the view menu bar or use the Ctrl+M key. When this option will be used, new window will appear and from this window select the plot-TTP Diagram (plot p6). In this diagram the output of calculations appears as three points in the temperature as a function of time field for a particular IT temperatures representing 10, 50 and 90% austenite to ferrite transformation times (for the present study). When calculations at the other target IT temperature will also be incorporated and the three points at every IT temperature will be joined an I-TTP plot of alloy D is obtained. This plot will consist of three curves. The first curve will show 10%, second curve will show 50% and third curve will show 90% of austenite to ferrite transformation. The incorporation is done with append current buffer from the TTP-Buffer in the global main menu.
At this moment, it is also beneficial to export the experimental data. This will help to optimize the parameters to get the agreement between experimentally measured I-TTT and theoretically calculated I-TTP calculated 10 to 90% transformation times.
For each target IT temperature we are interested in 10, 50 and 90% transformation times. In this regard three additional series are required to store 10, 50 and 90% transformation times respectively for each IT temperatures. In the first ttp-curve type series, 10% of transformation time will be stored, so in the series submenu write 0.10 instead of y-data option in the options window and connect. Similarly 0.50 and 0.90 are written for storage of 50 and 90% transformation times.It has been observed in the comparison of thermal and dilatation profiles that for some target IT temperatures transformation has started before reaching the IT temperatures. In this regard it will be beneficial to also display the thermal profile at each IT temperature and additional series must be added by just allowing the temperature curve to display in plot submenu from the options window.

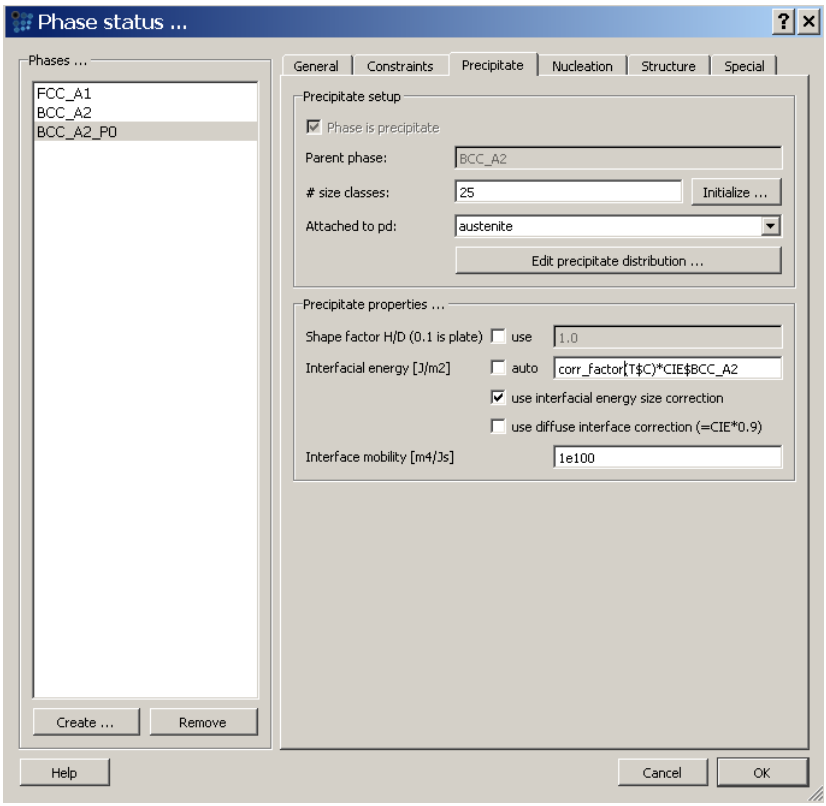

Figure 5.13: Screen shot of the final setting of the phase field, precipitate setup field and the precipitate properties field in the precipitate tab.

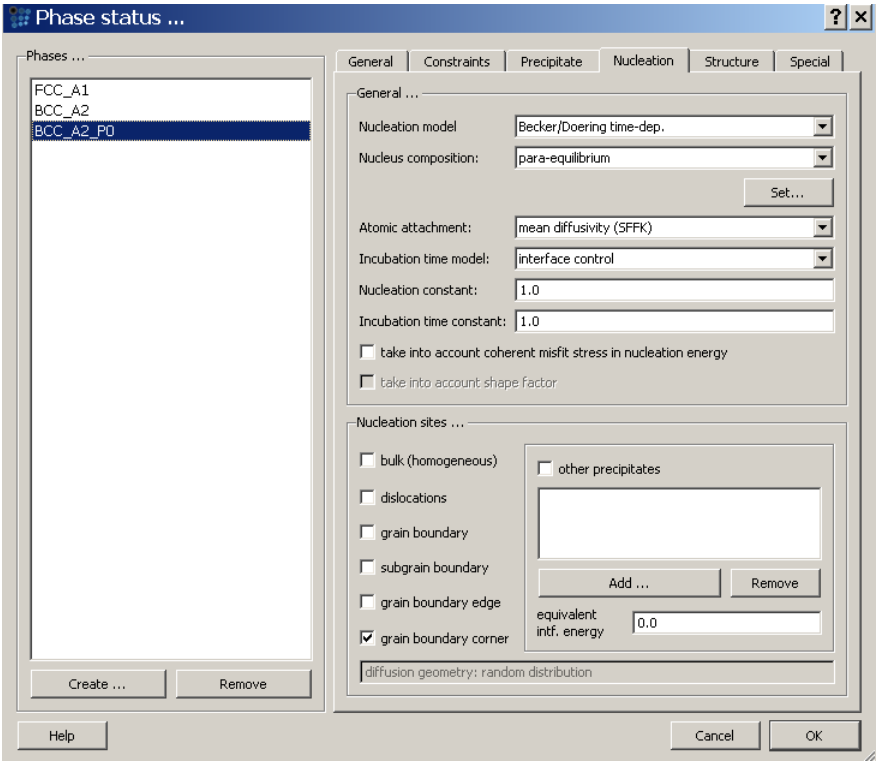

Figure 5.14: Screen shot of the final setting of the phase field, general field and the nucleation sites field in the nucleation tab.

Now to perform the calculations it is required to first define the heat treatment cycle. Selection of different options from the heat treatment submenu will be described as under.

Definition of heat treatment

For the definition of heat treatment cycle, select heat treatment options from the global menu bar or press alt+F8. When this option is used edit heat treatment window will appear. In the available treatment field create new heat treatment with the name "ht_1" (for example). Now in the data field press the new segment button. By doing so, a line is added in the list of data field starting with "0" entry. Now double click this list or press edit button after highlighting the data list. This will activate the edit heat treatment segment window. In this dialog box / window insert 950 (which is the austenitization temperature) in the start temperature option. From the mode options drop box select "End temperature & Heat/Cooling rate" option. In the end temperature option, insert 760 and in the heat/cooling rate option insert 40. After doing this define austenite from the select precipitation domain in the precipitation domain field on the right hand. Keep rest of the option (i.e. # interval = 25 and type = log) as default (figure 5.15) and move toward the next segment by pressing "+" button in the segment field. Now from the mode options drop box select "Heat/Cooling rate & Delta-time" option. In the Heat/Cooling rate option, insert 760 and in the delta-time option insert 1000 (by keeping in view that the experimental finish time for 90% completion is within 0.01 to 1000 s time frame). Keep rest of the options as default and press the "OK" button below the comment field. Now two lists are present in the data field of the edit heat treatment dialog box. This will define the heat treatment cycle (figure 5.16). This heat treatment cycle is actually the exact reflection of the heat treatment cycle defined in the dilatometer for experimental purpose. Once all the selections have been made press "OK" button and move toward calculation.

Calculations

Before starting the calculations, create three new plot of type XY-data (p1 plots).

In the first plot drag and drop T$C, in the second F$BCC_A2_P0 and in the third R_Mean$BCC_A2_P0 from the variables window.

Now move toward calc menu bar. From the calc menu bar select precipitate kinetics option or use Ctrl+k key. This will prompt the precipitation simulation dialog box. In this box, from the temperature control field, select the heat treatment "ht_1" from "from heat treatment" option (figure 5.17). Start the simulation by pressing "Go" button. Now in the figure 5.18 we can see that a radius of 13.7µm is obtained with the correction factor 0.74. Normally to obtain 0.74, we have to perform a series of simulation to optimize this parameter.

In order to register this calculation, in the global menu "append current buffer" option is used from the TTP-Buffer submenu. By doing so a message is prompted telling that existing data is updated and data set contains how many lines.

For calculating 10 to 90% transformation times for target IT temperatures of 720 and 660°C (for alloy D) same procedure was repeated with some minor change i.e. 760 will be replaced with 720 or 660 as end temperature in the edit heat treatment segment. Grain sizes and correction factors for these IT temperatures are incorporated in the form of tables. Two additional IT temperatures i.e. 790 and 600°C were added just to extend the trends beyond and before the experimental range (i.e. from 660 to 760°C).

The plotted diagram is shown in figure 5.19. Similar procedure will be used to calculate the I-TTP diagram of alloys A, B and C.

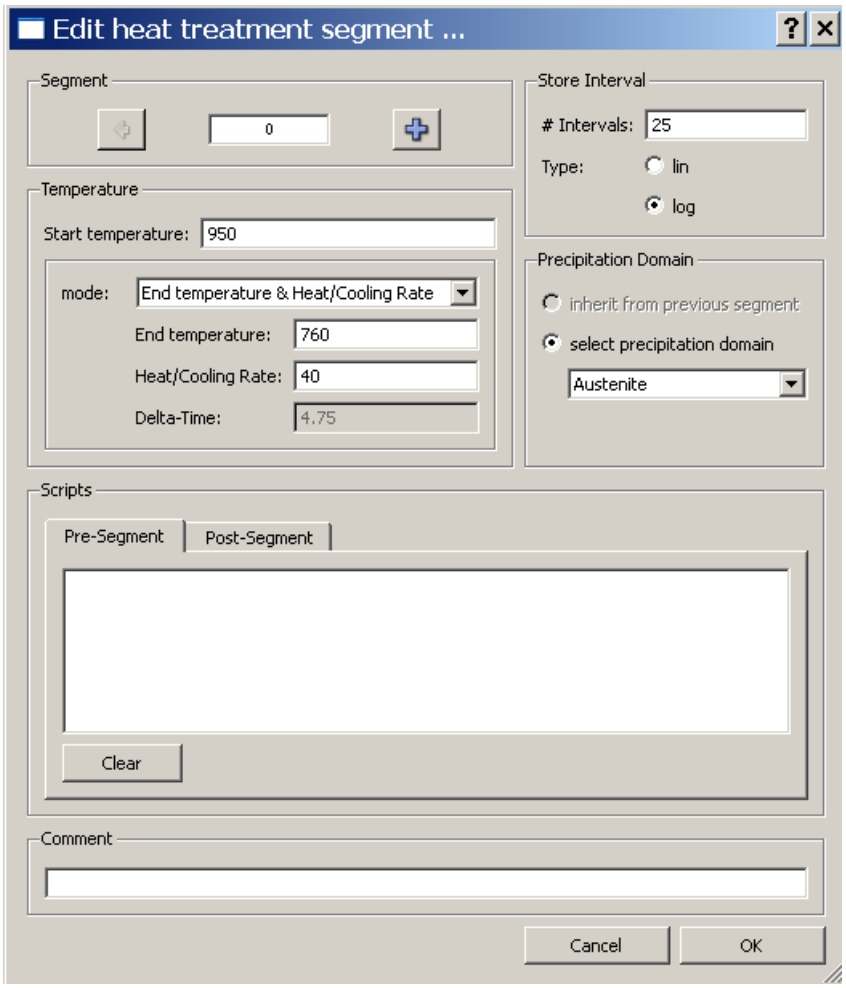

Figure 5.15: Edit heat treatment segment dialog box.

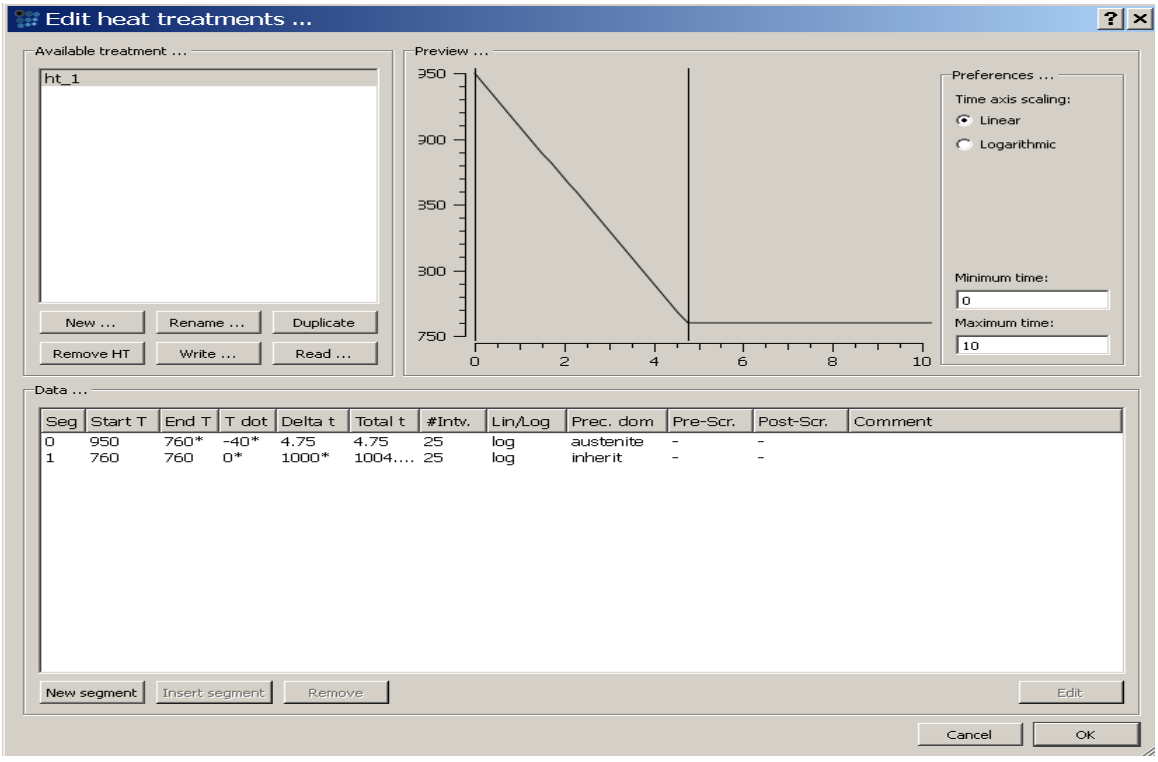

Figure 5.16: Edit heat treatment dialog box.

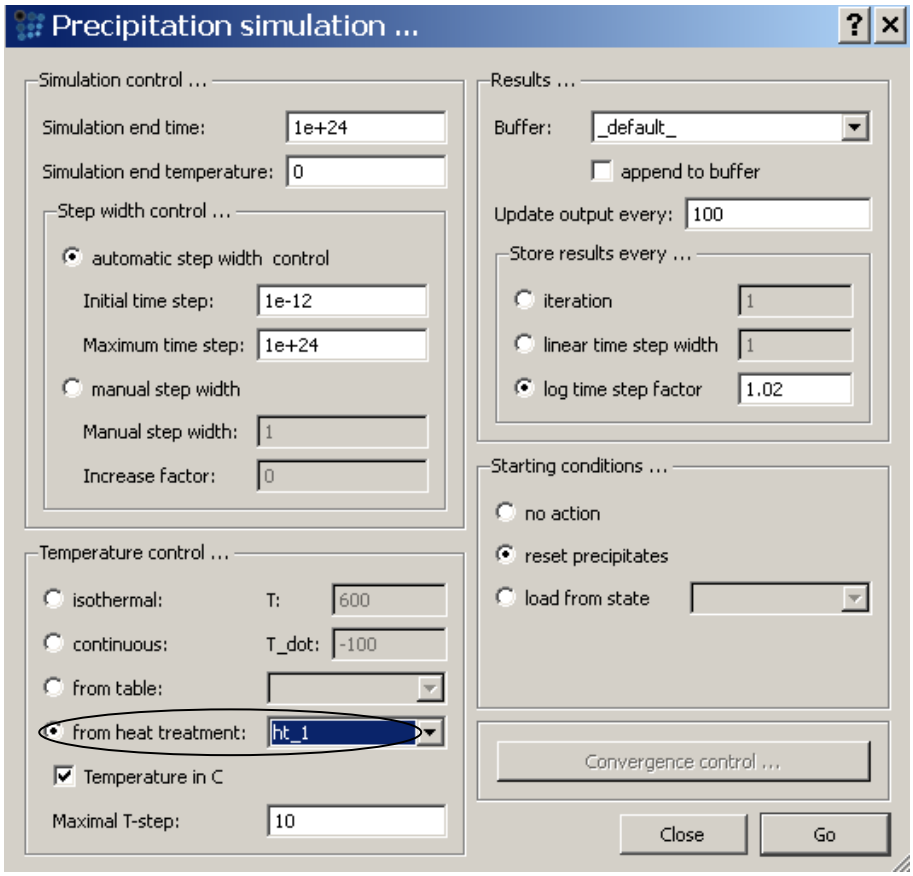

Figure 5.17: Screen shot of the selection of temperature control from the defined heat treatment program "ht_1".

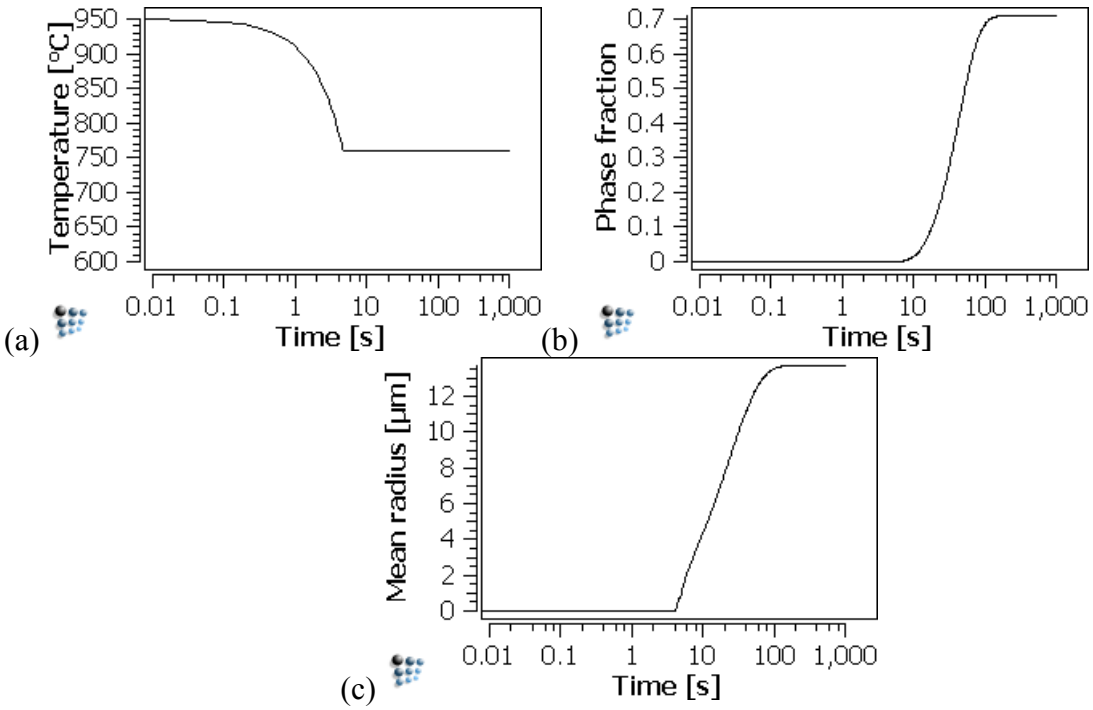

Figure 5.18: optimization of ~ 12.5µm mean radius with correction factor of 0.74 (to be used in the expression for correction of interfacial energy value i.e. 0.74*CIE$BCC_A2). (a) Designed heat treatment cycle, (b) Evolution of ferrite fraction as a result of annealing at isothermal temperature of 760°C, (c) Evolution of mean radius of ferrite grain nucleated at austenite grain corner.

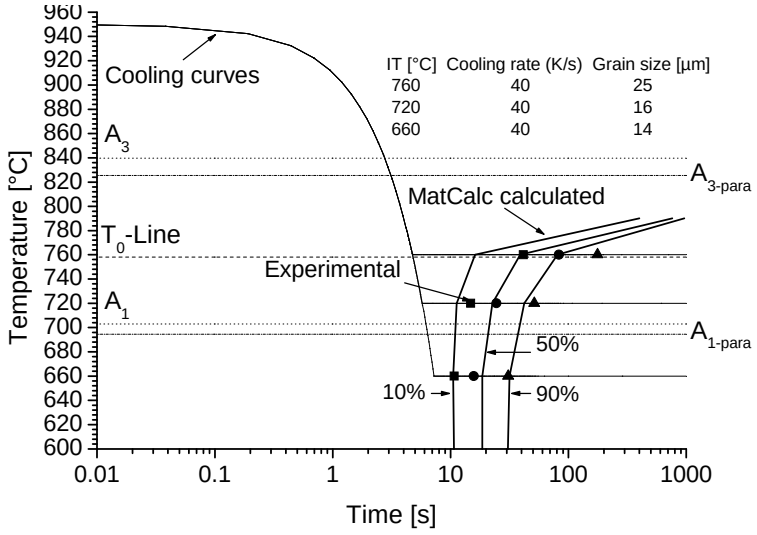

Figure 5.19: Calculated I-TTP diagram for alloy D simulated under paraequilibrium nucleation conditions.

5.3 Calculation of dilatation profiles of alloys A, B, C and D

In the present study, the onset of the austenite to ferrite transformation start temperature was obtained from the comparison of theoretical and measured dilatation profiles. Experimental dilatation profiles are shown in the previous chapter. In this section of the present chapter, the procedure for obtaining theoretical dilatation profiles is described. Calculations are performed by adopting the following steps.

Step 1: In this step, the required elements and phases are selected from the thermodynamic database. After these selections, the physical database is read. In order to accomplish these selections, open new workspace. From the global menu select database. When database tab is selected a new dialog box will appear. In this dialog box press the open tab. When this tab is pressed another dialog box will appear. Select the "mc_sample_fe.tdb" (version = 1.14) thermodynamic database. With its selection different options in the element and phase field becomes visible. From the elements field option select C, Mn and Si along with already selected Fe and VA and from the phase field select austenite (FCC_A1) and ferrite (BCC_A2). After selecting the required elements and phases, press the physical data tab on the left and read the "PhysData.pdb" (version = 1.03) physical database.
Step 2: After reading the thermodynamic and physical databases, insert the chemical composition of the Fe-C-Mn-Si model alloy. If for example alloy A is taken then following chemical composition is inserted in the chemical composition dialog box

C = 0.004 wt%, Mn = 0.06 wt% and Si = 0.006 wt%

Step 3: After giving the input parameters, arrangements for displaying the variation of strain with temperature are made in this step. This will help to get the output i.e. dilatation versus temperatures plot. For this purpose press ctrl+M and from the new dialog box select 'xy-data' plot. Now left click the xy-plot and from the option window double click the StepValue option. When this option is selected a new message box will appear. Write 'T$C' instead of 'StepValue' in this message box to read the temperature in degree Celsius (i.e. °C). Drag and drop variable 'STR$7800' from the variable window in the xy-plot area.

Step 4: In this step preliminary calculations will be performed before the main calculations. For this purpose calculate equilibrium at 900°C. Software will display following message in the output window after calculating equilibrium

T: 900 C (1173.16 K), GibbsEnergy: -54677.585 J
- OK -

Now find the austenite-ferrite boundary from the search phase boundary option. After calculation, the software will display following message in the output window

Tsol 'BCC_A2': 907.18 C (1180.34 K) iter: 10, time used: 0.08 s
- OK –

For paraequilibrium calculations this message is

Tsol 'BCC_A2': 906.24 C (1179.40 K) iter: 9, time used: 0.05 s
- OK –

And for massive calculations this message in the output window is

T0(FCC_A1/BCC_A2): 902.351 C (1175.51 K)
iter: 2, time used: 0.04 s
- OK

Step 5: Stepped calculations are performed in this step to get the variation of strain as a function of temperature plot. After getting the OK message in the output window for austenite-ferrite search phase boundary calculations press stepped calculation tab in the calc main menu bar. A new dialog box will appear. For temperature type stepped calculation give following inputs in the range field
Start = 600, stop=950, step interval=1 (linear)
(for massive calculations also select the vary T only, do not calculate equilibrium box)
After giving the inputs, start calculations and receive the OK message in the output window. When this message is received, the xy-plot will display the strain profile for alloy A for example.
Step 6: Replace strain with change in length using following formulation

Change in length (dilatation or ΔL) = original length*strain, Original length = 10 mm

As the austenitization temperature is 950°C so make arrangements in such a way that change in length starts with 950°C i.e. the amount of dilatation or contraction at austenitization temperature is zero. For 1100°C austenitization contraction or dilatation will be zero at 1100°C.
Repeat the above described method to calculate the dilatation profile in paraequilibrium and massive conditions. Figure 5.20 is displaying these profiles for alloys A, B, C and D with 950°C of austenitization and figure 5.21 is showing these profiles with 1100°C austenitzation temperature.

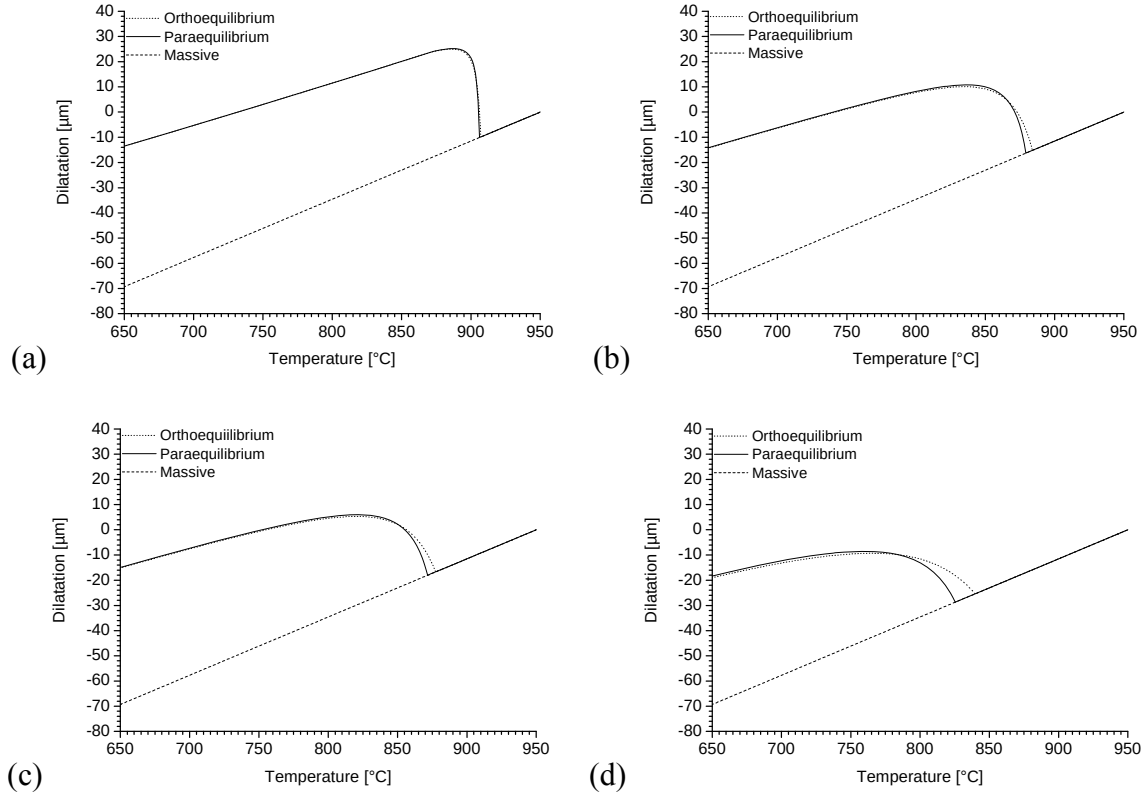

Figure 5.20: Theoretical dilatation profiles of (a) alloy A, (b) alloy B, (c) alloy C and alloy D with austenitization temperature of 950°C.

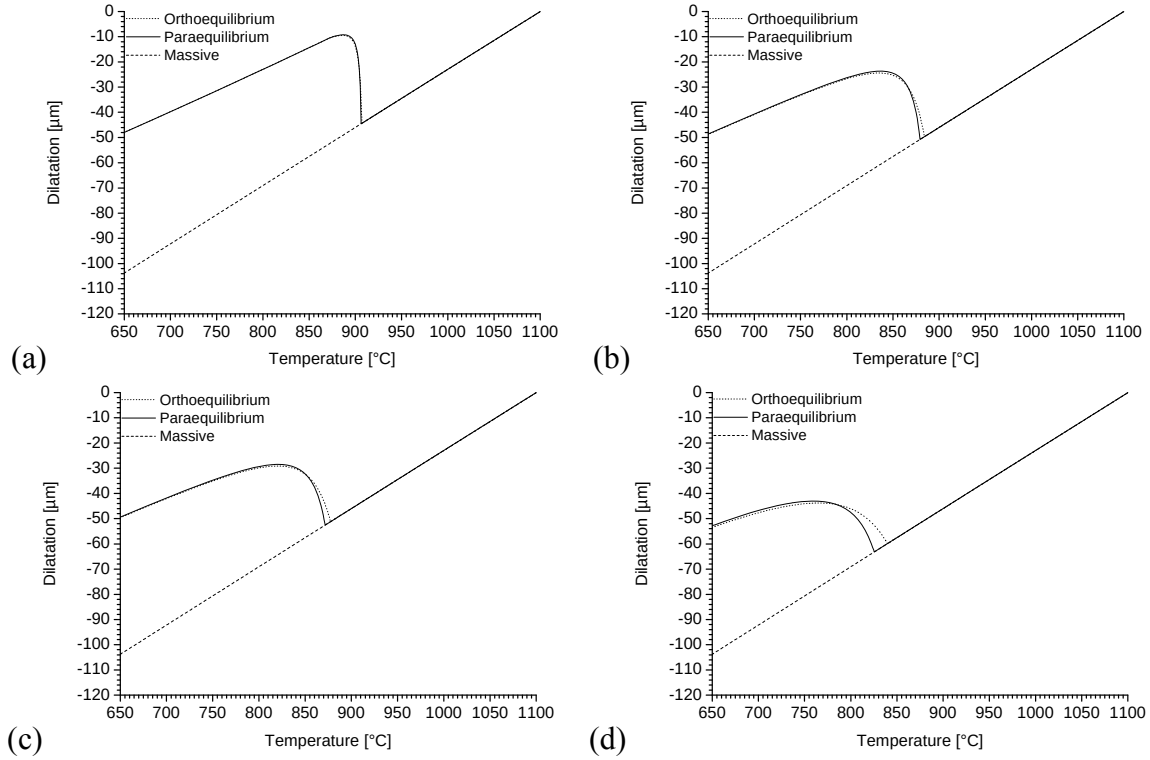

Figure 5.21: Theoretical dilatation profiles of (a) alloy A, (b) alloy B, (c) alloy C and alloy D with austenitization temperature of 1100°C.

CHAPTER 6: RESULTS AND DISCUSSION

High-speed quenching dilatometer was used to generate the dilatation profiles of alloys A, B, C and D (chapter 4). These profiles were used to construct the isothermal time temperature transformation (I-TTT) diagrams of these alloys. For theoretical analysis, software packages MatCalc and DICTRA were used to simulate the isothermal time temperature precipitation (I-TTP) diagrams of these alloys (chapter 5). All simulations were calibrated with the experimental data.
In order to investigate the mechanism responsible for controlling the kinetics of the austenite to ferrite transformation, I-TTT and I-TTP diagrams were compared. It is assumed that simulations lead to a good agreement between measured and calculated I-TTT and I-TTP diagrams in the regions where the phase transformation is controlled by diffusion. The regions of interface-controlled or two-stage transformation can clearly be distinguished by significant deviation from the diffusion-controlled calculations. This is due to the fact that both MatCalc and DICTRA are using diffusion databases for kinetics assessments with the principal difference that MatCalc is using nucleation kinetics and DICTRA does not. In this regard, MatCalc also requires nucleus composition and the nucleation site information. For interpretation of the nucleation conditions, phase diagrams of all steels used in the present study were calculated in both ortho and paraequilibrium conditions and are shown in figure 5.5. Generally, ferrite is nucleated on grain boundaries and grain corners (GC) are the most probable nucleation sites ([1], [3]). Kozeschnik and Gamsjäger [1] in their work have found that spherical geometry was capable of covering the features of diffusion controlled transformations of austenite to ferrite. For the same reasons, spherical geometry was the choice in simulation for both software packages.

6.1 Comparison of I-TTT and I-TTP diagrams for alloy A

The comparison between measured I-TTT and calculated (both with MatCalc and DICTRA) I-TTP diagrams for hollow and solid samples of alloy A is shown in figure 6.1. A_3, A_1, $A_{3\text{-para}}$, $A_{1\text{-para}}$ and T_0 temperatures in figure 6.1 for alloy A are calculated with the MatCalc software package. The representative microstructure of alloy A obtained as a result of thermal treatment at a target IT temperature of 780°C is shown for example in figure 6.2. Grain size variation with respect to target IT temperatures for hollow and the solid samples are given in table 6.1.
The agreement between measured I-TTT and calculated I-TTP diagram for hollow samples of alloy A does not exist at all target IT temperatures from 780 to 890°C irrespective of whether calculation is done with MatCalc or DICTRA. With DICTRA the above said comparison is only possible in two phase austenite plus ferrite region, while with MatCalc this comparison is also possible in single extrapolated ferrite region along with austenite plus ferrite two phase region. This difference is due to the fact that DICTRA calculations are based on full equilibrium while for MatCalc this is not the case. Deviation of 10 to 90% transformation I-TTP curves from I-TTT curves is particularly pronounced for IT temperatures from 780 to 870°C, which is in the extrapolated ferrite single phase region. On the other hand, for solid samples of alloy A (for both T_{aus} = 950°C or T_{aus} = 1100°C), the agreement is satisfactory for a range of IT temperatures from 870°C and above. Again, for IT temperature of 860°C and below, the agreement between measured and calculated transformation times is bad.

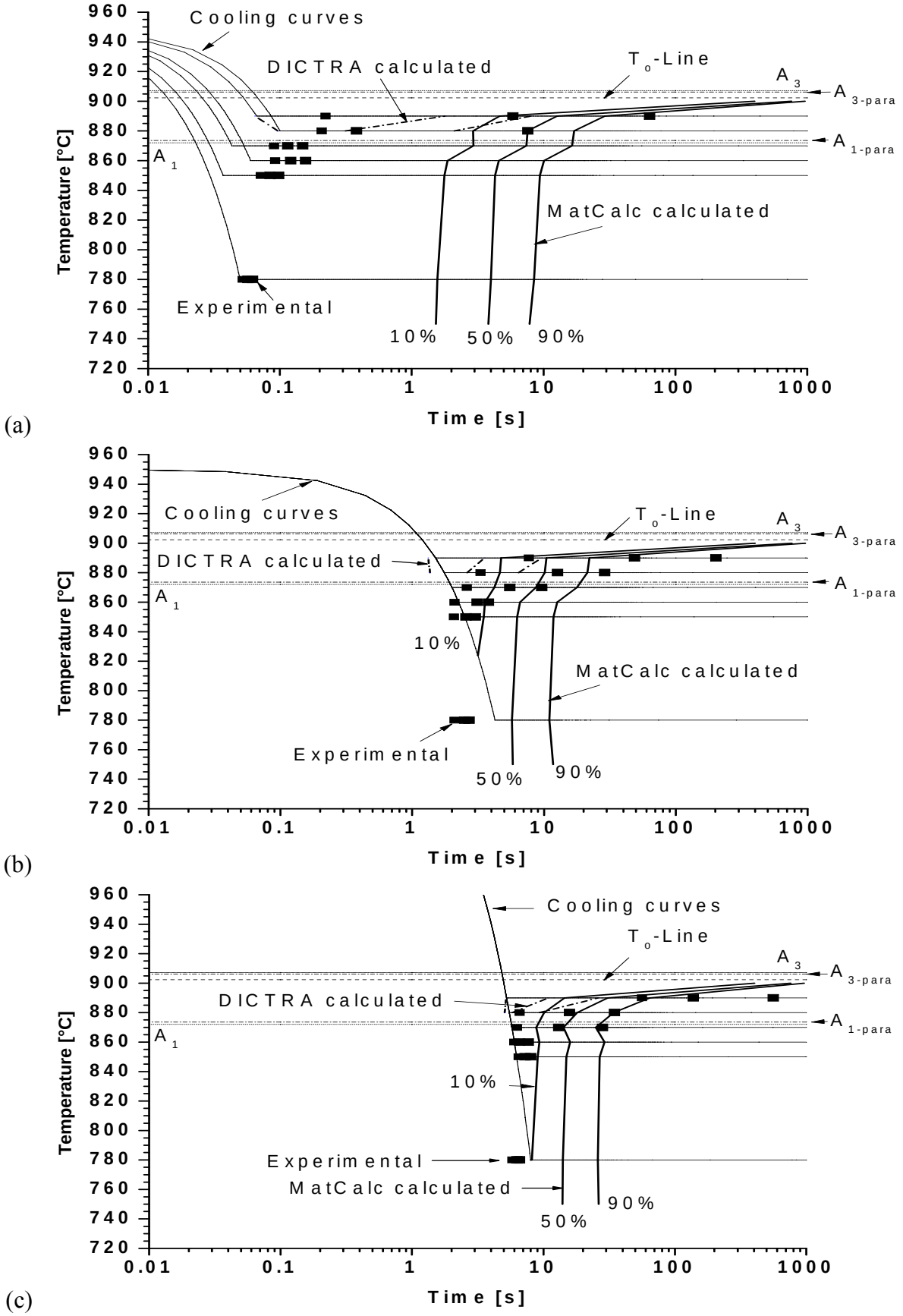

Figure 6.1: Comparison of measured I-TTT diagrams (points) and calculated I-TTP diagrams (curves) of alloy A for (a) hollow samples with T_{aus} of 950°C, (b) solid samples with T_{aus} of 950°C and (c) solid samples with T_{aus} of 1100°C.

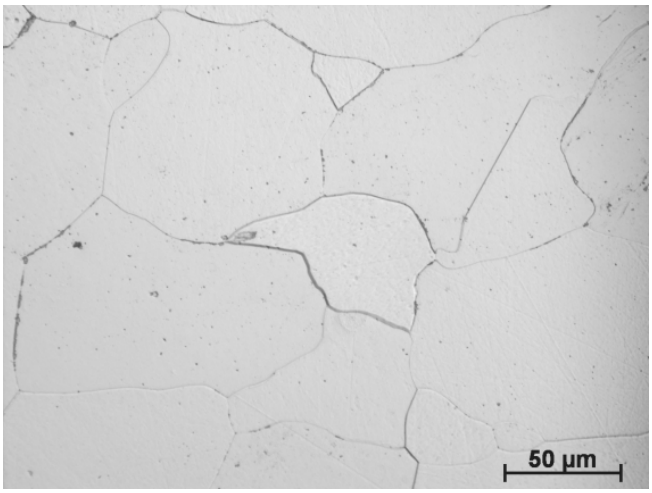

Figure 6.2: Microstructure of alloy A obtained at a target IT temperature of 780°C showing massive ferrite.

Table 6.1: Grain size variation with respect to target IT temperatures for alloy A

Alloy	Target IT Temperature[°C]	Measured grain size (µm)		
		Hollow samples with T_{aus}=950°C	Solid samples with T_{aus}=950°C	Solid samples with T_{aus}=1100°C
A	890	70	65	109
	880	69	81	92
	870	74	76	86
	860	62	70	108
	850	62	68	96
	780	59	69	106

Observations regarding onset of γ to α transformations

There were some interesting observations regarding the onset of the austenite to ferrite transformation. These observations, obtained from the thermal and their corresponding dilatation profiles, are summarized in table 6.2. These observations have some link with the operative mechanism. From table 6.2, it was found that in all IT-temperature cases for hollow samples and IT temperatures of 860°C and below for solid samples of alloy A, transformation has started before reaching the IT temperatures. This particular observation is in line with previous results [1].

Evolution of ferrite fraction

For an analysis of the time scale, in which the transformation has started and completed, and to visualize the two-stage nature of the austenite to ferrite transformation, the evolution of the ferrite fraction profiles are shown in figure 6.3.

Hollow samples

It is evident from figure 6.3a that hollow samples of alloy A in the ferrite single phase region, are showing very fast transformation kinetics finishing within 1s or less than 200ms. Two-stage transformation behavior was not evident. It seems that transformation was completely controlled by the very fast massive transformation kinetics in response to very high quenching rates up to 3400K/s. This behavior is also apparent in the lacking agreement between measured and calculated 10 and 90% transformation times for hollow samples quenched to IT temperatures from 780 to 870°C. However, in the two phase region (figure 6.3a) from IT temperatures of 880 to 890°C, the results are showing two-stages transformation, where the control of reaction kinetics shifts from very fast interface-controlled transformation to slow diffusion-controlled transformation behavior. It is important to note that effects of thermal

undershoots and overshoots are eliminated before calculating the ferrite fraction evolution profiles for hollow samples by comparing with the theoretical dilatation profiles. This procedure assures the observation that an IT temperature of 890°C still leads to a very small amount of massive reaction in the beginning.

Table 6.2: Onset of the austenite to ferrite transformation in alloy A

Alloy A	Target IT [°C]	Cooling rate [K/s]	Onset of transformation
Hollow (T_{aus}= 950°C)	890	900	Before IT
	880	700	Before IT
	870	1850	Before IT
	860	1500	Before IT
	850	2700	Before IT
	780	3400	Before IT
Solid (T_{aus}= 950°C)	890	40	After IT
	880	40	After IT
	870	40	After IT
	860	40	Before IT
	850	40	Before IT
	780	40	Before IT
Solid (T_{aus}= 1100°C)	890	40	After IT
	880	40	After IT
	870	40	After IT
	860	40	Before IT
	850	40	Before IT
	780	40	Before IT

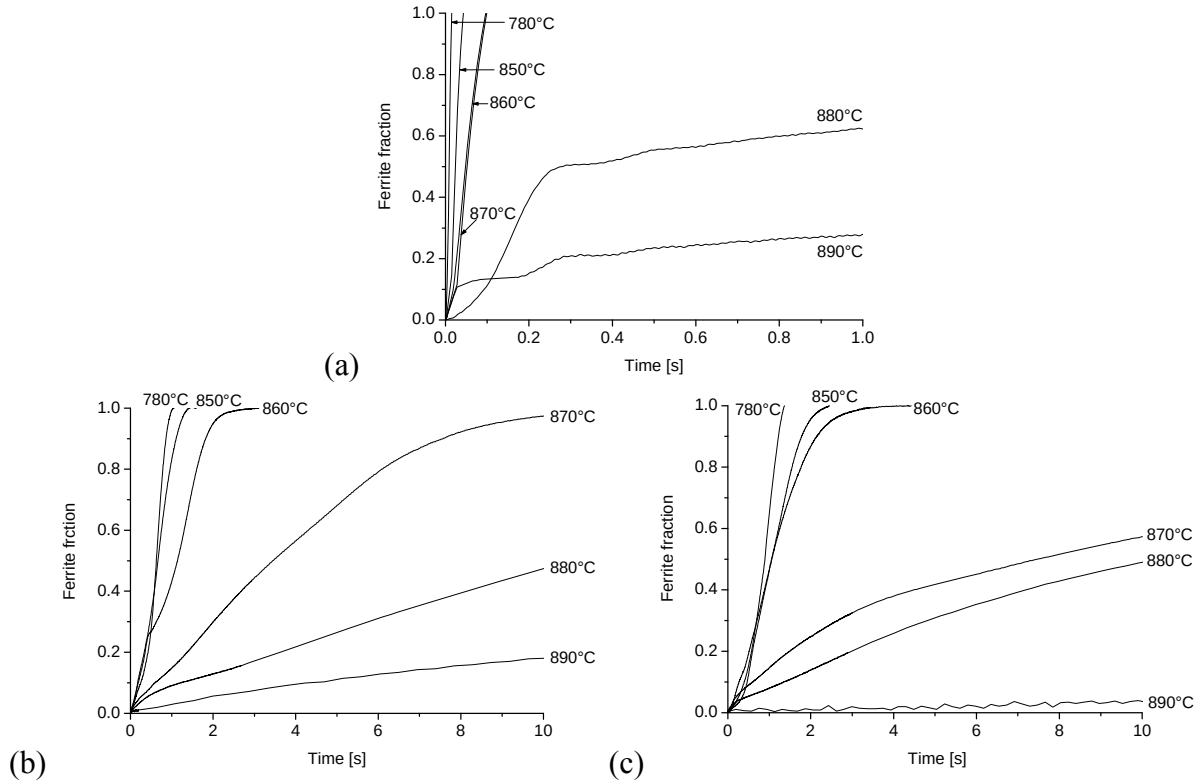

Figure 6.3: Ferrite fraction evolution profiles of alloy A for (a) hollow samples with T_{aus} of 950°C, (b) solid samples with T_{aus} of 950°C and (c) solid samples with T_{aus} of 1100°C.

Solid samples

In contrast, two regimes are evident in the solid samples of alloy A (figure 6.3b & c). A high temperature regime, from 870 to 890°C, where satisfactory agreement exists between measured and MatCalc calculated transformation times, and a low temperature regime, from 780 to 860°C, where agreement does not exist and at the same time transformation has started before reaching the IT temperature. This fact is particularly pronounced for a target IT temperature of 780°C, where transformation has completed before reaching the target IT temperature. It seems from this observation that target IT temperatures of 850 and 860°C are showing two-stage transformation characteristics because of their slow kinetics, while, at 780°C, complete interface-controlled massive transformation is evident. The only difference between the solid samples austenitized at 950°C and those austenitized at 1100°C is the time in which transformation has completed. The higher austenitization temperature has increased the austenite grain size which has decelerated the kinetics because the partitioning species has to travel slightly more distance.

It is also necessary to mention that a discrepancy exists between MatCalc and DICTRA, and DICTRA simulated and experimentally measured results in the high temperature regime. This discrepancy is due to the fact that MatCalc takes into account the ferrite nucleation kinetics whereas DICTRA does not. The comparison of measured and calculated I-TTT and I-TTP diagrams (figure 6.1b &c) clearly emphasize that MatCalc results are more close to the experimentally measured I-TTT points in the high temperature regime (i.e. 870 to 890°C in solid samples of alloy A). The calculated I-TTP diagrams are showing strong dependence on nucleation behavior.

Correction factors for the calibration of interfacial energies

A correction factor is required to calibrate the interfacial energy for a particular target IT temperature. The calculated interfacial energy for ultra-low carbon steel is compared for Fe-C alloy and Fe-C-Mn-Si alloy (in ortho and paraequilibrium conditions) in figure 6.4. For ultra-low carbon steel the difference between these values is not so great. However with the addition of carbon this difference will be visible in the next coming sections where low carbon steel (alloys B, C and D) will be discussed. The correction factor as a function of target IT temperatures for alloy A is shown in figure 6.5. The comparison of calculated and corrected values of interfacial energies at a particular target IT temperatures are shown in figure 6.6.

It is necessary to mention here that generally the correction factor values lies between 0 and 1. The vicinity of 0 is showing correction at low supersaturation and the vicinity of 1 is showing the correction for higher supersaturation. For alloy A correction factors were showing slightly higher values than 1 at IT temperature of 780°C (figure 6.5). These values are obtained on the basis of optimizing the final ferrite radius which is the product of the applied thermal cycle. In the hollow sample, which was quenched to IT temperature of 780°C, the obtained radius was 29.5µm. Correction factor upto 0.99 has given the value of 23µm radius. Similarly solid sample which was austenitized at 950°C and quenched to the IT temperature of 780°C, the simulated radius was 17µm for correction factor value of 1 against the required radius of 34µm (i.e. obtained from thermal cycle). In the same way, solid sample which was austenitized at 1100°C and quenched to IT temperature of 780°C has given simulated radius value of 26µm for correction factor value of 1 against the required radius of 49µm (actually obtained from thermal cycle). In the present study only experimental IT temperatures were used to get the value of the correction factor. The hollow samples of ultra-low carbon steel were the only exception where the correction factor needs to be calculated at an additional IT temperature of 750°C. This additional step was required because the established trend of correction factor was predicting the simulated value of 60µm radius at an IT temperature of 750°C. This value of radius is very high. In order to adjust this problem a value of correction

factor of 0.995 was chosen which has given a value of 29µm of radius at an IT temperature of 750°C. This value is almost equivalent to the optimized radius at an IT temperature of 780°C. This approach seems logical because, if we consider the table 6.1, then it can be found that the low IT temperatures (i.e. below 860°C) were showing almost the same values of radius.

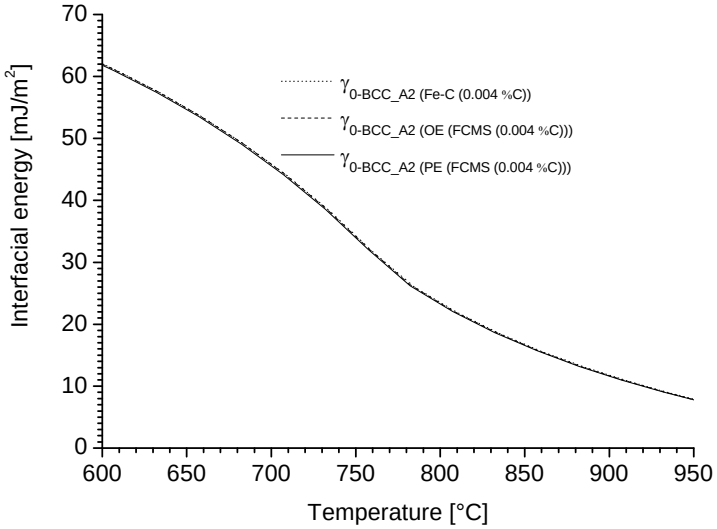

Figure 6.4: Comparison of interfacial energy ($\gamma_{0\text{-BCC\_A2}}$) of ferrite calculated for Fe-C and Fe-C-Mn-Si (orthoequilibrium (OE) and paraequilibrium (PE) conditions) for alloy A having 0.004%C. (Here FCMS = Fe-C-Mn-Si).

Assessment of the austenite to ferrite onset temperatures and driving forces

As has been described above that MatCalc simulated I-TTP diagrams are close to the I-TTT diagrams and hence are showing dependence on nucleation kinetics. It is therefore also possible to calculate the driving force available for equilibrium and massive nucleation with the method described by [1]. According to this method for equilibrium nucleation, alloying elements are allowed to partition in both ortho and paraequilibrium conditions (i.e. C, Mn and Si in orthoequilibrium (OE) and only C in paraequilibrium (PE) conditions) for the present study. After the nucleation the product obtained is called equilibrium ferrite as it is obtained as a result of partitioning which involves diffusion of alloying elements. The partitioning delays the onset of the austenite to ferrite transformation.

On the other hand if nucleation of ferrite occurs without partitioning of alloying elements then the ferrite obtained will be called massive ferrite. In such cases both parent austenite and the product ferrite would have the same chemical composition and transformation involves only volume change so they will exhibit very rapid transformation kinetics.

The calculated values of equilibrium and massive austenite-ferrite boundaries and their corresponding dilatations are summarized in table 6.3 and the driving force profiles as a function of temperature are shown in figure 6.7 for alloy A.

The austenite to ferrite transformation start temperature can be found from the measured dilatation or contraction of austenite before the evolution of ferrite phase by finding a temperature against this dilatation from the calculated dilatation versus temperature graph (chapter 5). Then this temperature can be used to find the driving force available for transformation.

The calculated values of driving forces from the measured dilatation or contraction of austenite for various target IT temperatures of ultra-low carbon steel are displayed in table 6.4.

The hollow samples of alloy A are showing that the austenite to ferrite transformation has started just below the equilibrium or at or just below the massive calculated phase boundaries.

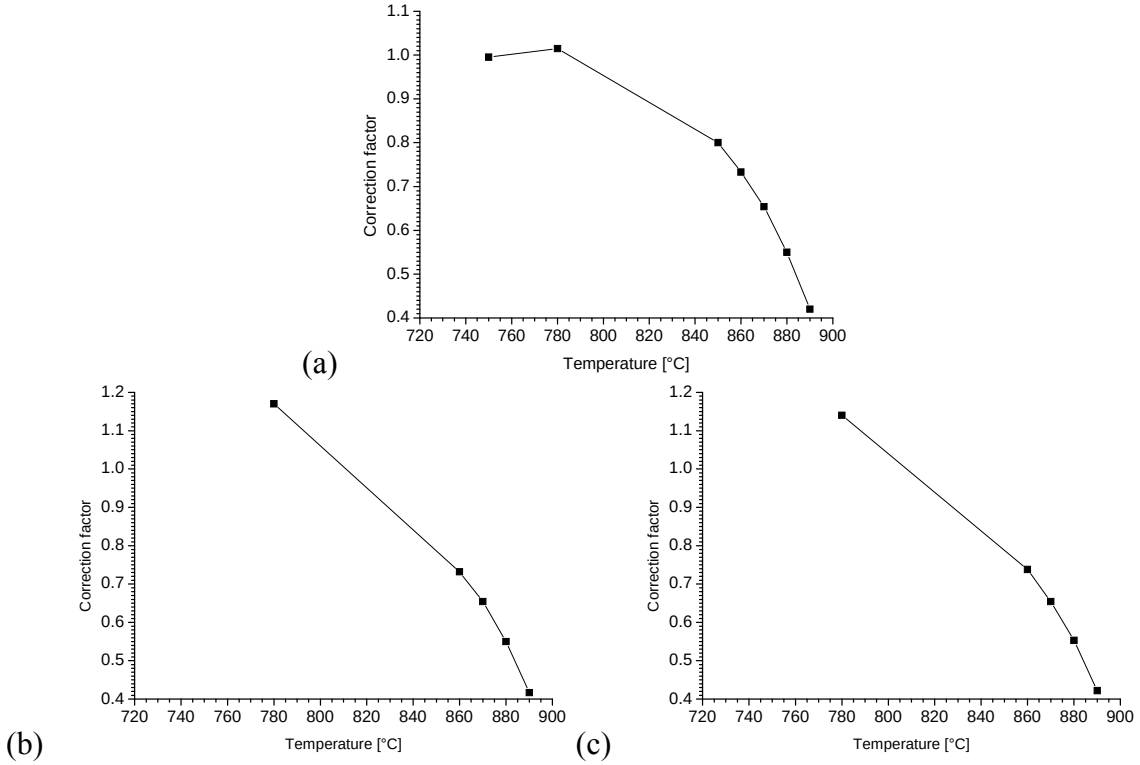

Figure 6.5: Optimized correction factor for interfacial energy as a function of target IT temperatures for (a) hollow samples of alloy A with T_{aus} = 950°C, (b) solid samples of alloy A with T_{aus} = 950°C and (c) solid samples of alloy A with T_{aus} = 1100°C.

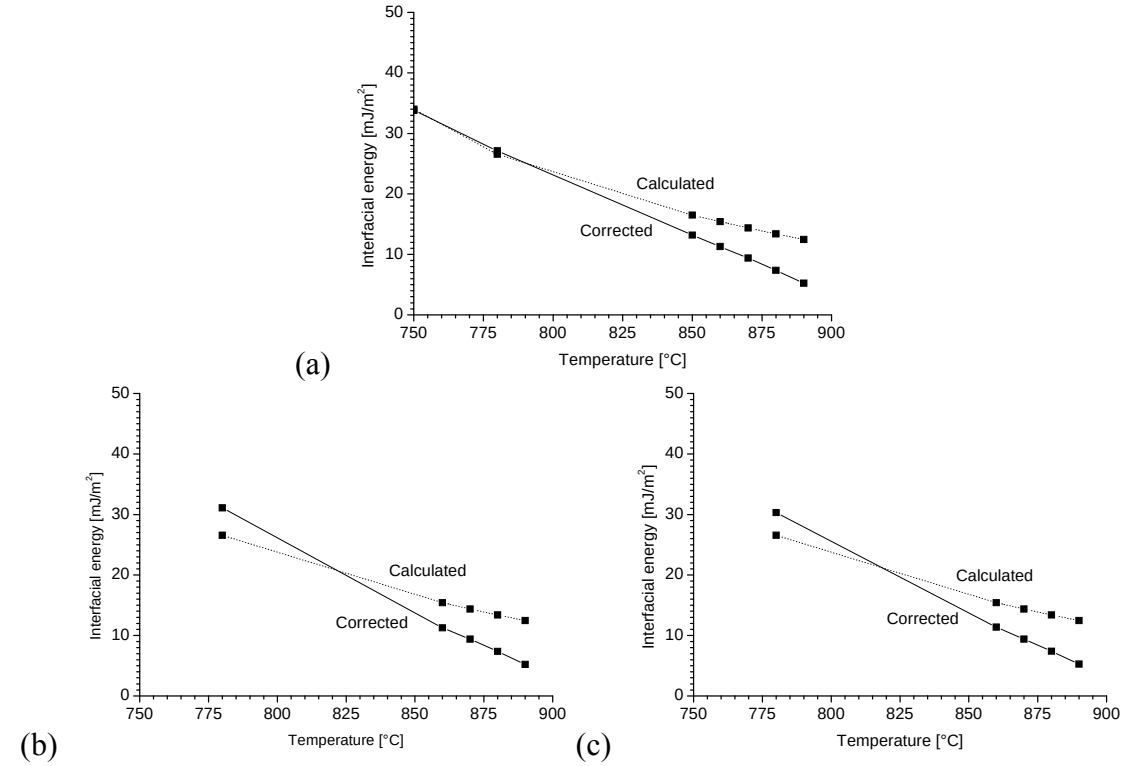

Figure 6.6: Comparison of calculated and corrected values of interfacial energy at target IT temperatures for (a) hollow samples of alloy A with T_{aus} = 950°C, (b) solid samples of alloy A with T_{aus} = 950°C and (c) solid samples of alloy A with T_{aus} = 1100°C.

Table 6.3: Calculated austenite-ferrite boundaries and their corresponding dilatations

Alloy	Alloy							
	Fe-C-Mn-Si (FCMS)							
	Transformation start temperature [°C] and its corresponding dilatation [µm]							
	Calculated for equilibrium ferrite					Calculated for massive ferrite		
	T [°C]		ΔL [µm]			T [°C]	ΔL [µm]	
	OE	PE		OE	PE			
A	907.2	906.2	1	-9.8	-10	902.4	1	-11
			2	-44.3	-44.5		2	-45.4
1	For sample austenitized at 950°C			2		For sample austenitized at 1100°C		

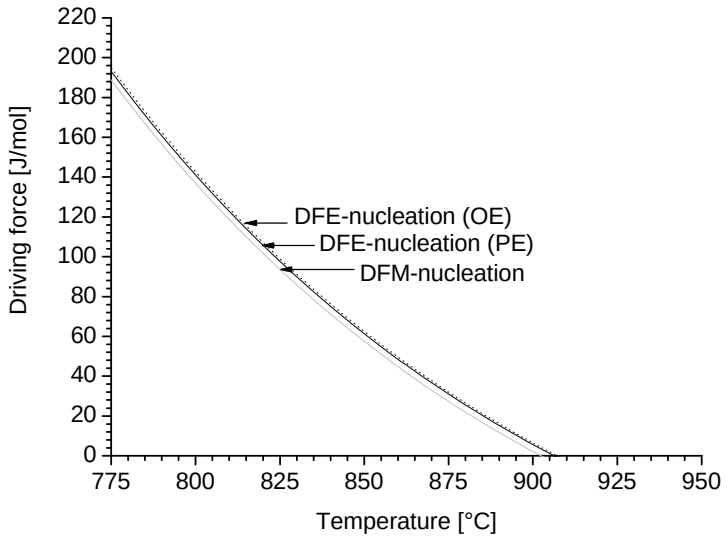

Figure 6.7: Chemical driving force for nucleation in ultra-low carbon steel, calculated in orthoequilibrium (OE), paraequilibrium (PE) and massive nucleation conditions. (The abbreviation DFE and DFM stands for driving force for equilibrium and driving force for massive respectively).

The agreement between I-TTT and I-TTP for hollow samples of alloy A does not exist and the evolution of ferrite fraction profiles (figure 6.3) are also indicating that hollow samples are showing rapid initiation of the austenite to ferrite transformation. From these facts it can be assumed that the nucleation of the austenite to ferrite was partitionless i.e. massive in nature.
The dilatation or contraction of austenite before the onset of ferrite evolution was also showing the possibility of massive nucleation. Theoretically a contraction of 10µm is required to have the equilibrium nucleation and 11µm is required for massive nature of nucleation. All specimens except target IT temperature of 880°C (which is showing a contraction of 10.2µm) are showing that the dilatation is greater than 11µm. The target IT temperature of 880°C was also clearly showing a two-stage austenite to ferrite transformation kinetics (figure 6.2). The first rapid part was clearly showing a hint that the nucleation at that target IT temperature of 880°C was massive in nature. In the present study fresh samples were used for heat treatment and experiments were performed more than once to check the repeatability of the behavior. In this regard, the dilatation profile for all the samples thermal cycled to target IT temperature of 880°C are compared in figure 6.8.
From this figure 6.8, it can clearly be seen that the dilatation of all samples are showing distinct two-stage transformation behavior and at the same time they are also showing almost or slightly greater than 11µm of contraction of austenite before onset of ferrite phase. By considering this situation a contraction of 11µm is used for analysis instead of 10.2µm.

For solid samples austenitized at 950°C, the agreement between I-TTT and I-TTP is satisfactory for the range of temperature from 870 to 890°C. The driving force for target IT temperatures of 870, 880 and 890 was 23.4, 25.2 and 15.2J/mol respectively. At these target IT temperatures the contraction of austenite before the onset of ferrite remains almost constant which means that at these IT temperature the driving force is almost the same i.e. having the value of 14.7J/mol.

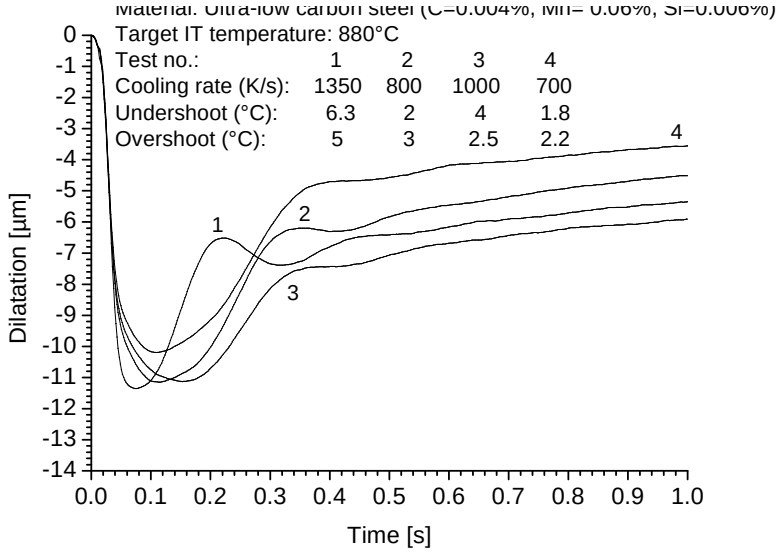

Figure 6.8: Comparison of the dilatation profiles of various fresh hollow samples of ultra-low carbon steel quenched to target IT temperature of 880°C.

Table 6.4: Target IT temperatures, measured cooling rates, dilatation, austenite to ferrite transformation start temperatures and the calculated driving forces for nucleation for alloy A

Alloy A	Target IT [°C]	Cooling rate [K/sec]	ΔL_{Exp} (measured)	Transformation start temperature [°C]	Driving force for nucleation of ferrite [J/mol]		
					Equilibrium ferrite		Massive ferrite
					OE	PE	
Hollow	890	900	-11.1	902	4.7	3.8	0.3
	880	700	[-10.2] -11	[905] 902	4.7	3.8	0.3
	870	1850	-12.2	898	8.4	7.5	4
	860	1500	-12	898	8.4	7.5	4
	850	2700	-12.6	896	10.3	9.4	5.9
	780	3400	-12.4	896	10.3	9.4	5.9
Solid (950°C)	890	40	-15	890	16.2	15.2	11.7
	880	40	-17	880	26.5	25.5	21.9
	870	40	-15.8	882	24.4	23.4	19.8
	860	40	-14.6	887	19.2	18.2	14.7
	850	40	-14.6	887	19.2	18.2	14.7
	780	40	-14.6	887	19.2	18.2	14.7
Solid (1100°C)	890	40	-49	890	16.2	15.2	11.7
	880	40	-46	880	26.5	25.5	21.9
	870	40	-52.5	871	36.5	35.5	31.8
	860	40	-50	883	23.3	22.3	18.8
	850	40	-50	883	23.3	22.3	18.8
	780	40	-46	900	6.5	5.7	2.1

The hollow samples have shown that the massive ferrite nucleation was possible at very low driving force. The driving force for target IT temperatures of 890, 880, 870, 860, 850 and 780 was 0.3, 0.3, 4, 4, 5.9 and 5.9J/mol respectively (table 6.4). This indicates that ferrite nucleation is easy. Clemm and Fisher [41] has shown that ferrite nucleation at grain boundary corner occurs instantaneously even without the necessity to overcome a nucleation barrier by thermal activation.
The solid samples austenitized at 1100°C are showing similar trend as has been seen for solid samples austenitized at 950°C. The only difference was the driving force which was observed at a target IT temperature of 780°C. The austenite to ferrite transformation was started at 900°C which is just below the austenite-ferrite boundary calculated either in equilibrium or massive conditions. The transformation completes before reaching the IT temperature and the driving force available in massive conditions seems to be used for the austenite to ferrite transformation which is 2.1J/mol.
The measured dilatation (contraction) for hollow samples, as shown in table 6.4, does not increase significantly with increasing undercooling, which is also an indication of the massive nature of transformation. In the samples there will always exist regions with more or less carbon or other alloying elements, which can start transforming almost without nucleation barrier and with both parent and the product phases having identical chemical composition. The only change is the volume change due to difference in density of austenite and ferrite. The ferrite, which is formed by the massive mechanism, consists of random equiaxed grains but the grain boundaries are more jagged (figure 6.2) [5].
For solid samples, with austenitization temperature of 950°C, the measured dilatation (contraction) increases when the IT temperature is decreased from 890 to 880°C. At 870°C it is decreased, for IT temperatures of 860 and 850°C it becomes constant and at an IT temperature of 780°C it is further decreased.
In the similar manner, for solid samples austenitized at 1100°C, the dilatation initially decreased and then increased for target IT temperatures of 890 to 870°C where a nice agreement exists between I-TTT and I-TTP diagrams.
In contrast for target IT temperature of 860 to 780°C where a poor agreement exist between I-TTT and I-TTP the dilatation instead of increasing decreases from -50µm to -46µm respectively due to difference in mechanisms. Again, this type of behavior is generally observed, if the transformation is controlled by the interface kinetics, i.e. carbon free regions are operative and transformation starts almost immediately.

6.2 Comparison of I-TTT and I-TTP diagrams for alloy B

The comparison of experimentally measured I-TTT and theoretically simulated I-TTP diagrams (calculated with MatCalc and DICTRA) are shown in figure 6.9 for alloy B. In this figure, A_3, A_1, $A_{3\text{-para}}$, $A_{1\text{-para}}$ and T_0 temperatures for alloy B, are calculated with the MatCalc software package. The representative microstructure of alloy B obtained as a result of thermal treatment at a target IT temperature of 700°C is shown for example in figure 6.10. Grain size variation with respect to target IT temperatures for hollow and the solid samples are given in table 6.5.

Observations regarding the onset of the γ to α transformations and ferrite evolution profiles
It seems, from the discussion in the previous section, that whether the austenite decomposition has started before or after reaching the target IT temperatures has also an important role in understanding the mechanism of the austenite to ferrite transformation. These observations from the comparison of thermal and dilatation profiles of alloy B (figure 4.18c & d for hollow samples, figure 4.19c & d for solid samples with T_{aus}=950°C and figure 4.20c & d for solid

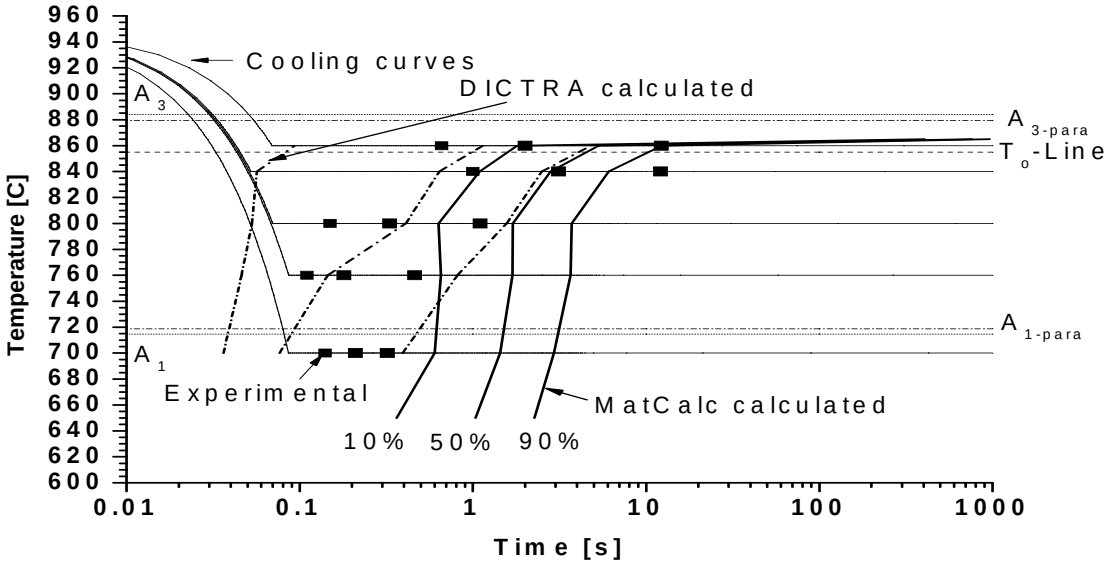

(a)

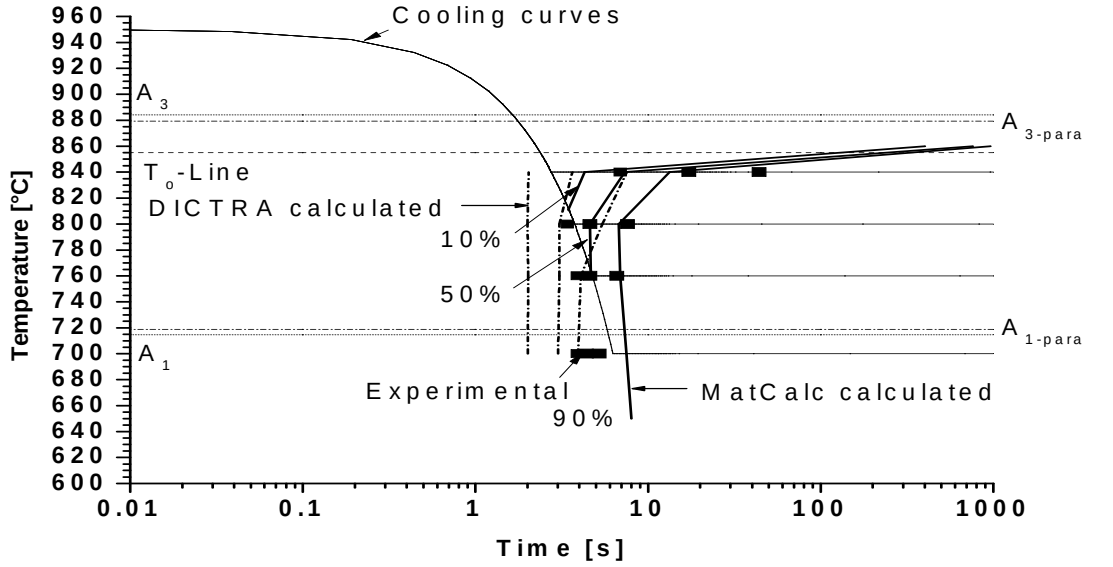

(b)

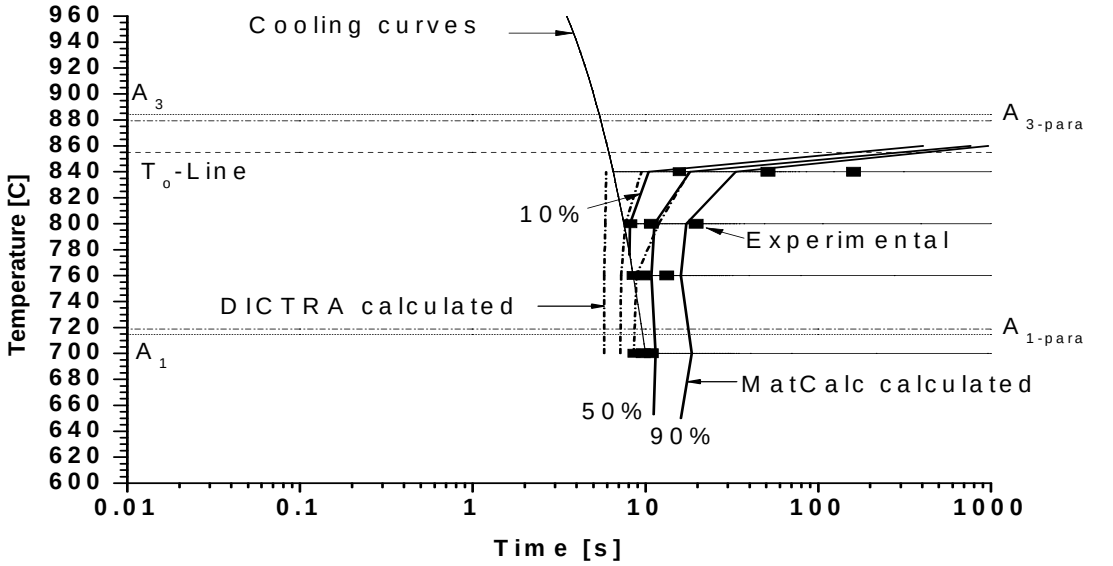

(c)

Figure 6.9: Comparison of measured I-TTT diagrams (points) and calculated I-TTP diagram (curves) of alloy B for (a) hollow samples with T_{aus} of 950°C, (b) solid samples with T_{aus} of 950°C and (c) solid samples with T_{aus} of 1100°C.

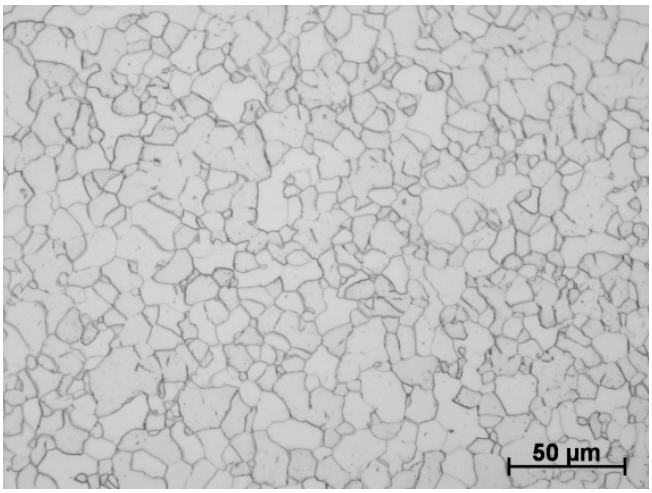

Figure 6.10: Microstructure of alloy B obtained at a target IT temperature of 700°C showing massive ferrite.

Table 6.5: Variation of grain sizes with target IT temperatures for various samples of alloy B

Alloy	Target IT Temperature[°C]	Measured grain size (µm)		
		Hollow samples with T_{aus}=950°C	Solid samples with T_{aus}=950°C	Solid samples with T_{aus}=1100°C
B	860	17		
	840	16	21	35
	800	15	17	26
	760	14	18	23
	700	15	17	23

Table 6.6: Onset of the austenite to ferrite transformation in alloy B

Alloy B	Target IT [°C]	Cooling rate [K/s]	Onset of transformation
Hollow (T_{aus}= 950°C)	860	1300	After IT
	840	2100	After IT
	800	2150	Before IT
	760	2200	Before IT
	700	2900	Before IT
Solid (T_{aus}= 950°C)	840	40	After IT
	800	40	Slightly before IT
	760	40	Before IT
	700	40	Before IT
Solid (T_{aus}= 1100°C)	840	40	After IT
	800	40	After IT
	760	40	Slightly before IT
	700	40	Before IT

samples with T_{aus}=1100°C) are summarized in table 6.6. It is helpful if these observations are supplemented with ferrite fraction evolution profiles for alloy B. These profiles are shown in figure 6.11.

MatCalc simulations for hollow samples

In hollow samples of alloy B, the agreement exists between experimentally measured I-TTT and MatCalc calculated I-TTP curves for target IT temperatures of 860 and 840°C. From table 6.6, we can also see that transformation for these target IT temperatures has started after reaching the IT temperatures. Moreover figure 6.11a is also showing that for these target IT

temperatures the kinetics was also very slow. This evidence is sufficient to conclude that for hollow samples, the austenite to ferrite transformation kinetics at target IT temperatures of 860 and 840°C is fully controlled by long-range diffusion.
The target IT temperatures of 800°C and below (700 to 760°C) are showing that, at these IT temperatures, the transformation has started before reaching the IT temperature (table 6.6). The agreement between I-TTT and I-TTP diagrams, for 700 to 760°C does not exist (figure 6.9a). At a target IT temperature of 800°C, this agreement was also bad and only some part of the simulated curves passes through the 10 to 90% time range (figure 6.9a) which gives us a hint that transformation mechanism was not neither completely massive nor diffusive.
For target IT temperatures of 760 and 700°C, the transformation has completed within 1s (figure 6.11a) while for 800°C it took more time. The evolution of the ferrite fraction profile was also showing relatively slow reaction kinetics. This observation suggests that eventually a two-stage transformation mechanism is driving the austenite to ferrite transformation kinetics at a target IT temperature of 800°C. In comparison 760 and 700°C are showing complete interface controlled transformation.

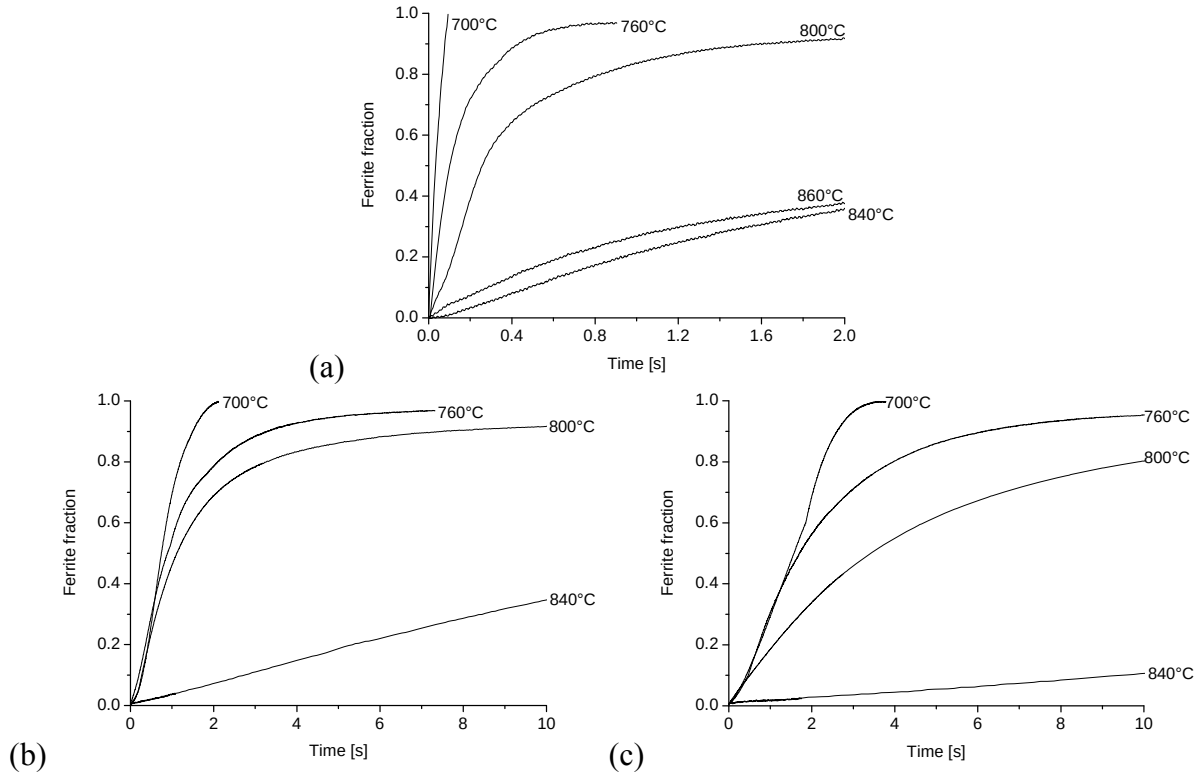

Figure 6.11: Ferrite fraction evolution profiles of alloy B for (a) hollow samples with T_{aus} of 950°C, (b) solid samples with T_{aus} of 950°C and (c) solid samples with T_{aus} of 1100°C.

MatCalc simulations for solid samples with T_{aus} = 950°C

In the solid sample, which is autenitized at 950°C and quenched to target IT temperature of 840°C, the transformation has started after reaching the target IT temperature (table 6.6) and at the same time the kinetics of transformation is also slow (figure 6.9b). Moreover the agreement between I-TTT and I-TTP diagram for this target IT temperature was also excellent. From these observations it is assumed that diffusion is the key mechanism which is driving the transformation.
At a target IT temperature of 800°C, this agreement also exists but the 10% transformation has started slightly before reaching the target IT temperature which is an indication that the mechanism responsible for initiating and finishing the austenite to ferrite transformation was different. Similarly the solid sample which was cooled to target IT temperature of 760°C is

showing that transformation has started before reaching the IT temperature. In comparison target IT temperature of 700°C is showing that austenite decomposition was completed before reaching the target IT temperature. These observations are showing that the austenite to ferrite transformation taking place at a target IT temperature of 800 and 760°C was two-stage, started with partitionless nucleation and later on shifted to diffusion mechanism which controls the kinetics of the rest of the transformation. The target IT temperature of 700°C was showing complete massive transformation kinetics.
As mentioned above that for target IT temperatures of 700 to 800°C, the transformation has started before reaching the target IT temperature (table 6.6) at the same time these three IT temperature are showing almost the same amount of dilatation (figure 4.19d) i.e. contraction of austenite before the onset of the austenite to ferrite transformation. This type of behavior has similarities with the work of [1] as was also observed in case of alloy A. This type of behavior can be seen where partitionless nucleation takes place. There are some areas present in the material which do not have the solute content and behave like pure iron. These areas begin to transform in a manner which does not allow any partiotioning. Parent and product phases have the same chemical compositions. As only volume changes are involved, the austenite to ferrite transformation was rapid in such cases.

MatCalc simulations for solid samples with $T_{aus.}$ = 1100°C
In comparison, austenitization at 1100°C has slowed down the kinetics and only 700°C is showing mismatch between MatCalc calculated I-TTP and measured I-TTT time values. Although the mismatch for target IT temperature of 760°C does not exist, but like the target IT temperature of 800°C for solid sample which was austenitized at 950°C, the 10% of transformation seems to occur slightly before the IT temperature. This observation is showing that the nature of mechanism is definitely changing as we are moving from higher to lower target IT temperatures.
The target IT temperatures of 800 to 840°C are showing complete diffusion controlled transformation mechanism. The target IT temperature of 760°C is showing that the transformation start and finish was different in nature from mechanism point of view. The deviation of I-TTP time record from the I-TTT time record is probably suggesting that the transformation started at this temperature with a massive mechanism.
The solid samples austenitized at 1100°C are showing the effects of higher austenitization temperature. These effects are particularly enunciated for low temperatures. At higher temperature i.e. 840°C both austenitization temperatures i.e. 950 and 1100°C are showing that the austenite to ferrite transformation has started after reaching the target IT temperature. The ferrite evolution profile at this IT temperature in case of austenitization at 1100°C was also showing very slow kinetics. Both austenitization temperatures were clearly indicating that the transformation mechanism controlling the kinetics of the austenite to ferrite reaction was lond-range diffusion. The only difference observed was that the higher austenitization temperature has shifted the completion of transformation to longer times.
At 800°C, the sample which was austenitized at 950°C and cooled to this IT temperature is showing a small massive portion. The higher austenitization temperature shifts the curve towards longer transformation times. This is the consequence of higher austenitization temperature that transformation has started after reaching the IT temperature and the agreement between experimentally measured and MatCalc calculated 10 to 90% times is excellent.
The target IT temperature of 760°C in case of 1100°C austenitization is showing a two-stage transformation mechanism. The transformation at this target IT temperature (table 6.6) has started slightly before reaching the IT temperature and higher austenitization temperature due to larger austenite grains has slowed down the kinetics of the austenite to ferrite transformation reaction (figure 6.11c).

Target IT temperature of 700°C, in case of austenitization temperature of 950°C, is showing only massive transformation mechanism. With austenitization at higher temperatures two-stage transformation is now responsible for controlling the kinetics of the reaction. This observation was obvious because the higher austenitization temperature of 1100°C increases the austenite grain size and this increase decreases the pace of the transformation and transformation took more than 1s for completion.

DICTRA simulations for hollow samples

From the figure 6.9 it seems evident that DICTRA calculations are lacking the agreement with the experimental measurements in general by a factor of two. This is again due to the fact that this software package does not consider the nucleation kinetics instead it is assuming that there is a viable nucleus, and that transformation will start when the phase to be formed is thermodynamically stable. The new phase automatically starts when the cooling curve hits the A_3 line.

However there are few target IT temperatures (700 to 800°C) in the figure 6.9a where it seems that the agreement is there. This agreement is showing that 10% transformation time is starting before reaching the target IT temperature. It means that the onset of the ferrite from austenite decomposition was extremely fast. Generally long-range diffusion requires some time and only partitionless transformations can show transformations well before reaching the target IT temperature.

DICTRA simulations for solid samples

In case of solid samples irrespective of whether they are austenitized at 950°C or 1100°C are also showing that 10% of the austenite to ferrite transformation has proceeded before reaching the target IT temperatures (Figure 6.9b and c). This fact is particularly noticed for target IT temperatures of 760°C and below where 10 to 90% of the austenite to ferrite transformation was completed before reaching the corresponding IT temperatures.

Massive transformation in low carbon steels

Kozeschnik and Gamsjäger [1] in their experiments with 0.007%C (ultra-low carbon steel) have given only 10s of soaking time at the austenitization temperature of 925°C which is only 16.8°C above the equilibrium austenite-ferrite boundary. They thought that solute redistribution was the main reason of promotion and demotion of massive rapid kinetics. In their experiments, on quenching, the austenite to ferrite transformation was suppressed to 897°C which gave undercooling values of only 11.2°C.

In contrast, Militzer [8] has given 600s at an austenitization temperature of 1050°C. He obtained approximately 50K of undercooling in a steel having 0.002%C along with 0.11%Mn and 0.009%Nb. A discrepancy exists between the results of Kozeschnik and Gamsjäger [1] and Millitzer [8]. Kozeschnik and Gamsjäger [1] thought that higher soaking times at higher austenitization temperature enabled solute atoms to segregate to the austenite grain boundaries. Now higher driving force is required to drive the transformation. At an equilibrium austenite-ferrite boundary, the system does not have sufficient driving force so it will require more undercooling until the system gets enough driving force to initiate the onset of the austenite to ferrite transformation.

Assessment of the austenite to ferrite onset temperatures and driving forces

In order to find out the undercooling and hence the driving force, austenite-ferrite phase boundary was calculated in orthoequilibrium, paraequilibrium and massive conditions for alloy B. These calculations were made with the method described in [1]. Their corresponding dilatations were also obtained from the calculated dilatation versus temperature profiles for two different austenitization temperatures of 950 and 1100°C which were employed in the

present study for alloy B. The temperatures and their corresponding dilatations are shown in table 6.7. In the next step, the dilatation or contraction of austenite is measured before the onset of the austenite to ferrite phase transformation (T_{st}). This contraction was used to find out the onset temperature of the austenite to ferrite transformation. This temperature will also help to find out the undercooling and hence the driving force (from figure 6.12) for alloy B.
The alloy B contains 0.029%C along with 0.326%Mn. The soaking time of 300s was used when the austenitization temperature was 950°C, while it was 600s in case of 1100°C of austenitization temperature. For hollow samples at 860 and 840°C, the driving force for massive nucleation is negative. Ferrite nucleation under paraequilibrium conditiond is also suppressed to 20K for 860°C for target IT temperature of 860°C and 23K for target IT temperature of 840°C.
When undercooling is decreased to almost 50K (or 26K for massive conditions) then the driving force of 34J/mol was sufficient to initiate the onset of massive ferrite nucleation. Solid samples which were austenitized at 950°C are presenting almost the similar results where onset of austenite to massive ferrite transformation was started with the availability of 41J/mol of driving force i.e. after almost 55K of undercooling.
When the soaking time as well as the austenitization temperature was increased to 1100°C, the amount of solute segregated to grain boundaries also increased. In order to push the solute along with the boundary, more driving force was required. This was the basic reason that massive nucleation is further decreased to 787°C. At this temperature a driving force of almost 105J/mol was available to initiate the austenite to massive ferrite.
It seems from the above discussion that the present results are affirming the arguments presented by Kozeschnik and Gamsjäger [1].
Equilibrium ferrite nucleation irrespective of whether it is austenitized at 950 or 1100°C started at an undercooling of almost 40K i.e. after availability of 53J/mol of driving force. This means that enhanced soaking times as well as the increased austenitization temperature has big influence on the onset of the austenite to ferrite transformation in terms of solute segregation at the grain boundaries.

Table 6.7: Calculated austenite-ferrite boundaries and their corresponding dilatation for alloy B

Alloy	Alloy							
	Fe-C-Mn-Si (FCMS)							
	Transformation start temperature [°C] and its corresponding dilatation [µm]							
	Calculated for equilibrium ferrite					Calculated for massive ferrite		
	T [°C]		ΔL [µm]			T [°C]	ΔL [µm]	
	OE	PE		OE	PE			
B	884	879.3	1	-15.2	-16.3	855	1	-21.9
			2	-49.7	-50.8		2	-56.4
1	For sample austenitized at 950°C			2		For sample austenitized at 1100°C		

Correction factors for the calibration of interfacial energies
The MatCalc calculations are calibrated with corrections to the interfacial energy by a correction factor at the entire target IT temperatures. The simulated interfacial energy profile as a function of temperature is shown in figure 6.13. The correction factor as a function of target IT temperatures is shown in figure 6.14. The correction factors are between 0 and 1. The comparison of calculated and corrected interfacial energies for alloy B is shown in figure 6.15.

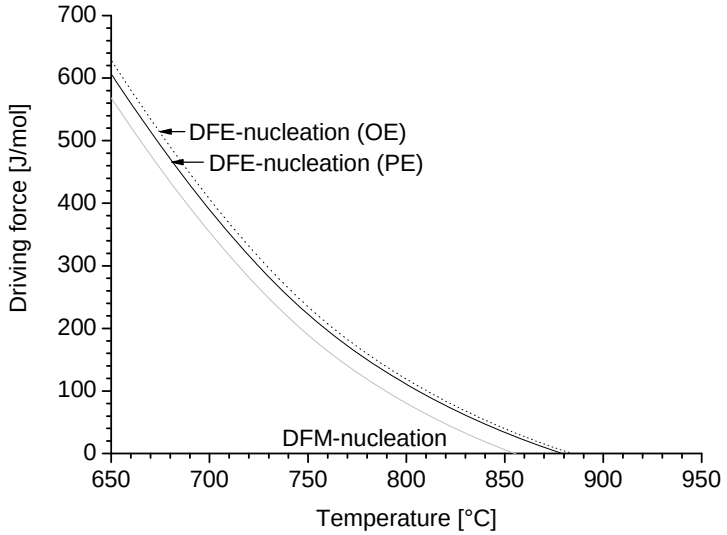

Figure 6.12: Chemical driving force for nucleation in alloy B, calculated in orthoequilibrium (OE), paraequilibrium (PE) and massive nucleation conditions. (The abbreviation DFE and DFM stands for driving force for equilibrium and driving force for massive respectively).

Table 6.8: Target IT temperatures, measured cooling rates, dilatation, the austenite to ferrite transformation start temperatures and the calculated driving forces for nucleation for alloy B

Alloy B	Target IT [°C]	Cooling rate [K/sec]	ΔL_{Exp} (measured)	T_{st} [°C]	ΔT [°C] From		Driving force for nucleation of ferrite [J/mol]		
					PE	M	Equilibrium ferrite		Massive (M) ferrite
							OE	PE	
Hollow	860	1300	-15	860	19.3		27	21.5	-5.8
	840	2100	-21.6	856	23.3		32	26.3	-1.2
	800	2150	-28	829	50.3	26	69.5	62.8	34
	760	2200	-28	829	50.3	26	69.5	62.8	34
	700	2900	-28	829	50.3	26	69.5	62.8	34
Solid (950°C)	840	40	-27.5	840	39.3		53.5	47	18.8
	800	40	-29	824	55.3	31	77.5	70.4	41.3
	760	40	-29	824	55.3	31	77.5	70.4	41.3
	700	40	-29	824	55.3	31	77.5	70.4	41.3
Solid (1100°C)	840	40	-67	840	39.3		53.5	47	18.8
	800	40	-67	840	39.3		53.5	47	18.8
	760	40	-72	787	92.3	68	144.8	135.7	104.8
	700	40	-72	787	92.3	68	144.8	135.7	104.8
ΔL = contraction		ΔT = undercooling		OE = orthoequilibrium				OE = paraequilibrium	

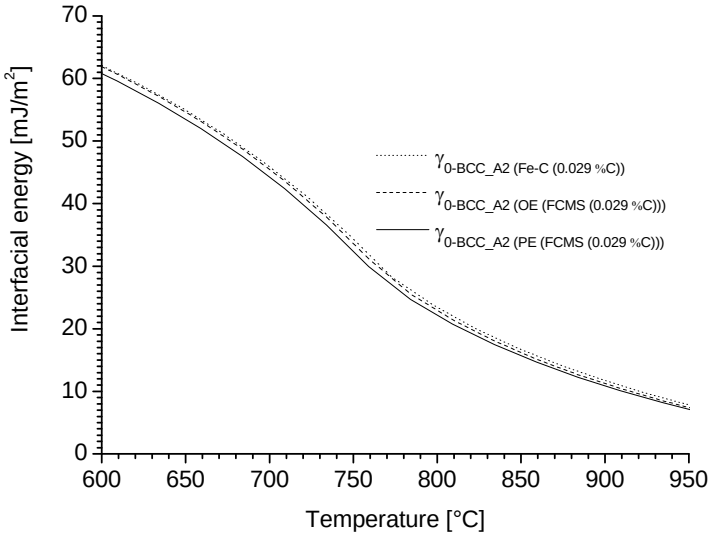

Figure 6.13: Comparison of interfacial energy ($\gamma_{0\text{-BCC\_A2}}$) of ferrite calculated for Fe-C and Fe-C-Mn-Si (orthoequilibrium (OE) and paraequilibrium (PE) conditions) for alloy B having 0.029%C.

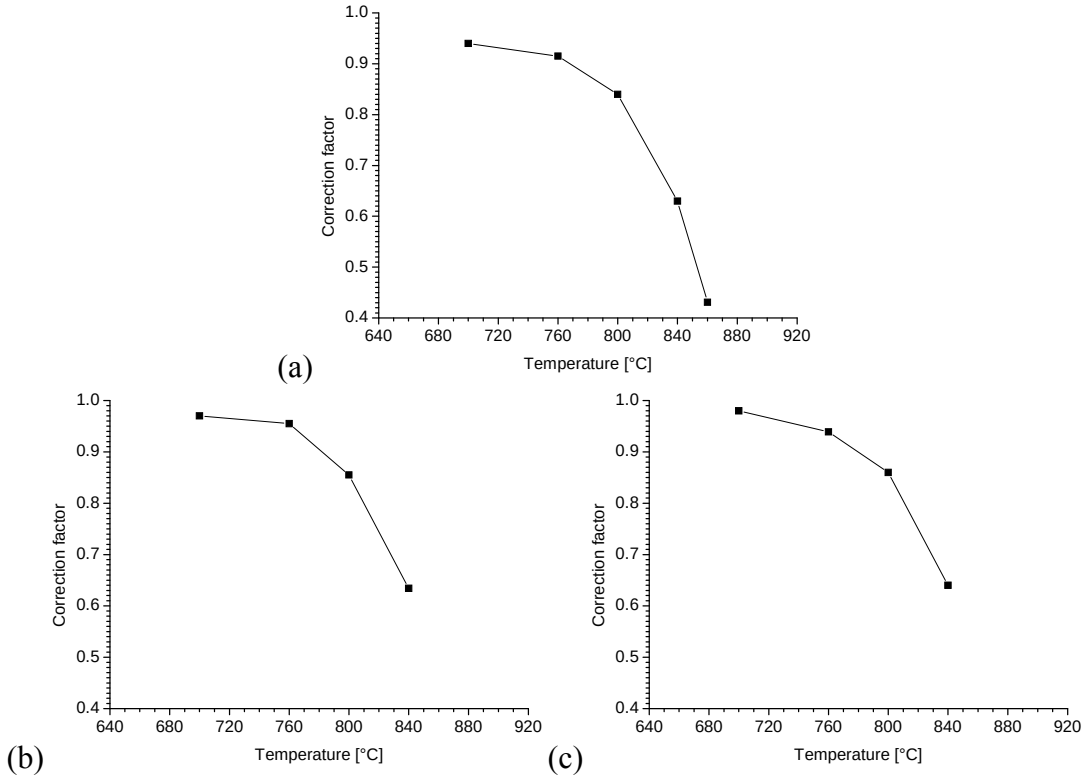

Figure 6.14: Optimized correction factor for interfacial energy as a function of target IT temperatures for (a) hollow samples of alloy B with T_{aus} = 950°C, (b) solid samples of alloy B with T_{aus} = 950°C and (c) solid samples of alloy B with T_{aus} = 1100°C.

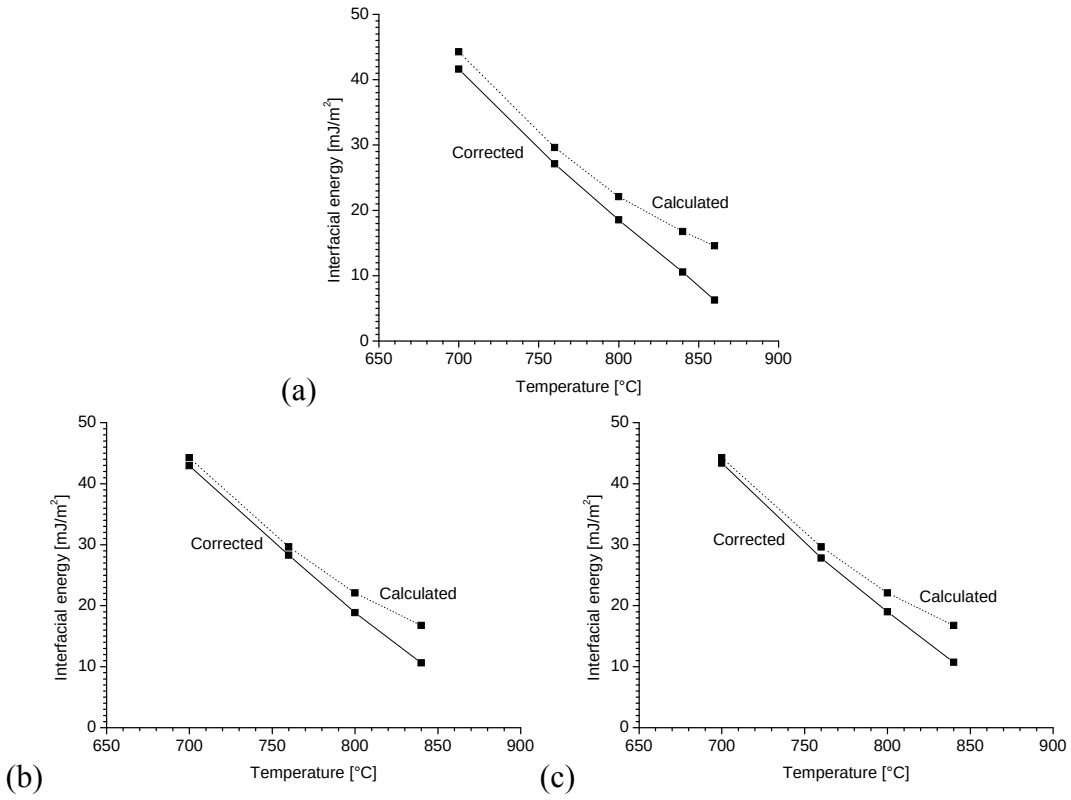

Figure 6.15: Comparison of calculated and corrected values of interfacial energy at target IT temperatures for (a) hollow samples of alloy B with T_{aus} = 950°C, (b) solid samples of alloy B with T_{aus} = 950°C and (c) solid samples of alloy B with T_{aus} = 1100°C.

6.3 Comparison of I-TTT and I-TTP diagrams for alloy C

The comparison of experimentally measured I-TTT and MatCalc and DICTRA simulated I-TTP diagrams are shown in figure 6.16 for alloy C. A_3, A_1, $A_{3\text{-para}}$, $A_{1\text{-para}}$ and T_0 temperatures are calculated with the MatCalc software package. The representative microstructure of alloy C obtained as a result of thermal treatment at a target IT temperature of 690°C is shown for example in figure 6.17. Grain size variation with respect to target IT temperatures for hollow and solid samples are given in table 6.9.

Observations regarding the onset of the γ to α transformations and ferrite evolution profiles

Observations that whether transformation has started before or after reaching the target IT temperature along with ferrite evolution profiles have pivotal role in understanding the mechanism involved for controlling the kinetics of the reaction. The observations obtained from the comparison of thermal and dilatation profiles are displayed in table 6.10 (figure 4.18e & f for hollow samples, figure 4.19e & f for solid samples with T_{aus}=950°C and figure 4.20e & f for solid samples with T_{aus}=1100°C) and the ferrite evolution profiles are shown in figure 6.18.

DICTRA simulations

Figure 6.16 is showing that agreement between experimentally measured I-TTT and DICTRA calculated I-TTP curves is slightly lacking for all solid samples. DICTRA calculated I-TTP curves are showing 10% of transformation before reaching the IT temperature. This is again due to the fact that DICTRA does not take into account the nucleation kinetics. For hollow samples the agreement between DICTRA calculated and measured 10 to 90% transformation

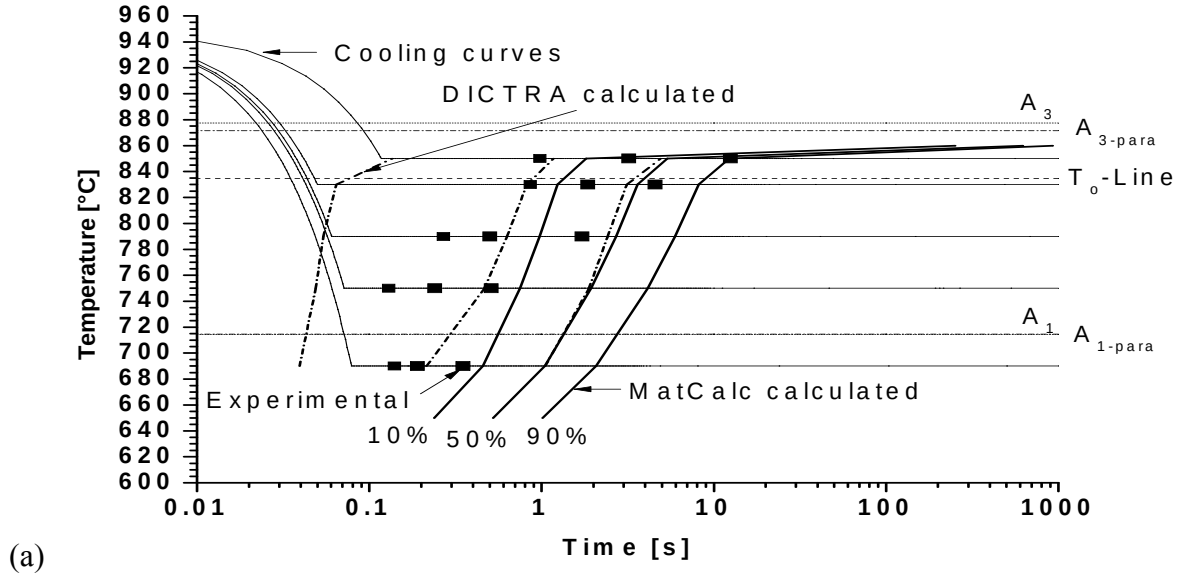

(a)

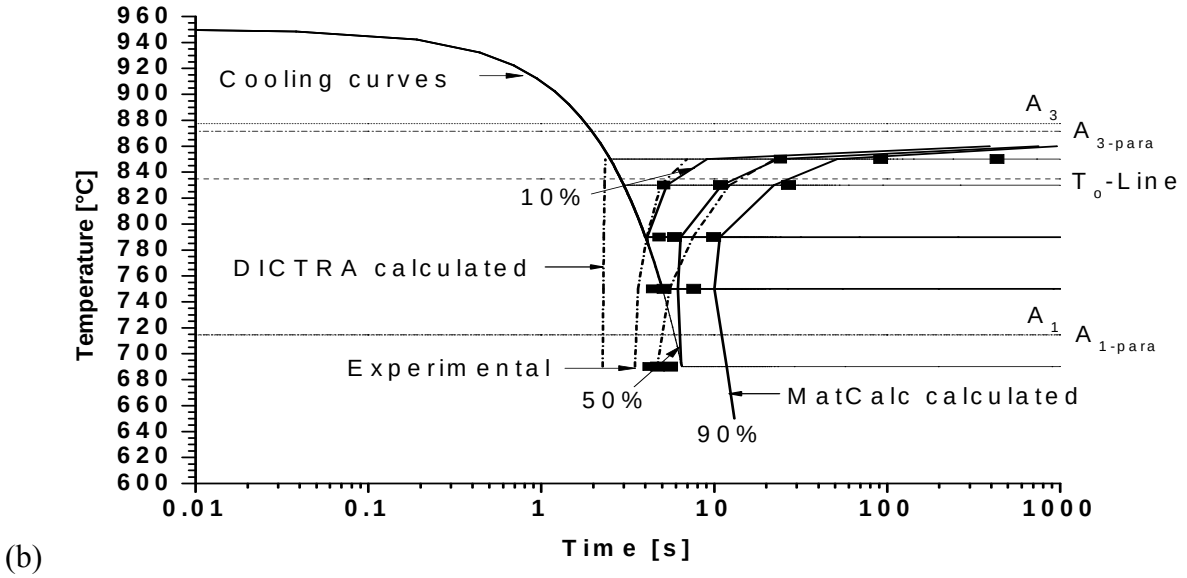

(b)

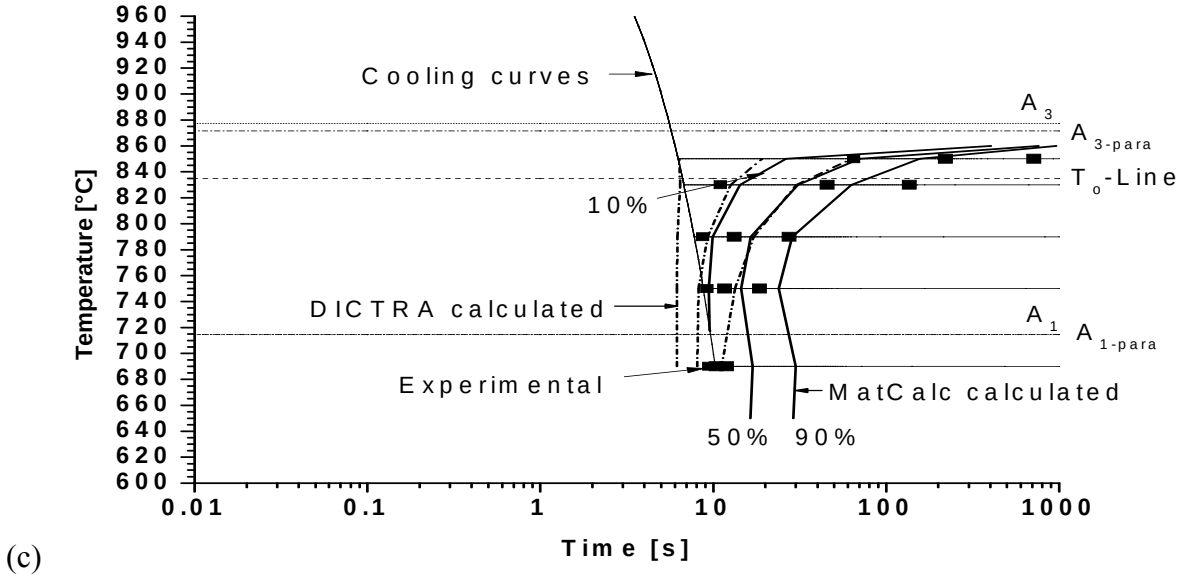

(c)

Figure 6.16: Comparison of measured I-TTT diagrams (points) and calculated I-TTP diagram (curves) of alloy C for (a) hollow samples with T_{aus} of 950°C, (b) solid samples with T_{aus} of 950°C and (c) solid samples with T_{aus} of 1100°C.

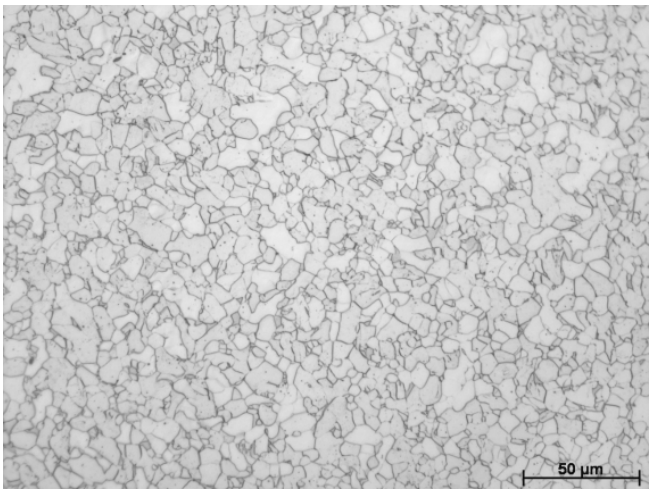

Figure 6.17: Microstructure of alloy C obtained at a target IT temperature of 690°C showing massive ferrite.

Table 6.9: Variation of grain sizes with target IT temperatures for various samples of alloy C

Alloy	Target IT Temperature[°C]	Measured grain size (µm)		
		Hollow samples with T_{aus}=950°C	Solid samples with T_{aus}=950°C	Solid samples with T_{aus}=1100°C
C	850	14	28	49
	830	15	23	38
	790	14	19	29
	750	13	18	27
	690	10	16	27

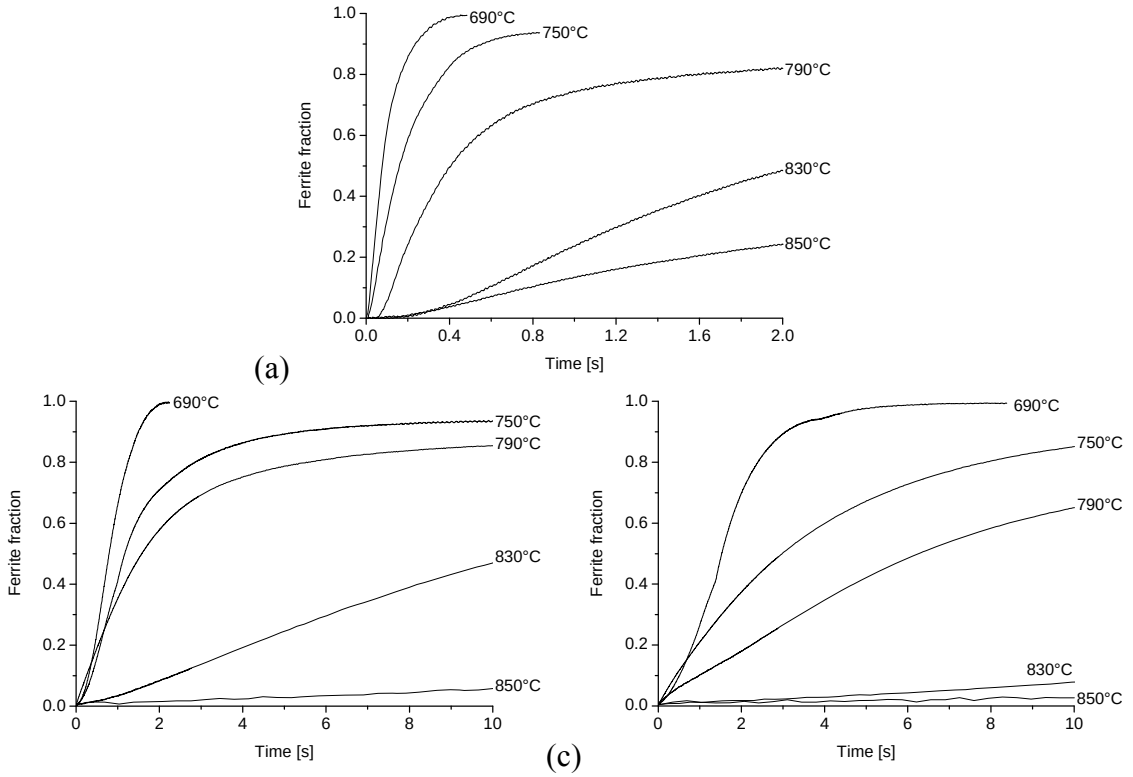

Figure 6.18: Ferrite fraction evolution profiles of alloy C for (a) hollow samples with T_{aus} of 950°C, (b) solid samples with T_{aus} of 950°C and (c) solid samples with T_{aus} of 1100°C.

Table 6.10: Onset of the austenite to ferrite transformation in alloy C

Alloy C	Target IT [°C]	Cooling rate [K/s]	Onset of transformation
Hollow (T_{aus}= 950°C)	850	850	After IT
	830	2400	After IT
	790	2650	Before IT
	750	2800	Before IT
	690	3300	Before IT
Solid (T_{aus}= 950°C)	850	40	After IT
	830	40	After IT
	790	40	Slightly before IT
	750	40	Before IT
	690	40	Before IT
Solid (T_{aus}= 1100°C)	850	40	After IT
	830	40	After IT
	790	40	After IT
	750	40	Slightly before IT
	690	40	Before IT

times for target IT temperature of 850°C was considerable. For target IT temperature of 830°C, agreement for 10 and 50% transformation times does not exists. For IT temperatures of 690 to 790°C, 10% transformation was calculated before reaching the IT temperature. This observation is against the experimentally measured 10% transformation times which are clearly showing that this much transformation occurred after reaching the target IT temperatures.

MatCalc simulations for hollow samples

In the hollow samples for target IT temperature of 830 and 850°C, the transformation has started after reaching the IT temperature (table 6.10). The ferrite evolution profiles (6.18a) for these temperatures were also showing slow kinetics. I-TTT and MatCalC calculated I-TTP times of 10 to 90% transformation are also presenting some degree of agreement. From these observations it seems clear that at these IT temperatures the mechanism which is controlling the kinetics of transformation is diffusion controlled. For target IT temperatures of 690 to 790°C, the onset of the austenite to ferrite transformation has started before reaching the IT temperature. Ferrite evolution profiles at target IT temperatures of 690 and 750°C are showing that transformation has completed within 1s (figure 6.18a). The lacking agreement for MatCalc calculated 10 to 90% transformation with the measured times is clearly showing that interface controlled reaction is controlling the kinetics of the austenite to ferrite transformation at these IT temperatures. In comparison, the kinetics of the austenite to ferrite transformation at an IT temperature of 790°C is comparatively slow with respect to 750 or 690°C (figure 6.18a). If we consider figure 6.16a, it will be observed that only some part of MatCalc calculated I-TTP is passing through measured 10 to 90% transformation time range for an IT temperature of 790°C.

The onset of transformation before reaching the target IT temperature, slow kinetics and presence of an agreement only at limited region might be an indication the two-stage transformation mechanism is operative at an IT temperature of 790°C. The reaction has initiated with partitionless nucleation and, later on, partitioning took place until the completion of the reaction.

MatCalc simulations for solid samples

For solid samples irrespective of whether they are austenitized at 950 or 1100°C, excellent agreement exist between experimentally measured I-TTT and MatCalc calculated I-TTP times for target IT temperature of 790 to 850°C (figure 6.16b & c). Moreover the onset of the austenite to ferrite transformation has started after reaching the IT temperatures. Target IT temperature of 790°C, with austenitization temperature of 950°C, was the only exception where the onset of the austenite to ferrite transformation was only slightly before the target IT temperature. At the same time, the evolution of the ferrite fraction (figure 6.18b & c) is also showing slow kinetics at these IT temperatures. This much evidence is sufficient to conclude that the kinetics of the austenite to ferrite reaction at these IT temperatures is completely controlled by long-range diffusion.

Solid samples which were austenitized at 950°C and cooled to 750 and 690°C are showing the onset of the austenite to ferrite transformation before reaching the target IT temperatures (figure 6.16b and table 6.10). Comparison of ferrite evolution profiles at these IT temperatures (figure 6.18b) is showing that kinetics at 690°C was rapid with respect to 750°C. At 750°C, comparison of I-TTT and MatCalc calculated I-TTP time is showing that agreement of calculated transformation is close to measured 50 to 90% transformation times. However 10% transformation time is showing that the onset of transformationhas started before reaching the IT temperature. This is an indication of the two-stage transformation.

At 690°C, the onset of the austenite to ferrite transformation and its 90% completion, before reaching the target IT temperature can be seen in figure 6.16b. This is a clear indication that for an IT temperature of 690°C, the austenite to ferrite transformation kinetics was completely controlled by the massive transformation mechanism.

The target IT temperature of 750°C, for the solid sample austenitized at 1100°C austenitization temperature in comparison to 950°C, is showing good agreement of I-TTT and MatCalc calculated 10 to 90% of I-TTP times. This agreement is clearly suggesting that the austenite to ferrite transformation was completely controlled by diffusion.

For a target IT temperature of 690°C (in case of 1100°C austenitization), the transformation has started before reaching the IT temperature (table 6.10 and figure 6.16c). However, figure 6.18c is showing relatively slower kinetics at the later stages of transformation. This is the indication that two-stage transformation is controlling the kinetics of the austenite to ferrite transformation. Due to higher austenitization temperature, the kinetics of the reaction was not as fast as was observed at this target temperature in case of 950°C of austenitization.

Assessment of the austenite to ferrite onset temperatures and driving forces

MatCalc calculated equilibrium and massive austenite-ferrite boundaries and their corresponding dilatation is shown in the table 6.11. Measured contraction of austenite before the onset of austenite transformation to ferrite for alloy C and their corresponding transformation start temperatures and the available driving forces at these temperatures are shown in figure 6.19 and summarized in the table 6.12.

Hollow samples

In hollow samples for IT temperatures of 830 and 850°C, the onset of the austenite to ferrite transformation was after reaching the IT temperatures. The driving force for massive nucleation at an IT temperature of 850°C was negative and at 830°C it was 6.8J/mol. At this temperature it seems that the driving force was not sufficient to nucleate the ferrite massively. With decrease of the target IT temperature to 790°C and increase of cooling rate to 2650K/s the contraction obtained was -25.5µm. The observed mechanism as described above was two-stage i.e. onset of the austenite to ferrite transformation was partitionless. For partitionless transformation the contraction should be at least -26.6µm (table 6.11). The observed difference may be thought as an experimental error. To adjust this error the contraction

considered was -26.6µm. This contraction has given 835°C as the onset temperature for the austenite to ferrite transformation (table 6.12).
For target IT temperature of 750 and 690°C, the mechanism which was driving the austenite to ferrite reaction kinetics was massive in nature. The driving force available to initiate the transformation at these IT temperatures was 22 and 11J/mol respectively. This means that this much of driving force was available to move the solute segregated on the newly nucleated grain boundaries to give interface controlled transformation.

Solid samples with T_{aus} = 950°C

For IT temperatures of 850 and 830°C, the transformation was completely controlled by diffusion in case of solid samples austenitized at 950°C. The transformation has started after reaching the target IT temperatures. At 850°C, driving force for massive nucleation was negative, and for 830°C the driving force of 6.8J/mol was not sufficient to move the solutes along the grain boundaries.
At 790°C, in the solid sample austenitized at 950°C, the transformation has started slightly before reaching the target IT temperature. At this IT temperature, excellent agreement exists between I-TTT and I-TTP 10 to 90% transformation times. The onset of the austenite to ferrite transformation has started at 830°C. At this temperature the driving force for equilibrium nucleation is 53J/mole. For 750 and 690°C austenite is showing same amount of contraction before the onset of ferrite. This means that for both IT temperatures almost the same amount of driving force (27J/mol) was available for massive ferrite nucleation.

Table 6.11: Calculated austenite-ferrite boundaries and their corresponding dilatation for alloy C

Alloy	Alloy							
	Fe-C-Mn-Si (FCMS)							
	Transformation start temperature [°C] and its corresponding dilatation [µm]							
	Calculated for equilibrium ferrite					Calculated for massive ferrite		
	T [°C]		ΔL [µm]			T [°C]	ΔL [µm]	
	OE	PE		OE	PE			
C	877.5	871.6	1	-16.7	-18	834.8	1	-26.6
			2	-51.2	-52.5		2	-61
1	For sample austenitized at 950°C			2		For sample austenitized at 1100°C		

Solid samples with T_{aus} = 1100°C

In solid samples which were austenitized at 1100°C and cooled to 850, 830, 790 and 750°C respectively, agreement between I-TTT and I-TTP 10 to 90% austenite to ferrite transformation time exists. This agreement is clearly indicating the fact that the diffusive mechanism is responsible for controlling the kinetics of the austenite to ferrite transformation. In case of 790 to 850°C the transformation has started after reaching the IT temperature. The driving force available at the IT temperatures of 790, 830 and 850°C is 121, 53 and 26J/mol respectively.
At higher austenitization temperature more solute has segregated on the grain boundaries. For the movement along newly nucleated ferrite grain boundaries or partitioning of this solute more time is required. At 750°C, the austenite to ferrite transformation has started before reaching the IT temperature. Onset of the austenite to ferrite transformation has started at 757°C for this IT temperature. The driving force for nucleation at this temperature was 195J/mol. This seems obvious, as higher driving force was available, so less time was consumed to transform ferrite from austenite. In case of 690°C of target IT temperature, the driving force to initiate the massive ferrite and to drag the segregated solute along the boundaries was also increased in case of 1100°C of austenitization temperature.

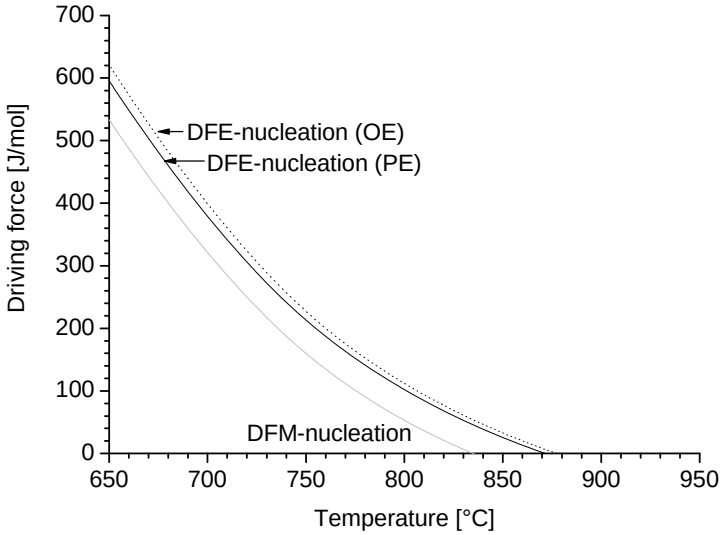

Figure 6.19: Chemical driving force for nucleation in alloy C, calculated in orthoequilibrium (OE), paraequilibrium (PE) and massive nucleation conditions. (The abbreviation DFE and DFM stands for driving force for equilibrium and driving force for massive respectively).

Table 6.12: Target IT temperatures, measured cooling rates, dilatation, the austenite to ferrite transformation start temperatures and the calculated driving forces for nucleation for alloy C

Alloy C	Target IT [°C]	Cooling rate [K/sec]	ΔL_{Exp} (measured)	T_{st} [°C]	ΔT [°C] (From PE)	Driving force for nucleation of ferrite [J/mol]		
						Equilibrium ferrite		Massive (M) ferrite
						OE	PE	
Hollow	850	850	-17.3	850	21.6	33.1	25.6	-19
	830	2400	-18	830	41.6	61.3	53.2	6.8
	790	2650	-25.5	840	35	54.5	46.4	0.3
			-26.6	834.6				
	750	2800	-30	820	51.6	77.1	68.3	21.2
	690	3300	-28.3	827	44.6	65.8	57.5	10.9
Solid (950°C)	850	40	-25	850	21.6	33.1	25.6	-19
	830	40	-30	830	41.6	61.3	53.2	6.8
	790	40	-30	830	41.6	61.3	53.2	6.8
	750	40	-31	816	55.6	83.5	74.6	27.1
	690	40	-31	816	55.6	83.5	74.6	27.1
Solid (1100°C)	850	40	-63	850	21.6	33.1	25.6	-19
	830	40	-69	830	41.6	61.3	53.2	6.8
	790	40	-77	790	81.6	131.6	121.1	71.4
	750	40	-79	757	114.6	208	194.5	142.1
	690	40	-80	752.6	119	220.1	206.4	153.3
ΔL = contraction		ΔT = undercooling		OE = orthoequilibrium			PE = paraequilibrium	

Correction factors for the calibration of interfacial energies

The MatCalc simulations are calibrated with corrections to the theoretical interfacial energy by a correction factor at the particular target IT temperatures. The theoretically calculated interfacial energy profile as a function of temperature is demonstrated in the figure 6.20. The correction factors as a function of target temperature is displayed in the figure 6.21. The comparisons of calculated and corrected interfacial energies at the particular IT temperatures are shown in figure 6.22.

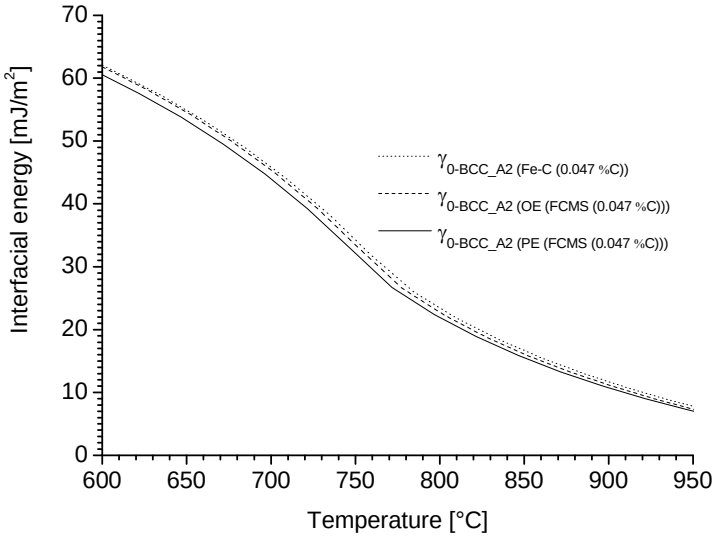

Figure 6.20: Comparison of interfacial energy ($\gamma_{0\text{-BCC\_A2}}$) of ferrite calculated for Fe-C and Fe-C-Mn-Si (orthoequilibrium (OE) and paraequilibrium (PE) conditions) for alloy C having 0.047%C.

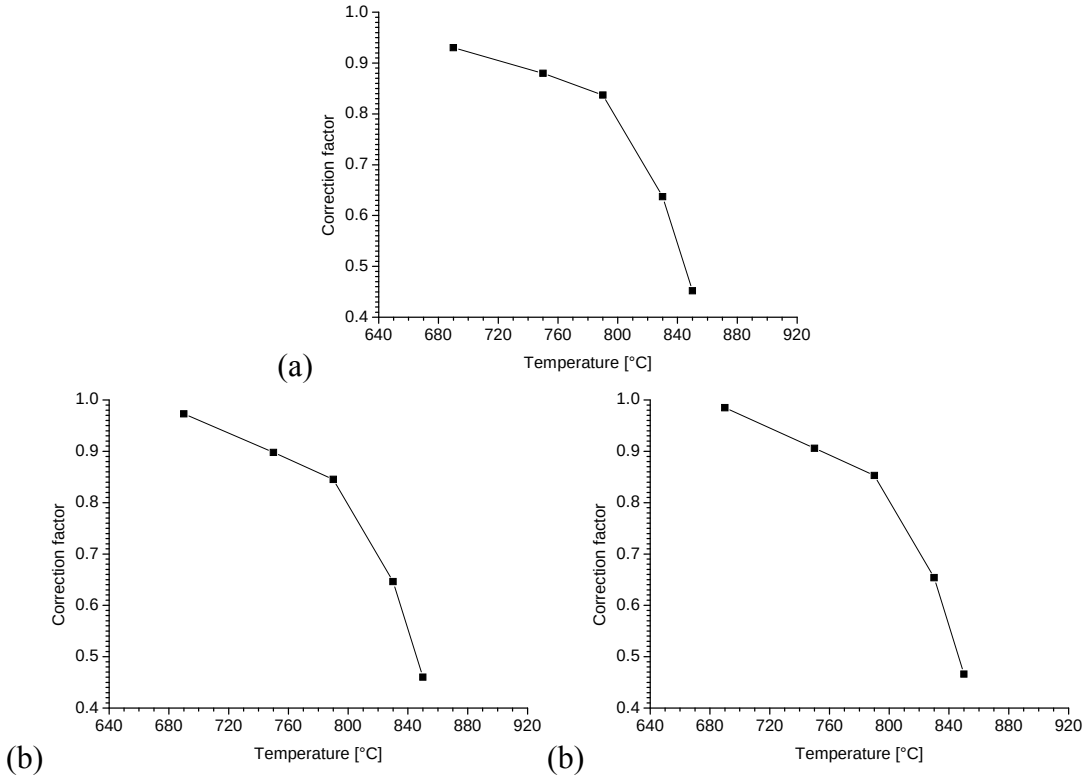

Figure 6.21: Optimized correction factor for interfacial energy as a function of target IT temperatures for (a) hollow samples of alloy C with T_{aus} = 950°C, (b) solid samples of alloy C with T_{aus} = 950°C and (c) solid samples of alloy C with T_{aus} = 1100°C.

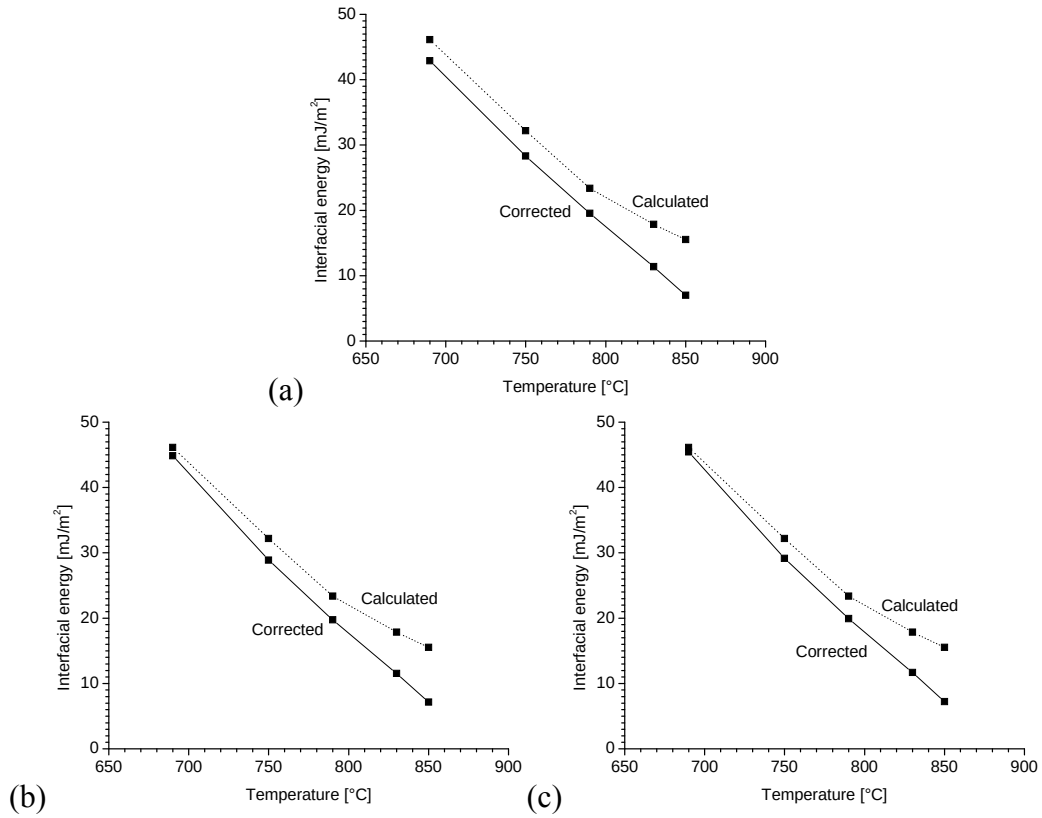

Figure 6.22: Comparison of calculated and corrected values of interfacial energy at target IT temperatures for (a) hollow samples of alloy C with T_{aus} = 950°C, (b) solid samples of alloy C with T_{aus} = 950°C and (c) solid samples of alloy C with T_{aus} = 1100°C.

6.4 Comparison of I-TTT and I-TTP diagrams for alloy D

The comparison of I-TTT with MatCalc and DICTRA simulated I-TTP diagrams are shown in figure 6.23 for alloy D. A_3, A_1, $A_{3\text{-para}}$, $A_{1\text{-para}}$ and T_0 temperatures are calculated with MatCalc. The representative microstructure of alloy D is shown in figure 6.24. Variation of grain sizes with respect to target IT temperatures is shown in table 6.13.

A excellent agreement exists between I-TTT and MatCalc calculated I-TTP diagram while this is missing by a factor of 2 for I-TTT and DICTRA calculated I-TTP curves. This discrepancy is again due to the fact the MatCalc is using and DICTRA is lacking nucleation kinetics. From the agreement of I-TTT and MatCalc calculated I-TTP, it can easily be inferred that the austenite decomposition kinetics is solely controlled by diffusion which allows partitioning of C to occur irrespective of the variation in cooling rates. This fact can also be visualized in ferrite evolution profiles (figure 6.25).

Again MatCalc simulations are calibrated with the correction factor in the calculated interfacial energies. The calculated interfacial energy profiles as a function of temperature are shown in figure 6.26. The effects of considering only Fe-0.111%C alloy and considering the Fe-0.111%C-0.932%Mn-0.167%Si alloy in both ortho and paraequilibrium conditions are easily evident. Fe-0.111%C alloy is showing higher values in comparison to the calculated values of interfacial energy both in ortho and paraequilibrium conditions for the Fe-0.111%C-0.932%Mn-0.167%Si alloy. In ortho and paraequilibrium conditions, paraequilibrium interfacial energies are showing lower values indicating that nucleation in these conditions are easy due to a smaller activation energy barrier. The correction factor trend in the calculated interfacial energies is shown in figure 6.27. The values of these correction factor lie between 0 and 1, which is generally as expected.

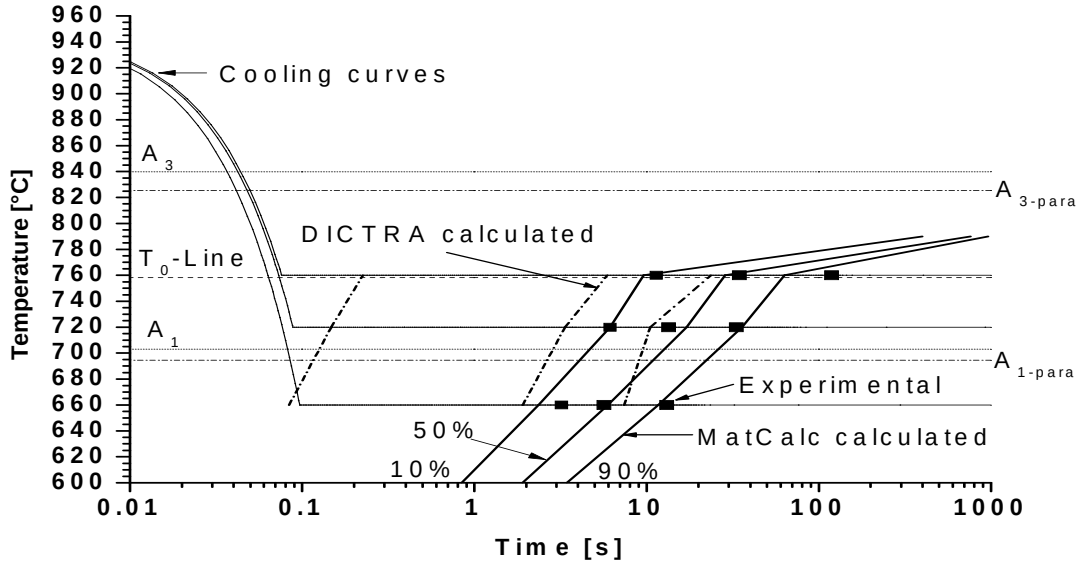

(a)

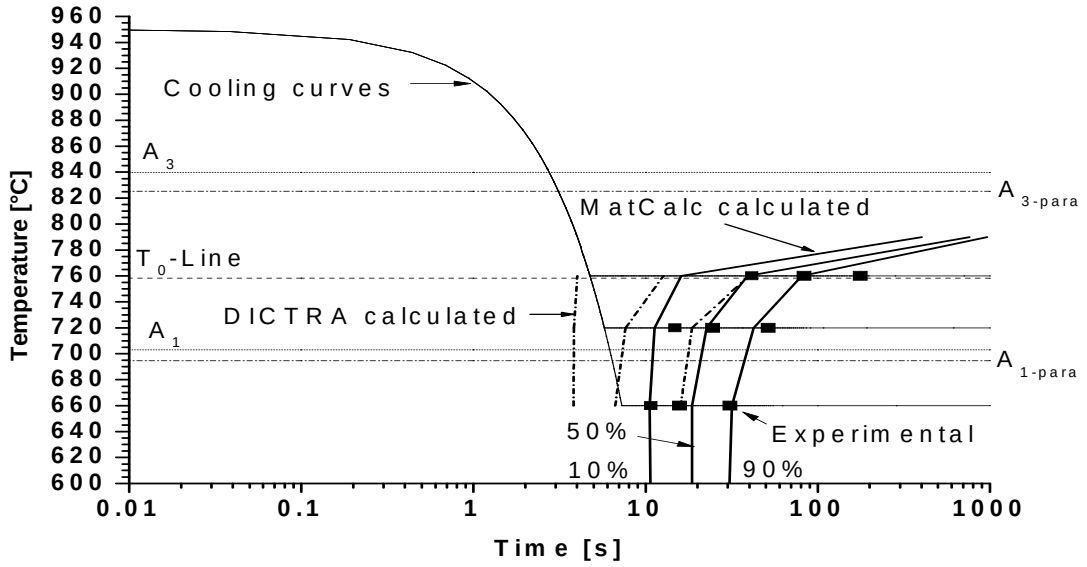

(b)

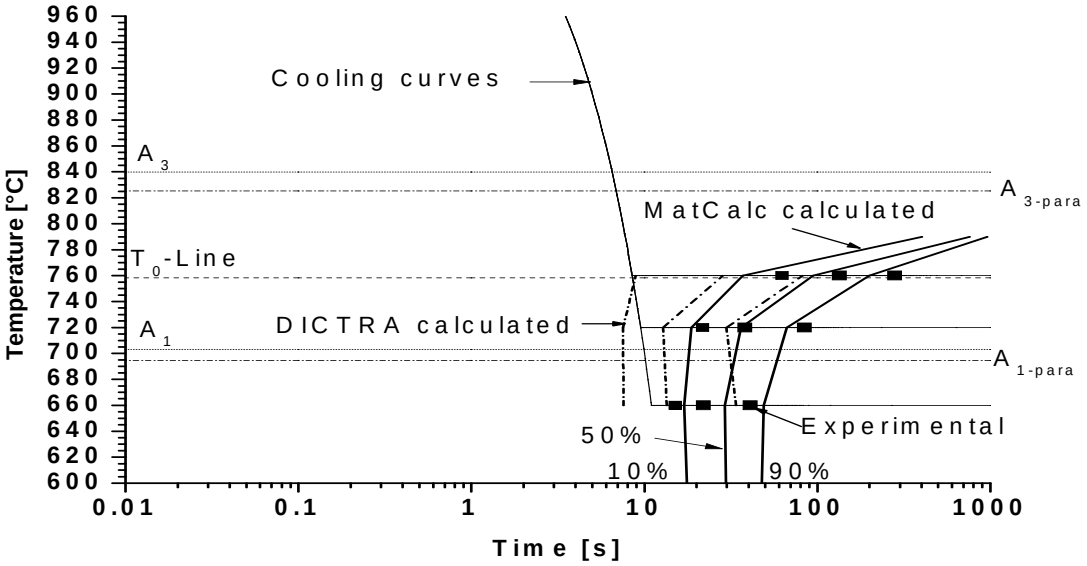

(c)

Figure 6.23: Comparison of measured I-TTT diagrams (points) and calculated I-TTP diagram (curves) for alloy D for (a) hollow samples with T_{aus} of 950°C, (b) solid samples with T_{aus} of 950°C and (c) solid samples with T_{aus} of 1100°C.

Figure 6.24: Microstructure of alloy D obtained at a target IT temperature of 760°C, showing mainly ferrite with pearlite islands.

Table 6.13: Variation of grain sizes with target IT temperatures for various samples

Alloy	Target IT Temperature[°C]	Measured grain size (µm)		
		Hollow samples with T_{aus}=950°C	Solid samples with T_{aus}=950°C	Solid samples with T_{aus}=1100°C
D	760	22	25	38
	720	16	16	20
	660	10	14	16

The comparison of the calculated and corrected interfacial energies at the experimental target IT-temperatures are shown in figure 6.28.
In all cases, the transformation has started after reaching the target IT temperature so they can be straight away used for calculation for driving forces available for transformation at the particular target IT temperatures. The driving force profiles calculated for orthoequilibrium, paraequilibrium and massive conditions are shown in figure 6.29 and are summarized in table 6.14.
At 760°C, the driving force for massive nucleation was negative which is clearly indicating that massive nucleation is not possible at all at this target IT temperature. The excellent agreement between experimentally measured I-TTT and MatCalc calculated I-TTP diagrams at target IT temperatures of 720 and 660°C are clearly suggesting that solute segregation has not allowed the new phase to nucleate at the equilibrium austenite-ferrite phase boundary.

6.4.1 Austenite decomposition and evolution of ferrite microstructure in alloy D

In this section, the decomposition of austenite and evolution of ferrite microstructure is described as the sample is cooled from an austenitization temperature of 950°C to the target IT temperature of 760°C. The evolution of the ferrite microstructure is shown schematically with the help of MatCalc simulations in figure 6.30. The calculated equilibrium and massive austenite-ferrite phase boundaries are summarized in table 6.15.
Figure 6.30a shows a sample which is cooled from an austenitization temperature of 950°C. According to DICTRA [13], when the cooling curve hits the equilibrium austenite-ferrite phase boundary i.e. 839.7°C, ferrite should be thermodynamically stable. However, figure 6.30b is showing that the driving force at this temperature is negative and the nucleation of ferrite is not possible. At 825.4°C, the driving force is positive only under paraequilibrium nucleation conditions (table 6.15).

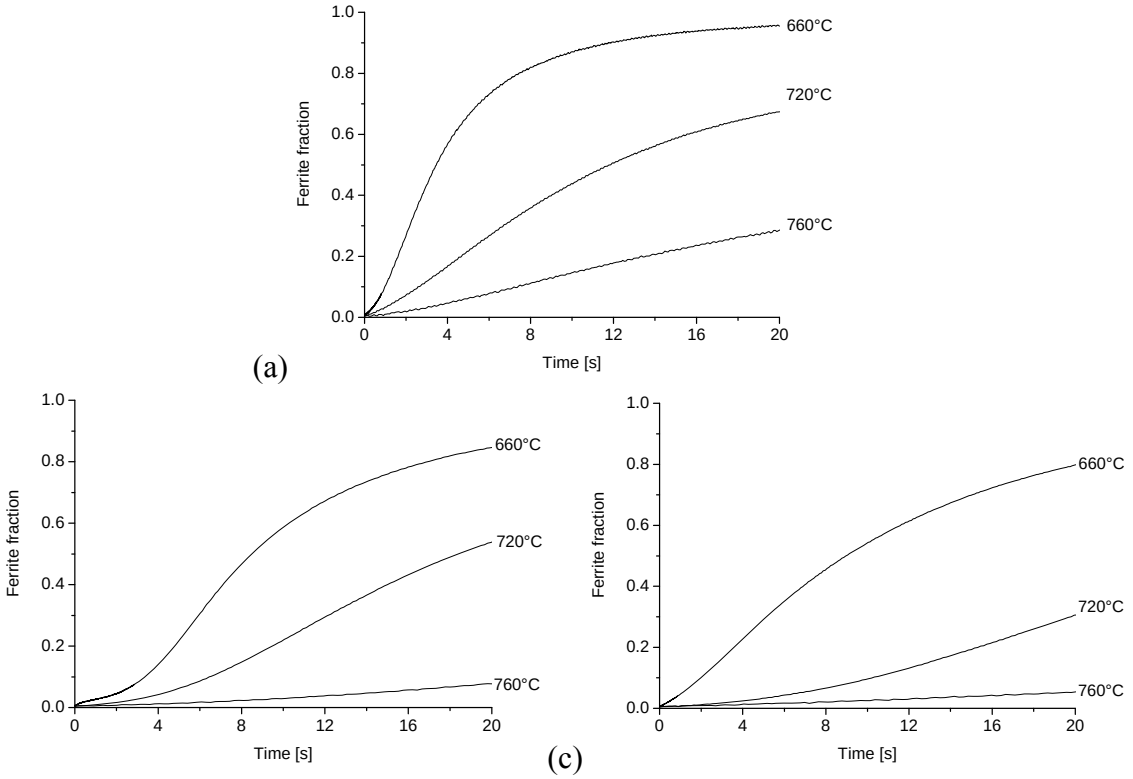

Figure 6.25: Ferrite fraction evolution profiles of alloy D for (a) hollow samples with T_{aus} of 950°C, (b) solid samples with T_{aus} of 950°C and (c) solid samples with T_{aus} of 1100°C.

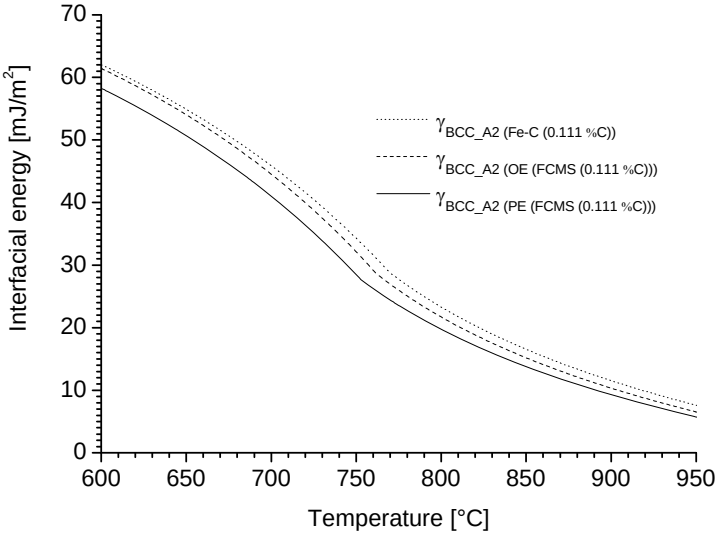

Figure 6.26 Comparison of interfacial energy ($\gamma_{0\text{-}BCC\_A2}$) of ferrite calculated for Fe-C and Fe-C-Mn-Si (orthoequilibrium (OE) and paraequilibrium (PE) conditions) for alloy D having 0.111%C.

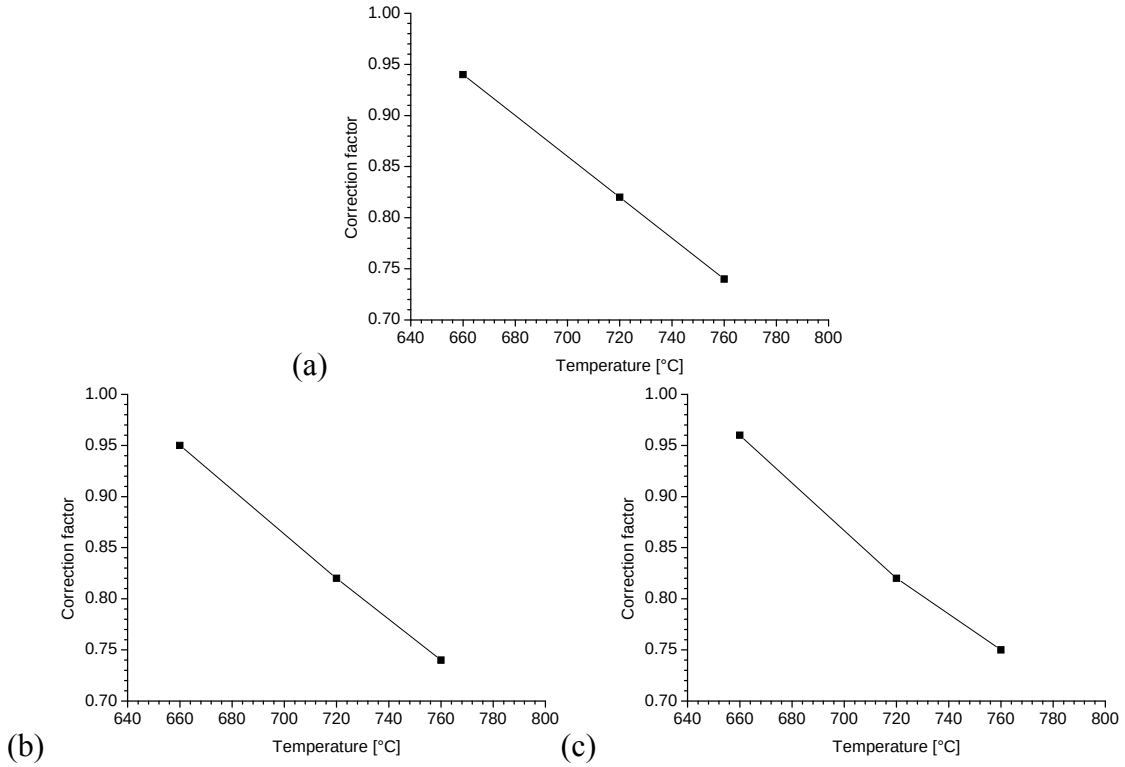

Figure 6.27: Optimized correction factor for interfacial energy as a function of target IT temperatures for (a) hollow samples of alloy D with T_{aus} = 950°C, (b) solid samples of alloy D with T_{aus} = 950°C and (c) solid samples of alloy D with T_{aus} = 1100°C.

Kozeschnik and Gamsjäger [1] has shown that in case of solute free boundaries the transformation can start close to the equilibrium or massive phase boundaries. In case of solute segregated boundaries, results of Militzer [8] have shown that the austenite to ferrite nucleation is suppressed to almost 40K below. In the present case, alloy D contains higher solute elements in comparison to alloys used in the study of [1] and [8]. Under such circumstances the austenite to ferrite nucleation has not started until the target IT temperature of 760°C is reached. In this case nucleation is suppressed to almost 65k. At this target IT temperature massive ferrite is not possible because the driving force for massive nucleation is negative.

Now as the cooling curve reaches the target IT temperature i.e. at 4.75s, the driving force approaches to 118J/mol (figure 6.30a and 6.30b). The nucleation rate and the number of ferrite precipitates rises due to availability of such a high driving force (figure 6.30c and 6.30d). Still, mean radius and ferrite fraction are in the emerging stage (figure 6.30e and 6.30f). When all the nucleation sites are occupied, the nucleation rate starts to decrease. The nucleation stage completes at approximately 26s and ferrite precipitate profile has reached a steady state value of $6.3e^{13}$ m^{-3} (figure 6.30c and 6.30d).

The next stage, from approximately 26 to 180s, is the diffusion-controlled growth of these nuclei, this continues until the equilibrium phase fraction of ferrite reaches its equilibrium value, as indicated by the plateau on the 'Phase fraction' curve. During this stage, the number of ferrite precipitates does not increase but there is an increase in radius which can just be detected on the figure 6.30e. There follows a period in which there is little or no change in any of the ferrite fraction, ferrite mean radius, number of ferrite precipitates and the driving force values.

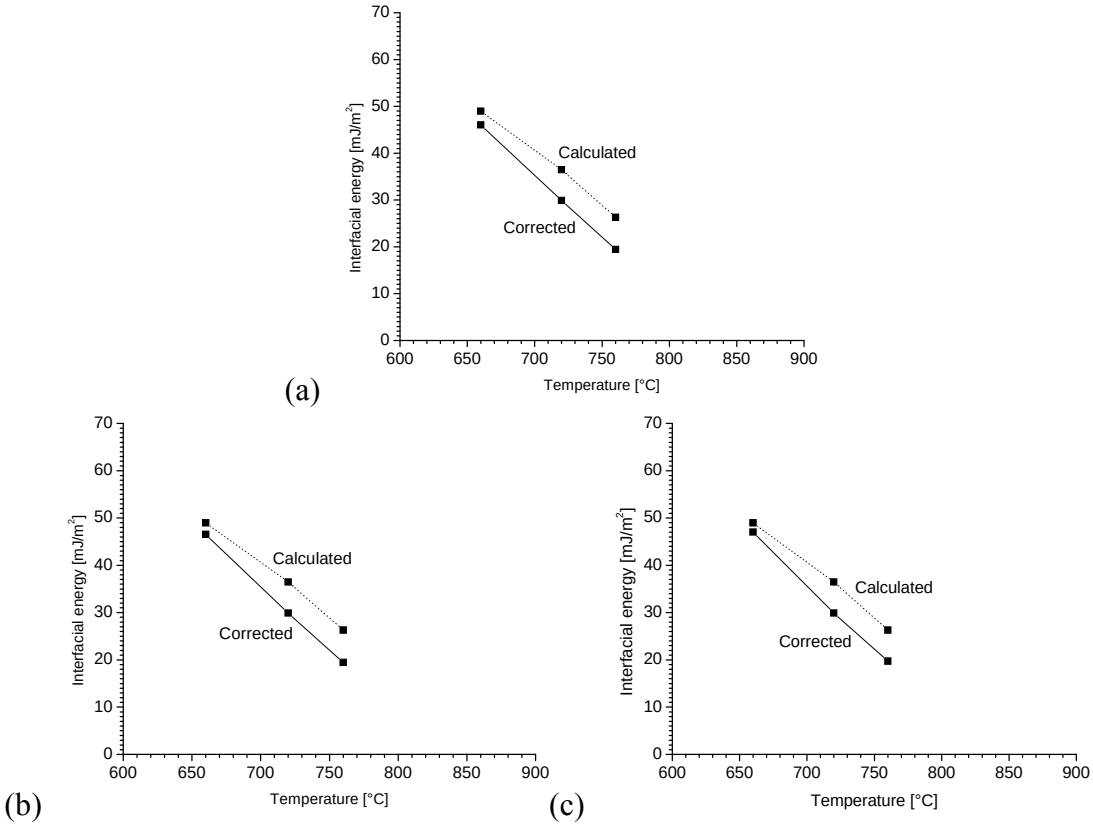

Figure 6.28: Comparison of calculated and corrected values of interfacial energy at target IT temperatures for (a) hollow samples of alloy D with T_{aus} = 950°C, (b) solid samples of alloy D with T_{aus} = 950°C and (c) solid samples of alloy D with T_{aus} = 1100°C.

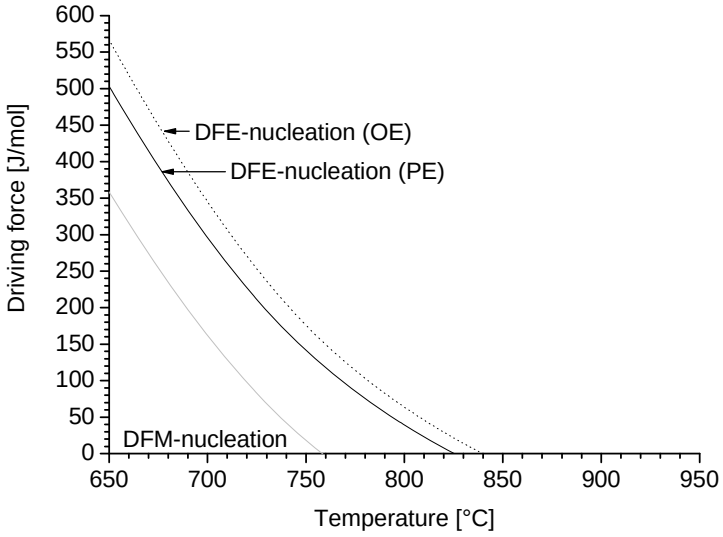

Figure 6.29: Chemical driving force for nucleation in alloy D, calculated in orthoequilibrium (OE), paraequilibrium (PE) ans massive nucleation conditions. (The abbreviation DFE and DFM stands for driving force for equilibrium and driving force for massive respectively).

Table 6.14: Calculated driving forces for nucleation of alloy D

Alloy	Target IT [°C]	Driving force for nucleation of ferrite [J/mol]		
		Equilibrium ferrite		Massive ferrite
		OE	PE	
D	760	149	118.2	-4
	720	270.6	227.3	97.2
	660	518.6	458.2	315.3

Table 6.15: Calculated equilibrium austenite-ferrite phase boundary for alloy D

Alloy	Austenite-ferrite phase boundary [°C]		
	Calculated for equilibrium ferrite		Calculated for massive ferrite
	OE	PE	
D	839.7	825.4	758.3

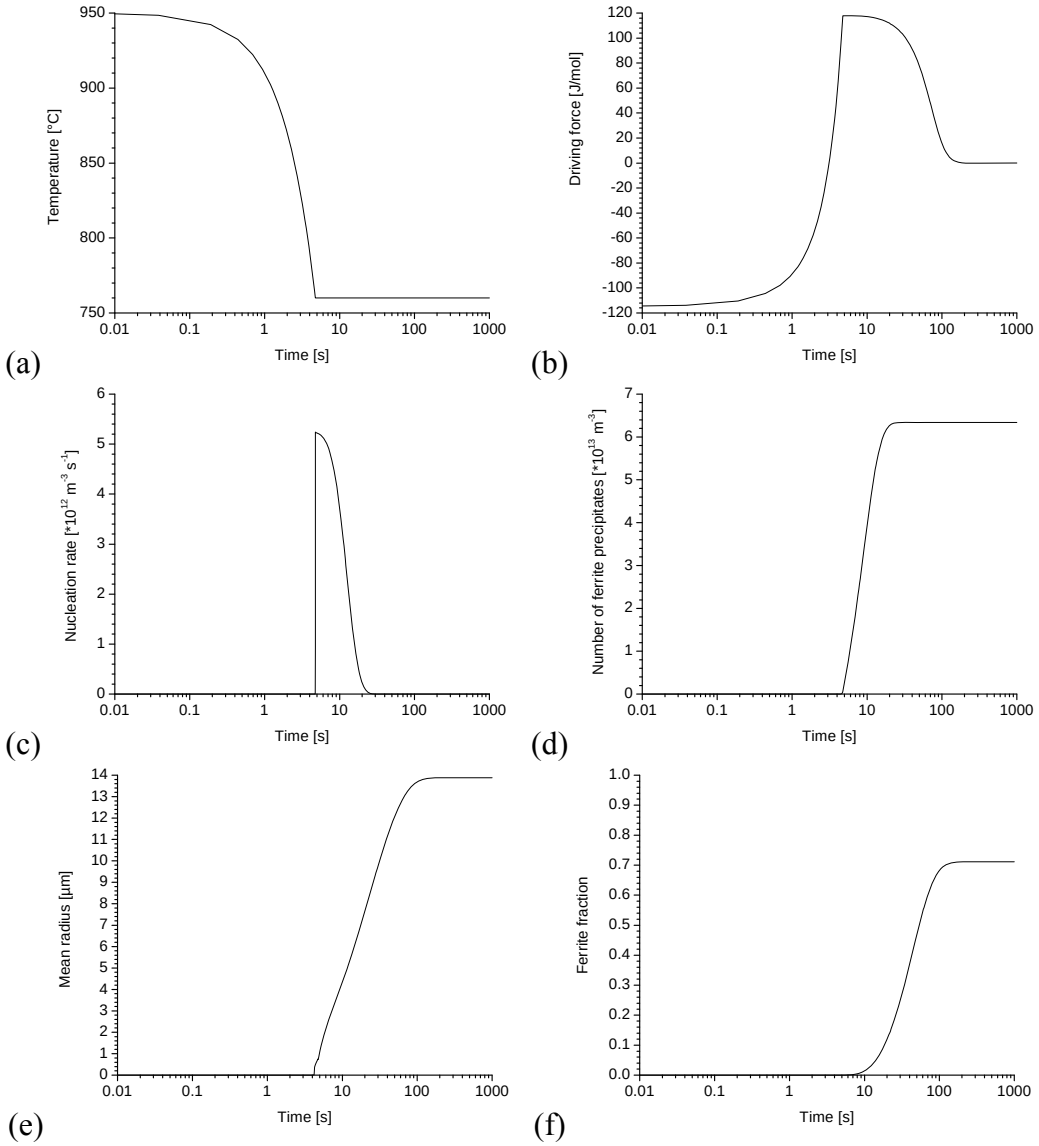

Figure 6.30: Cooling curve (a), driving force (b), nucleation rate (c), ferrite precipitates (d), mean radius (e) and ferrite fraction (f) evolution profiles during austenite decomposition as the sample is cooled from austenitization temperature of 950°C to the target IT temperature of 760°C.

CHAPTER 7: SUMMARY AND CONCLUSIONS

The isothermal austenite to ferrite transformation has been studied in ultra-low (alloy A) to low carbon (alloy B, C & D) steels. For experimental investigation, a high-speed quenching dilatometer was used to gather the information concerning austenite decomposition and ferrite evolution. The dilatation profiles were used to generate the experimental I-TTT (isothermal time-temperature-transformation) diagram. At the same time these dilatation profiles were also used in connection with simulated dilatation versus temperature plots to find out the onset of the austenite to ferrite transformation temperatures.
In order to understand the transformation mechanism, experimental investigations are supplemented with theoretical calculations. In this regard, the MatCalc and DICTRA simulation software packages were used. These calculations are calibrated with chemical compositions, thermal cycles and grain sizes (as obtained from the thermal cycles) as input parameters to synchronize them with the experimental results. These settings were used to generate the theoretical I-TTP (isothermal time-temperature-precipitation) diagrams both with MatCalc and DICTRA. In order to decide whether the kinetics of the reaction is controlled by diffusion, massive or two-stage transformation mechanism, the experimentally measured I-TTT and theoretically measured I-TTP diagrams were compared. Those target-IT temperatures where agreement exists between 10 to 90% measured and calculated transformation times, the diffusion controlled transformation mechanism was assumed to be operative, since these software packages are calculating the kinetics of the reaction on the basis of diffusion–controlled reactions. In this way we were able to separate the diffusive and massive / two-stage mechanisms controlling the reaction kinetics. In order to differentiate between massive and two-stage transformation mechanism, the extent of agreement is facilitated with ferrite evolution profiles and observations (from comparison of experimental thermal and dilatation profiles) as to whether the transformation has started before or after reaching the target IT temperatures.
The main conclusions obtained from the experimental and theoretical analysis of austenite decomposition in ultra-low to low carbon steel are:

1. With maximum cooling rates, two regimes in alloy A (ultra-low carbon) are evident. In the two phase austenite and ferrite region, the two-stage transformation mechanism is controlling the kinetics, while in the single phase ferrite region, samples are showing complete interface-controlled kinetics in response to cooling rates upto 3400K/s. With decreased cooling rate (to 40K/s), the diffusion-controlled regime extends from 890 to 870°C, while complete interface-controlled transformation is restricted to only 780°C. The intermediate target IT temperatures (850 and 860°C) have changed their behavior from complete interface-controlled transformation to two-stage transformation kinetics. Increased austenitization temperature does not play a significant role in terms of changing the transformation mechanism in alloy A.

2. With maximum cooling rates, three regimes were evident in alloy B. Relatively higher target IT temperatures (840 and 860°C) are showing only diffusion-controlled austenite to ferrite transformation kinetics. At an intermediate target IT temperature (800°C), a two-stage mechanism prevails, while at lower target IT temperatures (700 and 760°C), the transformation is completely interface-controlled. With a decreased cooling rate (to 40K/s), the diffusion regime is restricted to only 840°C. The two-stage regime is shifted from 800 to 760°C, while 700°C is showing complete interface-control. With increasing austenitization temperature, changes in mechanism regimes are observed. The diffusion regime is increased from 800 to 840°C, while, for the two-

stage regime, the increase is from 760 to 700°C. No target IT temperature is showing the complete interface controlled massive transformation mechanism.

3. With maximum cooling rates, three regimes are also evident in alloy C. Top two target IT temperatures (830 and 850°C) are showing only diffusion controlled austenite to ferrite transformation kinetics. At an intermediate target IT temperature (790°C), the two-stage mechanism prevails, while lower target IT temperatures (690 and 750°C) are showing complete interface-controlled massive transformation mechanism. With a decreased cooling rate (to 40K/s), the diffusion regime is increased from 850 to 790°C. The two-stage regime is restricted to 760°C, while 700°C is showing complete interface-controlled massive transformation. With increasing austenitization temperature, changes in mechanism regimes are also observed. The diffusion regime is increased from 850 to 750°C, while the two-stage regime is shifted from 750 to 690°C. No target IT temperature is showing complete interface-controlled massive transformation.

4. Alloy D is showing only diffusion-controlled transformation kinetics irrespective of whatever the cooling rate or type of sample is.

5. DICTRA calculated I-TTP diagrams are missing the agreement with the measured I-TTT diagram by roughly a factor of 2 where the kinetics of the austenite to ferrite transformation is controlled by a diffusive mechanism due to the lacking nucleation model.

6. MatCalc calculated I-TTP diagrams are calibrated with correction factors in the interfacial energies to yield correct ferrite grain sizes.

7. Interfacial energy profiles are showing that interfacial energy increases with decreasing temperature. This trend is amplified by the correction factors.

8. In the case of massive transformations, the kinetics of the reaction is extremely fast and transformation has completed in very small time. For alloy A, this time is clearly below 1s.

9. The change in chemical composition through partitioning requires time so the diffusion controlled transformation is showing significantly slower kinetics than the massive reaction.

10. At IT temperatures, where the austenite to ferrite transformation kinetics is controlled by the diffusion mechanism, nucleation occurred at grain boundaries, with grain corners being the most probable nucleation sites. The growth in such cases can be described with spherical geometry.

11. Austenitization at higher temperature leads to increased grain size, which shifts the I-TTP to longer transformation times.

CHAPTER 8: REFERENCES

[1] E. Kozeschnik, E. Gamsjäger: Metall. Mater. Trans., 37A (2006) 1791-1797.
[2] E. Kozeschnik: Modeling Interface Kinetics Applications, MCL-Summer school, July 5-7, 2001.
[3] H.K.D.H. Bhadeshia: Progr. Mater. Sci., 29 (1985) 321-386.
[4] J.W. Christian: Phase transformations, Vol. 1, Institute of Metallurgists, 1979.
[5] T. B. Massalski: Phase Transformations, ASM, Metals Park, Ohio, 1970, p. 433.
[6] D. A. Porter, K. E. Easterling: Phase transformations in Metals and Alloys, VNR International 1981.
[7] M.J. Bibby, J.G. Parr: J. Iron Steel Inst., (1964) 100-104.
[8] M. Militzer: Proc. Int. Conf. *Solid-Solid Phase Transformations '99*, Eds. M. Koiwa, K.Otsuka and T. Miyazaki, The Japan Inst. Metals, (1999), pp. 1521-1524.
[9] Y. C. Liu, F. Sommer , E. J. Mittemeijer: Acta Mater, 54(2006) 3383-3393.
[10] Y. Liu, D. Wang, F. Sommer, E. J. Mittemeijer: Acta Mater, 56 (2008) 3833-3842.
[11] J. Svoboda, F.D. Fischer, P. Fratzl, E. Kozeschnik : Mater. Sci. Eng., A385 (2004) 166-174.
[12] E. Kozeschnik, J. Svoboda, P. Fratzl, F.D. Fischer : Mater. Sci. Eng., A385 (2004) 157-165.
[13] J-O Andersson, T. Helander, L. Höglund, P. Shi, B. Sundman: Calphad, 26 (2002) 273-312.
[14] A. Van der Ven, L. Delaey: Progr. Mater. Sci., 40 (1996) 181-264.
[15] H.K.D.H. Bhadeshia: http://www.msm.cam.ac.uk/phase-trans/2004/MP6.movies.html.
[16] H.K.D.H. Bhadeshia: http://www.msm.cam.ac.uk/phase-trans/2004/C9.movies.html.
[17] H.K.D.H. Bhadeshia, S. R. Honeycombe: Steels; Microstructures and Properties, Elsevier Ltd., 3 ed., 2006.
[18] S. H. Avner: Introduction to Physical Metallurgy, McGraw-Hill Book Company, 2 ed., 1974.
[19] W. D. Callister: Fundamentals of materials science and Engineering, John Wiley & Sons, Inc., 5 ed., 2001.
[20] H.K.D.H. Bhadeshia: Bainite in Steels (Transformations, Microstructure and Properties), IOM Communications Ltd., 2 ed., 2001.
[21] H.K.D.H. Bhadeshia: http://www.msm.cam.ac.uk/phase-trans/2000/C9/lectures.html.
[22] D. R. Askeland, P. P. Fulay: Essentials of Materials Science and Engineering, Cengage Learning, 2 ed., 2010.
[23] http://en.wikipedia.org/wiki/Sound.
[24] H.K.D.H. Bhadeshia: http://www.msm.cam.ac.uk/phase-trans/2002/martensite.html.
[25] Z. Barber: Introduction to Materials Modelling, Maney Publishing, 2005.
[26] D. E. Coates: Met. Trans., 4 (1973) 2313-2325.
[27] A. Ali: PhD Thesis, University of Cambridge, 1991.
[28] E. Kozeschnik, J. M. Vitek: Calphad, 24 (2000) 495-502.
[29] G. Beranger, G. Henry, G. Sanz: The book of Steel, Intercept Ltd., 1996.
[30] K. G. F. Janssens, D. Raabe, E. kozeschnik, M. A. Miodownik, B. Nestler: Computational Materials Engineering; An Introduction to Microstructure Evolution, Elsevier Academic press, 2007.
[31] J. Rajek: PhD thesis, Graz University of Technology, 2005.
[32] R. Kampmann, R. Wagner: Acta Scripta Metall., 1984, 91-103.
[33] E. Kozeschnik, J. Svoboda, F. D. Fischer: Calphad, 28 (2004) 379-382.
[34] A. Borgenstam, E. Engström, L. Högland, J. Agren: Journal of Phase Equilibria, 21 (2000) 260-280.

[35] High-Speed Quenching Dilatometer (805A) Manual, BÄHR Thermoanalyse GMBH.
[36] AxioVision, Release 4.7, Carl Zeiss MicroImaging GmbH, 07740 Jena, Germany.
[37] CES EduPack 2009 software, Granta Design Limited, Cambridge, UK, 2009.
[38] M. Mehta: ASTM Specificatins A 1033-04, 2004.
[39] Rasband, W.S., ImageJ, U. S. National Institutes of Health, Bethesda, Maryland, USA, http://rsb.info.nih.gov/ij/, 1997-2009.
[40] Exceed software package: version 11.0.0.0, Copyright © 1991-2005 Hummingbird Ltd.
[41] P.J. Clemm, J.C. Fisher: Acta Metall., 3 (1955) 70-73.
[42] W. D. Swanson, J. G. Parr: JISI, 202 (1964) 104-105.

APPENDIX

APPENDIX-1: Chemical composition of alloys A, B, C and D

Table A1: Chemical composition of alloys A, B, C and D

Steel	Alloy	C [wt%]	Si [wt%]	Mn [wt%]	P [wt%]	S [wt%]	Cr [wt%]	Ni [wt%]	Cu [wt%]	Al [wt%]	Ti [wt%]	Mo [wt%]
ULC	A	0.004	0.006	0.06	0.004	0.004	0.025	0.02	0.01	0.002		
LC	B	0.029	0.009	0.326	0.008	0.0065	0.013	0.01	0.008	0.0388	0.005	0.004
	C	0.047	0.055	0.374	0.014	0.0123	0.035	0.023	0.023	0.0423	0.0014	0.007
	D	0.111	0.167	0.932	0.013	0.006	0.074	0.034	0.035	0.0530	0.0369	0.012

Table A1-continued

Steel	Alloy	V [wt%]	Sn [wt%]	Nb [wt%]	B [wt%]	N_2 [wt%]	As [wt%]	Pb [wt%]	Co [wt%]	Zr [wt%]	Sb [wt%]	Ca [wt%]
ULC	A		0.001			0.0032						
LC	B	0.001	0.0007			0.0039	0.0005	0.001	0.0017		0.003	0.0002
	C	0.001	0.004		0.0001	0.0045	0.003	0.001	0.0023		0.0039	0.0020
	D	0.003	0.0030	0.0019	0.0035	0.0065	0.004	0.001	0.0036		0.0050	0.0031

APPENDIX-2: Definitions of the terminologies used in table 4.2

MD-Piano 220: Struers advances the TECHNOLOGY of grinding and polishing with the introduction of the MD-System. The MD (Magnetic Disc) System is simply a better way to grind and polish specimens. This exciting new technology allows for fewer steps, reduced preparation time and costs, produces better quality specimens and makes the job easier [A1]. It reduces grinding processes to just two steps and cut the total preparation time. They are a direct replacement for SiC paper plus they are more economical and produce superior specimens. Just like SiC paper, MD-System grinding discs use water for cooling. The MD-Disc (platen) is the only magnetic supporting disc needed to support all MD-System grinding and polishing consumables [A2]. MD-Piano 220 should be used for single smaller specimens (<30 mm diameter) of all kinds of materials as well as larger specimens of softer materials (>400 HV) and composite materials with harder particles in soft matrix. MD-Piano 80, 120 and 220 can, thanks to their resin bonded diamonds, replace up to 100 pieces of SiC-Paper [A3].

MD-Largo: MD-Allegro and MD-Largo are composite discs for one step fine grinding. Both discs can be used with diamond suspension or spray. MD-Largo is designed for soft materials in the range HV 40-250, or for composites with a soft matrix. MD-Largo and MD-Allegro combine fine grinding in one step with typically 15-6μm DP-Suspension or DP-Spray instead of the normal steps like SiC-Paper 500, 1000 and 4000#. MD-Largo can also be used instead of fine grinding cloths. For very fragile materials or high requirements on planeness, MD-Largo can also be used with DiaPro-Largo that is equivalent to a 3 μm diamond suspension. Experience from the field has shown that MD-Largo has a lifetime equivalent to about 900-1000 pieces of SiC-Paper [A3].

MD-DUR: These cloths are based on thin textiles, which give a very stiff support and therefore a very high degree of plainness. The weave gives the highest degree of contact between textile and specimen resulting in very high removal rates. The cloths are used for intermediate polishing steps. The Dur textile is 100% pure silk [A4].

MD/DP-Mol: The Mol textile is 100% woven wool. The long fibres in the thin woven textile makes it well suited for polishing with 3 μm and finer diamonds when a less aggressive polish is required. The specially developed treatment of the wool fibers gives this textile a very long lifetime [A4].

MD/OP-Chem: The Chem cloth is neoprene foam with open cells that act as small wells carrying large amounts of fluid. As the specimen travels over these wells they become compressed, this generates a pumping action that ensures a high degree of contact between the attacking fluid and the specimen. The medium hard, spongy structure of the Chem cloth has a high degree of chemical resistance. It is ideal for oxide polishing with chemically aggressive oxide media like alkaline colloidal silica and acidic alumina suspensions [A4].
Table 4.3 is presenting the MD-Polishing Cloth Selection Guide.

DP-P (9, 6, 3 and 1 μm) Suspensions: Here DP stands for diamond product. This high performance diamond product contains exclusively polycrystalline diamonds. These are stable suspension, designed for automatic dosing equipment. It is water-based (see e.g. [A7]).

OP-S Suspension: It is used for final polishing [A8].

DP-Blue Lubricant: Alcohol-based; for fine grinding and diamond polishing of most materials. It contains ethanediol [A7].

DP-Red Lubricant: Water and oil-based; final polishing of softer materials [A7].

Table 2A.1: MD-Polisihing cloth selection guide ([A5], [A6])

Cloth	Characteristic	Recommendations	Abrasive range	Resilience	Hardness
MD-Dac	Satin woven acetate	Polishing of all materials	9 - 3 µm	Medium	Hard
MD-Dur	Satin woven natural silk	Fine grinding and polishing of ferrous metals, non ferrous metals, coatings and plastics	9 - 1 µm	Medium	Hard
MD-Mol	Taffeta woven 100 % wool	Polishing of ferrous and non ferrous metals and polymers	≤ 3 µm	High	Soft
MD-Chem	Porous neoprene	Final polishing of all materials	< 1 µm	High	Soft

References used in Appendix-2

[A1] http://www.struers.com/default.asp?top_id=3&main_id=10&sub_id=138&doc_id=201.
[A2] http://www.struers.com/default.asp?top_id=3&main_id=14&doc_id=213.
[A3] http://www.vividtechnologies.net/pdf/struers/grinding_polishing/md_system.pdf.
[A4] http://www.struers.com/resources/elements/12/89399/Polishing%20Cloths%20 brochure%20English.pdf.
[A5] http://www.struers.com/resources/elements/12/114285/62145010_Consumables %20Cat_2010.pdf.
[A6] http://www.struers.com/resources/elements/12/114221/MD_SystemBrochureEnglish .pdf.
[A7] http://www.vividtechnologies.net/pdf/struers/grinding_polishing/diamond_products.pdf.
[A8] http://www.struers.com/default.asp?doc_id=352.

APPENDIX-3: Complete thermal and their corresponding dilatation profiles for alloys B, C and D

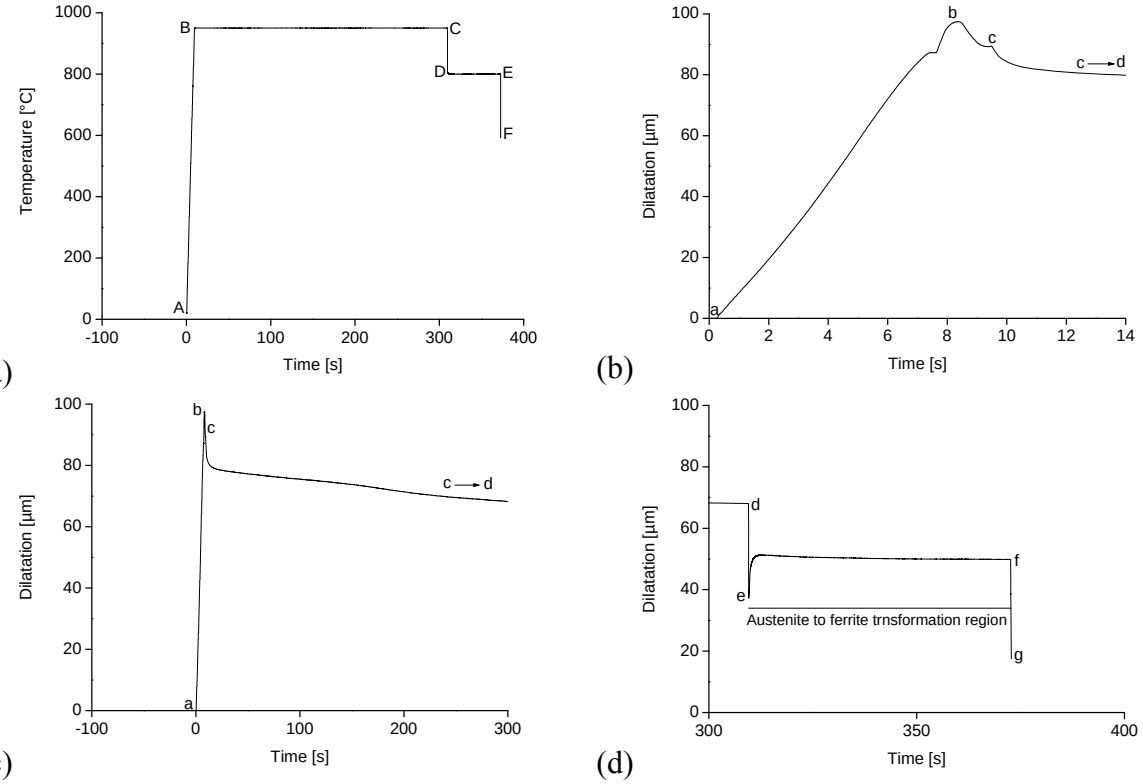

Complete thermal and its corresponding dilatation profile for hollow sample of alloy B.

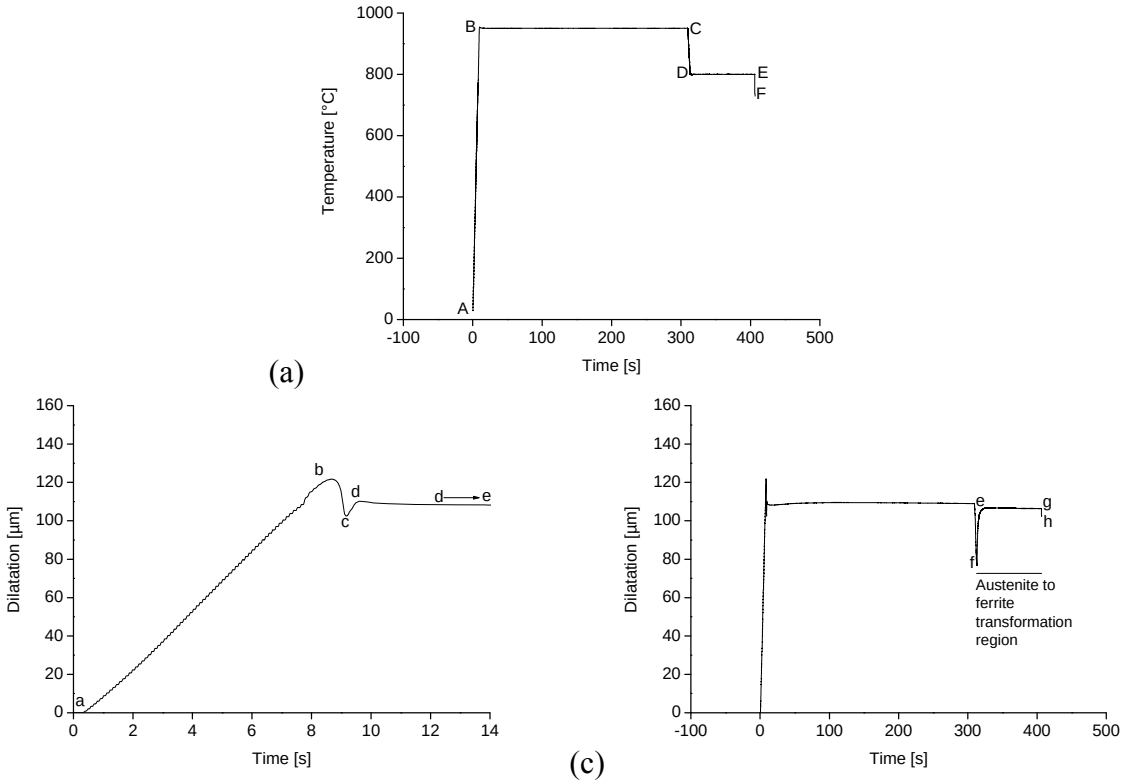

Complete thermal and its corresponding dilatation profile for solid sample of alloy B with T_{aus} = 950°C.

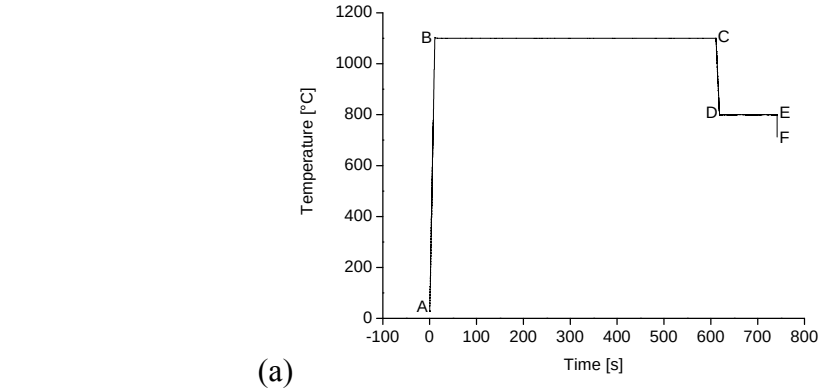

(a)

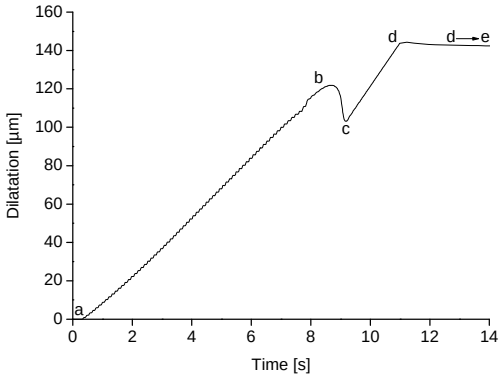

(b)

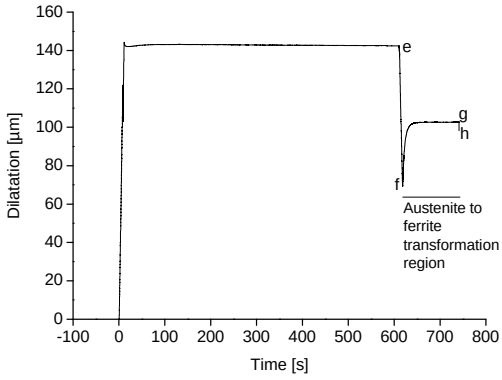

(c)

Complete thermal and its corresponding dilatation profile for solid samples of alloy B with T_{aus} = 1100°C.

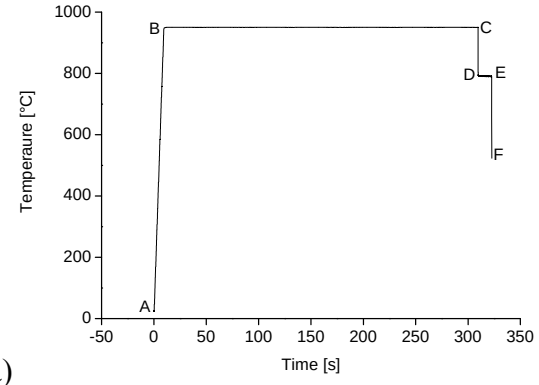

(a)

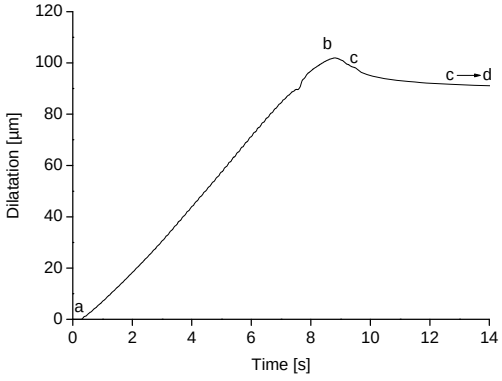

(b)

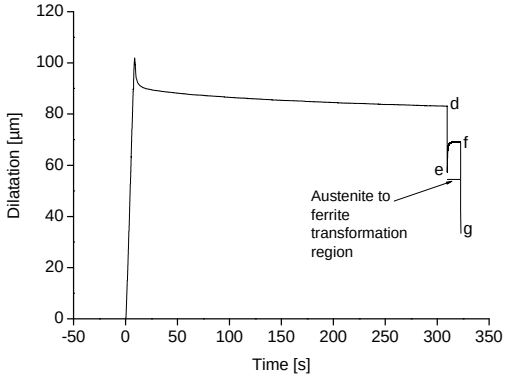

(c)

Complete thermal and its corresponding dilatation profile for hollow sample of alloy C.

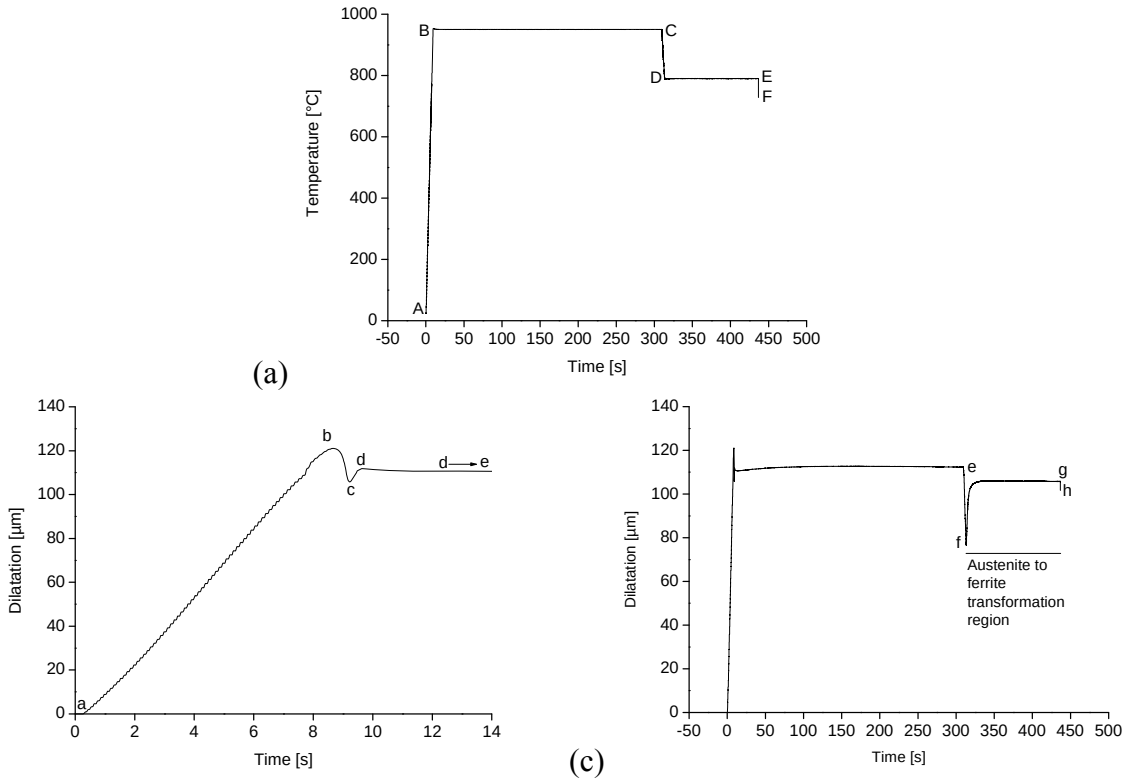

Complete thermal and its corresponding dilatation profile for solid sample of alloy C with T_{aus} = 950°C.

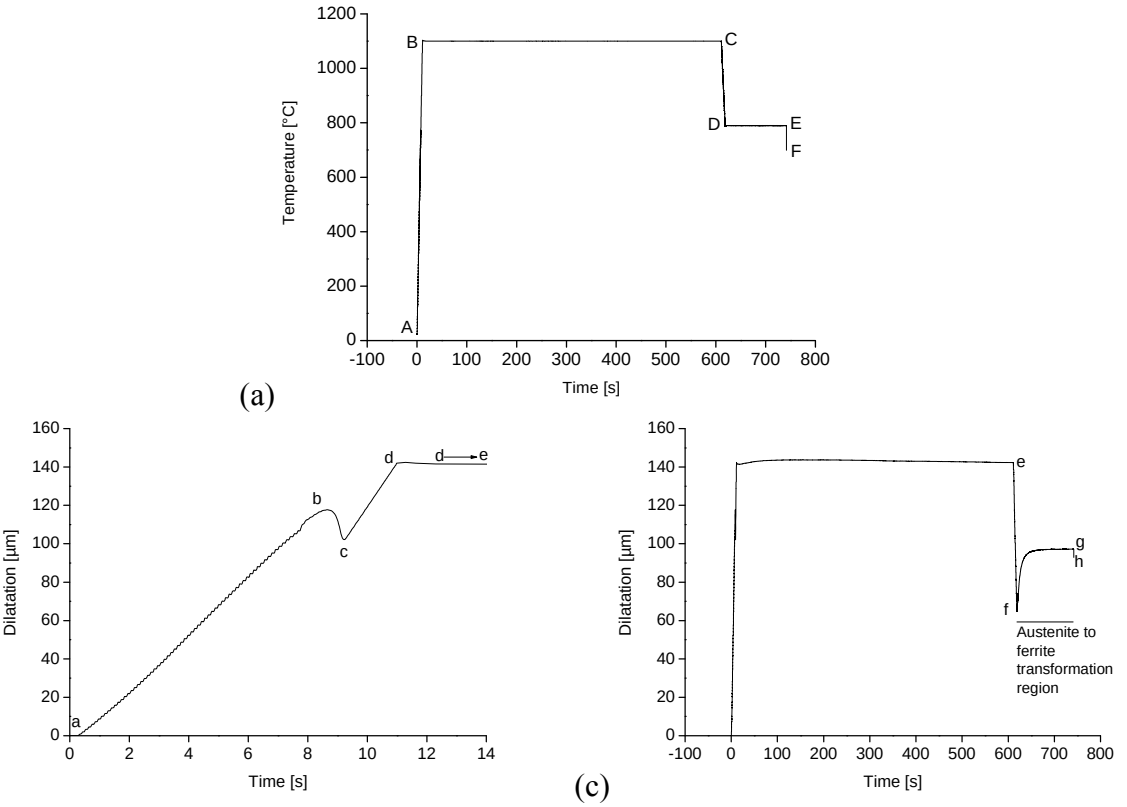

Complete thermal and its corresponding dilatation profile for solid sample of alloy C with T_{aus} = 1100°C.

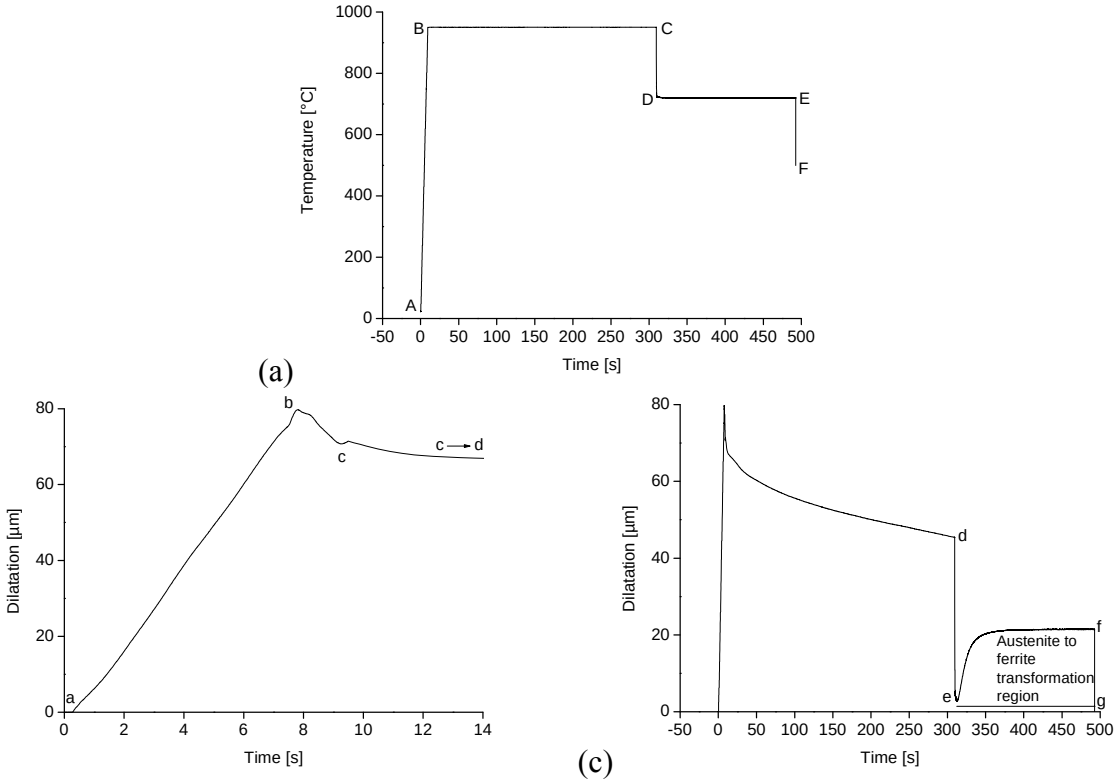

Complete thermal and its corresponding dilatation profile for hollow sample of alloy D.

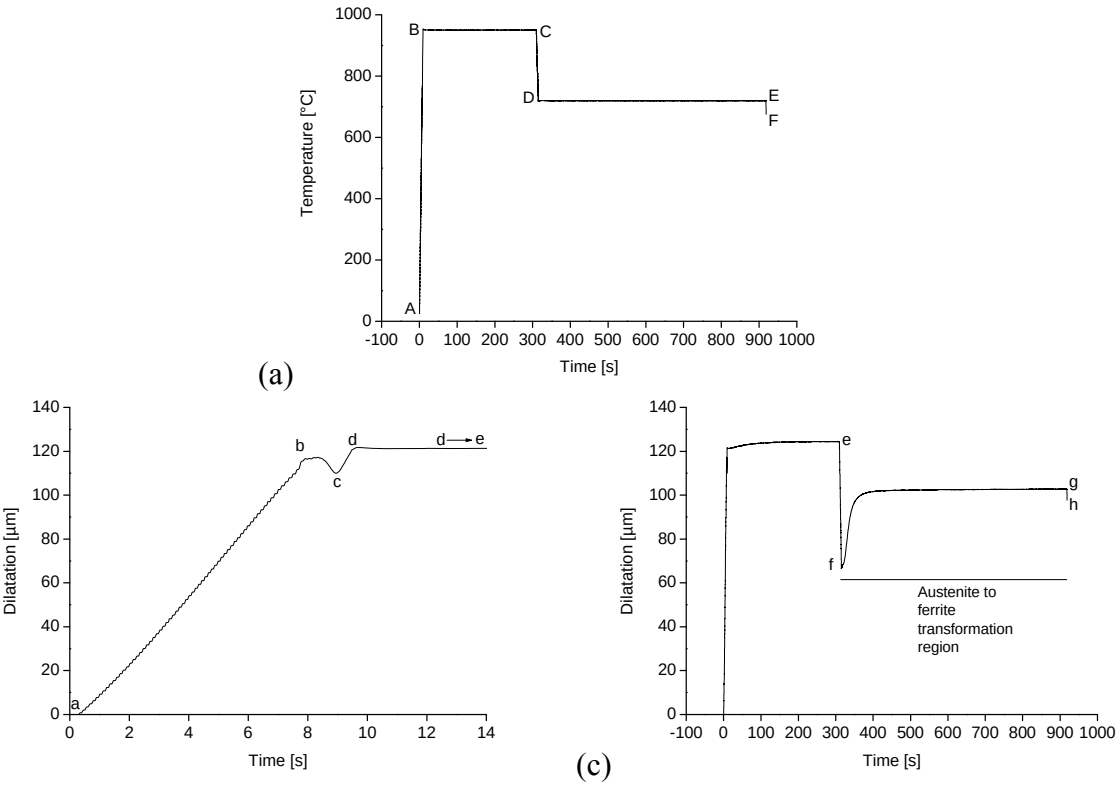

Complete thermal and its corresponding dilatation profile for solid sample of alloy D with T_{aus} = 950°C.

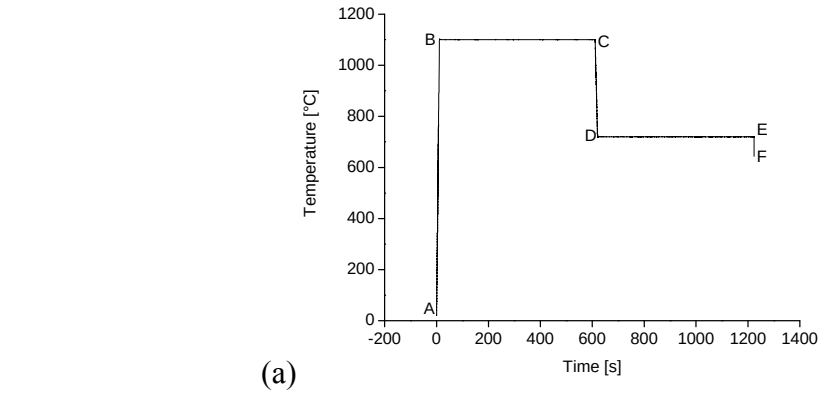

(a)

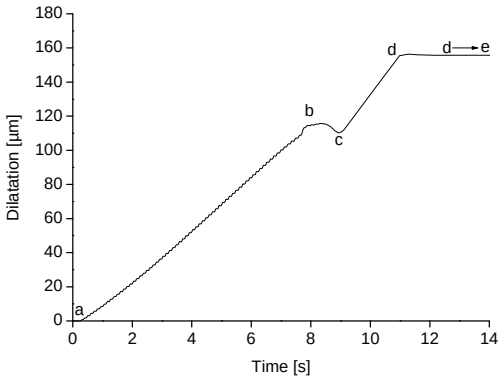

(b)

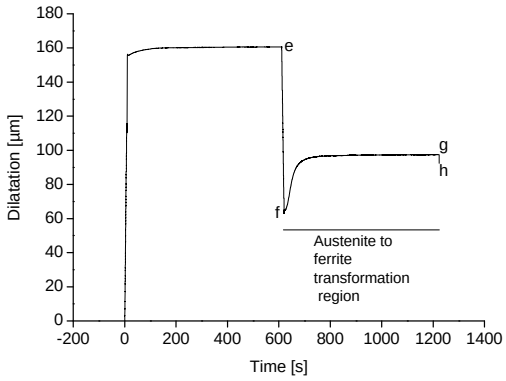

(c)

Complete thermal and its corresponding dilatation profile for solid sample of alloy D with T_{aus} = 1100°C.

APPENDIX-4: Procedure for heating the samples in protecting atmosphere instead of vacuum

BÄHR-Thermoanalyse GmbH

BÄHR-Knowledge Base: DIL805: Heat a sample in protecting atmosphere instead of vacuum
19.12.2006

1. Objective:

Heat a sample in protecting atmosphere instead of vacuum with a DIL805 to avoid evaporation.

To do this the desired atmosphere has to be produced manually **before** starting the data recording.
This atmosphere will be kept in the corresponding segments during the data recording.
Therefore in the corresponding segments **no gas and no vacuum** should be programmed in the temperature program.

2. Modus operandi:

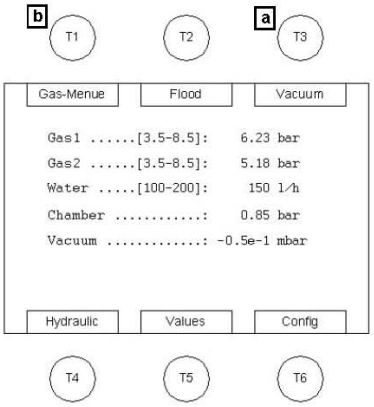

2.1.

a) Before starting the data recording press the button T3 ***Vacuum*** at the control panel.
The vacuum will be switched on.

Please wait, until there is a vacuum of
5.0 * 10^{-4} mbar.

2.2.

b) In the same menue at the control panel press the button T1 ***Gas-Menue*** before starting the data recording.
Now you will enter the Gas-Menue.

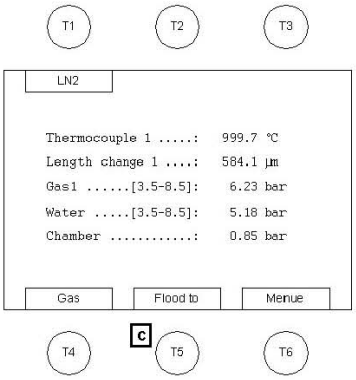

2.3.

c) Before starting the data recording press the button T5 ***Flood to*** at the control panel inside the Gas-Menue.

Now the chamber will be flooded until an under pressure of 0.2 bar will be reached.

BÄHR-Thermoanalyse GmbH

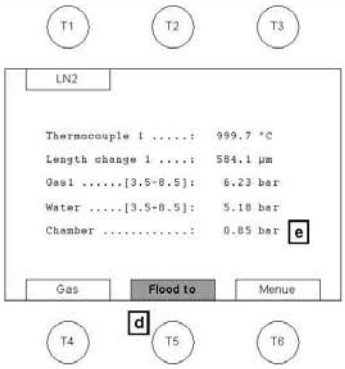

2.4.

d) The button T5 ***Flood to*** will be shown inverse while flooding.

e) You can control the value of under pressure at the control panel.

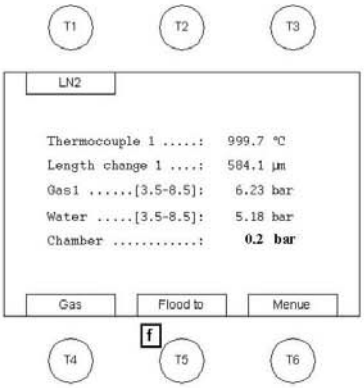

2.5.

f) If an under pressure of 0.2 bar is reached, the button T5 ***Flood to*** will be shown no more inverse and the flooding is stopped.

2.6.

Now you can start an experiment under the given atmosphere.

Important:
Please note, that you have to program **no gas and no vacuum** in the corresponding segments in the temperature program.

 2/2

APPENDIX-5: Complete thermal and their corresponding dilatation profiles of alloys A, B, C and D during the austenite to ferrite transformation

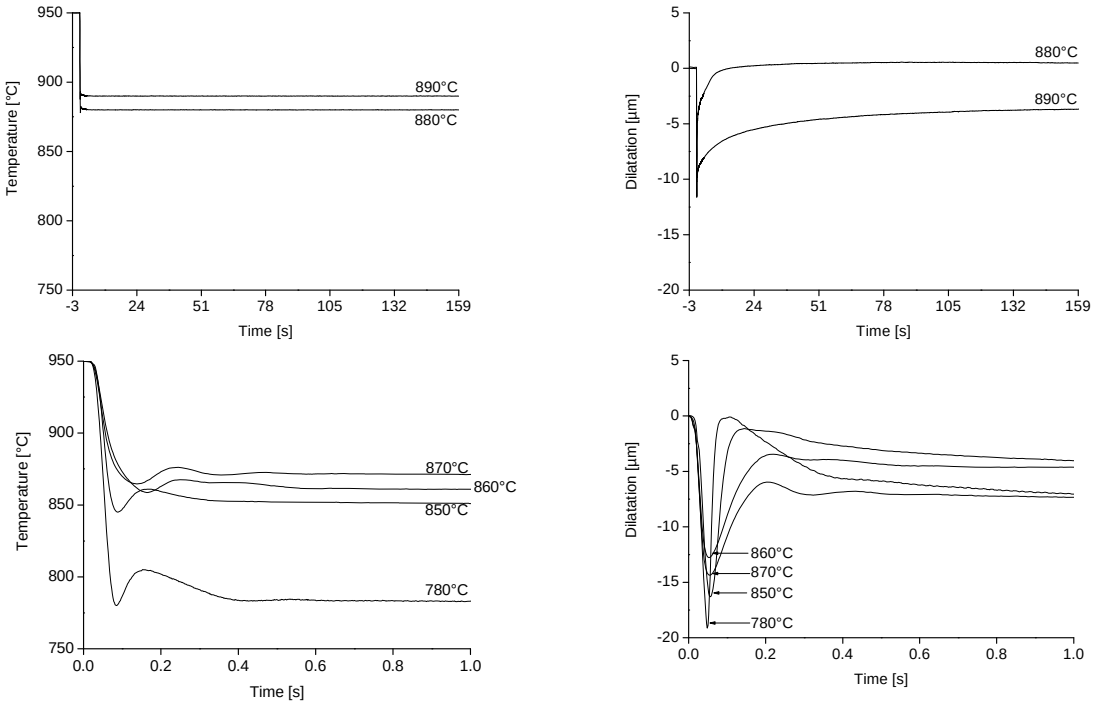

Hollow samples of alloy A

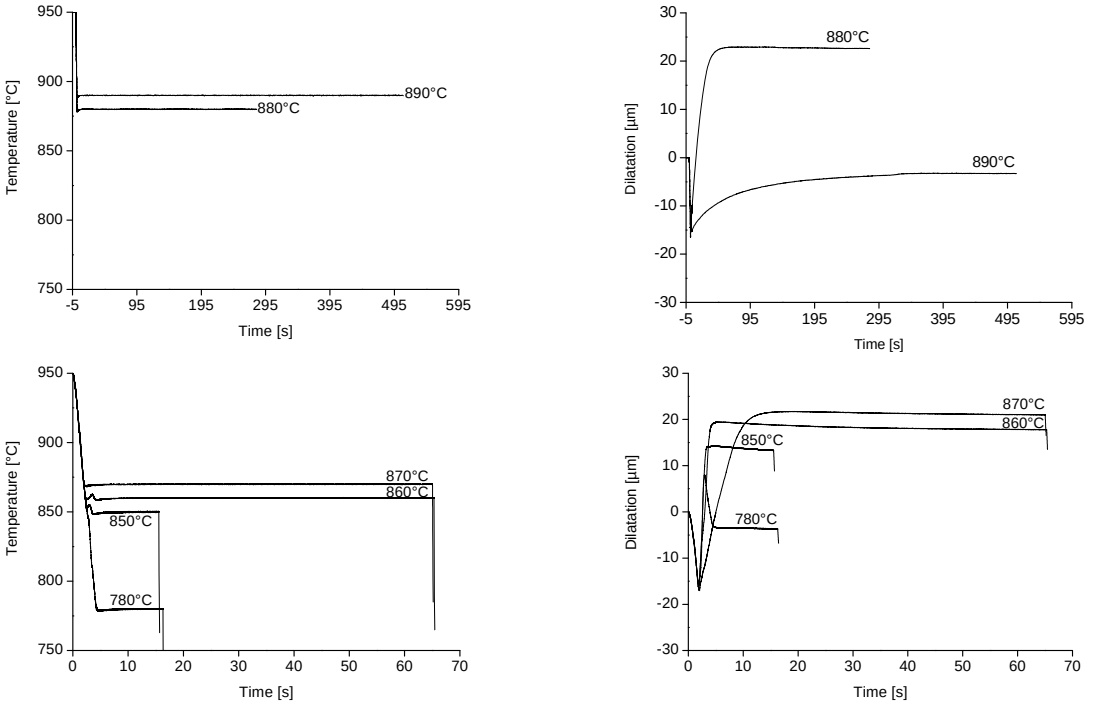

Solid samples of alloy A with T_{aus} of 950°C

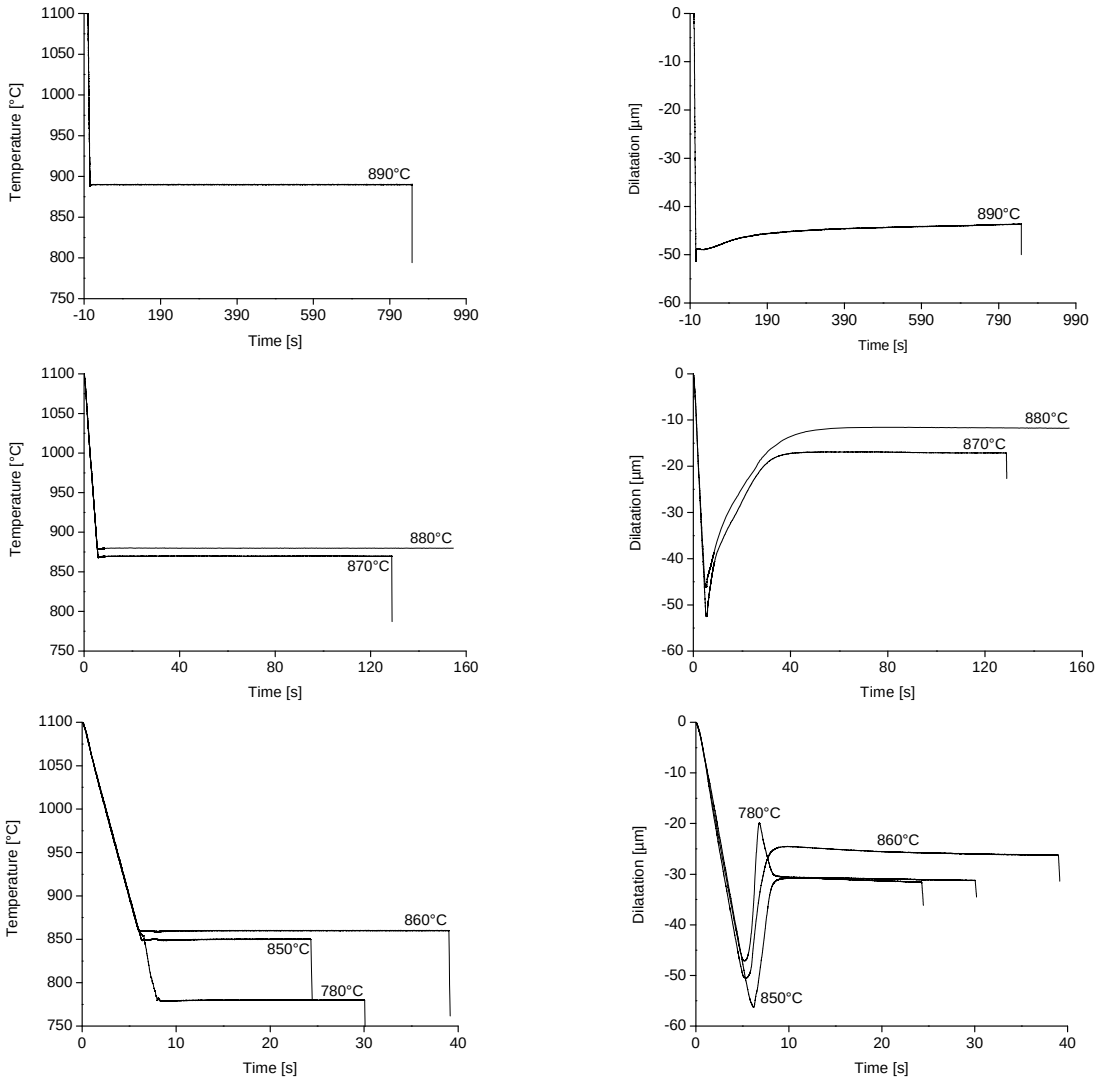

Solid samples of alloy A with T_{aus} of 1100°C

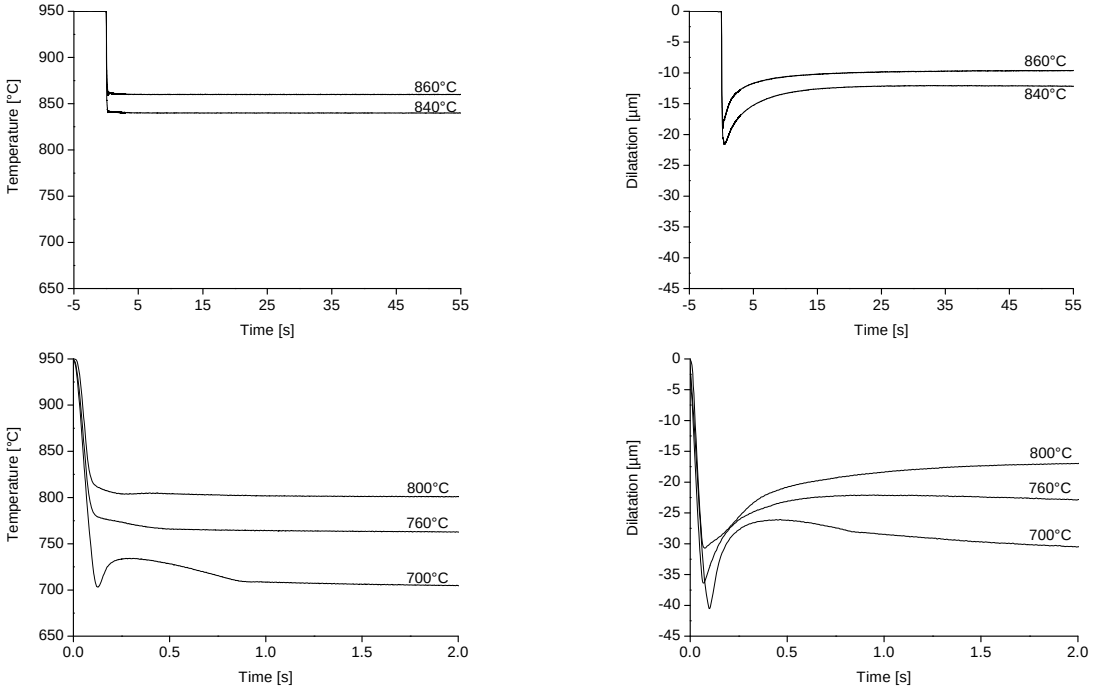

Hollow samples of alloy B

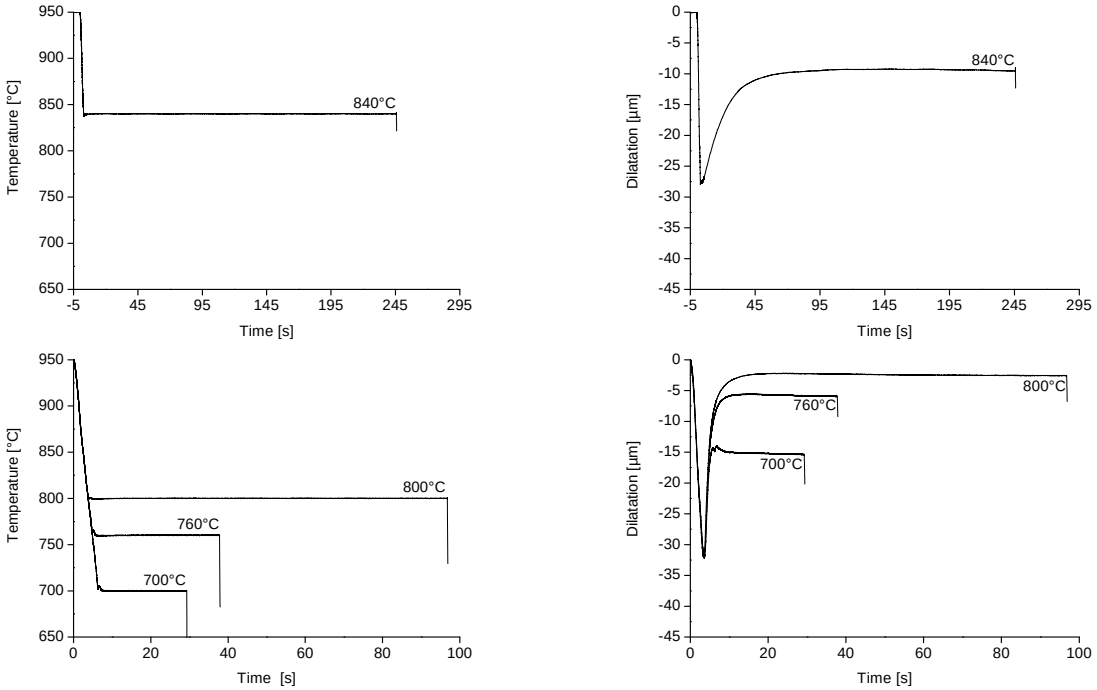

Solid samples of alloy B with T_{aus} of 950°C

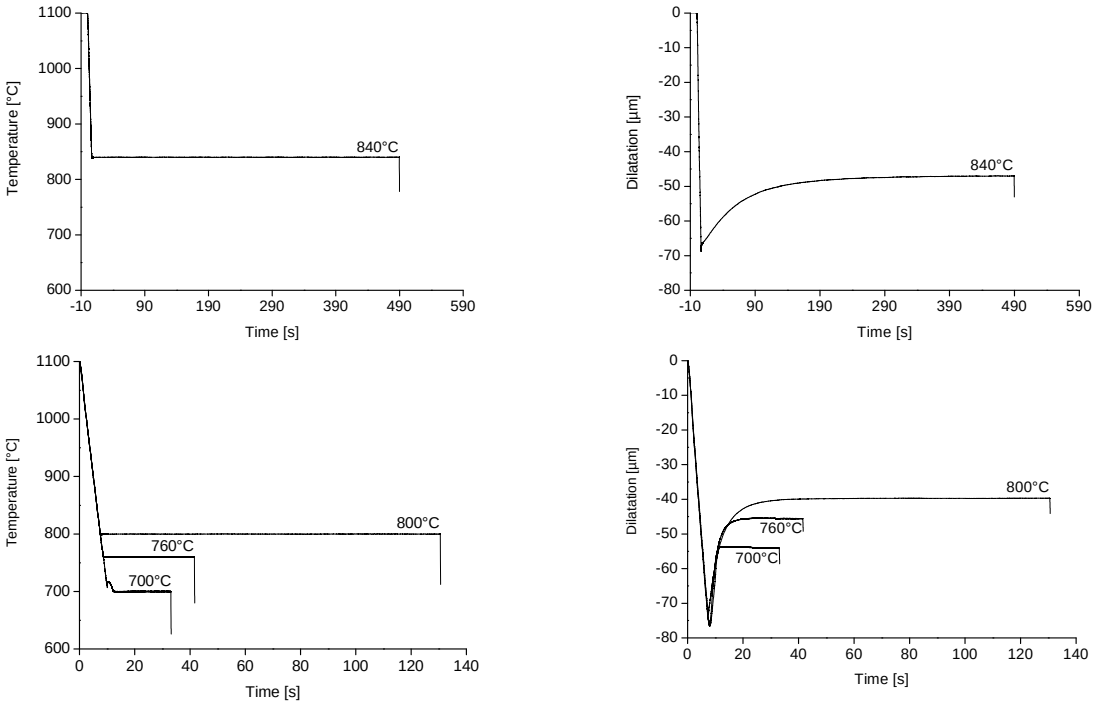

Solid samples of alloy B with T_{aus} of 1100°C

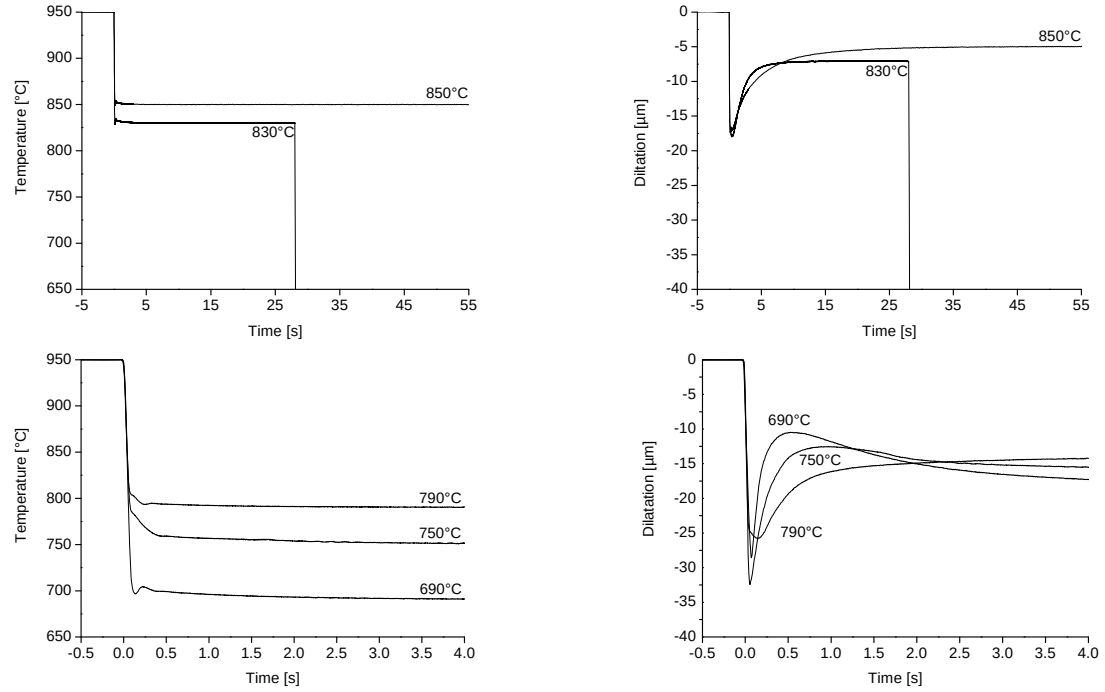

Hollow samples of alloy C

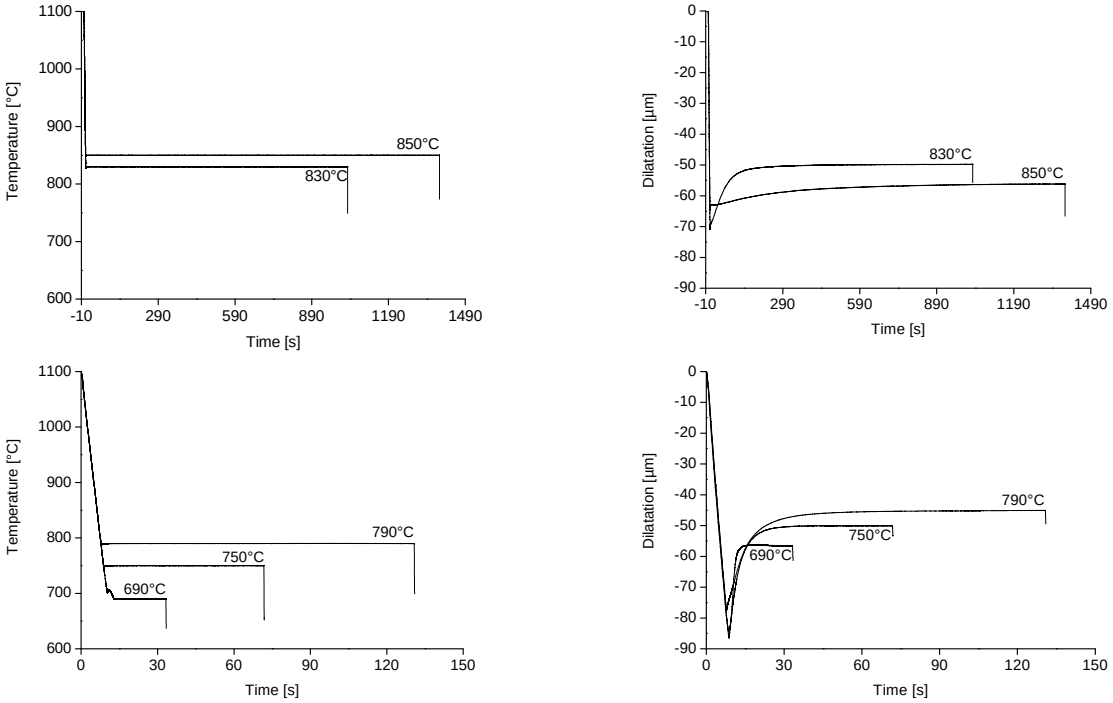

Solid samples of alloy C with T_{aus} of 950°C

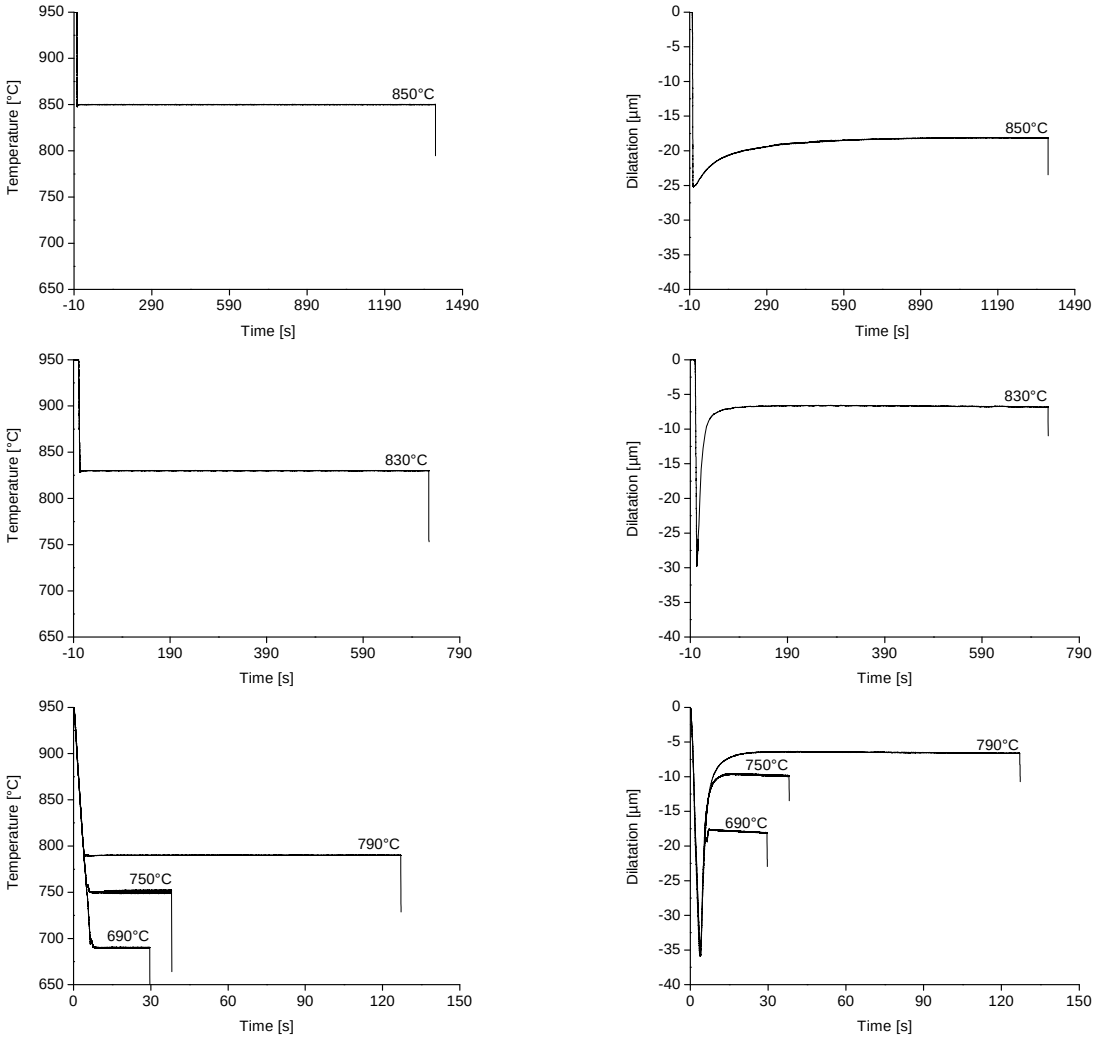

Solid samples of alloy C with T_{aus} of 1100°C

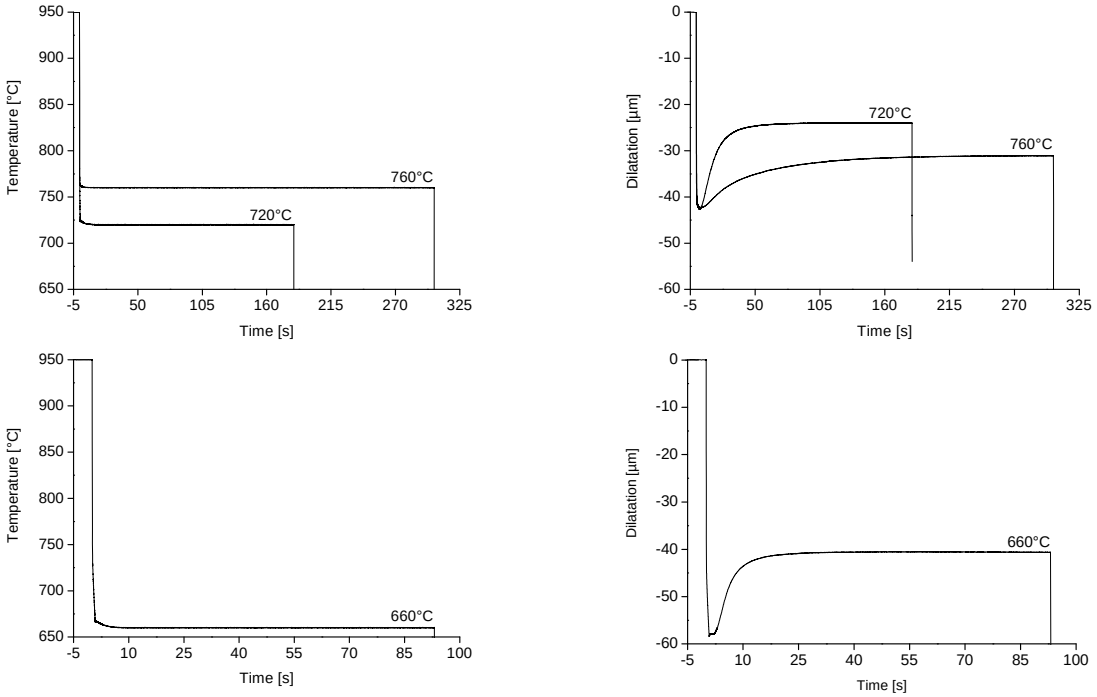

Hollow samples of alloy D

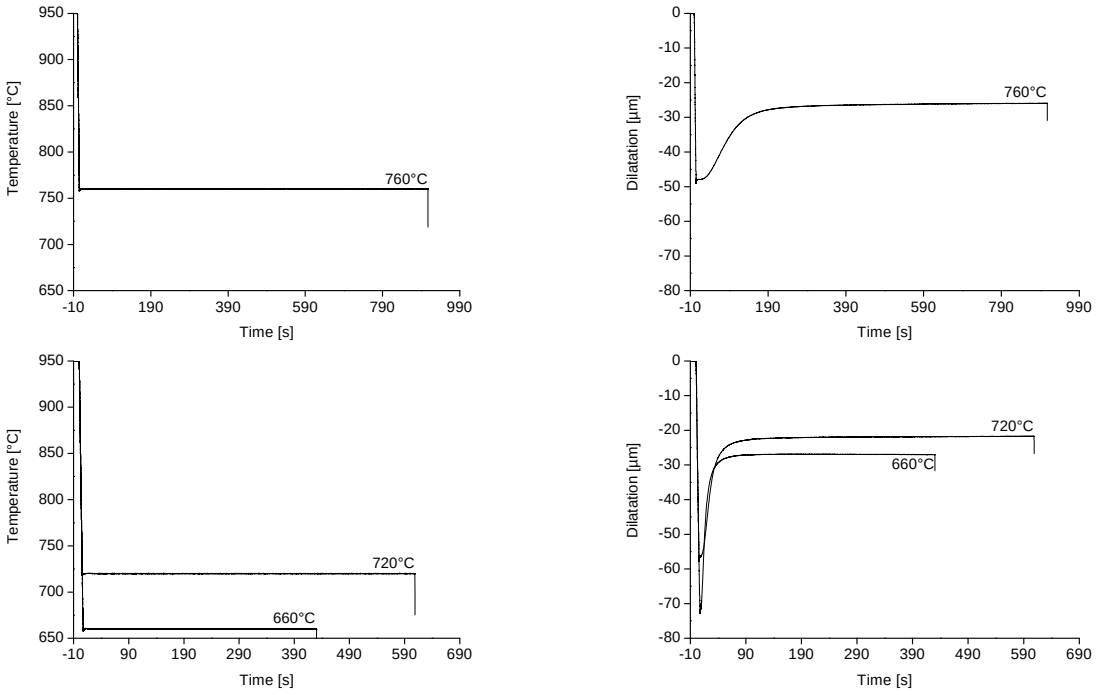

Solid samples of alloy D with T_{aus} of 950°C

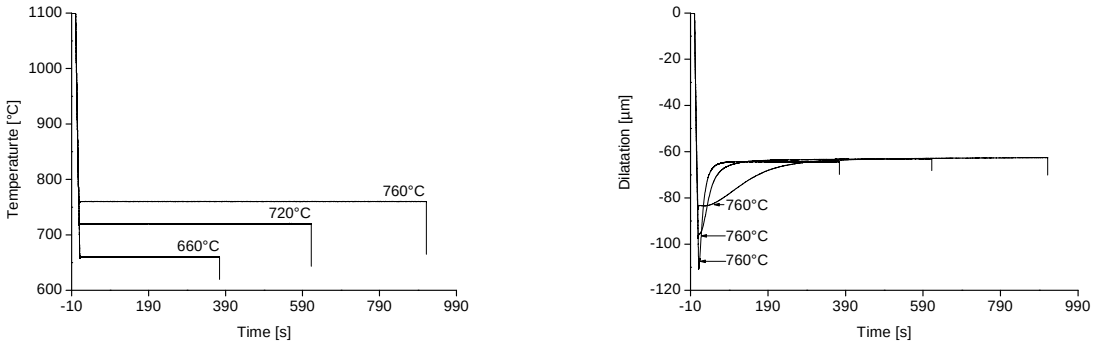

Solid samples of alloy D with T_{aus} of 1100°C

APPENDIX-6: Description of log file / marcofile used for obtaining position of interface profile with DICTRA

Generally for simulation purposes, a macrofile is made in the DICTRA software package. All variations are made in this macrofile and then it is executed for generation of desired profiles. For making a macrofile following command is used in the linux command line

Set_log_file

Afterward it will ask for the name of the file. If the name of the file, for example, is 'Farhan_I-TTP_alloy D' then the software will make the log file with the extension '.LOG' (i.e. Farhan_I-TTP_alloy D.LOG). Renaming this file with the extension '.DCM' will create the macrofile with the name 'Farhan_I-TTP_alloy D.dcm'.
Now the above mentioned log file and its reflection in the macrofile will be described. The macrofile / log file roughly can be divided into 10 blocks. The details of these blocks are given as under

(i). Database block: In this block, the database, elements and phases are defined. The database used was TDB-TCFE6 (TCS steel / Fe-Alloys Database V6). The elements used were iron (Fe), carbon (C), manganese (Mn) and silicon (Si) and the phases selected were austenite (fcc) and ferrite (bcc). Following block will show how entries are made in the log file and how these entries will appear in macrofile.

Log file	macrofile
D I C T R A service version 24(pl4) on Linux Copyright (1993,1995) Foundation for Computational Thermodynamics, Stockholm, Sweden Double precision version linked at 20-06-07 13:57:11 **SYS:set-log-file** **File name: Farhan_I-TTP_alloy D** **Heading:CREATING LOG FILE_FARHAN-PHD-KOZESCHNIK-2010** SYS: **SYS:go da** ... the command in full is GOTO_MODULE THERMODYNAMIC DATABASE module running on UNIX / KTH Current database: TCS Steels / Fe-Alloys Database v6 VA DEFINED IONIC_LIQ:Y L12_FCC B2_BCC B2_VACANCY HIGH_SIGMA DICTRA_FCC_A1 REJECTED **TDB_TCFE6:def-sp Fe C Mn Si** ... the command in full is DEFINE_SPECIES FE C MN SI DEFINED **TDB_TCFE6:rej ph * all** ... the command in full is REJECT GAS:G LIQUID:L BCC_A2 FCC_A1 HCP_A3 DIAMOND_FCC_A4 GRAPHITE CEMENTITE M23C6 M7C3 M5C2 KSI_CARBIDE A1_KAPPA KAPPA FE4N_LP1 FECN_CHI LAVES_PHASE_C14 M3SI CR3SI FE2SI MSI M5SI3 AL4C3 FE8SI2C SIC REJECTED **TDB_TCFE6:res ph fcc bcc** ... the command in full is RESTORE FCC_A1 BCC_A2 RESTORED **TDB_TCFE6:get** ... the command in full is GET_DATA REINITIATING GES5 ..... ELEMENTS ..... SPECIES ..... PHASES .... the command in full is AMEND_PHASE_DESCRIPTION	go da def-sp fe c mn si rej ph * all res ph fcc bcc get app _

... the command in full is AMEND_PHASE_DESCRIPTION PARAMETERS ... Rewind to read functions 23 FUNCTIONS .... List of references for assessed data 'A. Dinsdale, SGTE Data for Pure Elements, Calphad, 15 (1991), 317-425' 'P. Franke, estimated parameter within SGTE, 2007; Fe-C, Ni-C, Mo-C, C-Mn' 'P. Gustafson, Scan. J. Metall., 14 (1985), 259-267; TRITA 0237 (1984); C-FE' 'W. Huang, Metall. Trans. A, 21A (1990), 2115-2123; TRITA-MAC 411 (Rev 1989); C-FE-MN' 'J. Lacaze and B. Sundman, Metall. Mater. Trans. A, 22A (1991), 2211-2223; Fe-Si and Fe-Si-C' 'W. Huang, Calphad, 13 (1989), 243-252; TRITA-MAC 388 (rev 1989); FE-MN' 'J.E. Tibballs, SI Norway (1991) Rep. 890221-5; Mn-Si' 'J. Miettinen and B. Hallstedt, Calphad, 22 (1998), 231-256; Fe-Si and Fe-Si-C' 'A. Forsberg and J. Agren, J. Phase Equil., 14 (1993), 354-363; Fe-Mn-Si' 'X.-G. Lu, M. Selleby and B. Sundman, CALPHAD, Vol. 29, 2005, pp. 68-89; Molar volumes' 'X.-G. Lu, Thermo-Calc Software AB, Sweden,2006; Molar volumes' 'A. Markstrom, Swerea KIMAB, Sweden; Molar volumes' The list of references can be obtained in the Gibbs Energy System also by the command LIST_DATA and option R -OK-	

(ii). Mobility database: In this block mobility database was defined. Once again elements (Fe, C, Mn and Si) and phases (fcc and bcc) are defined. In the present simulations, mob2 (TCD Alloys Mobility Database V2) mobility database was used. Following block will show how entries are made in the log file and how these entries will appear in macrofile.

Log file	macrofile
TDB_TCFE6:app ... the command in full is APPEND_DATABASE Use one of these databases TCFE6 = TCS Steels/Fe-Alloys Database v6 PURE4 = SGTE Unary (Pure Elements) TDB v4 PSUB = TCS Public Pure Substances TDB v1 PBIN = TCS Public Binary Alloys TDB v1 PTERN = TCS Public Ternary Alloys TDB v1 PKP = Kaufman Binary Alloys TDB v1 PCHAT = Chatenay-Malabry Binary Alloys TDB v1 PG35 = G35 Binary Semi-Conductors TDB v1 PION = TCS Public Ionic Solutions TDB v2 PAQ2 = TCS Public Aqueous Soln (SIT) TDB v2 PAQS2 = TCS Public Aqueous Soln (HKF) TDB v2 PGEO = Saxena Pure Minerals Database v1 ALCCRNI = Al-C-Cr-Ni Database from ND COCRRE = Co-Cr-Re Database from ND COST99 = COST 99 database ALFENI = Al-Fe-Ni Database ALDATA = Al Database MOB2 = TCS Alloys Mobility Database v2 PFRIB = Fridberg Dilute Fe-Alloys MDB v1 FES = fes DUPA = dupa USER = User defined Database **DATABASE NAME /TCFE6/: mob2** Current database: TCS Alloys Mobility Database v2 VA DEFINED GAS:G REJECTED **APP:def-sys Fe C Mn Si** ... the command in full is DEFINE_SYSTEM FE C MN SI DEFINED **APP:rej ph * all** ... the command in full is REJECT BCC_A2 CEMENTITE DIAMOND_A4 FCC_A1 FE4N GRAPHITE HCP_A3 KSI_CARBIDE LIQUID:L M23C6 M5C2 M7C3	app mob2 def-sys fe c rej ph * all res ph fcc bcc get

REJECTED **APP:res ph fcc bcc** ... the command in full is RESTORE FCC_A1 BCC_A2 RESTORED **APP:get** ... the command in full is GET_DATA ELEMENTS ..... SPECIES ..... PHASES ..... PARAMETERS ... Rewind to read functions 4 FUNCTIONS .... List of references for assessed data 'This parameter has not been assessed' 'J. Agren: Scripta Met. 20(1986)1507-1510; C diffusion in fcc C-Fe' 'B. Jönsson: Scand. J. Metall. 23(1994)201-208; Fe and Ni diffusion fcc Fe-Ni' 'Assessed from data presented in Landholt-Börnstein, Volume 26, ed. H. Mehrer, springer (1990); Impurity diffusion of Fe in fcc Mn.' 'K. Nohara and K.-I. Hirano, Trans. Iron Steel Inst. Jpn., Suppl. 11 (1971)1267.; Impurity diffusion of Mn in fcc Fe.' 'Assessed from data presented in Landholt-Börnstein, Volume 26, ed. H. Mehrer, springer (1990); Impurity diffusion of Mn in fcc Mn.' 'D. Bergner et al., Defect and Diffusion Forum 66-69(1989)409. Impurity diffusion of Si in fcc Fe.' 'B. Jönsson: Z. Metallkunde 85(1994)498-501; C and N diffusion in bcc Cr-Fe-Ni' 'B. Jönsson: Z. Metallkunde 83(1992)349-355; Cr, Co, Fe and Ni diffusion in bcc Fe' 'B. Jönsson: Unpublished research bcc Fe-Si 1994' 'Assessed from data presented in Landholt-Börnstein, Volume 26, ed. H. Mehrer, springer (1990); Impurity diffusion of Mn in bcc Fe.' The list of references can be obtained in the Gibbs Energy System also by the command LIST_DATA and option R	

(iii). Heat treatment block: Following block will show how thermal cycle is entered in log file and then how these will appear in macrofile.

Log file	macrofile
APP:go d-m ... the command in full is GOTO_MODULE NO TIME STEP DEFINED **DIC>set-cond** ... the command in full is SET_CONDITION **GLOBAL OR BOUNDARY CONDITION /GLOBAL/:** **VARIABLE :T** **LOW TIME LIMIT /0/:** **T(TIME)=1223-time*40;** **HIGH TIME LIMIT /*/:4.75** **ANY MORE RANGES /N/: y** **T(TIME)=1033;** **HIGH TIME LIMIT /*/:*** **ANY MORE RANGES /N/: N**	go d-m set-cond GLOBAL T 0 1223-time*40; 4.75 y 1033; * N

(iv). Matrix block: Austenite was entered as matrix as during austenitization the only phase we have is austenite. In the austenite grain, ferrite is nucleated and afterwards its growth takes place. The entrance of austenite in the log file and its appearance in macrofile is shown as under

Log file	macrofile
DIC>enter-region **REGION NAME :austenite**	enter-region austenite

(v). Grain size block: In this block, austenite radius (half grain size) is registered. In the logfile and the macrofile these entries will look like

Log file	macrofile
DIC>enter-grid ... the command in full is ENTER_GRID_COORDINATES **REGION NAME : /AUSTENITE/:** **WIDTH OF REGION /1/: 12.5e-6** **TYPE /LINEAR/: geometric** **NUMBER OF POINTS /50/:** **VALUE OF R IN THE GEOMETRICAL SERIE :1.05**	enter-grid AUSTENITE 12.5e-6 geometric 50 1.05

(vi). Precipitate geometry definition block: The instruction for precipitate geometry in the log file and its appearance in the macrofile will look like

Log file	macrofile
DIC>enter-geo ... the command in full is ENTER_GEOMETRICAL_EXPONE **GEOMETRICAL EXPONENT /0/: 2**	enter-geo 2

(vii). Phase entry block: In our simulations, austenite is transformed to ferrite so two phases i.e. austenite (fcc) and ferrite (bcc) is defined once again. Austenite is entered as matrix phase and ferrite as inactive phase at time t=0. The entry of these in the log file and their appearance in the macrofile is shown as under

Log file	macrofile
DIC>enter-ph ... the command in full is ENTER_PHASE_IN_REGION ACTIVE OR INACTIVE PHASE /ACTIVE/: REGION NAME : /AUSTENITE/: PHASE TYPE /MATRIX/: PHASE NAME: /NONE/: fcc DIC> **DIC>enter-ph** ... the command in full is ENTER_PHASE_IN_REGION ACTIVE OR INACTIVE PHASE /ACTIVE/: inact ATTACH TO REGION NAMED /AUSTENITE/: ATTACHED TO THE RIGHT OF AUSTENITE /YES/: no PHASE NAME: /NONE/: bcc DEPENDENT SUBSTITUTIONAL SPECIES ? (FE,MN,SI) :fe REQUIRED DRIVING FORCE FOR PRECIPITATION: /1E-05/: 1e-4 CONDITION TYPE /CLOSED_SYSTEM/:	enter-phase ACTIVE AUSTENITE MATRIX fcc enter-phase inact AUSTENITE no bcc fe 1e-5 CLOSED_SYSTEM

(viii). Composition block: In the log file and macrofile this composition is registered as under

Log file	macrofile
DIC>enter-comp ... the command in full is ENTER_COMPOSITIONS **REGION NAME : /AUSTENITE/:** **PHASE NAME: /FCC_A1/: fcc#1** **DEPENDENT SUBSTITUTIONAL SPECIES ? (FE,MN,SI) :fe** **COMPOSITION TYPE /SITE_FRACTION/: w-p** **PROFILE FOR /C/:** **TYPE /LINEAR/:** **VALUE OF FIRST POINT :0.111** **VALUE OF LAST POINT : /.111/:** **PROFILE FOR /MN/:** **TYPE /LINEAR/:** **VALUE OF FIRST POINT :0.932** **VALUE OF LAST POINT : /.932/:** **PROFILE FOR /SI/:** **TYPE /LINEAR/:** **VALUE OF FIRST POINT :0.167** **VALUE OF LAST POINT : /.167/:** ... the command in full is CREATE_NEW_EQUILIBRIUM ... the command in full is COMPUTE_EQUILIBRIUM ... the command in full is COMPUTE_EQUILIBRIUM ... the command in full is COMPUTE_EQUILIBRIUM ... the command in full is COMPUTE_EQUILIBRIUM	enter-comp AUSTENITE fcc#1 fe w-p C LINEAR 0.111 .111 MN LINEAR 0.932 .932 SI LINEAR 0.167 .167

... the command in full is COMPUTE_EQUILIBRIUM **(Cont)** DIC>	

(ix). Simulation time block: In this block simulation time is defined. In the log file and macrofile, simulation time is registered as under

Log file	macrofile
DIC>set-sim-time **... the command in full is SET_SIMULATION_TIME** **END TIME FOR INTEGRATION /.1/: 1000** **AUTOMATIC TIMESTEP CONTROL /YES/:** **MAX TIMESTEP DURING INTEGRATION /100/:** **INITIAL TIMESTEP : /1E-07/:** **SMALLEST ACCEPTABLE TIMESTEP : /1E-07/:**	set-sim-time 1000 yes 100 1E-07 1E-07

(x). Simulation condition block: In this block simulation conditions are defined. These conditions are defined in the log file and macrofile as under

Log file	macrofile
DIC>s-s-c **... the command in full is SET_SIMULATION_CONDITION** **NS01A PRINT CONTROL : /0/:** **FLUX CORRECTION FACTOR : /1/:** **NUMBER OF DELTA TIMESTEPS IN CALLING MULDIF: /2/:** **CHECK INTERFACE POSITION /NO/:** **VARY POTENTIALS OR ACTIVITIES : /ACTIVITIES/:** **ALLOW AUTOMATIC SWITCHING OF VARYING ELEMENT : /YES/:** **SAVE WORKSPACE ON FILE (YES,NO,0-99) /YES/:** **DEGREE OF IMPLICITY WHEN INTEGRATING PDEs (0 -> 0.5 -> 1): /.5/: 1** **MAX TIMESTEP CHANGE PER TIMESTEP : /2/:** **USE FORCED STARTING VALUES IN EQUILIBRIUM CALCULATION /NO/:** **ALWAYS CALCULATE STIFFNES MATRIX IN MULDIF /YES/:** **DIC>save undercool1 y** ... the command in full is SAVE_WORKSPACES This file contains results from a previous SIMULATE_REACTION command. The SAVE command will save the current status of the program but destroy the results from the previous simulation.	s-s-c 0 1 2 NO ACTIVITIES YES YES 1 2 NO YES save undercool1 y set-inter

At this point the logfile is complete and now it should be saved to preserve the settings. Rename the logfile with the extension '.dcm'. For example in our case the log file was 'Farhan_I-TTP_alloy D.LOG', renaming will produce macrofile with the name 'Farhan_I-TTP_alloy D.dcm'.

Simulation start block: Now execute the macrofile. In DICTRA command lines for execution look like

D I C T R A service version 24(pl4) on Linux
Copyright (1993,1995) Foundation for Computational Thermodynamics,
Stockholm, Sweden
Double precision version linked at 20-06-07 13:57:11

SYS:m
Macro filename::

In the file name give the name of the macrofile (e.g. Farhan_I-TTP_alloy D.dcm). The software will start calculations. When following message is displayed then calculations are completed

MUST SAVE WORKSPACE ON FILE
WORKSPACE SAVED ON FILE
RECLAIMING WORKSPACE
DELETING TIME-RECORD FOR TIME 2.5214441
DELETING TIME-RECORD FOR TIME 2.7430689

```
 DELETING TIME-RECORD FOR TIME    2.7430690
 DELETING TIME-RECORD FOR TIME    2.7430692
 DELETING TIME-RECORD FOR TIME    2.7430696
 DELETING TIME-RECORD FOR TIME    2.7430704
 DELETING TIME-RECORD FOR TIME    2.7430720
 DELETING TIME-RECORD FOR TIME    2.7430752
.
.
DELETING TIME-RECORD FOR TIME    9.2609480
 DELETING TIME-RECORD FOR TIME    15.477494
 DELETING TIME-RECORD FOR TIME    27.910585
 DELETING TIME-RECORD FOR TIME    52.776768
 DELETING TIME-RECORD FOR TIME    102.50913
 DELETING TIME-RECORD FOR TIME    201.97386
 DELETING TIME-RECORD FOR TIME    301.97386
 DELETING TIME-RECORD FOR TIME    401.97386
 DELETING TIME-RECORD FOR TIME    501.97386
 DELETING TIME-RECORD FOR TIME    601.97386
 DELETING TIME-RECORD FOR TIME    701.97386
 DELETING TIME-RECORD FOR TIME    801.97386

 KEEPING TIME-RECORD FOR TIME    901.97386
 AND FOR TIME                 1000.0000
 WORKSPACE RECLAIMED
```

(xii). Output block: Our output profile is position of interface as a function of time. So first our objective is to obtain this profile in graphical form. For graphical output following setting have to be made

```
DIC>post

  POST PROCESSOR VERSION   1.7
  Implemented by Bjorn Jonsson

POST-1:s-d-a y position austenite lower
POST-1:s-d-a x time
  INFO: Time is set as independent variable
POST-1:s-p-c
CONDITION /INTERFACE/:
INTERFACE :austenite
UPPER OR LOWER INTERFACE OF REGION AUSTENITE#1 /LOWER/:
POST-1:
POST-1:set-axis-type x log
POST-1:s-s-s x n 0.01 1000
POST-1:
POST-1:plot screen
```

The exceed software will display the position of interface as a function of time.

(xiii). Transporting data block: This block is additionally added to transport the data for redrawing in other software packages such as excel or origin. The data is transported in tables. To obtain the table following instruction have to be passed to the software.

```
POST-1:enter
Function or table /FUNCTION/: table
NAME:b
Variable(s)poi(aus,l)
POST-1:tab
Name :b
Output file /SCREEN/: alloyD
```

As the above commands are executed, we get a file with the name ‘alloyD’. This contains the portable data for redrawing the position of interface as a function of time in excel or origin.

APPENDIX-7: List of equipment and software packages used

1. High-Speed Quenching Dilatometer 805A (by BÄHR Thermoanalyse)

2. Spot Welding Machine

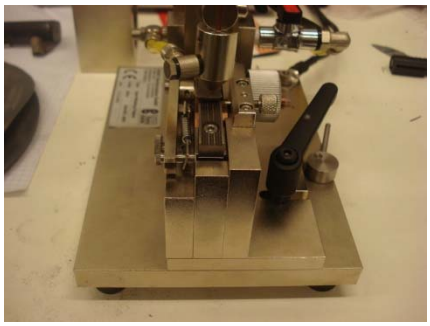

3. Grinding and Polishing Equipment (by STRUERS)

TEGRA DOSER-5

TEGRA FORCE-5

TEGRA POL-31

COMPLETE EQUIPMENT

4. MICROSCOPE (by ZEISS)

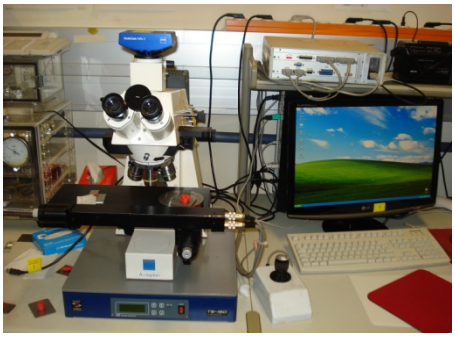

5. MatCalc ([11], [12])
6. DICTRA [13]
7. AxioVision [36]
8. CES EduPack 2009 software [37]
9. ImageJ [39]
10. Exceed [40]